Nanomaterials Design for Lithium-Sulfur Batteries

A thesis presented for the award of the degree of

Doctor of Philosophy

From

University of Technology Sydney

By

Yi Chen, B.Eng., M.Eng.

June, 2020

CERTIFICATE OF ORIGINAL AUTHORSHIP

I, Yi Chen declare that this thesis, is submitted in fulfilment of the requirements for the award of Doctor of Philosophy, in the School of Mathematical and Physical Sciences, Faculty of Science at the University of Technology Sydney.

This thesis is wholly my own work unless otherwise reference or acknowledged. In addition, I certify that all information sources and literature used are indicated in the thesis.

This document has not been submitted for qualifications at any other academic institution.

This research is supported by the Australian Government Research Training Program.

Production Note:
Signature: Signature removed prior to publication.

Date: 25/02/2020

DEDICATION

This thesis is dedicated to my family. Appreciate their love and support.

ACKNOWLEDGEMENTS

First of all, I would like to offer my heartfelt appreciation to my supervisor, Professor Guoxiu Wang, for his invaluable instruction and guidance. Professor Wang has full passion for scientific research, which largely affects and inspires me during my PhD period.

I would also like to thank my co-supervisor, Dr. Dawei Su, for his selfless help, patient guidance and constant support during my PhD period.

Special thanks are expressed to my colleagues in the Centre for Clean Energy Technology at UTS, for their kind help and cooperation during the past years. I would like to specially thank the lab manger, Dr. Jane Yao, for her professional management on the lab, which can make us fully devote our time into research.

In addition, I would like to thank the administrative and technical support from I received from Ronald Shimmon, Katie McBean, Herbert Yuan, Mark Lockrey, Alexander Angeloski, Linda Xiao, Mark Berkahn. I also take this chance to thank the financial support from Australian Renewable Energy Agency and Australian Research Council.

Last but not least, I would like to express my deeply grateful to my parents for their selfless love and fully support over the past years. Thank you, Dad and Mom!

PUBLICATIONS

(1) **Y. Chen**, D. Su, Q. Zhang, G. Wang, 60 Years of Lithium-Sulfur Batteries: From Academic Research to Commercial Viability, ***Adv. Mater.***, Submitted.

(2) **Y. Chen**, S. Choi, D. Su, X. Gao, G. Wang, Self-standing sulfur cathodes enabled by 3D hierarchically porous titanium monoxide-graphene composite film for high-performance lithium-sulfur batteries, ***Nano Energy***, 2018, 47, 331-339. (IF=15.548)

(3) **Y. Chen**, W. Zhang, D. Zhou, H. Tian, D. Su, C. Wang, D. Stockdale, F. Kang, B. Li, G. Wang, Co-Fe Mixed Metal Phosphide Nanocubes with Highly Interconnected-Pore Architecture as an Efficient Polysulfide Mediator for Lithium-Sulfur Batteries, ***ACS Nano***, 2019, 13, 4731-4741. (IF=13.903)

(4) D. Zhou, **Y. Chen**, B. Li, H. Fan, F. Cheng, D. Shanmukaraj, T. Rojo, M. Armand, G. Wang, A Stable Quasi-Solid-State Sodium-Sulfur Battery, ***Angew. Chem. Int. Ed.***, 2018, 57, 10168-10172. (IF=12.102)

(5) H. Tian, X. Yu, H. Shao, L. Dong, **Y. Chen**, X. Fang, C. Wang, W. Han, G. Wang, Unlocking Few-Layered Ternary Chalcogenides for High-Performance Potassium-Ion Storage, ***Adv. Energy Mater.***, 2019, 9, 1901560. (IF=24.884)

(6) H. Tian, H. Shao, **Y. Chen**, X. Fang, P. Xiong, B. Sun, P. H. Notten, G. Wang, Ultra-stable sodium metal-iodine batteries enabled by an in-situ solid electrolyte interphase, ***Nano Energy***, 2019, 57, 692-702. (IF=15.548)

(7) X. Gao, D. Zhou, **Y. Chen**, W. Wu, D. Su, B. Li, G. Wang, Strong charge polarization effect enabled by surface oxidized titanium nitride for lithium-sulfur batteries, ***Commun. Chem***., 2019, 2, 1-10.

(8) J. Song, X. Guo, J. Zhang, **Y. Chen**, C. Zhang, L. Luo, F. Wang, G. Wang, Rational design of free-standing 3D porous MXene/rGO hybrid aerogels as polysulfide reservoirs for high-energy lithium-sulfur batteries, ***J. Mater. Chem. A***, 2019, 7, 6507-6513. (IF=10.733)

(9) J. Xu, W. Zhang, **Y. Chen**, H. Fan, D. Su, G. Wang, MOF-derived porous N-Co_3O_4@N-C nanododecahedra wrapped with reduced graphene oxide as a high capacity cathode for lithium-sulfur batteries, ***J. Mater. Chem. A***, 2018, 6, 2797-2807. (IF=10.733)

TABLE OF CONTENTS

LIST OF TABLES

LIST OF FIGURES

sphere, and ii) effective lithium polysulfides entrapment and structural integrity of MoS_2-encapsulated hollow sulfur sphere upon lithiation/delithiation. (b-d) *In-situ* TEM images of MoS_2-encapsulated hollow sulfur spheres upon continuous lithiation and delithiation process. (a-d) Reproduced from reference[209]. Copyright 2017, American Chemical Society. (e) Schematic of the synthesis process of MoS_{2-x}/rGO composite and the conversion of sulfur species on its surface. (f) HR-TEM image of MoS_{2-x}/rGO composite. (g) Comparison of the cycling performances of rGO/S, MoS_2/rGO/S and MoS_{2-x}/rGO/S cathodes at 0.5C. (e-g) Reproduced from reference[210]. Copyright 2017, Royal Society of Chemistry. (h) SEM and (i) TEM images of ZnS nanospheres. (j) CVs of Li_2S_6 and Li_2S_6-free symmetrical cells with ZnS-CB as working electrodes. (k) Illustration of the promoted redox reaction of polysulfide conversion by the catalyzing of ZnS nanospheres during discharge. (l) Comparison of the cycling performances of ZnS-CB/S and CB/S cathodes at 0.2C. (h-l) Reproduced from reference[211]. Copyright 2018, Elsevier. (m) Digital images of Li_2S_6 solution after interaction with carbon and different kinds of metal sulfides. Atomic geometries and binding energies of Li_2S_6 adsorption on (n) Ni_3S_2, (o) SnS_2, (p) FeS, (q) CoS_2, (r) VS_2 and (s) TiS_2, respectively. (m-s) Reproduced from reference[212]. Copyright 2017, National Academy of Sciences. 51

Figure 1.18 (a) In situ XRD measurements of a Li|Mo_6S_8/S_8 cell. (b) Illustration of the discharge process of intercalation-conversion hybrid cathodes of Mo_6S_8/S_8. (c) Cycling performance of the hybrid cathodes with 6.2 mg cm^{-2} S_8 loading and 6.1 mg cm^{-2} Mo_6S_8 loading. (d) The pouch-cell configuration constructed by the Mo_6S_8/S_8 cathode with an ultralow electrolyte/active material ratio of ~1.2 μL mg^{-1} and ~2×Li excess (100 μm for one side). (a-d) Reproduced from reference[213]. Copyright 2019, Nature Publishing Group. (e) XRD pattern of the MoS_3. The inset shows the schematic structure of the 1D chain-like MoS_3. (f) TEM image of MoS_3/CNT composite. (g) Charge-discharge curves of MoS_3 cathodes in carbonate based electrolyte. (h) Cycling performance of the MoS_3 cathode. (e-f) Reproduced from reference[214]. Copyright 2017, National Academy of Sciences. 55

Figure 1.19 (a) SEM image of mesoporous TiN. Reproduced from reference[241]. Copyright 2016, Wiley-VCH. (b) Schematic of the mesoporous TiN-O-OMC. (c) TEM and (d) HR-TEM images of mesoporous TiN-O-OMC. (b-d) Reproduced from reference[244]. Copyright 2019, Nature Publishing Group. (e) SEM image of Co_4N nanosheets assembled mesoporous sphere. (f) Optical images of Li_2S_6 solutions after adding equal amounts of super P, Co_3O_4 and Co_4N, respectively. (g) Co $2p_{3/2}$ XPS spectra of CoN_4 phase and Co_4N/Li_2S_6, respectively. (h) Cycling performances and Coulombic efficiencies of Co_4N/S cathodes at 2C and 5C, respectively. (e-h) Reproduced from reference[246]. Copyright 2017, American Chemical Society. (i) Optical image of VN/G composite foams. (j) TEM image of VN/G composite. (i,j) Reproduced from reference[247]. Copyright 2017, Nature Publishing Group. (k) Schematic of sulfur loaded-VN nanobubble. (l) TEM image of a single VN nanobubble. (k,l) Reproduced from reference[248]. Copyright 2017, American Chemical Society. 59

Figure 1.20 (a) EIS and (b) CV of Li_2S_6 symmetric cells with different working electrodes. (c) Potentiostatic discharge curves of a Li_2S_8/tetraglyme solution at 2.05 V on different substrates. The lighter and darker colors represent the precipitation of Li_2S and reduction of Li_2S_8/Li_2S_6, respectively. (d-f) SEM images of the precipitated Li_2S on different substrates as indicated in c. (g) Cycling performances of TiC@G/S and TiO_2@G/S electrodes at 0.2C. (a-g) Reproduced from reference[250]. Copyright 2016, Wiley-VCH. TEM images of (h) W_2C NPs-CNFs, (i) Mo_2C NPs-CNFs and (j) TiC NPs-CNFs, respectively (scale bars=200 nm). (k) Photographs of the Li_2S_6 adsorption by different powders in DOL/DME (1:1, v/v) solution. Optimized geometries of Li_2S_6 adsorbed on (001) planes of (l) W_2C, (m) Mo_2C and (n) TiC, respectively. (o) CV curves of Li_2S_6 symmetric cells using W_2C NPs-CNFs, Mo_2C

ABSTRACT

Lithium-sulfur (Li-S) batteries, which rely on the redox reactions, show great promise for next-generation energy storage owing to their high theoretical energy density, environmental benignity and low cost of sulfur. However, the practical application of Li-S batteries has been largely impeded by the low conductivity of sulfur and the shuttle effect of polysulfides. One of the most effective strategies to overcome these problems is to disperse insulating sulfur active material within other conductive matrixes that are capable of physically adsorbing and/or chemically binding sulfur and its intermediate polysulfides. In this thesis, we designed two types of host materials that can be used to improve the electrochemical performance of Li-S batteries.

A new self-standing host enabled by a 3D hierarchically-porous titanium monoxide-graphene composite film was designed to overcome the main challenges of Li-S batteries. The hierarchically porous graphene scaffold can not only facilitate rapid lithium ion and electron transport, but also provide sufficient spaces to accommodate sulfur species. In addition, the ultrafine and polar titanium monoxide nanoparticles embedded in the three-dimensional graphene networks show strong chemical anchoring for polysulfides, and their inherent metallic conductivity accelerates the redox reaction kinetics. Benefiting from this attractive architecture, the freestanding titanium monoxide-graphene/sulfur cathode demonstrated superior electrochemical performance for Li-S batteries.

Uniform Co-Fe mixed metal phosphide (Co-Fe-P) nanocubes with highly interconnected-pore architecture were synthesized as sulfur host for Li-S batteries. With the

highly interconnected-pore architecture, inherently metallic conductivity and polar characteristic, the Co-Fe-P nanocubes not only offer sufficient electrical contact to the insulating sulfur for high sulfur utilization and fast redox reaction kinetics, but also provide abundant adsorption sites for trapping and catalyzing the conversion of lithium polysulfides to suppress the shuttle effect. As a result, the sulfur-loaded Co-Fe-P (S@Co-Fe-P) nanocubes exhibited superior electrochemical performances both in coin cells and pouch cells.

INTRODUCTION

With the ever-increasing world population and massive consumption of fossil fuels, there is urgent need to develop renewable and clean energy to satisfy the rising demand for energy in our modern lifestyle.[1-3] However, the renewable energy sources such as solar and wind power are intermittent in nature. Therefore, it is crucial to utilize advanced energy storage systems to store the energy when it is present in excess and release it back to grid when it is necessary, thus to sustain a continuous power supply for our daily life.[4, 5] This is where rechargeable batteries can play a vital role in electrochemically storing and releasing the energy reversibly.[6-9] Unfortunately, lithium-ion batteries, which have dominated the portable electronics over the past three decades, are unable to meet the high-energy demand for emerging applications such as grid-scale energy storage and electrical vehicles.[4, 10-15] This is because the conventional lithium-ion batteries rely on the intercalation-type electrode materials and the lithium ions can only be intercalated topologically into certain specific sites, which limits their charge-storage capacity and energy density.[16-21] Therefore, exploring new battery chemistries beyond the horizon of current lithium-ion batteries is crucial for a sustainable future.[22, 23]

To realize a high energy density with new battery chemistries, seeking new types of electrode materials is a prerequisite.[24] Lithium metal, which has the highest theoretical specific capacity of 3860 mA h g^{-1} among the anode materials and the lowest electrochemical potential of -3.04 V versus the standard hydrogen electrode, is regarded as the “Holy Grail” anode material for next-generation batteries.[25-29] Sulfur, which is abundant, cheap and

environmentally benign, can offer a high theoretical specific capacity of 1675 mA h g^{-1} when paired with lithium metal, which is among the highest in solid cathode materials.[30] This is because the sulfur cathode undergoes a conversion reaction mechanism rather than the intercalation chemistry. Together with an average cell voltage of 2.15 V, the coupled lithium-sulfur (Li-S) battery can attain a high theoretical energy density of 2500 W h kg^{-1}, which is much higher than that of current lithium-ion batteries.[16, 17, 31-34]

In spite of these attractive benefits, the practical implementation of Li-S batteries is plagued with several bottlenecks, including the poor conductivity of sulfur and lithium sulfide, the dissolution and shuttle effect of polysulfides, and the huge volume change upon cycling.[33, 35] These dilemmas lead to low sulfur utilization efficiency and rapid capacity decay upon cycling. Therefore, various methods have been developed to solve these problems, including melting sulfur into the conductive matrix,[31, 36, 37] modification of separators,[38-40] appending interlayers,[41, 42] developing new electrolytes or additives,[43-46] and applying functionalized binders.[44, 47-51] Among these strategies, infiltrating sulfur into host materials is the most popular method due to their superior conductivity, large surface area and diversity in nanostructures.[31, 37, 52, 53]

This thesis mainly focuses on designing effective host materials to encapsulate sulfur for improving the performance of Li-S batteries. Each chapter of this thesis is outlined as follows:

(1) Chapter 1 is the literature review which mainly introduces the research background and progress of Li-S batteries. First, it describes the mechanism and challenges of Li-S batteries. We start by stating the principles and challenges of Li-S batteries, followed by

reviewing the designing strategies to address these problems and improve the performance of Li-S batteries. The designing strategies can be classified into 5 parts: designing nanostructured sulfur based composite cathode, seperator modification, binder improvement, electrolyte optimization and lithium metal protection.

(2) Chapter 2 is the general experimental methods and characterizations. It can be divided into three parts including materials preparation, materials characterization and electrochemical measurements. Solid state reaction and solution reaction are mainly used to prepare the materials used in this doctoral work. The structure and morphology of the prepared materials are characterized by X-ray diffraction (XRD), scanning electron microscopy (SEM), transmission elelctron microscopy (TEM), X-ray photoelectron spectroscopy (XPS), Raman spectroscopy, etc. Cell assemble and electrochemical measurements were also presented.

(3) In chapter 3, a new sulfur host material enabled by Magnéli phase titanium monoxide nanoparticle-graphene composite (TiO-G) film was fabricated to combine the merits of a self-standing property, high conductivity, polar characteristic and high porosity in one host. The freestanding interconnected graphene scaffold with three-dimensional (3D) architecture provides excellent electron transport properties, and its hierarchically porous structure facilitates electrolyte wettability and rapid lithium ion transport throughout the entire electrode architecture. Furthermore, the highly polar and ultrafine TiO nanoparticles throughout the graphene networks not only show strong chemical entrapment for the intermediate polysulfides, but also accelerate the redox reaction kinetics. Benefiting from this attractive architecture, the TiO-G/S cathode delivered a high specific capacity of 1350 mAh

g^{-1} at 0.1 C, a Coulombic efficiency approaching 100%, and a high rate performance of 832 mAh g^{-1} at 2 C. In addition, when the areal sulfur loading was increased to 5.2 mg cm^{-2}, the TiO-G/S electrode delivered a high areal capacity of 3.2 mAh cm^{-2} after 300 cycles at 0.2 C, demonstrating excellent cycling stability compared with other recently reported sulfur cathodes with high areal sulfur loadings.

(4) In chapter 4, uniform Co-Fe mixed metal phosphide (Co-Fe-P) nanocubes with highly interconnected-pore architecture were synthesized as an efficient polysulfide mediator for Li-S batteries. The obtained Co-Fe-P nanocubes have several pivotal advantages as sulfur host materials for Li-S batteries. Firstly, the abundant and interconnected-pore architecture provides sufficient space for sulfur loading and buffers the volume change upon cycling. Secondly, the polar Co-Fe-P nanocubes with interconnected-pore architecture can supply adequate interfaces to chemically anchor the intermediate polysulfides and further promote the kinetics of polysulfide conversion, thus suppressing the shuttle effect. Thirdly, the inherently metallic conductivity facilitates the redox reaction kinetics and maximizes the sulfur utilization efficiency. Benefiting from the above merits, the sulfur-loaded Co-Fe-P (S@Co-Fe-P) nanocubes exhibited high specific capacity, superior rate performance and excellent cycling stability for Li-S batteries. Moreover, the S@Co-Fe-P electrode showed high areal capacity with good stability at a high areal sulfur loading of 5.5 mg cm^{-2}. Impressively, the commercial size soft-package Li-S batteries based on S@Co-Fe-P cathodes also demonstrated superior cycling stability with good flexibility, indicating their great potential for practical applications.

The last chapter (chapetr 5) of this thesis summarizes the research outcomes of this doctoral work and future dirctions of related research is also presented.

Chapter 1 Literature Review

1.1 Principles and challenges of Li-S batteries

Li-S batteries work relying on the reversible redox reactions between lithium and S_8 (**Figure 1.1**a). During discharge, the lithium metal at the anode side is oxidized to release lithium ions and electrons, which pass through the electrolyte and external circuit respectively to the sulfur cathode side. At the cathode side, the sulfur is reduced to generate lithium sulfide by accepting the lithium ions and electrons. The backward reactions occur during the charge process.

Discharge:

Anode: $Li \rightarrow Li^+ + e^{-1}$

Cathode: $S_8 + 16Li^+ + 16e^{-1} \rightarrow 8Li_2S$

Charge:

Cathode: $8Li_2S \rightarrow S_8 + 16Li^+ + 16e^{-1}$

Anode: $Li^+ + e^{-1} \rightarrow Li$

Although the described electrochemical reactions look so simple, the actual reactions are quite complex, which involve a two stage transformation process during the discharge. **Figure 1.1**b exhibits a typical charge-discharge voltage profile of Li-S batteries in ether-based electrolytes. During discharge, cyclo-S_8 is first lithiated to form soluble Li_2S_8, and subsequently to Li_2S_6 and Li_2S_4 with an average potential of about 2.3 V, which contributes 25% of the theoretical capacity of sulfur (418 mA h g^{-1}). Upon further lithiation, the soluble Li_2S_4 is transformed into solid short chain sulfides Li_2S_2 and Li_2S that

re-precipitate on the electrode, corresponding to an average voltage of about 2.1 V, which makes up 75% of the theoretical capacity of sulfur (1254 mA h g^{-1}). During the subsequent charging process, Li_2S releases lithium ions into electrolyte and was reconverted into intermediate lithium polysulfides, followed by forming the original product S_8, resulting in a reversible cycle.

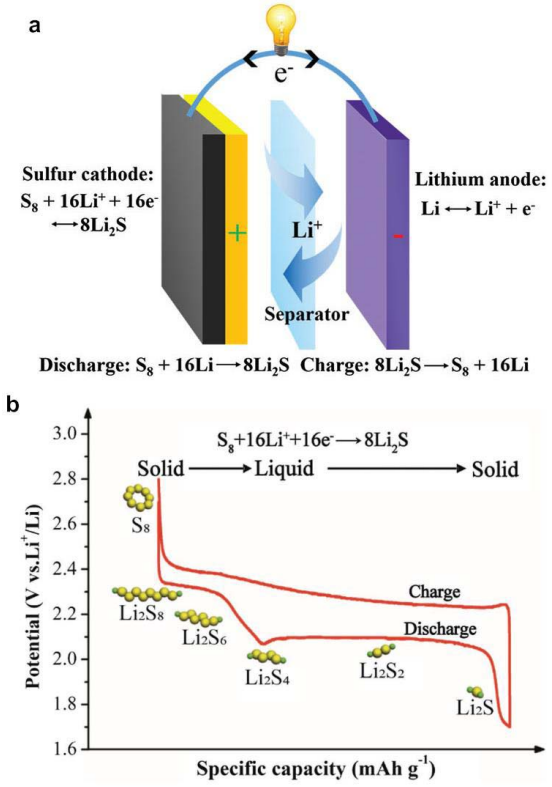

Figure 1.1 (a) Schematic of the electrochemistry for Li-S batteries. Reproduced from reference[17]. Copyright 2016 Royal Society of Chemistry. (b) A typical charge-discharge voltage profile of Li-S batteries in ether-based electrolyte. Reproduced from reference[54]. Copyright 2017, Wiley-VCH.

Despite the high energy advantage of Li-S batteries, the practical application of Li-S batteries is plagued with several intractable challenges. On the sulfur cathode side, the challenges include the following aspects.

(i) The low conductivity of sulfur and lithium sulfide. Both sulfur and its discharged product lithium sulfide are insulating for electrons and lithium ions, which limits the redox kinetics at the cathode side. This can lead to low sulfur utilization and eventually low specific capacity.

(ii) The dissolution and shuttle effect of intermediate polysulfides. The intermediate polysulfides generated during the cycling process are readily to be dissolved into the electrolyte, followed by shuttling from the cathode to the anode side. This can result in the low Coulombic efficiency and severely capacity fading.

(iii) The volume expansion during the lithiation from sulfur to lithium sulfide. Given the different density of sulfur (2.07 g cm^{-3}) and lithium sulfide (1.66 g cm^{-3}), the sulfur undergoes a huge volume expansion of about 80% upon full lithiation. This can lead to the pulverization of electrode after repeated volume change of the cathode upon cycling, which results in the poor cycling performance.

On the lithium anode side, there are also some intractable problems that need to be resolved before the large-scale practical application of Li-S batteries. These include the following issues.

(i) The side reactions between lithium metal and polysulfides. As mentioned above, the intermediate polysulfides are readily to shuttle from the cathode to the anode part, which leads to the following reaction with lithium metal. This side reaction can result in the low Coulombic efficiency and inferior cycling performance.

(ii) The growth of lithium dendrites. Due to the inhomogeneous distribution of current density on the surface of lithium metal, the lithium ions are easily to nucleate on the

protuberance and form lithium dendrites. The growth of lithium dendrites leads to the continuous breaking and consuming of solid electrolyte interface (SEI) layer, which further consumes the lithium metal and electrolyte. Another concern is that the ever-growing lithium dendrites can potentially penetrate the separator and cause the internal short circuits, which leads to the safety problems.

(iii) The large volume change of lithium metal during the stripping and plating process. As a convention electrode without a host to store the lithium ions, the lithium metal anode suffers from severely volume change during the repetitive lithium stripping and plating. Some of the lithium would be smashed and detached from the original lithium metal to become dead lithium. This can result in the unstable SEI layer and low Coulombic efficiency.

To overcome these intractable obstacles, various strategies including encapsulating sulfur within host materials, separator modification, binder improvement, electrolyte optimization and lithium metal protection will be elaborated in detail in the following parts to improve the performance of Li-S batteries.

1.2 Sulfur cathode host design

One of the most effective strategies to improve the performance of Li-S batteries is to disperse insulating sulfur active material within other conductive matrixes that are capable of physically adsorbing and/or chemically binding sulfur and its intermediate polysulfides, which has been extensively studied over the past decade.[35, 55-57] Based on the composition and properties, the matrixes can be classified into carbon materials, organic materials, metal oxides, metal organic frameworks (MOFs), metal hydroxides, metal sulfides, metal nitrides,

metal carbides, metal phosphides, metal borides, other emerging metal compounds and pure metal, which will be discussed respectively in the following sections.

1.2.1 Carbon materials as host

Owing to their large surface area, high electrical conductivity and diversity in nanostructures, carbon materials have been widely studied as sulfur host materials during the early stage of Li-S batteries.[33] A major breakthrough was achieved in 2009 when Nazar and co-workers pioneered the work of using CMK-3 as sulfur host for Li-S batteries.[31] The CMK-3 consists of an array of hollow carbon nanorods with a diameter of 6.5 nm, which are separated by 3 nm channel voids (**Figure 1.2**a). Sulfur was infiltrated into the voids via a melt-diffusion strategy at 155 °C where sulfur has the lowest viscosity. **Figure 1.2**b shows the SEM image of the CMK-3 before and after the sulfur loading, indicating that sulfur has distributed uniformly in the channels and maintains an intimate contact with the conductive carbon walls. Benefitting from this exquisite nanoarchitecture design, the CMK-3/S demonstrated a high discharge capacity of 1005 mA h g^{-1} with a stable cycling over 20 cycles (**Figure 1.2**c), representing a great breakthrough at that time. Additional modification of the carbon surface with hydrophilic polyethylene glycol (PEG) molecule can further increase the discharge capacity to 1320 mA h g^{-1}. In addition to the CMK-3, the Nazar group also developed mesoporous carbon spheres with ultra-high pore volume of 2.32 cm^3 g^{-1} and large specific surface area of 2445 m^2 g^{-1}.[58] The mesoporous carbon-sulfur composite exhibited a high initial discharge capacity of 1200 mA h g^{-1} with a capacity retention of 61% after 100 cycles at 1C.

Instead of using elemental sulfur as cathode, the utilization of its discharged product Li_2S as the starting material has also represented a promising direction owing to its compatibility with the much safer Li-free anodes such as graphite or Si based anodes.[59, 60] Additionally, since metallic lithium has been pre-incorporated into the cathode structure, the large volume expansion of sulfur during discharge in the traditional cathode can be eliminated. To this end, Cui and co-workers designed a novel lithium metal-free battery which consists of Li_2S/CMK-3 as cathode and Si nanowires as anode.[61] Benefiting from the unique structure advantage of CMK-3, the Li_2S/CMK-3 cathode based battery demonstrated much better electrochemical performance compared to the Li_2S powder based battery. Furthermore, the full cell achieved a high specific energy of about 349 W h kg^{-1}, which shows potential practical applications in the future.

Hollow nanostructures have received extensive research interest in recent years due to their large void space, high specific surface area and low density.[62-65] They demonstrate great potential in a wide range of applications from biomedicine to energy related systems.[62, 66-68] In 2011, Archer's group pioneered the work of using porous hollow carbon spheres as the host to encapsulate sulfur and trap the polysulfides (**Figure 1.2**d).[37] They used silica spheres as the template and pitch as carbon source to synthesize the hollow carbon spheres. This hollow structure design can not only provide abundant void space to store sulfur, but also accommodate the volume expansion upon lithiation. As shown in **Figure 1.2**e, the hollow carbon@sulfur composite delivered a high initial discharge capacity of 1071 mA h g^{-1} and retained a capacity of 974 mA h g^{-1} after 100 cycles at 0.5C, demonstrating its stable cycling performance. Afterwards, Lou and co-workers fabricated double-shelled hollow carbon

nanospheres by using SnO_2 hollow spheres as the template.[69] Such complex hollow spheres can maximize the advantages of hollow nanostructures for sulfur encapsulation and suppress the outward diffusion of polysulfides. When evaluated as the cathode for Li-S batteries, this composite showed superior electrochemical performance with high specific capacity and good cycling performance.

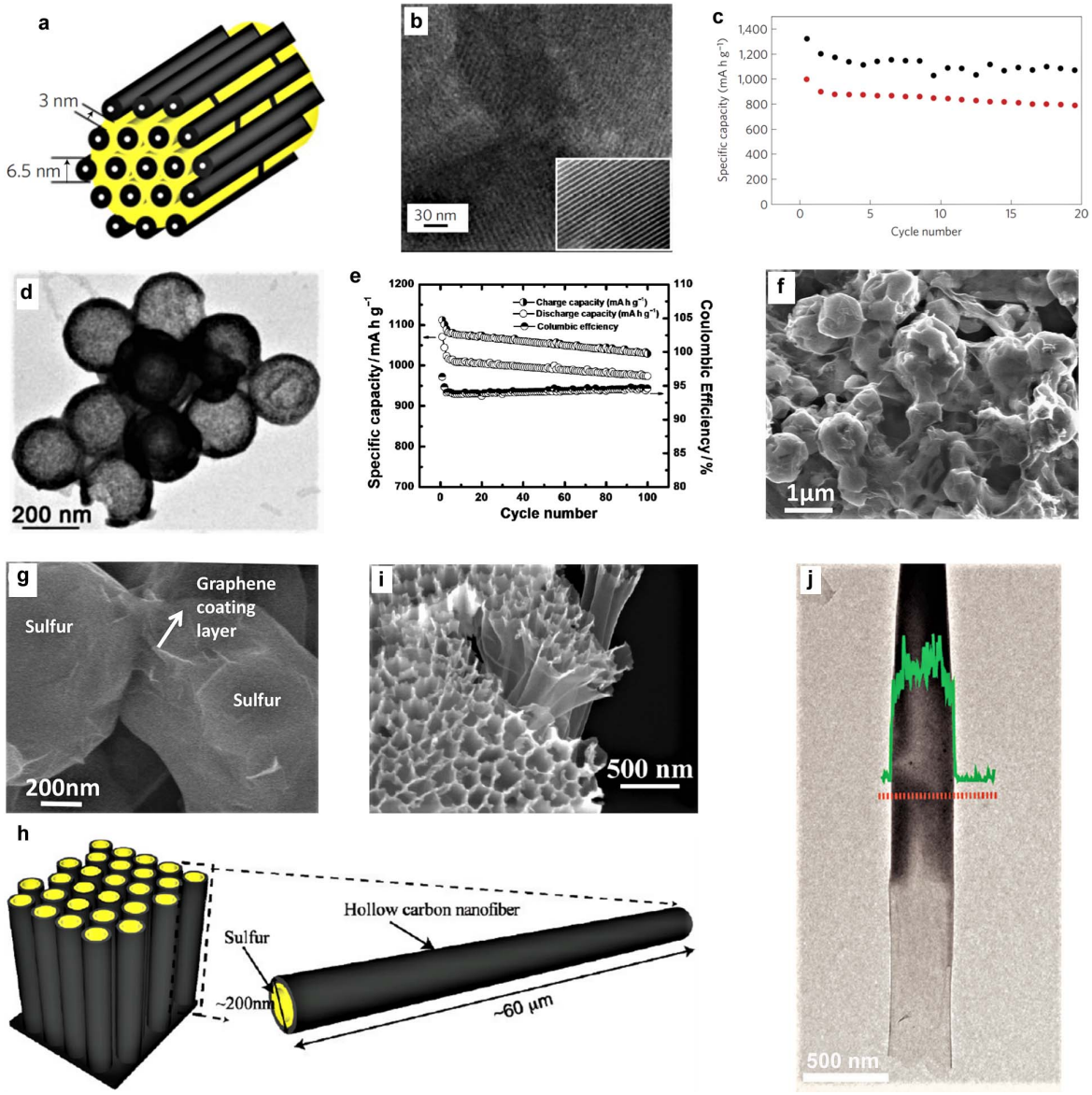

Figure 1.2 (a) Schematic illustration of sulfur confined in CMK-3. (b) TEM image of sulfur-loaded CMK-3. The inset indicates the pristine CMK-3 with same magnification. (c) Cycling performances of CMK-3/S (red) and CMK-3/S-PEG (black) at current density of 168

mA g^{-1}. (a-c) Reproduced from reference[31]. Copyright 2009, Nature Publishing Group. (d) TEM image of porous hollow carbon@sulfur spheres. (e) Cycling performance and Coulombic efficiency of porous hollow carbon@sulfur composite at 0.5C. Reproduced from reference[37]. Copyright 2011, Wiley-VCH. SEM images of graphene-wrapped sulfur particles at (f) low and (g) high magnifications. Reproduced from reference[36]. Copyright 2011, American Chemical Society. (h) Schematic, (i) SEM and (j) TEM images of hollow carbon nanofiber-encapsulated sulfur. The green line in Figure j represents counts of sulfur signal along the dashed orange line. Reproduced from reference[70]. Copyright 2011, American Chemical Society.

Graphene is a two-dimensional material with merits of large surface area, excellent conductivity and superior flexibility, making it a promising substrate to anchor active materials for energy applications.[53, 71-74] In 2011, Dai and Cui's group pioneered the work of using graphene-wrapped sulfur particles as a novel cathode for Li-S batteries (**Figure 1.2**f,g).[36] They first functionalized the sulfur microspheres with poly(ethylene glycol) (PEG) molecules and then assembled them with mildly oxidized graphene oxide nanosheets to form the graphene-wrapped sulfur particles via the electrostatic interaction. The graphene coating layer can not only endow the electrical conductivity of the graphene-sulfur composite, but also effectively entrap the polysulfides. Additionally, the PEG layer can further trap the polysulfides and accommodate the volume change upon cycling. As a result, the graphene-sulfur composite demonstrated much improved cycling stability compared to the sulfur cathode without graphene wrapping. Apart from using as sulfur host, the graphene was also used as the host material for Li_2S based cathode. Li et al. prepared a freestanding Li_2S/reduced graphene oxide (rGO) paper electrode by directly dropping Li_2S/ethanol

solution onto the porous rGO paper and then dried at 300 °C for 2h, during which the Li_2S precipitated into nanospheres.[75] The flexible rGO nanosheets prevented the agglomeration of Li_2S particles and ensure their homogeneous distribution in the rGO paper. As a result, the Li_2S/rGO paper electrode showed superior cycling performance with a discharge capacity of 816 mA h g^{-1} after 150 cycles at 0.1C and excellent rate performance of 597 mA h g^{-1} at 7C. In 2017, Amine's group has developed a new approach to fabricate Li_2S-graphene composite by directly burning lithium foils in a CS_2 vapor atmosphere.[76] By using this simple strategy, they obtained graphene-wrapped Li_2S nanoparticles. Because the Li_2S cores and graphene shells nucleated and formed simultaneously to generate the Li_2S-graphene nanocapsules, the obtained composite had very high compactness, which was beneficial to achieve high Li_2S loading. Moreover, as the lithium was already lithiated into the Li_2S@graphene capsules, the volume expansion could be eliminated and the compact graphene shells could preserve the structural integrity of the composite. Accordingly, the conductivity of the composite was ensured and the polysulfide shuttle was effectively suppressed. As a result, the composite delivered a high reversible capacity of 1160 mA h g^{-1} and high areal capacity of 8.1 mA h cm^{-2} at an ultrahigh Li_2S loading of 10 mg cm^{-2}. They also fabricated a full cell using Li_2S@graphene as cathode and graphite as anode. Remarkably, the Li_2S@graphene-graphite full cell displayed a high discharge capacity of 730 mA h g^{-1} with stable cycling performance, indicating their potential practical applications.

Owing to their high aspect ratio, one-dimensional nanomaterials such as carbon nanotubes are able to render long-range conductivity for the electrode, making them very intriguing for employ as sulfur host. However, as the diameter of carbon nanotubes is very small and the

impermeable nature of their walls, it is very difficult to infiltrate sulfur into the inner hollow space of carbon nanotubes. In this case, the sulfur was generally coated on the outer surface of the carbon nanotubes and the intermediated polysulfides were easily dissolved into the electrolyte upon long cycling. Thus, it would be very beneficial to design hollow carbon nanofibers with much larger diameter to confine the active sulfur species inside the inner hollow space. To this end, Cui and co-workers prepared the hollow carbon nanofiber (HCNF)-encapsulated sulfur by first carbonizing the polystyrene on the anodic aluminum oxide (AAO) template and then infiltrating sulfur into the tubes via the melt-diffusion strategy (**Figure 1.2**h-j).[70] The AAO template was then etched away by immersing it into the acid solution. Benefiting from the hollow structure, the S@HCNF electrode demonstrated high discharge capacities of about 1400 and 1300 mA h g^{-1} at 0.2 and 0.5C, respectively. Nevertheless, the cycling performance of hollow carbon nanofiber encapsulated sulfur composite was not satisfactory, perhaps due to the weak physical interaction between polar lithium polysulfides and the nonpolar carbon walls, resulting in the detachment of sulfur species from the carbon walls.[77]

Apart from using mesoporous and macroporous carbon materials, microporous carbon spheres with a narrow pore size of about 0.7 nm were also used to confine the sulfur molecules by Gao's group (**Figure 1.3**a,b).[78] The charge-discharge profiles of microporous carbon-sulfur composite showed only one discharge platform at about 1.8 V in carbonate-based electrolyte (**Figure 1.3**c), instead of typical two-platform charge-discharge voltage profiles in conversional ether-based electrolyte. It was postulated that the sulfur molecules existed in the form of short-chain sulfur, which led to the one-stage conversion

process from S_4 to S_2/S without the formation of high-order lithium polysulfides during the discharge. As a result, the microporous carbon with 42% sulfur content exhibited very stable cycling performance with capacities over 800 mA h g^{-1} at the current density of 400 mA g^{-1} (**Figure 1.3**d). It was worth noting that when the sulfur content was higher than the theoretical loading content of 49.5% based on the total pore volume of the carbon spheres, the obtained microporous carbon/sulfur composite exhibited very low discharge capacity (**Figure 1.3**d). This could be attributed to that the oversaturated sulfur existed in the form S_8 on the surface of microporous carbon spheres and its intermediate product long-chain polysulfides attacked the carbonate electrolyte, resulting the poor electrochemical performance.

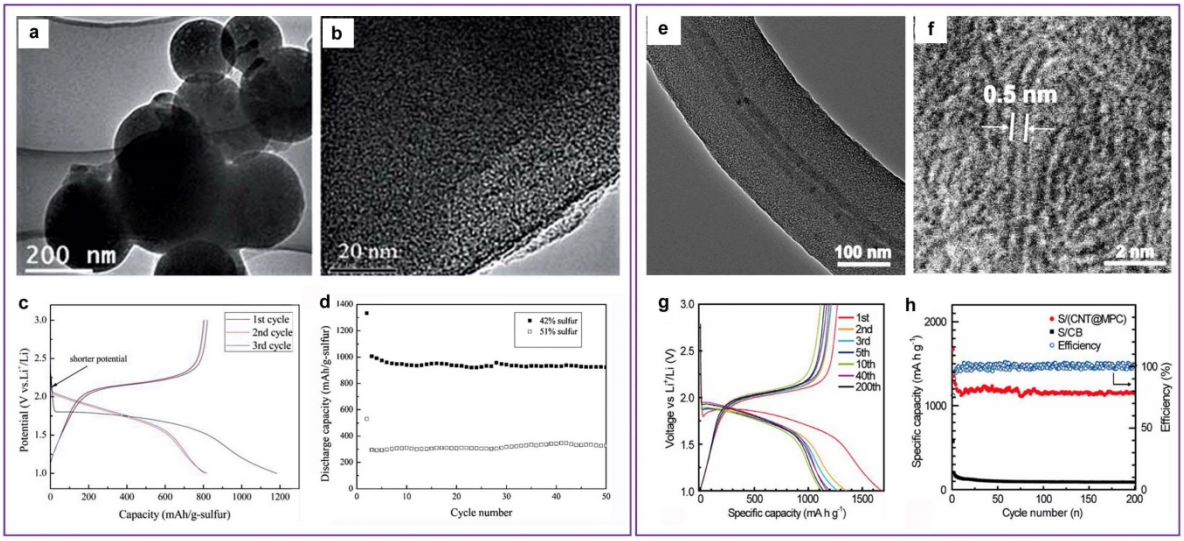

Figure 1.3 (a,b) TEM images of microporous carbon spheres at different magnifications. (c) Voltage profiles of sulfur-microporous carbon sphere composite with 42% sulfur content at current density of 400 mA g^{-1} in carbonate-based electrolyte. (d) Cycling performances of sulfur-carbon sphere composites at current density of 40 mA g^{-1} with 42 wt% and 51 wt% sulfur contents, respectively. (a-d) Reproduced from reference[78]. Copyright 2010, Royal Society of Chemistry. (e) TEM image of a CNT@microporous carbon nanocable. (f) HR-TEM image shows the carbon channels in the coating layer. (g) Charge-discharge voltage

curves of S/CNT@microporous carbon at 0.1C in carbonate-based electrolyte. (h) Cycling performances and Coulombic efficiencies of S/CNT@microporous carbon and S/CB at 0.1C. (e-h) Reproduced from reference[79]. Copyright 2012, American Chemical Society.

To give more insight on the short-chain sulfur molecules, Guo's group has performed theoretical calculations on the sulfur allotropes from S_2 to S_8.[79] It was calculated that chain-like small sulfur molecules (S_2~S_4) have at least one dimension lower than 0.5 nm, while for cyclo-sulfur molecules (S_5~S_8), have at least two-dimensions larger than 0.5 nm. As a proof-of-concept, they prepared the microporous carbon matrix with pore size of about 0.5 nm (**Figure 1.3**e,f), in which only small sulfur molecules from S_2~S_4 can be confined in the micropores. Raman spectra were performed to confirm the disappearance of S_8 in the microporous carbon-sulfur composite. Using this composite as cathode, it showed reversible electrochemical reactions in the carbonate-based electrolyte and the charge-discharge voltage profiles showed one platform (**Figure 1.3**g), which was in good agreement with Gao's work. High discharge capacity of 1142 mA h g^{-1} was delivered at 0.1C after 200 cycles, demonstrating remarkable cycling stability (**Figure 1.3**h).

Although carbon materials have embraced great progress as sulfur host for Li-S batteries, the cycling performance was not satisfactory giving that the nonpolar carbon can only provide weak physical adsorption for the polar polysulfides. Modification of carbon surface with heteroatoms or functional groups was believed to be an effective strategy to enhance the chemical affinity for polar lithium polysulfides and restrain their shuttle effect.[35] In 2011, Zhang's group proposed that functional groups such as hydroxyl and epoxy groups on graphene oxide can strengthen the binding of sulfur to the C-C bonds due to the induced

ripples by the functional groups.[80] Because of the strong chemical anchoring ability of the functional groups to polysulfides, the graphene oxide-sulfur composite showed stable cycling performance at 0.1C over 50 cycles. In 2014, Lou et al. functionalized rGO with amino groups to enhance the trapping ability to polysulfides.[81] The ethylenediamine (EDA)-functionalized rGO exhibited a much higher binding energy with polysulfides (1.13-1.38 eV) compared to that of rGO (0.34 eV). With the merits of conductive graphene and polar amino groups, the EDA-S-rGO showed stable cycling performance with a capacity retention of 80% after 350 cycles. Although the abundant functional groups on GO can chemically immobilize the intermediate polysulfides, the conductivity of GO is not good, which led to the poor rate performance.

Alternatively, chemical doping of carbon materials would be a promising choice to enhance their chemical binding capability while ensure their conductivity. In 2014, the Zhang group designed a kind of novel nitrogen-doped aligned carbon nanotube-graphene (N-ACNT/G) sandwiches as the scaffolds to accommodate sulfur for high-rate Li-S batteries (**Figure 1.4**a).[82] Parallel graphene nanosheets were penetrated with the aligned carbon nanotubes, leading to a sandwich-like hierarchical architecture with 3D continuous conductive framework (**Figure 1.4**b,c). Moreover, the nitrogen doping has induced abundant defects and active sites for improving the chemical adsorption capability for polysulfides. When N-ACNT/G was used as the sulfur scaffold, a high initial discharge capacity of 1152 mA h g^{-1} at 1C was attained and it retained a high discharge capacity of 880 mA h g^{-1} after 80 cycles. Even at the ultrahigh current rate of 5C, a high reversible capacity of 770 mA h g^{-1} was delivered. Such impressively high rate performance can be attributed to the efficient 3D

electron pathways and ion diffusion channels originating from this unique sandwich-like structure.

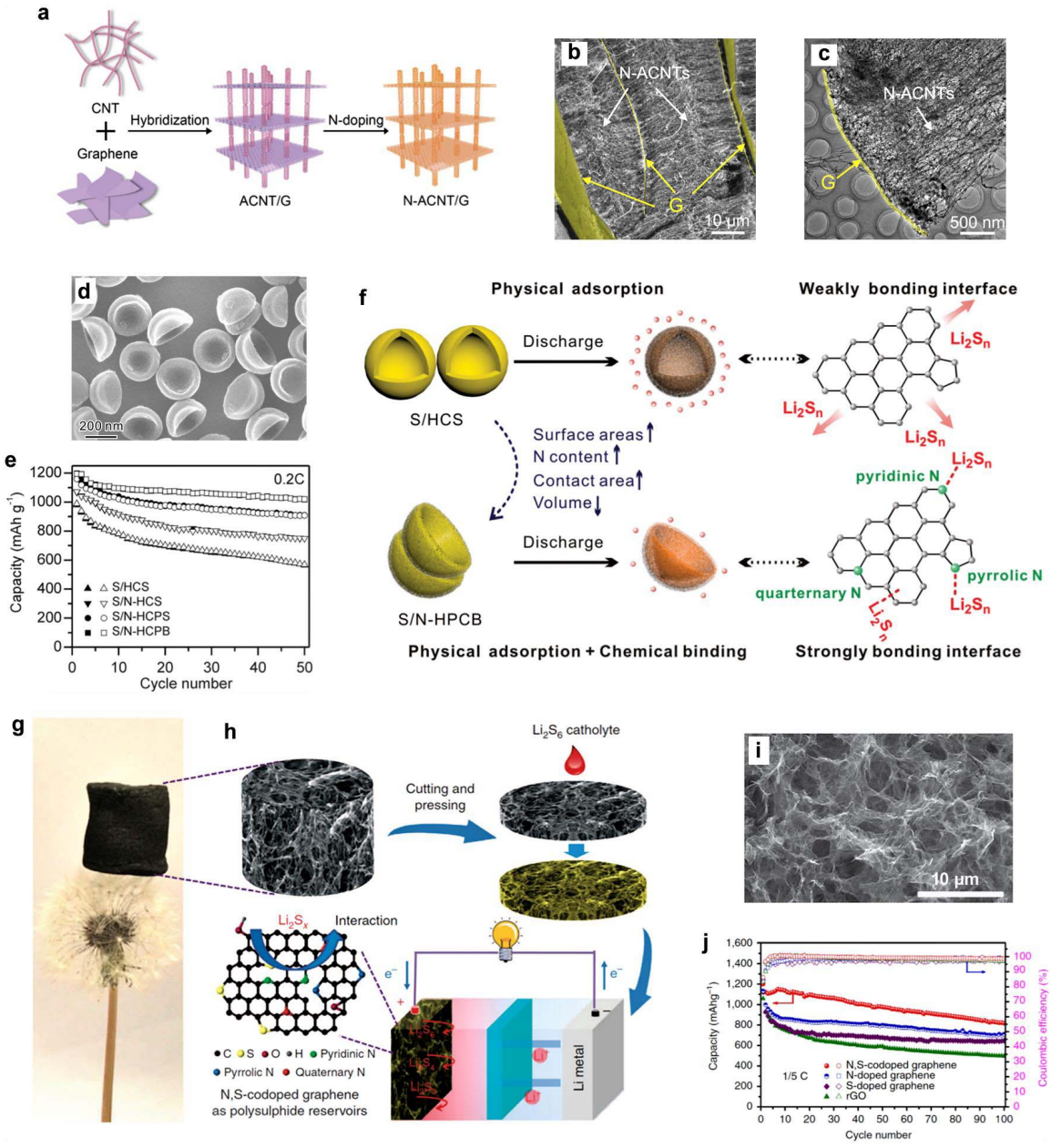

Figure 1.4 (a) Schematic of the synthetic process for nitrogen-doped aligned CNT/graphene (N-ACNT/G) hybrid. (b) SEM and (c) TEM images of N-ACNT/G hybrids. (a-c) Reproduced from reference[82]. Copyright 2014, Wiley-VCH. (d) SEM image of N-doped hollow porous carbon bowls (N-HPCB). (e) Cycling performances of S/N-HPCB, S/N-HPCS, S/N-HCS and S/HCS at 0.2C. (f) Schematic of the confinement effect of polysulfides by HCS and N-HPCB.

(d-f) Reproduced from reference[83]. Copyright 2016, Wiley-VCH. (g) Photograph of a dandelion supported N,S-codoped graphene sponge. (h) Schematic of the fabrication process for N,S-codoped graphene electrodes and Li-polysulfide batteries. (i) SEM image of the N,S-co-doped graphene sponge. (j) Cycling performances and Coulombic efficiencies of N,S-codoped graphene, N-doped graphene, S-doped graphene and rGO. (g-j) Reproduced from reference[84]. Copyright 2015, Nature Publishing Group.

Similar to the case of graphene and carbon nanotubes, the surface of porous carbon can also be modified with heteroatoms to enhance their chemical affinity for polysulfides. In 2016, the Zheng group has synthesized a kind of novel N-doped hollow porous carbon bowls (N-HPCS) with ultrahigh surface area of 2161 $m^2 g^{-1}$ and large pore volume of 1.50 $m^3 g^{-1}$ (**Figure 1.4**d).[83] After loaded with sulfur, the S/N-HPCS composite showed higher discharge capacity and better cycling performance compared to S/N-HPCS, S/N-HCS and S/HCS (**Figure 1.4**e). The significantly improved capacity and cycling performance of N-HPCS can be attributed to its unique architecture (**Figure 1.4**f). Because the nonpolar HCS can only generate weak physical adsorption to the polar polysulfides, the S/HCS cannot undertake long-term cycling. However, the incorporation of N atoms into the nonpolar carbon can effectively tune its surface structure and chemically immobilize sulfur and polysulfides through the strong bonding interface.

Instead of using solid sulfur as the starting active material, the dispersion of dissolved polysulfide catholyte into the 3D freestanding structure has received much attention recently. In 2015, the Manthiram group has fabricated a lightweight 3D N/S-codoped graphene sponge as the current collector to load polysulfide catholyte for Li-polysulfide batteries.[84] The N,S-co-doped graphene sponge was prepared by the hydrothermal reaction between GO and

thiourea, followed by the freeze-drying process (**Figure 1.4**g). The N,S-codoped graphene shows highly interconnected porous structure. The 3D current collector was obtained by cutting and pressing the sponge into slices. After that the prepared Li_2S_6 catholyte was directly dropped into the 3D slices to form the polysulfide working electrode (**Figure 1.4**h). The Li-polysulfide batteries using N,S-co-doped graphene as current collectors showed much improved electrochemical performance compared with that of N-doped graphene, S-doped graphene and rGO (**Figure 1.4**j). The enhanced electrochemical performance can be attributed to the synergistic effect of N,S co-doping that leads to the stronger chemical binding with polysulfides compared to the single N or S-doping cases and un-doped one.

Additionally, many other types of heteroatom-doped carbon materials, such as N,B-co-doped graphene nanoribbons[85], graphene-supported nitrogen and boron rich carbon layer,[86] and N,P dual doped graphene[87] have also been used to improve the electrochemical performance of Li-S batteries. Although the incorporation of functional groups or heteroatoms into carbon materials were effective strategies to improve the affinity for polysulfides, the contents of heteroatom doping or the functional groups were relatively low, which cannot provide abundant active sites to chemically anchor the polysulfides. In this regard, the pure carbon-based materials were not the optimal choice for using as sulfur host for Li-S batteries.

1.2.2 Organic materials as host

Organic materials represent an emerging family of materials for energy applications that can be precisely controlled at the molecule level.[88-90] The organic materials have a diversity of

functional groups which are beneficial for polysulfide trapping. In addition, the elastic and flexible nature of polymer can accommodate the volume variation upon cycling.

Conductive polymers such as polypyrrole and polythiophene were one of the earliest organic materials used as sulfur host.[91-95] These sulfur-polymer composites formed via the melt diffusion method at 155 °C usually do not have strong chemical binding and the cycling performances were not satisfied. To achieve longer cycle life and confine sulfur within the polymer backbone at the molecule level, Liu's group heated sulfur with polyaniline (PANI) at 280 °C to trigger the vulcanization reaction, which produced a 3D cross-linked sulfur-PANI (SPANI) polymer backbone with both inter- and/or intra-chain disulfide bonds (**Figure 1.5**a-d).[96] Owing to the strong confinement effect at the molecule level, the SPANI nanotubes displayed stable cycling performance with a discharge capacity of 432 mA h g^{-1} after 500 cycles at 1C, corresponding to a 76 % capacity retention, which represented an impressive long-cycling performance.

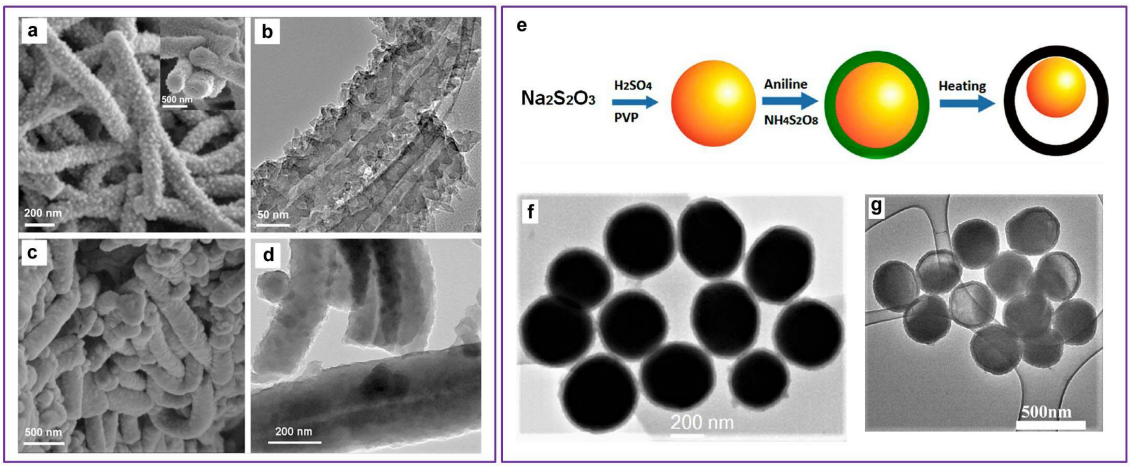

Figure 1.5 (a) SEM and (b) TEM images of PANI nanotubes. (c) SEM and d) TEM images of SPANI composite. (a-d) Reproduced from reference[96]. Copyright 2012, Wiley-VCH. (e) Schematic illustration of the synthesis process of sulfur-PANI yolk-shell nanostructure. (f)

TEM image of sulfur-PANI core-shell spheres. (g) TEM image of yolk-shell structured sulfur-PANI spheres. (e-g) Reproduced from reference[97]. Copyright 2013, American Chemical Society.

To accommodate the volume expansion of sulfur during lithiation, yolk-shell nanostructures of PANI-sulfur spheres were further designed by Abruña's group (**Figure 1.5**e).[97] Colloidal sulfur nanospheres were first prepared by the reaction between $Na_2S_2O_3$ and H_2SO_4 in the presence of a small amount of polyvinyl pyrrolidone (PVP). The PANI-coated sulfur nanospheres were then obtained by the oxidation of aniline with ammonium persulphate in the diluted sulfuric acid solution (**Figure 1.5**f). After heating the core-shell PANI-sulfur nanospheres at 180 °C for 12h under Ar atmosphere to volatilize partial sulfur, yolk-shell PANI-sulfur nanospheres were achieved (**Figure 1.5**g). At the same time, sulfur was reacted with PANI to form the cross-linked disulfide network via the vulcanization. Benefitting from this unique structure design, the sulfur-PANI yolk-shell sphere cathodes displayed high initial specific capacities of 1101 and 920 mA h g^{-1} at 0.2 and 0.5C, along with 70% and 68% capacity retention after 200 cycles, respectively. The superior cycling performance was attributed to the dual confinement of both physical and chemical entrapment.

Instead of using the yolk-shell morphology, another strategy to accommodate the volume expansion of sulfur is to design intrinsic hollow sulfur spheres. To this end, the Cui group has prepared a kind of novel PVP-encapsulated hollow sulfur nanospheres *via* a one-step soft-template approach.[98] The hollow sulfur structure design can effectively accommodate volume expansion during discharge and the cycling performance has been improved a lot.

However, the rate performance was relatively weak due to the insulating nature of both sulfur and PVP shell. In order to further improve the electrochemical performance of the cathode, conductive polymers were further employed to encapsulate the hollow sulfur nanospheres (**Figure 1.6**a).[99] **Figure 1.6**b,c show the SEM and TEM images of the monodisperse hollow sulfur nanospheres before the conductive polymer coating. The hollow sulfur nanospheres exhibit the uniform spherical morphology with a diameter of about 400 nm. After coating a thin layer of conductive polymers, the sulfur nanospheres maintained the spherical morphology and hollow structure (**Figure 1.6**d-g). The thickness of the conductive polymer shells is about 20 nm. Electrochemical measurements demonstrated that the conductive polymer coating can effectively improve the cycling performance and the poly(3,4-ethylenedioxythiophene) (PEDOT)-coated hollow sulfur nanospheres showed the best performance among these three kinds of different conductive polymers. It delivered an initial discharge capacity of 1165 mA h g^{-1} and maintained a high discharge capacity of 780 mA h g^{-1} at 0.5C after 500 cycles. Theoretical calculations were also performed to elucidate the interactions between these conductive polymers and lithium sulfides. It was found that all of these three conductive polymers can form strong chemical bindings with lithium sulfides. The PEDOT (1.08 eV) shows a stronger binding energy with Li_2S than that of PANI (0.59 eV) and PPY (0.50 eV). The strong binding affinity for polysulfides can effectively suppress their shuttle effect, which led to the better cycling performance of PEDOT-coated hollow sulfur nanospheres. In particular, combining the carbon-sulfur composite with PEDOT coating can further entrap the polysulfides.[100]

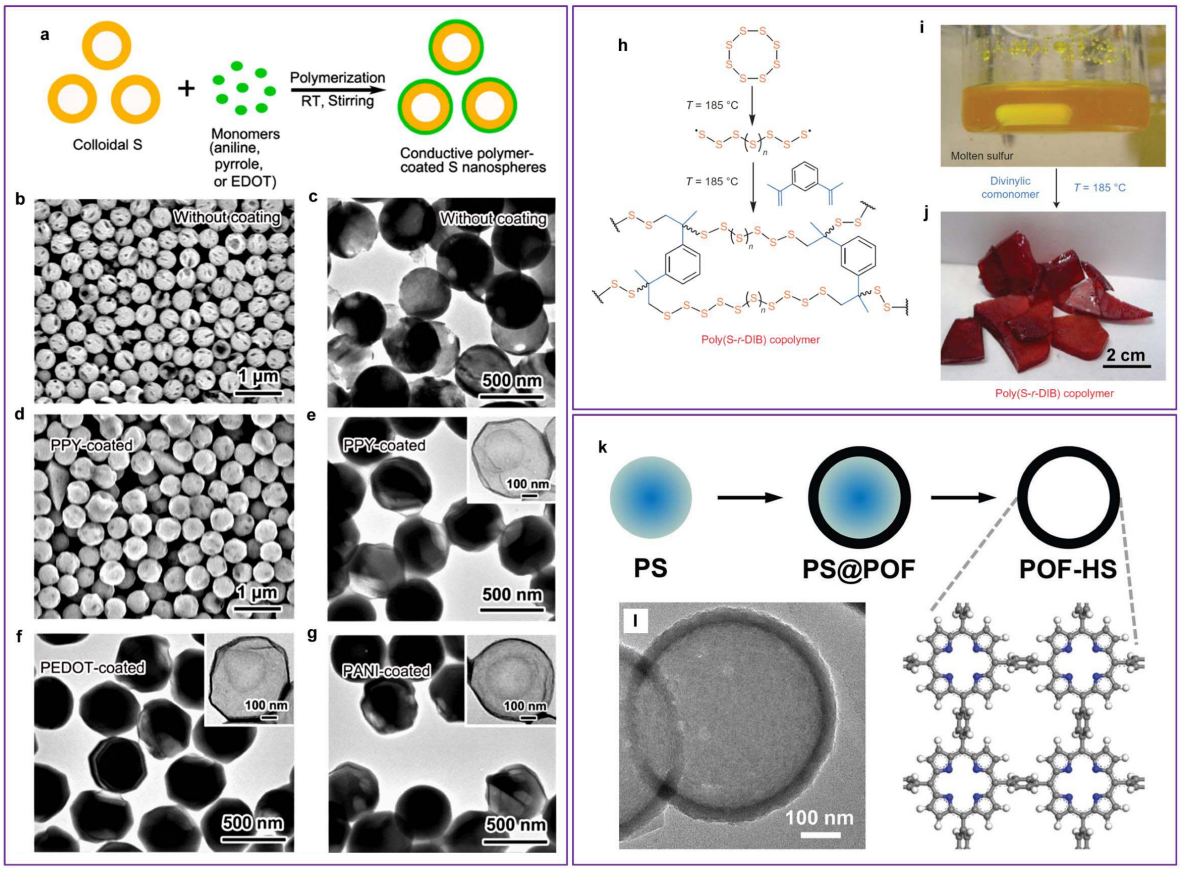

Figure 1.6 Schematic of the synthetic process of conductive polymer-coated hollow sulfur nanospheres. (b) SEM and (c) TEM images of hollow sulfur nanospheres without polymer coating. (d) SEM and (e) TEM images of PPY-coated hollow sulfur nanospheres. (f) PEDOT-coated and (g) PANI-coated hollow sulfur nanospheres. (a-g) Reproduced from reference[99]. Copyright 2013, American Chemical Society. (h) Schematic illustration of the synthetic process for poly(S-r-DIB) copolymer. (i) Photograph of molten sulfur at 185 °C. (j) Photograph of poly(S-r-DIB) solid with 30 wt% DIB. (h-j) Reproduced from reference[101]. Copyright 2013, Nature Publishing Group. k) Schematic of the synthesis process of porphyrin organic framework hollow spheres. (l) TEM image of porphyrin organic framework hollow spheres. (k-l) Reproduced from reference[102]. Copyright 2018, Wiley-VCH.

In 2013, Pyun et al. proposed a kind of sulfur-copolymer as a new kind of cathode for Li-S batteries.[101] To do so, they heated solid sulfur to 185 °C until a clear orange colored molten phase was formed (**Figure 1.6**i), during which the eight-membered ring S_8 was first

transformed into a linear polysulfane with diradical chain ends and subsequently polymerized into polymeric sulfur of high molecule weight. After that a certain amount of 1,3-diisopropenylbenzene (DIB) was injected into the molten sulfur medium and stirred at 185 °C for 10 min (**Figure 1.6**i,j), during which the polymeric sulfur with diradical chain ends copolymerized with DIB molecule to form the poly(S-r-DIB) copolymer as illustrated in **Figure 1.6**h. Using this copolymer as sulfur cathode, it showed very similar electrochemical behavior to that of S_8, including the two typical discharge platforms at 2.3 V and 2.05 V. It exhibited an initial discharge capacity of 1100 mA h g^{-1} and maintained a capacity of 823 mA h g^{-1} after 100 cycles at 0.1C. Although high capacity with relatively stable cycling performance was achieved using this unique copolymer as active material, the rate performance was relatively poor especially at a high rate of 2C. This is because the conductivity of poly(S-r-DIB) copolymer is very low. To increase the conductivity and rate performance of the cathode, the Li group further infiltrated the sulfur-DIB copolymer into the hollow carbon nanofibers (CNF) to form the S-DIB@CNF composite.[103] By combining the unique structure advantage of S-DIB copolymer and the long-range conductivity behavior of CNF, the S-DIB@CNF exhibited high discharge capacity, high rate performance and superior cycling stability with a capacity decay of only 0.05% over 450 cycles at 1C. Besides CNF, graphene was also used to enhance the conductivity of sulfur copolymer.[104]

As one of the emerging crystalline porous materials, covalent organic frameworks (COFs) have received extensive interest in recent years owing to their large surface area and ready functionality.[105] Their structures and heteroatom components can be precisely designed in principle through selection of proper building blocks to optimize the designed functionality.

This provides a promising way to design COFs with well-defined structures and compositions to encapsulate sulfur within their intrinsic pores. In 2016, Tang and co-workers designed N and B doped COFs to fill sulfur for Li-S batteries.[106] The high density and uniform distribution of positively polarized B and negatively polarized O within the pores can guarantee simultaneous adsorption of S_x^{2-} and Li^+ in soluble lithium polysulfides to restrain their shuttle effect. As a result, a high initial discharge capacity of 1032 mA h g^{-1} was attained at 0.5C and a capacity of 770 mA h g^{-1} was remained after 200 cycles. Additionally, other types of COFs, such as 2D pyrene-based COFs[107] and COF nanosheets assembled microspheres[108], have also been developed as sulfur host for Li-S batteries.

Recently, Zhang's group has prepared porphyrin organic framework (POF) hollow spheres as sulfur host (**Figure 1.6**k,l).[102] Polystyrene (PS) sphere templates were first prepared *via* the traditional emulsion polymerization method. POFs were then coated on the PS spheres. Finally, the hollow POF spheres were obtained by dissolving PS@POF spheres into toluene to remove the PS templates (**Figure 1.6**l). By virtue of the polar characteristic and hollow structure, the sulfur-loaded POF spheres demonstrated a high discharge capacity of 955 mA h g^{-1} at 0.5C and maintained a capacity of 773 mA h g^{-1} after 200 cycles.

Quinone-based organics have demonstrated great potential to promote the redox reactions in Li-S batteries.[109] For example, Chen and co-workers reported that the keto groups in anthraquinone (AQ) can confine polysulfides by forming strong Lewis acid-based chemical bonding.[110] After combining S-AQ with the conductive rGO, the S-AQ-G composite showed superior cycling performance with a low capacity decay rate of only 0.019% per cycle over 300 cycles.

Sulfurized polyacrylonitrile (SPAN) is a special kind of organosulfur that has drawn attention in recent years because it can be stably cycled in traditional carbonate-based electrolytes. It was first reported by Wang et al. in 2002.[111] The SPAN was fabricated by heating a mixture of sulfur and polyacrylonitrile (PAN) at 300 °C for 6h to form unsaturated chains with conjugated electrons. The dehydrogenation resulted in the cyclization of PAN, contributing to the formation of framework. Using this SPAN as the cathode, an initial capacity of 850 mA h g^{-1} and a retained capacity of over 600 mA h g^{-1} after 50 cycles were delivered. It was worth noting that only one discharge plateau appeared at about 1.8 V, suggesting the disappearance of intermediate polysulfide formation during the discharge process. However, the intrinsic reaction mechanism upon cycling was not totally understood. Very recently, based on their previous work, the Wang group further explored a SPAN based cathode combined with a fluoroethylene carbonate (FEC)-based electrolyte for ultra-long cycle life Li-S batteries.[112] A high capacity of over 1200 mA h g^{-1} was attained and it could be stably cycled for 4000 cycles at 6C, demonstrating promising direction for practical applications.

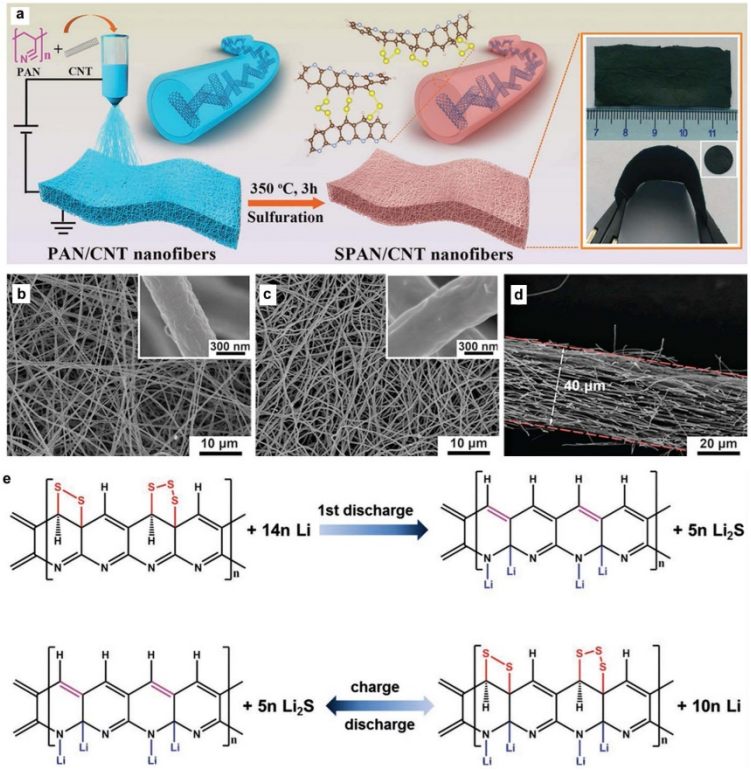

Figure 1.7 (a) Schematic of the synthetic process for SPAN/CNT electrodes. SEM images of b) PAN/CNT film and (c) SPAN/CNT film. The insets show the corresponding enlarged images. (d) Cross-sectional SEM image of SPAN/CNT electrode. (e) The proposed electrochemical conversion mechanism of SPAN cathode during discharge-charge process. Reproduced from reference[113]. Copyright 2019, Wiley-VCH.

Recently, Liu and co-workers proposed that SPAN existed in the form of short $-S_2-$ and $-S_3-$ chains covalently binding to the pyrolyzed PAN backbone (**Figure 1.7**).[113] They proposed that the electrochemical reduction of SPAN by Li^+ was a single-phase solid-solid reaction with Li_2S as the sole discharge product without the formation of any intermediate polysulfides (**Figure 1.7**e). Meanwhile, the parasitic reaction between Li^+ and C=N bonds occurred during the first discharge, and the residual Li^+ enhanced the conductivity of the backbone. Using the freestanding SPAN/CNT nanofibers as cathode, high discharge capacity of 1180 mA h g^{-1} without capacity fading over 1000 cycles was achieved at the current

density of 800 mA g^{-1}. Although SPAN shows great advantage in terms of cycling performance compared to other sulfur based composite cathodes, the sulfur content (normally below 40%) and voltage plateau (about 1.8 V) are not satisfactory for realizing a high energy density.

1.2.3 Metal oxides as host

Metal oxides typically comprise metal cations and oxygen anions in the polar metal-oxygen bonds, endowing abundant polar active sites to adsorb polysulfides.[56, 114] Additionally, owing to the intrinsic high tap density of metal oxides compared with carbon and organic materials, the utilization of metal oxides as cathode host materials would potentially increase the volumetric energy density of a practical Li-S battery. In this section, some typical polar metal oxides, such as TiO_2, MnO_2, CeO_2, Nb_2O_5, Ti_4O_7, TiO and Fe_3O_4, will be discussed to demonstrate the potential of metal oxides for using as host materials in Li-S batteries.

TiO_2 is one of the most studied polar metal oxide host materials for Li-S batteries. In 2013, Cui and co-workers pioneered the work of using sulfur-TiO_2 yolk-shell nanostructures as a novel cathode for Li-S batteries (**Figure 1.8**a).[115] Sulfur-TiO_2 core-shell structures were first synthesized by the hydrolysis process. To create the internal void space for accommodating the volume expansion upon lithiation, toluene was employed to dissolve part of the sulfur to produce a yolk-shell morphology (**Figure 1.8**b,c). In addition, the hydrophilic Ti-O groups and surface hydroxyl groups were believed to play a key role in chemically binding with the polar polysulfides. As a result, the S-TiO_2 yolk-shell cathode exhibited an initial discharge capacity of 1030 mA h g^{-1} at 0.5C with a capacity decay rate of only 0.033%

per cycle over 1000 cycles (**Figure 1.8**d), representing the best cycling performance at that time. Because of the semiconducting nature of TiO_2, carbon materials were also combined with TiO_2 to improve the overall conductivity of the electrode. To this end, many kinds of nanostructured TiO_2-C composites, such as carbon coated TiO_2 nanowire arrays,[116] C@TiO_2@C hollow microspheres,[117] TiO_2 nanowire-embedded graphene hybrid membrane,[118] TiO_2 nanosheets[119] and hollow TiO_2-webbed carbon nanotubes,[120] have then been developed as efficient sulfur hosts to enhance the electrochemical performance of Li-S batteries.

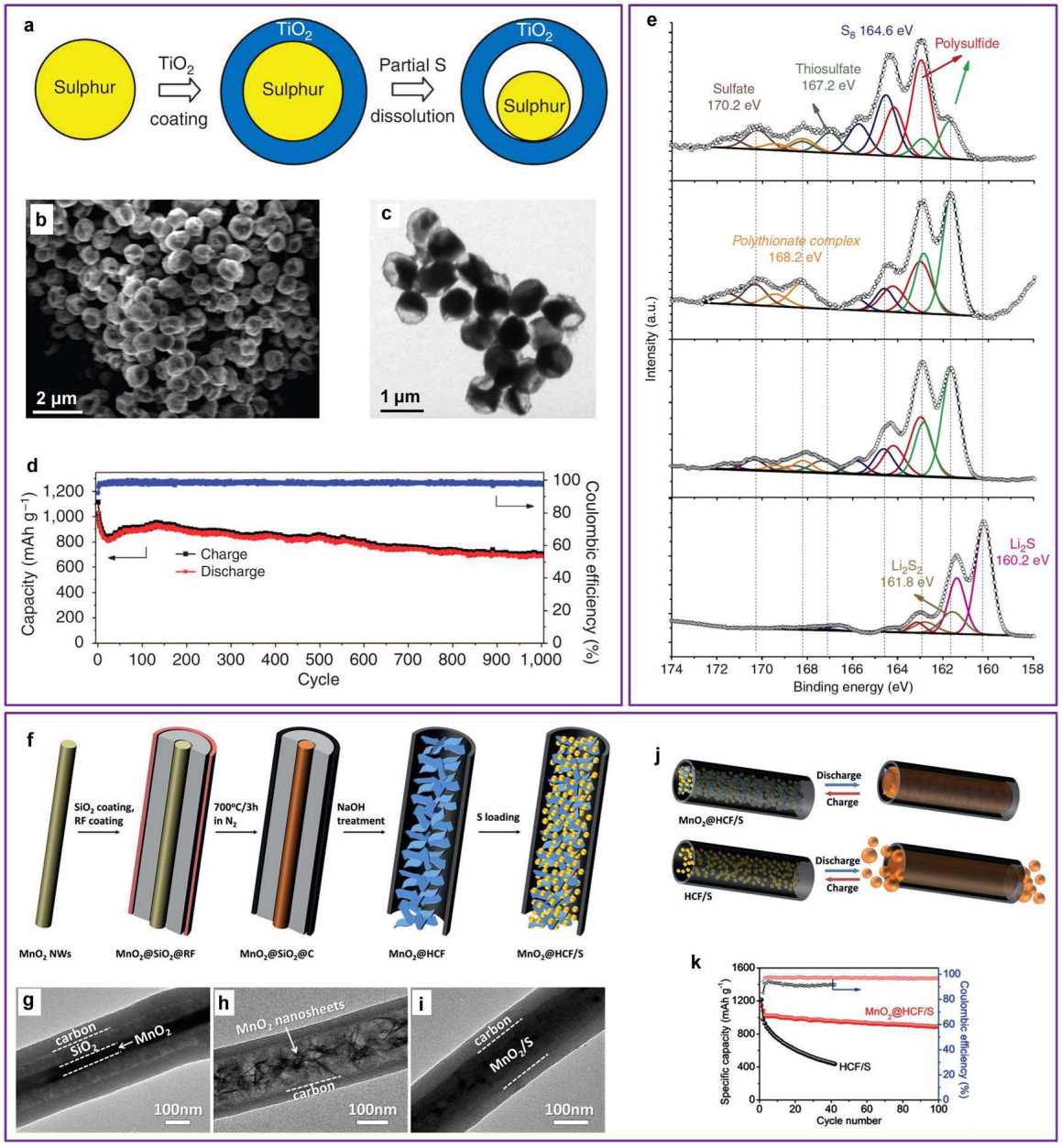

Figure 1.8 (a) Schematic of the synthesis process for sulfur-TiO_2 yolk-shell nanostructure. (b) SEM and (c) TEM images of yolk-shell structured sulfur-TiO_2 spheres. (d) Cycling performance of sulfur-TiO_2 yolk-shell sphere cathode at 0.5C for 1000 cycles. (a-d) Reproduced from reference[115]. Copyright 2013, Nature Publishing Group. (e) XPS of S/MnO_2 nanosheets electrodes after discharge to certain states: from top to bottom: discharged to 2.15 V, discharged to 2.15 V and then aged in the cell for 20h, discharged to 800 mA h g^{-1}, and discharged to 1.8 V. Reproduced from reference[121]. Copyright 2015, Nature Publishing Group. (f) Schematic of synthesis process of MnO_2@HCF/S. TEM images

of g) MnO_2@SiO_2@C, (h) MnO_2@HCF and i) MnO_2@HCF/S. (j) Illustration of polysulfide trapping by MnO_2@HCF. (k) Cycling performances of MnO_2@HCF/S and HCF/S at 0.2C. f-k) Reproduced from reference[122]. Copyright 2015, Wiley-VCH.

Using MnO_2 as sulfur host material was first proposed by Nazar and co-workers in 2015.[121] Ultrathin MnO_2 nanosheets were synthesized by reducing GO with $KMnO_4$. After loading sulfur within the MnO_2 nanosheets with a content of 75% *via* a melt-diffusion method, the S/MnO_2 composite delivered an initial discharge capacity of 1300 mA h g^{-1} at C/20 and a capacity decay rate of only 0.036% per cycle over 2000 cycles at 2C, among the best cycling performance at that time. To elucidate the interactions between MnO_2 and sulfur species, ex-situ X-ray photoelectron spectroscopy (XPS) measurements were performed on the S/MnO_2 composite electrodes after discharged to specific states (**Figure 1.8**e). Two new peaks appeared at 167.2 eV and 168.2 eV during the discharge process, which could be attributed to the formation of thiosulfate and polythionate, respectively (**Figure 1.8**e). Unlike previous strategies to anchor polysulfides by physical barrier or simple chemical interaction, a new mechanism based on transfer mediator was proposed to bind polysulfides and promote the redox activity. In particular, the initial formed lithium polysulfides reacted with MnO_2 to produce thiosulfate species, and then further reacted with long-chain polysulfides to form polythionate complex and short-chain polysulfides. This process occurred progressively on discharge until full conversion to Li_2S_2/Li_2S was achieved.

As the conductivity of both sulfur and MnO_2 was very poor, the use of pure MnO_2 as sulfur host would not be an optimal choice. To this end, Lou's group pioneeringly designed hollow carbon nanofibers decorated with MnO_2 nanosheets (MnO_2@HCF) as sulfur host

(**Figure 1.8**f-i).[122] This structural design not only enabled the electrode with long-range conductivity but also with both physical confinement and chemical absorption, restraining the dissolution and shuttle effect of polysulfides (**Figure 1.8**j). By virtue of these advantages, the MnO_2@HCF/S electrodes exhibited high capacity with superior cycling stability even at a high areal sulfur loading of 3.5 mg cm^{-2} (**Figure 1.8**k). Subsequently, carbon nanoboxes confined with MnO_2 nanosheets were also designed to encapsulate sulfur to improve the electrochemical performance of Li-S batteries.[123] Apart from carbon materials, conductive polymer such as polypyrrole was also developed to combine with MnO_2 to improve the overall conductivity of the cathode.[124]

Recently, Nazar's group further prepared the unique core-shell structured hollow sulfur-MnO_2 spheres by the *in-situ* redox reaction between sulfur and $KMnO_4$.[125] The bifunctional MnO_2 shell could not only act as the physical barrier to restrain the out diffusion of polysulfides, but also chemically trap the polysulfides. In addition, the unique hollow structure can accommodate the volume change upon cycling. Using hollow sulfur-MnO_2 core-shell spheres as cathodes, the electrode showed an ultralow capacity decay rate of only 0.039% per cycle over 1700 cycles at a high sulfur content of 80%.

Implanting polar metal oxide nanocrystals into mesoporous carbon was also explored to combine the physical barrier with chemical entrapment to confine polysulfides. Jin's group has embedded ultrafine CeO_2 nanocrystals into micromesoporous nitrogen-rich carbon nanospheres for using as sulfur host.[126] The inserted polar CeO_2 nanocrystals can trap and promote the polysulfide conversion, while the micromesoporous carbon spheres provide abundant pore structures to encapsulate sulfur. Using CeO_2/C as sulfur host, it exhibited high

capacity of 721 mA h g^{-1} at 2C after 1000 cycles with an ultralow capacity decay rate of only 0.024% per cycle. Long's group integrated ultrafine Nb_2O_5 nanocrystals into mesoporous carbon microspheres.[127] Apart from the enhanced anchoring ability for polysulfides *via* both the physical and chemical entrapment, the Nb_2O_5 nanocrystals can also act as an efficient electrocatalyst to accelerate the polysulfide redox kinetics. As a result, the Nb_2O_5/C/S cathode showed an excellent rate performance of 887 mA h g^{-1} at 5C.

Although the overall conductivity of metal oxide based hosts can be improved to some extent by integrating with conductive carbon materials, the charge transfer at the interfaces between insulating oxides and sulfur species would not be efficient. To this end, polar metal oxides with metallic conductivity were further explored to use as sulfur hosts. In 2014, the Nazar group reported the use of Ti_4O_7 as a metallic and polar host for sulfur cathode (**Figure 1.9**a).[128] The visual adsorption tests suggest that the Ti_4O_7 has stronger chemical adsorption capability for polysulfides compared to that of carbon materials (**Figure 1.9**b). The S_T^{-1} and S_B^{-1} XPS spectra of Li_2S_4 show obvious positive shift after the interaction with Ti_4O_7 (**Figure 1.9**c), indicating the strong interaction between lithium polysulfides and Ti_4O_7. Operando X-ray absorption near edge structure (XANES) measurements indicated the more efficient redox kinetics of polysulfide conversion on Ti_4O_7 than carbon (**Figure 1.9**d). Based on these results, the authors proposed that the polar and metallic Ti_4O_7 surface can not only enhance the adsorption of polysulfides, but also the redox chemistry of polysulfides (**Figure 11**e). As a result, the Ti_4O_7/S composite showed high capacity of 1069 mA h g^{-1} with superior cycling stability at 0.2C for 100 cycles.

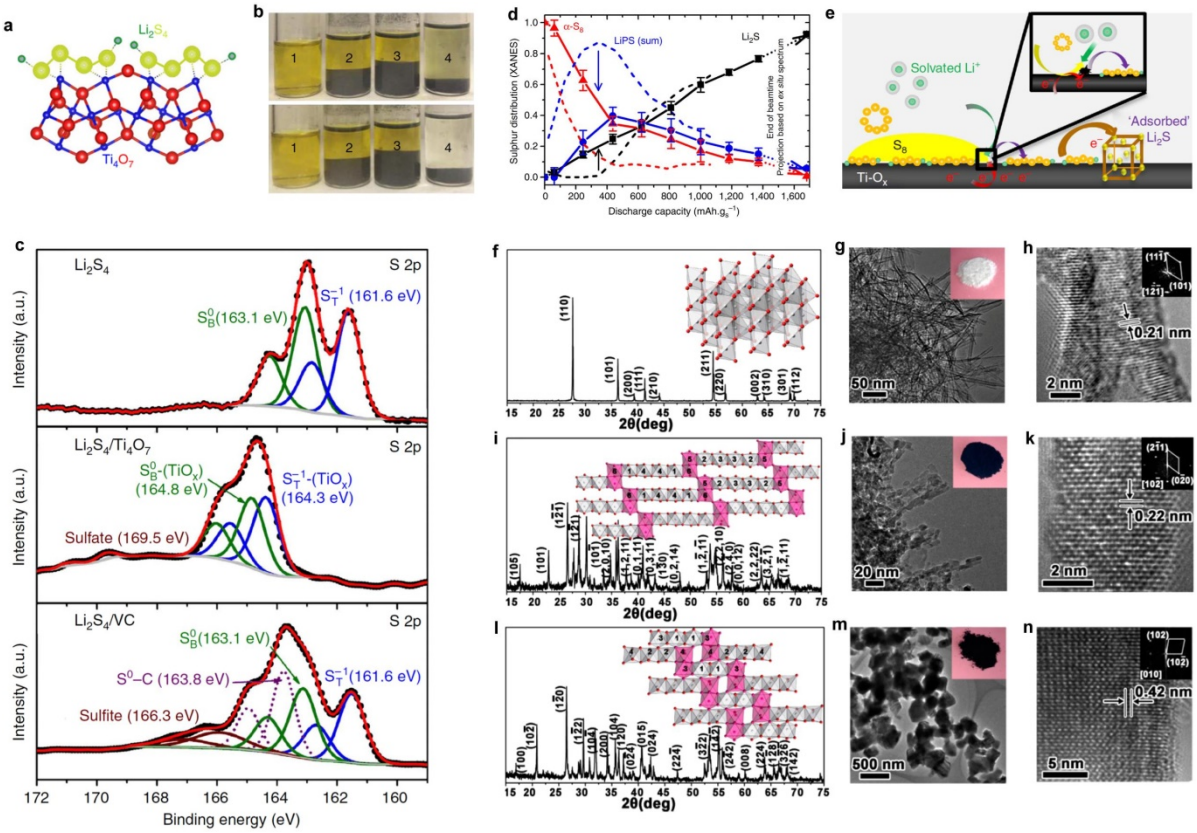

Figure 1.9 (a) Schematic of the interaction between Li_2S_4 and Ti_4O_7. (b) Photographs of Li_2S_4/THF solution before (top) and after (bottom) contact with nothing (1), graphite (2), VC carbon (3) and Ti_4O_7 (4). (c) High-resolution XPS S 2p spectra of Li_2S_4, Li_2S_4/Ti_4O_7 and Li_2S_4/VC, respectively. (d) Distribution of sulfur species upon discharge determined by operando XANES. The solid and dashed lines represent Ti_4O_7/S-6 and VC/S-6, respectively. (e) Illustration of surface-mediated reduction of S_8 on Ti_4O_7. (a-e) Reproduced from reference[128]. Copyright 2014, Nature Publishing Group. XRD patterns of (f) rutile TiO_2, (i) Magnéli phase Ti_6O_{11} and (l) Ti_4O_7, respectively. The insets are the corresponding stackings of the oxygen octahedral. TEM images of g) TiO_2, (j) Ti_6O_{11} and (m) Ti_4O_7, respectively. The insets are the corresponding digital photos. HR-TEM images of (h) TiO_2, k) Ti_6O_{11} and n) Ti_4O_7, respectively. The insets show the corresponding fast Fourier transform (FFT) diffraction patterns. (f-n) Reproduced from reference[129]. Copyright 2014, American Chemical Society.

Almost at the same time, Cui's group synthesized a series of Magnéli phase Ti_nO_{2n-1} nanomaterials to use as sulfur host (**Figure 1.9**f-n).[129] By reducing TiO_2 nanotubes (**Figure 1.9**f-h) respectively at 950 °C and 1050 °C for 4 h in pure hydrogen, Ti_6O_{11} nanowires (**Figure 1.9**i-k) and Ti_4O_7 (**Figure 1.9**l-n) nanoparticles were formed respectively. Unlike TiO_2, the oxygen-deficient Ti_4O_7 not only owns highly metallic conductivity (~10^3 S cm^{-1}),[17] but also low coordinated Ti sites. Theoretical calculations suggested that the low coordinated Ti sites were the most favorable adsorption sites for sulfur species to form the strong Ti-S bonds, which was confirmed by the XPS analysis. As a result, the S/Ti_4O_7 composite exhibited impressive cycling performance of 1044 mA h g^{-1} with 99% capacity retention after 100 cycles at 0.1C. Additionally, the cycling performances followed the order of S/Ti_4O_7>S/Ti_6O_{11}>S/TiO_2, which was in accordance with the conductivities of these oxides.

Although the surface of Ti_4O_7 had strong chemical interactions with the polysulfides, the irregular particle forms mentioned above can only provide limited interfaces to absorb polysulfides, which was not benefit to achieve high sulfur content as well as high sulfur loading. To this end, Ti_4O_7 microspheres with highly interconnected mesoporous structure were further designed by Caruso's group (**Figure 1.10**a-c).[130] Mesoporous TiO_2 microspheres were first prepared as template (**Figure 1.10**b), followed by infiltrating resol into the template. After the carbothermal reduction process, mesoporous Ti_4O_7 microspheres were obtained (**Figure 1.10**c). The Ti_4O_7 microspheres have a high surface area of 197.2 m^2 g^{-1} and large pore volume of 0.39 cm^3 g^{-1}, which provide sufficient spaces and interfaces to accommodate and adsorb the polysulfides. By virtue of the high conductivity, physical and chemical confinement of this unique architecture, the mesoporous Ti_4O_7 spheres-sulfur composite

exhibited specific capacity of 1317 mA h g^{-1} at 0.1C and low decay in capacity of 12% after 400 cycles at 0.2C.

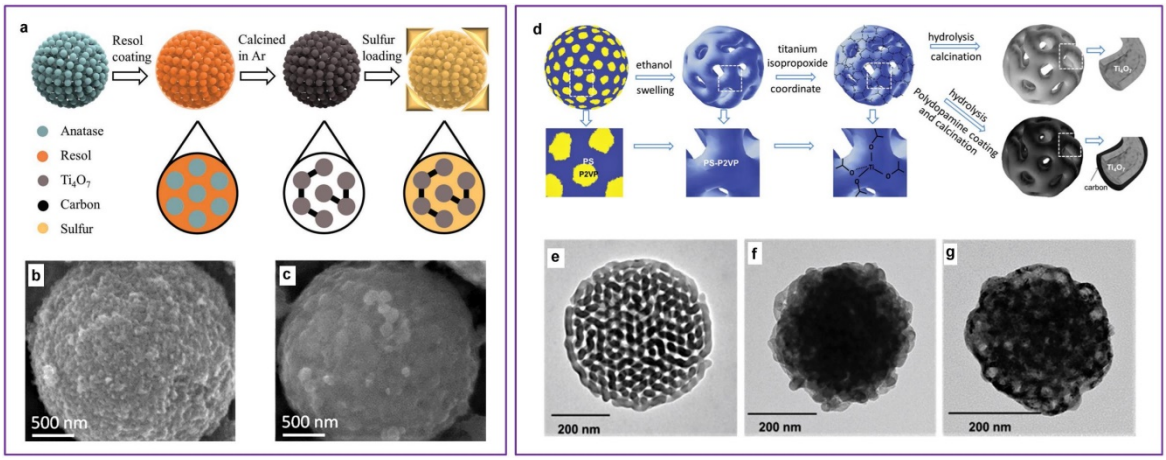

Figure 1.10 (a) Schematic of the synthetic process for mesoporous Ti_4O_7 microspheres. SEM images of (b) mesoporous TiO_2 microspheres and (c) mesoporous Ti_4O_7 microspheres. a-c) Reproduced from reference[130]. Copyright 2016, Wiley-VCH. (d) Schematic of the synthetic procedure for Ti_4O_7 nanoparticles with interconnected-pore architecture. TEM images of (e) porous PS-P2VP particles, (f) TiO_2@PS-P2VP particles and (g) porous Ti_4O_7 particles. (d-g) Reproduced from reference[131]. Copyright 2017, Wiley-VCH.

Subsequently, Lu's group also prepared the porous Ti_4O_7 spheres with interconnected-pore structure as sulfur host (**Figure 1.10**d-g).[131] To do so, a selective swelling strategy was first used to produce the mesoporous poly(styrene-*b*-2-vinylpyridine) (PS-P2VP) spheres as template (**Figure 1.10**e). Then, TiO_2@PS-P2VP spheres were obtained by the hydrolysis of titanium isopropoxide adsorbed on the PS-P2VP template (**Figure 1.10**f). Finally, mesoporous Ti_4O_7 spheres were obtained by the thermal reduction process (**Figure 1.10**g). The obtained mesoporous Ti_4O_7 spheres have a high surface area of 592 m^{-2} g^{-1}, and most of the mesopores centered at 5 nm, which are beneficial for both the physical and chemical confinement of polysulfides. When used as the sulfur host for Li-S batteries, the mesoporous

Ti_4O_7/S composite showed much improved electrochemical performance compared to that of TiO_2/S composite. When combining a thin layer of carbon coating on the mesoporous Ti_4O_7 spheres, the electrochemical performance could be further enhanced to a capacity of 1411 mA h g^{-1} at 0.1 C with a low capacity decay rate of 0.099% per cycle over 300 cycles.

Apart from Ti_4O_7 and Ti_6O_{11}, Magnéli phase TiO was also developed as sulfur host for Li-S batteries because its conductivity is nearly one order of magnitude higher than that of Ti_nO_{2n-1} (n=4~10).[132, 133] In 2016, Lou and co-workers pioneeringly designed TiO@C hollow spheres as sulfur host (**Figure 1.11**a).[134] Uniform polystyrene (PS) spheres with a diameter of about 490 nm were first prepared as template (**Figure 1.11**b), followed by coating with TiO_2 and polydopamine (PDA) to form the PS@TiO_2@PDA spheres (**Figure 1.11**c). After heating the PS@TiO_2@PDA spheres at 1000 °C for 4 h under the atmosphere of N_2/H_2 (95:5), TiO@C hollow spheres were obtained (**Figure 1.11**d). Sulfur was infiltrated into the TiO@C hollow spheres by a vapor phase infusion method at 300 °C (**Figure 1.11**e). DFT calculations indicate that TiO has much stronger chemical adsorption capability towards polysulfides compared to TiO_2. Owing to the unique surface chemical properties and hollow structure, the TiO@C/S cathode showed stable cycle life up to 500 cycles at 0.2C with a low capacity decay rate of 0.08% per cycle.

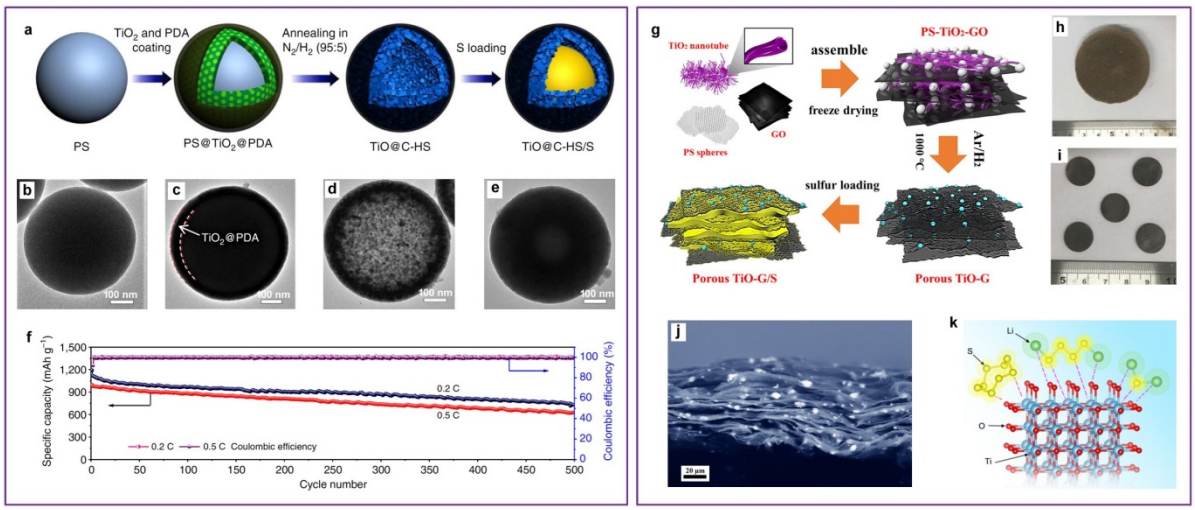

Figure 1.11 (a) Schematic of synthetic process for TiO@C-HS/S spheres. TEM images of (b) PS, (c) PS@TiO_2@PDA, (d) TiO@C-HC and (e) TiO@C-HS/S spheres, respectively. (f) Cycling performances of TiO@C-HS/S cathodes at 0.2 and 0.5C. (a-f) Reproduced from reference[134]. Copyright 2016, Nature Publishing Group. (g) Schematic of synthesis procedure of 3D hierarchically porous TiO-G/S film. Digital photos of (b) PS-TiO_2-GO sponge and (i) TiO-G film electrodes. (j) Cross-sectional backscattered electron image of sulfur-loaded TiO-graphene film. k) Illustration of the interactions between TiO and sulfur species. (g-k) Reproduced from reference[135]. Copyright 2018, Elsevier.

In order to reduce the inactive part of the electrode and increase the specific energy, our group has developed a 3D hierarchically porous TiO-graphene (TiO-G) composite film both as the current collector and host for sulfur loading (**Figure 1.11**g-i).[135] **Figure 1.11**j shows the cross-sectional backscattered electron image of the freestanding TiO-G/S film and the white dots represent the signal of Ti element due to the different contrast between the metal and nonmetal elements. This indicates that ultrafine TiO nanoparticles distribute uniformly across the freestanding film. **Figure 1.11**k illustrates the possible interactions between TiO and sulfur species. The conductive and polar TiO nanoparticles play a key role in binding with polysulfides, while the graphene provides continuous conductive networks for electron

transport. As a result, the TiO-G/S composite film demonstrated superior cycling stability even at a high areal sulfur loading of 5.2 mg cm^{-2}.

Recently, the Fe_3O_4-C yolk-shell nanobox structure was also designed to host sulfur by Manthiram's group.[136] Fe_2O_3 nanocubes were first prepared by a co-precipitation method, followed by coating with polydopamine (PDA) to form the core-shell PDA@Fe_2O_3 nanocubes. After annealing and etching process, C@Fe_3O_4 yolk-shell nanoboxes were obtained. Finally, sulfur was infiltrated into the voids of the C@Fe_3O_4 yolk-shell nanoboxes *via* a melt-diffusion strategy. The polar and conductive Fe_3O_4 (5×10^4 S m^{-1})[137] core can not only trap the polysulfides through the strong chemical interactions between them but also accelerate the electron transport upon cycling. In addition, the carbon nanoboxes acted as the nanoscale electrochemical reaction chamber to further suppress the out diffusion of polysulfides. As a result, the C@Fe_3O_4/S delivered high specific capacity of 1104 mA h g^{-1} with long cycling performance even at a high sulfur content of 80 wt% and sulfur loading of 5.5 mg cm^{-2}.

Besides the metal oxides mentioned above, many other metal oxides such as SiO_2,[138-144] Co_3O_4,[145-147] MgO,[148-151] Fe_2O_3,[152] Al_2O_3,[148, 153-155] V_2O_5,[156-160] V_2O_3,[161] VO_2,[162] ZnO,[163-165] WO_3,[166] CaO,[148] MoO_2,[167, 168] MoO_3,[169] La_2O_3,[148] SnO_2,[170-172] Nb_2O_5,[173] $ZnCo_2O_4$,[174] $NiFe_2O_4$,[175] perovskite $Ba_{0.5}Sr_{0.5}Co_{0.8}Fe_{0.2}O_{3-\delta}$,[176] and perovskite $La_{0.6}Sr_{0.4}CoO_{3-\delta}$,[177] have also been explored as sulfur host for Li-S batteries. It should be pointed out that most of the metal oxide nanostructures are coupled with conductive polymers or carbon materials to increase the overall conductivity of the cathode rather than relying on their intrinsic conductivity to obtain the best performance for Li-S batteries.

1.2.4 Metal organic frameworks as host

Metal organic frameworks (MOFs) are a kind of crystalline materials made of the periodic coordination of metal ions and organic linkers. Thus they can be rationally designed at the molecule level by selectively choosing the units of metal ions and organic linkers. MOFs have the highly porous framework which can provide sufficient channels for the transportation of lithium ions. In addition, the abundant functional groups and Lewis acid sites can supply efficient anchoring sites for sulfur species. In this section, typical MOF structures will be discussed as sulfur host materials to improve the cycling performance of Li-S batteries.

In 2011, Tarascon's group pioneered the use of MOFs as host material for sulfur impregnation (**Figure 1.12**a).[178] Chromium trimesate MIL-100 (Cr) (MIL: Materiaux Institut Lavoisier) was selected to encapsulate sulfur owing to its unique structural advantages which would potentially improve the performance of Li-S batteries. MIL-100 (Cr) consists of two types of mesoporous cages (2.5-2.9 nm) connected through microporous pentagonal window with a size of about 0.5 nm and hexagonal window with a size of about 0.9 nm (the inset in **Figure 1.12**a). The small entrance windows of MIL-100 (Cr) with a balanced weak binding with polysulfides were believed to reversibly capture and release polysulfides upon cycling, while the mesoporous cages with a large pore volume of 1 cm^3 g^{-1} provided sufficient space for sulfur accommodation. Therefore, S@MIL-100 (Cr) showed improved cycling performance (**Figure 1.12**a). However, due to the insulating nature of MIL-100 (Cr), the sulfur utilization efficiency was not very satisfactory. In addition, the sulfur content in S@MIL-100 (Cr) was also very low.

In 2014, Xiao and co-workers proposed that the Lewis acid-base interactions between MOFs and lithium polysulfides would play a vital role on the electrochemical performance of Li-S batteries (**Figure 1.12**b,c).[179] In their work, MOFs with different Lewis acidic metal centers were prepared to compare the electrochemical performances. The Ni-MOF/S showed better cycling performance compared to Co-MOF/S, although Co-MOF has higher conductivity than Ni-MOF. This can be attributed to the stronger coordination between Lewis acidic Ni (II) center and the polysulfide base, as confirmed by the DFT calculations showing that the binding energy between Ni-MOF and polysulfides is consistently higher than that between Co-MOF and polysulfides.

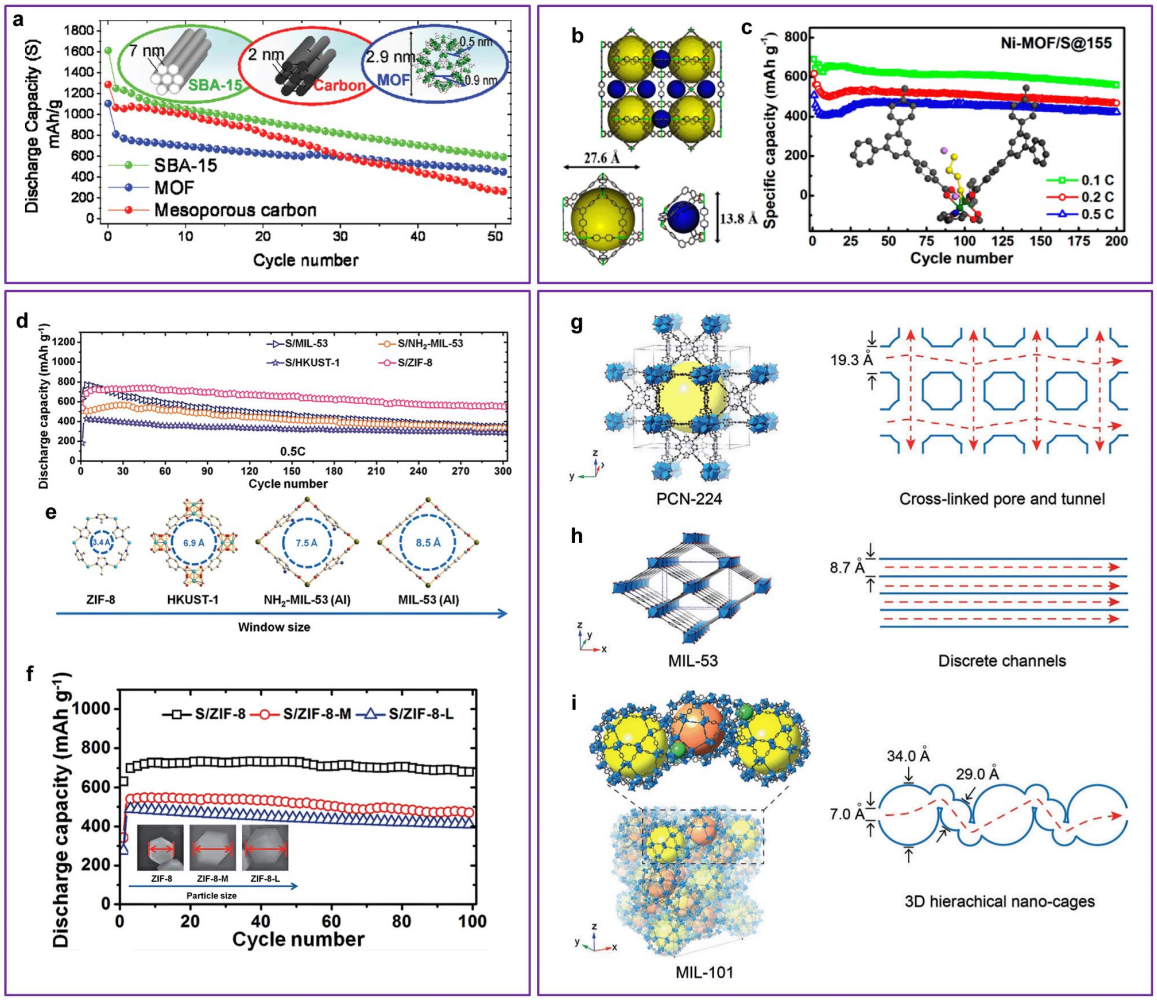

Figure 1.12 (a) Cycling performances of S@MIL-100(Cr), S@SBA-15 and S@mesoporous

carbon. The insets illustrate the corresponding microstructures. Reproduced from reference[178]. Copyright 2011, American Chemical Society. (b) Crystal structure of Ni-MOF containing two different types of pores. (c) Cycling performances of Ni-MOF/S at 0.1, 0.2 and 0.5C. The inset illustrates the interactions between polysulfides and paddle-wheel unit in Ni-MOF. (b,c) Reproduced from reference[179]. Copyright 2014, American Chemical Society. (d) Comparison of cycling performances of S/MIL-53, S/NH_2-MIL-53, S/HKUST-1 and S/ZIF-8 at 0.5C. (e) Schematic of the largest apertures of the four different MOFs. (f) Cycling performances of S/ZIF-8 with different particle sizes. The inset shows the SEM images of ZIF-8 with particle sizes of 150 nm, 1 μm and 3 μm (from left to right), respectively. (d-f) Reproduced from reference[180]. Copyright 2014, Royal Society of Chemistry. Crystal structures of (g) PCN-224, (h) MIL-53, (i) MIL-101, respectively, and illustrations of corresponding ion diffusion pathways in their pores. (g-i) Reproduced from reference[181]. Copyright 2018, Wiley-VCH.

Besides the interactions between MOFs and polysulfides, Li and co-workers found that the particle and aperture size of MOFs were also very important to the performance of Li-S batteries.[180] The authors synthesized four kinds of MOFs, ZIF-8, HKUST-1, NH_2-MIL-53(Al), MIL-53(Al), with different aperture sizes of 0.34 nm, 0.69 nm, 0.75 nm and 0.85 nm, respectively (**Figure 1.12**e). Based on the cycling performances of these MOF based host materials (**Figure 1.12**d), the authors claimed that smaller window size, associated with functionalities in the open framework that had affinity with polysulfide anions, can help achieve a more stable cycling. ZIF-8 with different particle sizes from 150 nm to 1 μm and 3 μm were also compared in **Figure 1.12**f, indicating that smaller particle size was beneficial to realize a high sulfur utilization efficiency with high capacity. In another report, Lin and co-workers proposed that MOFs with aperture size lower than the molecule size of S_8 (0.68 nm) could not effectively confine sulfur into the cavities of MOFs (**Figure 1.13**c).[182] To

prove this claim, EDX measurements were performed on S@HKUST-1/CNT, S@MOF-5/CNT and S@ZIF-8/CNT before and after CS_2 washing process. The results showed that sulfur was well detected in the HKUST-1/CNT and MOF-5/CNT thin films, but less sulfur was retained in the ZIF-8/CNT film after CS_2 washing process. Accordingly, the S@HKUST-1/CNT and S@MOF-5/CNT films demonstrated much better cycling performance compared to the S@ZIF-8/CNT film. These results seems to be inconsistent with the above results reported by Li and coworkers (**Figure 1.12**d,e). It should be pointed out that so many factors such as particle size, window size, functional groups and Lewis acidic metal sites can all influence the overall electrochemical performance of MOF based host materials, thus more studies should be paid to the mechanism of its improvement in Li-S batteries. Soft-package Li-S cells based on the S@HKUST-1/CNT cathodes with ultrahigh sulfur loadings demonstrated high areal capacity with superior cycling performance, indicating its great potential for practical applications (**Figure 1.13**e).

Besides the pore window and pore size, Deng and co-workers also studied the effect of pore geometry of MOFs on the performance of Li-S batteries.[181] PCN-224, MIL-53, and MIL-101 with respectively cross-linked pore and tunnel, discrete channels, and 3D hierarchical nano-cages were prepared as illustrated in **Figure 1.12**g-i. As indicated, the cross-linked pore structure of PCN-224 can provide the most efficient ions diffusion pathways among the three MOFs. When used as cathodes for Li-S batteries, the PPY-coated S@PCN-224 showed the best performance among these three MOFs with excellent rate performance of 670 and 440 mA h g^{-1} at 10C after 200 and 1000 cycles.

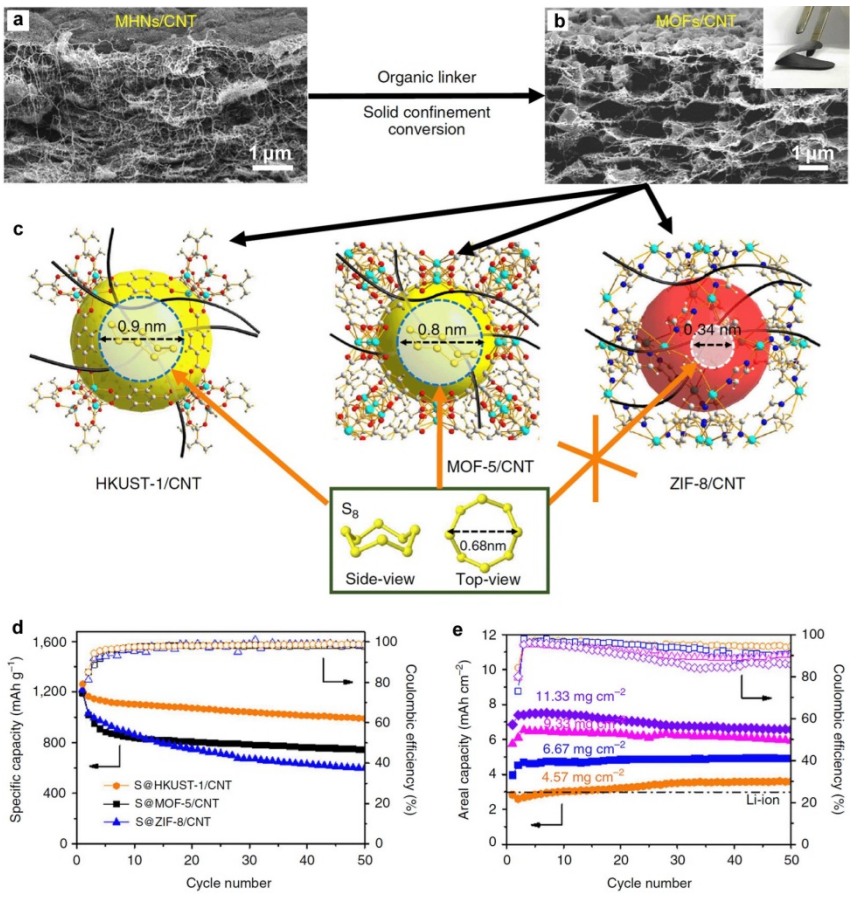

Figure 1.13 SEM images of (a) MHNs/CNT and (b) MOFs/CNT. The inset in b shows the photograph of the self-standing MOFs/CNT thin film. (c) Crystal structures of three different kinds of MOFs. (d) Cycling performances and Coulombic efficiencies of S@HKUST-1/CNT, S@MOF-5/CNT and S@ZIF-8/CNT. (e) Cycling performances of soft-package Li-S cells using S@HKUST-1/CNT cathodes at different sulfur loadings. Reproduced from reference[182]. Copyright 2017, Nature Publishing Group.

Besides the typical MOFs discussed above, our group demonstrated that Prussian blue $Na_2Fe[Fe(CN)_6]$ can effectively confine sulfur species within its cavities (**Figure 1.14**).[183] To further restrain the out-diffusion of lithium polysulfides upon cycling and improve the conductivity of the electrode, a thin layer of conductive PEDOT was coated on the $S@Na_2Fe[Fe(CN)_6]$ nanocrystals. Owing to the dual confinement effect by $Na_2Fe[Fe(CN)_6]$

and PEDOT, the S@$Na_2Fe[Fe(CN)_6]$@PEDOT showed improved electrochemical performance compared to the S@$Na_2Fe[Fe(CN)_6]$.

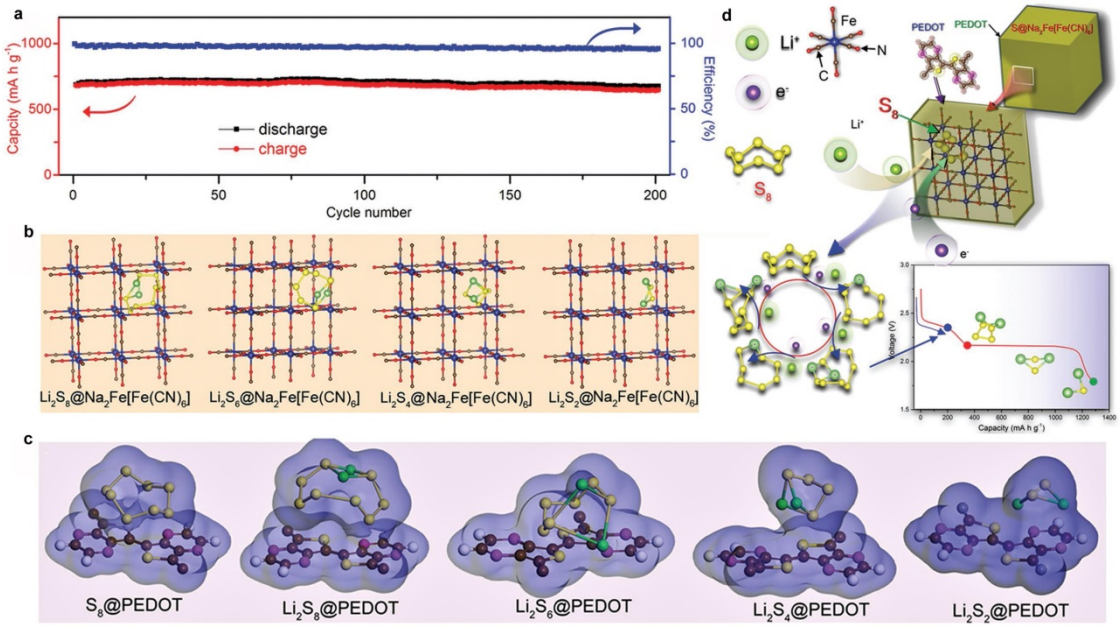

Figure 1.14 (a) Cycling performance of S@$Na_2Fe[Fe(CN)_6]$@PEDOT at 5C. (b) The atomic model configurations of Li_2S_x (x=8, 6, 4 and 2) in $Na_2Fe[Fe(CN)_6]$. (c) The optimized interaction of PEDOT with sulfur species. (d) Illustration of the S@$Na_2Fe[Fe(CN)_6]$@PEDOT system in the early stage of the discharge process. Reproduced from reference[183]. Copyright 2017, Wiley-VCH.

1.2.5 Metal hydroxides as host

Metal hydroxides are another type of polar materials with abundant hydrophilic and hydroxyl groups on their surfaces, which can afford efficient chemical entrapment for polysulfides. Moreover, the electrocatalytic properties of metal hydroxides may also enhance the redox reaction kinetics in Li-S batteries.[184] In 2015, Yu and co-workers reported the use of ultrathin layered $Ni(OH)_2$ as the encapsulation material for sulfur cathode (**Figure 1.15**a-e).[185] Sulfur@carbon black (S@CB) hybrids were first synthesized by mixing and melting sulfur

with CB. The SEM image of S@CB indicated that numerous sulfur aggregations appeared on the surfaces of CB particles (**Figure 1.15**c) due to the insufficient pore volume for sulfur accommodation. To avoid the sulfur loss during the electrochemical reaction, S@CB was further uniformly packaged by the layered $Ni(OH)_2$ thin film through the solution reaction between Ni salts with ammonium (**Figure 1.15**d). When evaluated as the cathode, the S@CB@$Ni(OH)_2$ electrode showed much improved cycling performance with a retained capacity of about 1250 mA h g^{-1} after 500 cycles and higher Coulombic efficiency compared to the S@CB electrode at 0.2C (**Figure 1.15**e). This suggested that the $Ni(OH)_2$ encapsulation layer indeed played a vital role on suppressing the out-diffusion of polysulfides, thus ensuring the high sulfur utilization and long-cycling performance. In addition, the Ni hydroxide thin film on S@CB can also irreversibly react with lithium ions to *in-situ* produce robust and protective Li-Ni mixed hydroxide thin film with good lithium ion accessibility and abundant functional groups to trap the polysulfides. Almost at the same time, Niu et al. also reported the coating of S@CB with $Ni(OH)_2$ to enhance the cycling performance of Li-S batteries.[186] The difference is that $Ni(OH)_2$ nanoparticles were used as the encapsulation layer instead of the thin-film structure. Due to the insufficient confinement effect of nanoparticles compared to nanosheets, the cycling performance of $Ni(OH)_2$ nanoparticles encapsulated S@CB was not as well as that of $Ni(OH)_2$ thin film encapsulated S@CB. At the same time, this group also reported the use of $Co(OH)_2$ nanosheets to encapsulate S@CB to enhance the performance of Li-S batteries.[187]

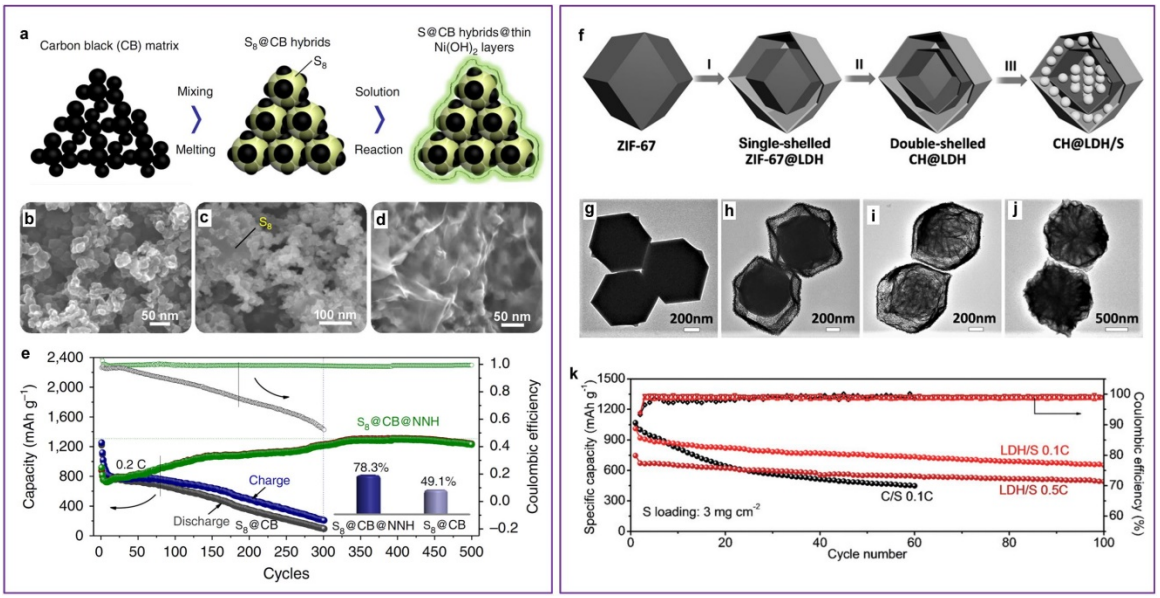

Figure 1.15 (a) Schematic of the synthesis process for S@CB hybrids@thin $Ni(OH)_2$ layers. SEM images of (b) CB powder, (c) S_8@CB and (d) S_8@CB@$Ni(OH)_2$ hybrids. (e) Cycling performances and Coulombic efficiencies of S_8@CB and S_8@CB@$Ni(OH)_2$ at 0.2C for 500 cycles. The inset shows the sulfur utilization efficiency. (a-e) Reproduced from reference[185]. Copyright 2015, Nature Publishing Group. (f) Schematic illustration of the synthesis process for $Co(OH)_2$@LDH/S. TEM images of (g) ZIF-67, (h) single-shelled ZIF-67@LDH, i) doubled-shelled $Co(OH)_2$@LDH nanocages, and (j) $Co(OH)_2$@LDH/S. (k) Cycling performance of $Co(OH)_2$@LDH/S and C/S at 0.1C. (f-k) Reproduced from reference[188]. Copyright 2016, Wiley-VCH.

Lou's group designed a novel type of doubled shelled $Co(OH)_2$/layered double hydroxides (LDH) nanocages as sulfur host for Li-S batteries.[188] The synthesis process was illustrated in **Figure 1.15**f. ZIF-67 polyhedrons were first prepared as the sacrificial template (**Figure 1.15**g). Then, yolk-shelled ZIF-67@LDH polyhedrons were prepared by reacting ZIF-67 with $Ni(NO_3)_2$ (**Figure 1.15**h). After that, double-shelled $Co(OH)_2$@LDH nanocages were obtained by reacting the yolk-shelled ZIF-67@LDH with Na_2MoO_4 (**Figure 1.15**i). Finally, sulfur was loading to the nanocages via a melt-diffusion method (**Figure 1.15**j). The

double-shelled hollow structure can not only maximize the advantages of hollow nanostructures to physically confine a high content of active sulfur, but also provide abundant interfaces with hydrophilic and polar groups to bind with polysulfides to further restrain the loss of active species. By virtue of this exquisite nanoarchitecture and unique surface chemical properties, the $Co(OH)_2$@LDH/S composite showed much enhanced cycling performance compared to C/S at a high sulfur loading of 3 mg cm^{-2} (**Figure 1.15**k). Afterwards, this group also developed a kind of Ni-Fe layered double hydroxide hollow polyhedrons as sulfur host to enhance the performance of Li-S batteries.[189]

Overall, metal hydroxides with functional hydrophilic groups can provide efficient chemical entrapment for polysulfides, combining the facile preparation method making them a promising type of encapsulation materials for sulfur cathodes. However, the low conductivity of metal hydroxides limits the electron transport, thus it is better to combine them with carbon materials to increase the overall conductivity. In addition, the interaction mechanism between metal hydroxides and polysulfides is not very clear and needs to be further investigated.

1.2.6 Metal sulfides as host

Metal sulfides are another class of typical polar inorganics that have been extensively studied as sulfur host for Li-S batteries. Compared to metal oxides, MOFs and metal hydroxides, metal sulfides usually have higher electronic conductivity and some of the metal sulfides even have metallic or half-metallic phases. Moreover, the metal sulfides own strong sulfiphilic property to sulfur-containing species, affording robust chemical anchoring ability

for polysulfides. In this section, some typical metal sulfides, such as TiS_2, VS_2, CoS_2, Co_3S_4, Co_9S_8, MoS_2, ZnS and Mo_6S_8 will be discussed as cathode host materials for Li-S batteries.

The layered transition metal disulphides have received great interests for a wide range of applications in recent years due to their unique 2D nanostructures.[190-195] In 2014, the Cui group pioneered the use of 2D titanium disulphide (TiS_2) to encapsulate Li_2S for high performance Li-S batteries.[196] The Li_2S@TiS_2 core-shell nanostructures were prepared by the *in situ* reaction between $TiCl_4$ and partial Li_2S surface to form the TiS_2 coating (**Figure 1.16**a). This *in situ* reaction can ensure a conformal and uniform coating of TiS_2 thin layer on the Li_2S surface. The Li_2S@TiS_2 nanostructures were then annealed at 400 °C under Ar atmosphere to allow crystallization of the TiS_2 shell to increase the conductivity (**Figure 1.16**b). Owing to the semimetal property of TiS_2, the electronic conductivity of Li_2S@TiS_2 was measured to be 5.1×10^{-3} S cm^{-1}, which is almost 10 orders of magnitude higher than that of bare Li_2S. In terms of confining sulfur species, the unique 2D layered structure of TiS_2 can not only act as a physical barrier to entrap these species within the shell during cycling, but also provide strong chemical interactions with Li_2S. The calculated binding energy between TiS_2 and Li_2S was about 2.99 eV, which was about ten times higher than that between Li_2S and carbon materials. Owing to the dual effect of physical confinement and chemical adsorption, the Li_2S@TiS_2 core-shell nanostructures showed very high capacity with superior cycling stability compared to bare Li_2S (**Figure 1.16**c). In addition, the synthesis process of TiS_2-encapsulated Li_2S can be extended to other 2D layered materials such as ZrS_2 and VS_2. The Li_2S@ZrS_2 and Li_2S@VS_2 also showed impressive electrochemical performances. Recently, Manthiram and co-workers prepared TiS_2-polysulfide hybrid cathode with high

sulfur loading and low electrolyte consumption for Li-S batteries.[197] Owing to the conductive and polar property of TiS_2, the Li_2S-polysulfide cathode showed high areal capacity of 10 mA h cm^{-2} with good stability at a high areal sulfur loading of 12 mg cm^{-2} and a low electrolyte/sulfur ratio of 5 μL mg^{-1}, demonstrating potential practical applications.

CoS_2 is also a half-metallic crystal phase with an appreciable conductivity of 6.7×10^3 S cm^{-1}.[198] Zhang and co-workers reported that CoS_2 can power Li-S battery performance by propelling polysulfide redox at the interfaces between CoS_2 and electrolyte.[199] The sulfiphilic CoS_2 can not only chemically anchor the polysulfides but also accelerate the fast redox reaction, as illustrated in **Figure 1.16**d. To give more insight on the catalysis effect of CoS_2 for polysulfide conversion, CV tests were performed for symmetrical Li_2S_6 cells (**Figure 1.16**e). Compared to the negligible current response of Li_2S_6-free symmetric cells, the Li_2S_6-symmetric cells with CoS_2/G as electrodes show significantly enlarged current density, indicating the superior catalytic effect of CoS_2 for polysulfide conversion. Using 15% CoS_2/graphene as host material, the electrode showed a high initial discharge capacity of 1003 mA h g^{-1} at 2C and exhibited a very low capacity decay rate of only 0.034% per cycle over prolonged 2000 cycles (**Figure 1.16**f).

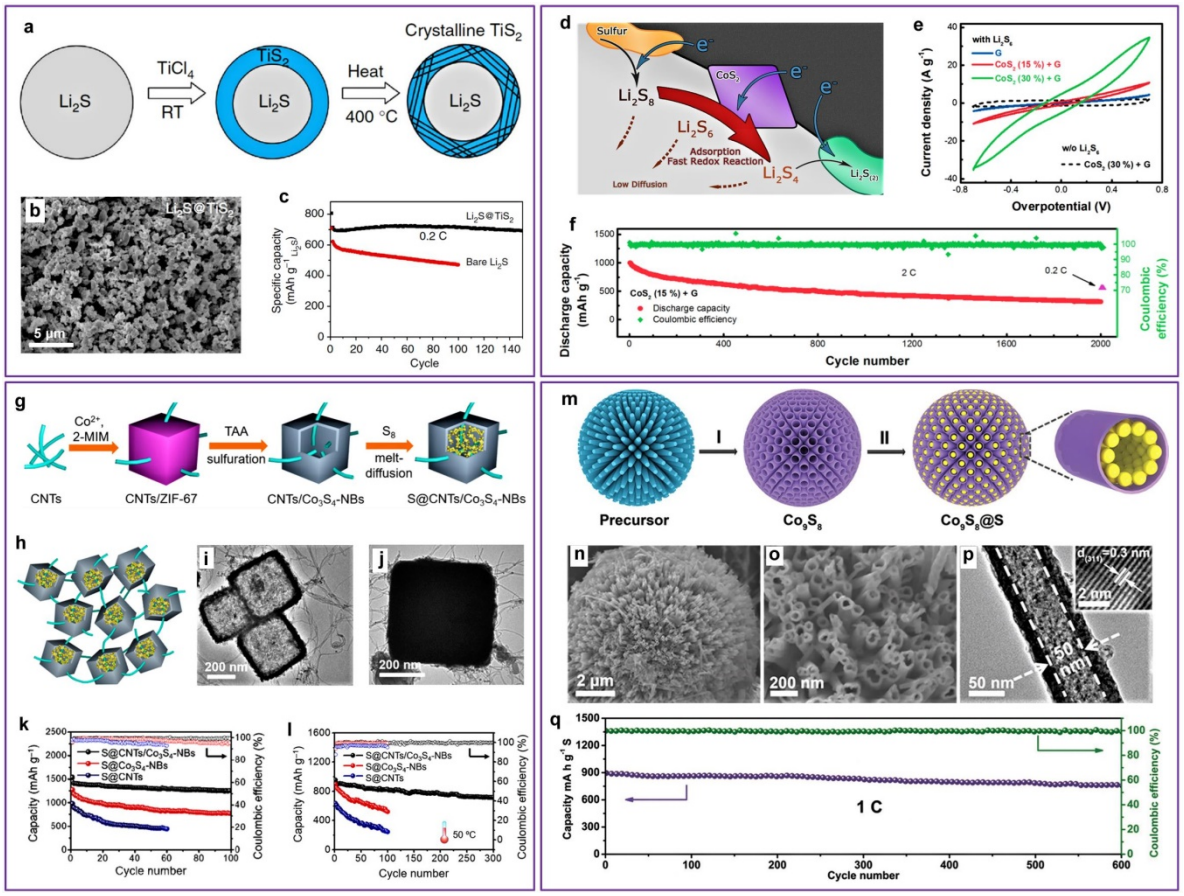

Figure 1.16 (a) Schematic of the synthetic process for $Li_2S@TiS_2$ core-shell nanostructures. (b) SEM image of $Li_2S@TiS_2$ core-shell nanostructures. (c) Cycling performances of $Li_2S@TiS_2$ and bare Li_2S cathodes at 0.2C (1C=1166 mA g^{-1}_{Li2S}). (a-c) Reproduced from reference[196]. Copyright 2014, Nature Publishing Group. (d) Illustration of CoS_2 promoted polysulfide redox reaction. (e) CV curves of symmetrical Li_2S_6 cells with different electrodes. f) Cycling performance and Coulombic efficiency of CoS_2 (15%) + G-based sulfur cathode at 2C for 2000 cycles, followed by 10 cycles at 0.2C. (d-f) Reproduced from reference[199]. Copyright 2016, American Chemical Society. (g) Schematic of the synthetic process for $S@CNTs/Co_3S_4$ nanoboxes. (h) Schematic diagram of the three-dimensional interlaced carbon nanotubes threaded hollow Co_3S_4 nanoboxes. (i) TEM image of $CNTs/Co_3S_4$ nanoboxes. (j) TEM image of $S@CNTs/Co_3S_4$ nanoboxes. Cycling performances of different electrodes at 0.2C under (k) ambient conditions and (l) 50 °C. g-l) Reproduced from reference[200]. Copyright 2017, American Chemical Society. (m) Schematic illustration of the fabrication process of honeycomb-like spherical $S@Co_9S_8$ nanostructures. (n,o) SEM images of honeycomb-like Co_9S_8 nanostructures. (p) TEM image of the Co_9S_8 nanostructures. (q)

Cycling performance of S@Co_9S_8 cathode at 1C for 600 cycles. (m-q) Reproduced from reference[201]. Copyright 2018, Wiley-VCH.

Co_3S_4 is a polar and metallic crystal phase with a high conductivity of 3.3×10^5 S m^{-1}.[202] In 2017, Jin and co-workers prepared a kind of novel sulfur host based on interlaced carbon nanotubes threaded hollow Co_3S_4 nanoboxes.[200] Carbon nanotubes (CNTs) threaded ZIF-67 nanocubes were first prepared by the *in situ* nucleation and growth of ZIF-67 nanocubes on the interlaced CNTs (**Figure 1.16**g). After the following sulfuration and annealing process, CNTs threaded hollow Co_3S_4 nanoboxes were obtained **(Figure 1.16**i). Finally, sulfur was infiltrated into the CNTs/Co_3S_4 nanoboxes via a melt-diffusion process (**Figure 1.16**j). **Figure 1.16**h illustrated the 3D continuous architecture of S@CNTs/Co_3S_4 nanoboxes. Benefitting from the unique 3D conductive networks, physical and chemical entrapment of Co_3S_4 nanoboxes for sulfur species, the S@CNTs/Co_3S_4 nanoboxes demonstrated high specific capacity and better stability compared to the S@Co_3S_4 nanoboxes and S@CNTs (**Figure 1.16**k). Moreover, even at a high temperature of 50 °C, the S@CNTs/Co_3S_4 cathode also showed high capacity with remarkable cycling stability. Recently, similar CNTs/Co_3S_4 nanoboxes were prepared as sulfur host by Cao and co-workers,[203] and superior rate performance of 850 mA h g^{-1} at 5C was attained. Apart from chemical entrapment by Co_3S_4, catalysis effect was also proposed to contribute to the enhanced electrochemical performance. Additionally, Co_3S_4 nanotubes were also developed as sulfur host to improve the electrochemical performance of Li-S batteries.[204]

Co_9S_8 is another kind of polar metal sulfides with high metallic conductivity of 290 S cm^{-1} at room temperature.[114] Unique Co_9S_8 nano tubules assembled honeycomb-like spheres were

prepared to encapsulate sulfur by Xu and co-workers (**Figure 1.16**m-p).[201] The one-dimensional Co_9S_8 nanotubes can act as a conduit to accelerate the transport of electrons and ions. In addition, the hollow tubule structure possesses large internal void space to accommodate sulfur and buffer volume variation upon cycling. Moreover, the polar and conductive Co_9S_8 can effectively trap polysulfides and promote their conversion. As a result, when used as sulfur host for Li-S batteries, the composite showed high capacity with stable cycling performance (**Figure 1.16**q). Besides this, Jin's group has designed Co_9S_8/C hollow nanopolyhedras using ZIF-67 as template.[205] After loading sulfur into the hollow structure, the S@Co_9S_8/C nanopolyhedras exhibited much better cycling performance compared to the S@C composite, again suggesting Co_9S_8 played a vital role in improving the performance of Li-S batteries.

As a typical kind of layered transition metal disulphides, MoS_2 has received extensive research interests in recent years, especially in hydrogen evolution reactions.[190, 191, 206-208] MoS_2 was also swarmed into Li-S batteries recently. In 2017, MoS_2-wrapped hollow sulfur spheres were designed by Zheng and co-workers (**Figure 1.17**a).[209] To evaluate the volume change of MoS_2-encapsulated hollow sulfur spheres during discharge and charge process, an *in situ* TEM measurement was performed. As shown in **Figure 1.17**b-d, the hollow space inside sulfur spheres (indicated with arrows) was filled after the lithiation process and recovered to its original morphology after the reverse delithiation. This suggested that the flexible MoS_2 layer as well as the hollow space could effectively accommodate the volume expansion and maintain the structure integrity upon cycling. Owing to this unique structural advantage, the MoS_2-encapsulated spheres demonstrated remarkable electrochemical

performance with an initial capacity of 1660 mA h g^{-1} and prolonged cycle life of more than 1000 cycles.

To further improve the conductivity of MoS_2 based hosts, sulfur-deficient MoS_2 (MoS_{2-x})/rGO composite was prepared by annealing MoS_2/GO composite in a reductive atmosphere of 10% H_2/Ar mixture (**Figure 1.17**e,f).[210] It was found that the sulfur deficiencies played a vital role in catalyzing the polysulfide conversion reaction and thus largely accelerated the redox kinetics upon cycling. By virtue of this unique surface property of MoS_{2-x}, the MoS_{2-x}/rGO/S composite exhibited much better cycling performance compared to the MoS_2/rGO/S and rGO/S (**Figure 1.17**g).

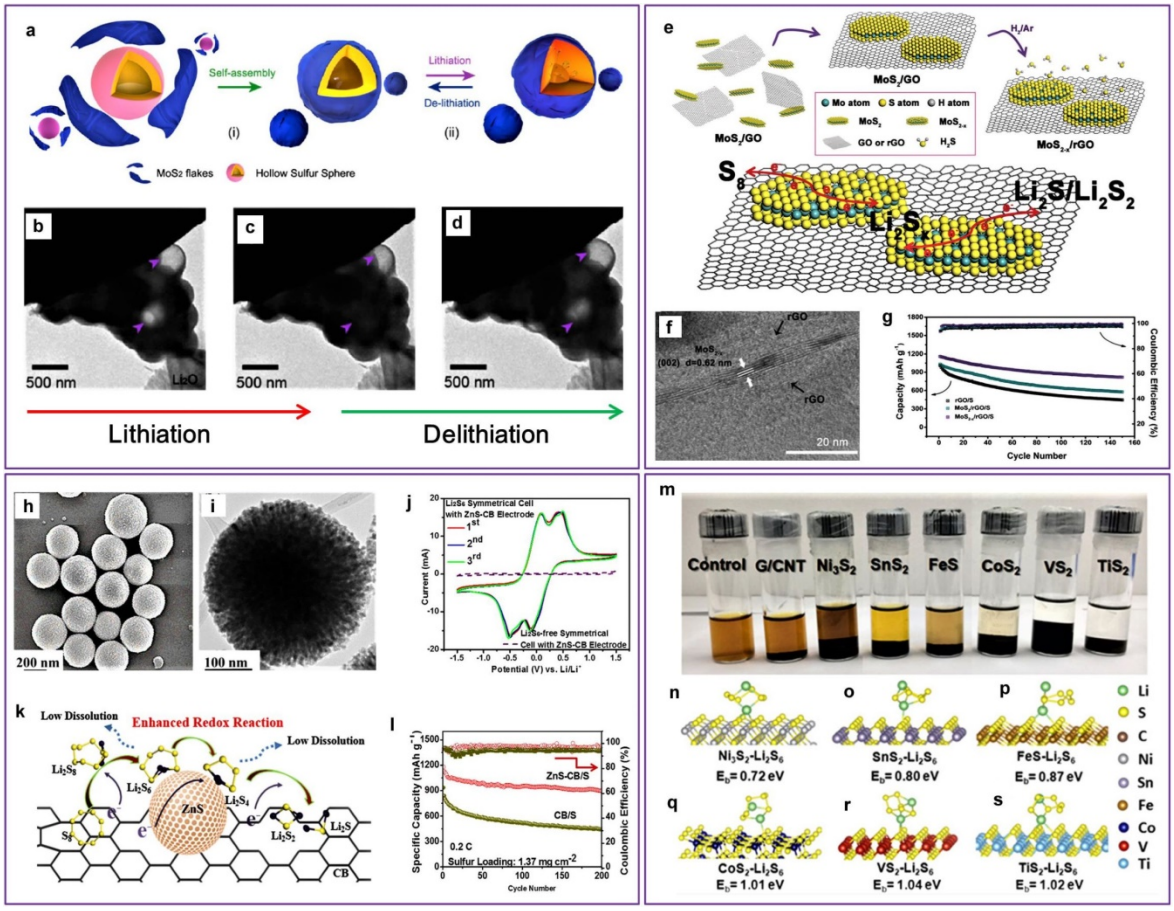

Figure 1.17 (a) Schematic illustration of i) the synthesis process of MoS_2-encapsulated hollow sulfur sphere, and ii) effective lithium polysulfides entrapment and structural integrity

of MoS_2-encapsulated hollow sulfur sphere upon lithiation/delithiation. (b-d) *In-situ* TEM images of MoS_2-encapsulated hollow sulfur spheres upon continuous lithiation and delithiation process. (a-d) Reproduced from reference[209]. Copyright 2017, American Chemical Society. (e) Schematic of the synthesis process of MoS_{2-x}/rGO composite and the conversion of sulfur species on its surface. (f) HR-TEM image of MoS_{2-x}/rGO composite. (g) Comparison of the cycling performances of rGO/S, MoS_2/rGO/S and MoS_{2-x}/rGO/S cathodes at 0.5C. (e-g) Reproduced from reference[210]. Copyright 2017, Royal Society of Chemistry. (h) SEM and (i) TEM images of ZnS nanospheres. (j) CVs of Li_2S_6 and Li_2S_6-free symmetrical cells with ZnS-CB as working electrodes. (k) Illustration of the promoted redox reaction of polysulfide conversion by the catalyzing of ZnS nanospheres during discharge. (l) Comparison of the cycling performances of ZnS-CB/S and CB/S cathodes at 0.2C. (h-l) Reproduced from reference[211]. Copyright 2018, Elsevier. (m) Digital images of Li_2S_6 solution after interaction with carbon and different kinds of metal sulfides. Atomic geometries and binding energies of Li_2S_6 adsorption on (n) Ni_3S_2, (o) SnS_2, (p) FeS, (q) CoS_2, (r) VS_2 and (s) TiS_2, respectively. (m-s) Reproduced from reference[212]. Copyright 2017, National Academy of Sciences.

Recently, our group discovered that the ZnS spheres can also act as an efficient electrocatalyst to promote lithium polysulfide/sulfide redox kinetics for high performance Li-S batteries.[211] The morphology of the ZnS nanospheres is shown in **Figure 1.17**h,i and abundant mesopores are easily observed on the surface of the spheres. The mesoporous structure can provide sufficient interfaces to adsorb the polysulfides. The CV of Li_2S_6 symmetrical cells experimentally confirmed the catalysis effect of ZnS nanospheres for promoting polysulfide conversion (**Figure 1.17**j). **Figure 1.17**k illustrates the entrapping-diffusion-conversion mechanism of polysulfides at the interface of ZnS. Using

ZnS-carbon black/S as cathode, a high discharge capacity of 896 mA h g^{-1} was delivered after 200 cycles at 0.2C.

Cui's group systematically investigated a series of metal sulfides as polar hosts for Li-S batteries (**Figure 1.17**m-s).[212] Based on the theoretical calculations, the binding energies between Li_2S_6 and Ni_3S_2, SnS_2, FeS, CoS_2, VS_2, and TiS_2 are 0.72, 0.80, 0.87, 1.01, 1.04, and 1.02 eV, respectively (**Figure 1.17**n-s), which are in good agreement with the Li_2S_6 adsorption tests (**Figure 1.17**m). This suggests that the stronger interaction can induce a better anchoring effect. The authors also found that the decomposition energy barrier of Li_2S is associated with the binding between isolated Li ions and the sulfur in sulfides and thus the sulfides can decrease the overpotential compared with commonly used carbon materials. When these sulfide materials were evaluated as hosts for Li-S batteries, the electrochemical performances accorded with the binding energies. This systematical and fundamental study provides a general guiding principle for the rational design of advanced sulfur host materials for Li-S batteries with high reversible capacity and long cycle life.

In order to increase the energy density of a practical Li-S battery, it is vital to reduce the inactive part in the cathode. An intriguing strategy is to use novel host materials that are also electrochemically active in the voltage range of Li-S batteries, so that they do not contribute dead weight. To this end, Li's group proposed a kind of intercalation-conversion hybrid cathodes by coupling intercalation-type Mo_6S_8 with conversion-type S_8 to realize a Li-S full cell very recently.[213] The *in situ* XRD measurement confirmed the intercalation process from Mo_6S_8 to $LiMo_6S_8$ and then to $Li_3Mo_6S_8$ and $Li_4Mo_6S_8$ gradually during discharge (**Figure 1.18**a). During charge process, all the phase evolution is reversible. Based on the XRD

analysis, an intercalation-conversion dual mechanism of Mo_6S_8/S_8 cathode during discharge was illustrated in **Figure 1.18**b. Coin cells were assembled to evaluate the electrochemical performance of Mo_6S_8/S_8 cathodes at 6.2 mg cm^{-2} S_8 loading and 6.1 mg cm^{-2} Mo_6S_8 loading. A high initial areal capacity of 7.8 mA h cm^{-2} with a good capacity retention of 83% after 100 cycles was achieved. Such good cycling performance at ultrahigh sulfur loading can be attributed to the strong chemical adsorption capability of $Li_xMo_6S_8$ to lithium polysulfides. To evaluate the full cell energy density of the $Li|Mo_6S_8/S_8$ cell for practical applications, a 1 Ah-level pouch-cell with ~2×Li excess was assembled. A high gravimetric energy density of 366 W h kg^{-1} and a volumetric energy density of 581 W h L^{-1} were simultaneously achieved (**Figure 1.18**d), demonstrating its great potential for practical applications. This study overcomes main limitations of pure anion-redox materials and will open new avenues for developing advanced host materials that are electrochemically active in the voltage range of Li-S batteries.

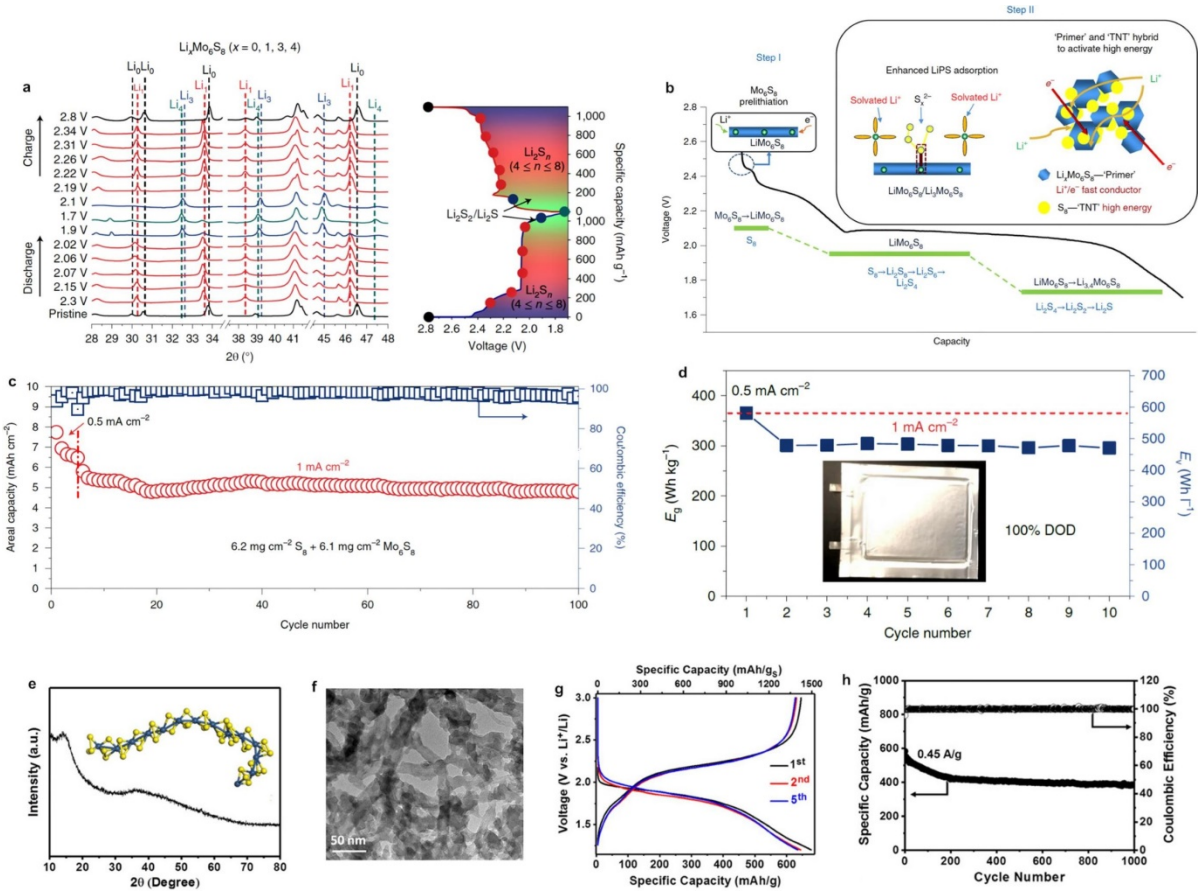

Figure 1.18 (a) In situ XRD measurements of a Li|Mo_6S_8/S_8 cell. (b) Illustration of the discharge process of intercalation-conversion hybrid cathodes of Mo_6S_8/S_8. (c) Cycling performance of the hybrid cathodes with 6.2 mg cm^{-2} S_8 loading and 6.1 mg cm^{-2} Mo_6S_8 loading. (d) The pouch-cell configuration constructed by the Mo_6S_8/S_8 cathode with an ultralow electrolyte/active material ratio of ~1.2 μL mg^{-1} and ~2×Li excess (100 μm for one side). (a-d) Reproduced from reference[213]. Copyright 2019, Nature Publishing Group. (e) XRD pattern of the MoS_3. The inset shows the schematic structure of the 1D chain-like MoS_3. (f) TEM image of MoS_3/CNT composite. (g) Charge-discharge curves of MoS_3 cathodes in carbonate based electrolyte. (h) Cycling performance of the MoS_3 cathode. (e-f) Reproduced from reference[214]. Copyright 2017, National Academy of Sciences.

Lu and co-workers reported the use of 1D chain-like MoS_3 as a kind of sulfur-equivalent cathode active material for Li-S batteries (**Figure 1.18**e,f).[214] Operando X-ray absorption spectroscopy (XAS) analysis suggested that no polysulfides were generated during the

charge-discharge process. **Figure 1.18**g exhibits the charge-discharge voltage curves of the MoS_3 cathode in the carbonate based electrolyte, showing one discharge plateau at about 1.8 V. The specific capacities delivered during the first cycle were 667 mA h g^{-1} when normalized to the total mass of MoS_3, and 1482 mA h g^{-1} when normalized to the sulfur weight. Because of no polysulfide intermediates generation upon cycling, the MoS_3 based cathode demonstrated an impressive cycling performance for over 1000 cycles (**Figure 1.18**h).

The use of metal sulfides as host materials for Li-S batteries is of wide interests. Many other types of metal sulfides, such as CoS_3,[215] CoS,[216-218] NiS,[219, 220] NiS_2,[221, 222] SnS_2,[223-225] CuS,[226] FeS_2,[227, 228] WS_2,[229] NbS_2,[230] CdS,[231] VS_2,[232-235] Ni_3S_2,[236] $NiCo_2S_4$,[237, 238] and VS_4[239, 240] were also explored as sulfur hosts for Li-S batteries. Although the conductivity of metal sulfides is normally higher than that of metal oxides, conductive carbon materials were still often introduced, in order to further decrease the internal resistance and increase the sulfur utilization during cycling.

1.2.7 Metal nitrides as host

Compared to metal oxides and sulfides, metal nitrides are another kind of polar materials with higher conductivity. Although metal nitrides show more advantages compared to metal sulfides for improving the electrochemical performance of Li-S batteries, the development of metal nitrides for Li-S batteries is in the early stage because of its much complicated synthesis process. In this section, typical metal nitrides, such as TiN, Co_4N and VN, will be discussed as efficient sulfur host for Li-S batteries.

Titanium nitride (TiN) is the most common metal nitride for using in Li-S batteries and has a high electronic conductivity of 46 S cm^{-1}.[60] Goodenough and co-workers first reported the use of mesoporous TiN as sulfur host for Li-S batteries.[241] The mesoporous TiN was prepared by a solid-solid phase separation method using zinc titanate ($ZnTiO_3$) as the precursor. **Figure 1.19**a shows the SEM image of the as-synthesized mesoporous TiN nanostructures. The TiN shows a BET specific surface area of 69.689 m^2 g^{-1} and pore volume of 0.32 cm^3 g^{-1} with a mesoporous pore size centering at about 3 nm. Such high pore volume and appropriate pore size were beneficial to disperse active sulfur mass. After loading sulfur into the mesoporous structure, the TiN/S composite showed better electrochemical performance compared to the mesoporous TiO_2/S and C/S cathodes. The improved electrochemical performance can be attributed to the high conductivity of TiN compared to TiO_2.

Lee and co-workers developed a hierarchically macro- and mesoporous TiN as a multifunctional sulfur host.[242] The coexistence of macro- and mesopore enables the stable accommodation of a large amount of sulfur, the effective control of polysulfide shuttle, and fast transport of electrons and lithium ions. Additionally, the TiN surface exhibited high affinity to polysulfides and catalytic activity for polysulfide conversion. As a result, the macro- and mesoporous TiN based sulfur cathode demonstrated a reversible capacity of 557 mA h g^{-1} even after 1000 cycles at 5C with an ultralow capacity decay rate of only 0.016% per cycle, which is much better compared to that of the mesoporous TiN based sulfur cathode.

TiN was also combined with carbon materials to improve the performance of Li-S batteries. Ding and co-workers designed C@TiN dual shell nanospheres as multifunctional host for

Li-S batteries.[243] Sulfonated hollow PS spheres were first prepared as the template, followed by coating a layer of TiO_2 *via* the sol-gel method. After annealing in NH_3 atmosphere at 800 °C for 2h, the mesoporous C@TiN dual-shell nanospheres were obtained. Finally, C@TiN-S composite were obtained by infiltrating sulfur into the void space of the hollow spheres. The porous TiN layer can act as a conductive sulfiphilic and lithiophilic host to accelerate the redox reaction of polysulfides, while the unique dual shell structure design can provide both physical and chemical entrapment to restrain the diffusion of polysulfides. Benefiting from these multiple advantages, the C@TiN-S cathode demonstrated impressive electrochemical performance compared to the C@TiO_2-S composite.

Recently, our group reported the surface oxidized quantum-dot-size TiN embedded in mesoporous carbon (TiO-O-OMC) as efficient sulfur host for Li-S batteries (**Figure 1.19**b-d).[244] The surface oxidized TiN can effectively entrap the polysulfides and boost their redox kinetics, while the carbon framework provides efficient conductive networks and physical confinement for polysulfides. As a result, the TiO-O-OMC/S cathode exhibited a high discharge capacity of 1264 mA h g^{-1} at 0.2C with a low capacity decay rate of 0.06% per cycle.

To achieve higher sulfur loading for Li-S batteries, Mai's group has designed a 3D nitrogen-doped graphene/TiN nanowires composite as a self-standing host.[245] 3D graphene/$H_2Ti_3O_7$ composite were first prepared by the hydrothermal self-assembly process between GO and $H_2Ti_3O_7$ nanowires. After heat treatment at 800 °C in NH_3 atmosphere, 3D nitrogen-doped graphene/TiN composite were obtained. The porous graphene networks provide efficient pathways for both lithium ions and electrons, while the TiN nanowires have

a strong chemical anchoring effect for polysulfides. As a result, with an ultrahigh sulfur loading of 9.6 mg cm^{-2}, the nitrogen-doped graphene/TiN based cathode demonstrated a high areal capacity of 12 mA h cm^{-2}, suggesting great potential for practical applications.

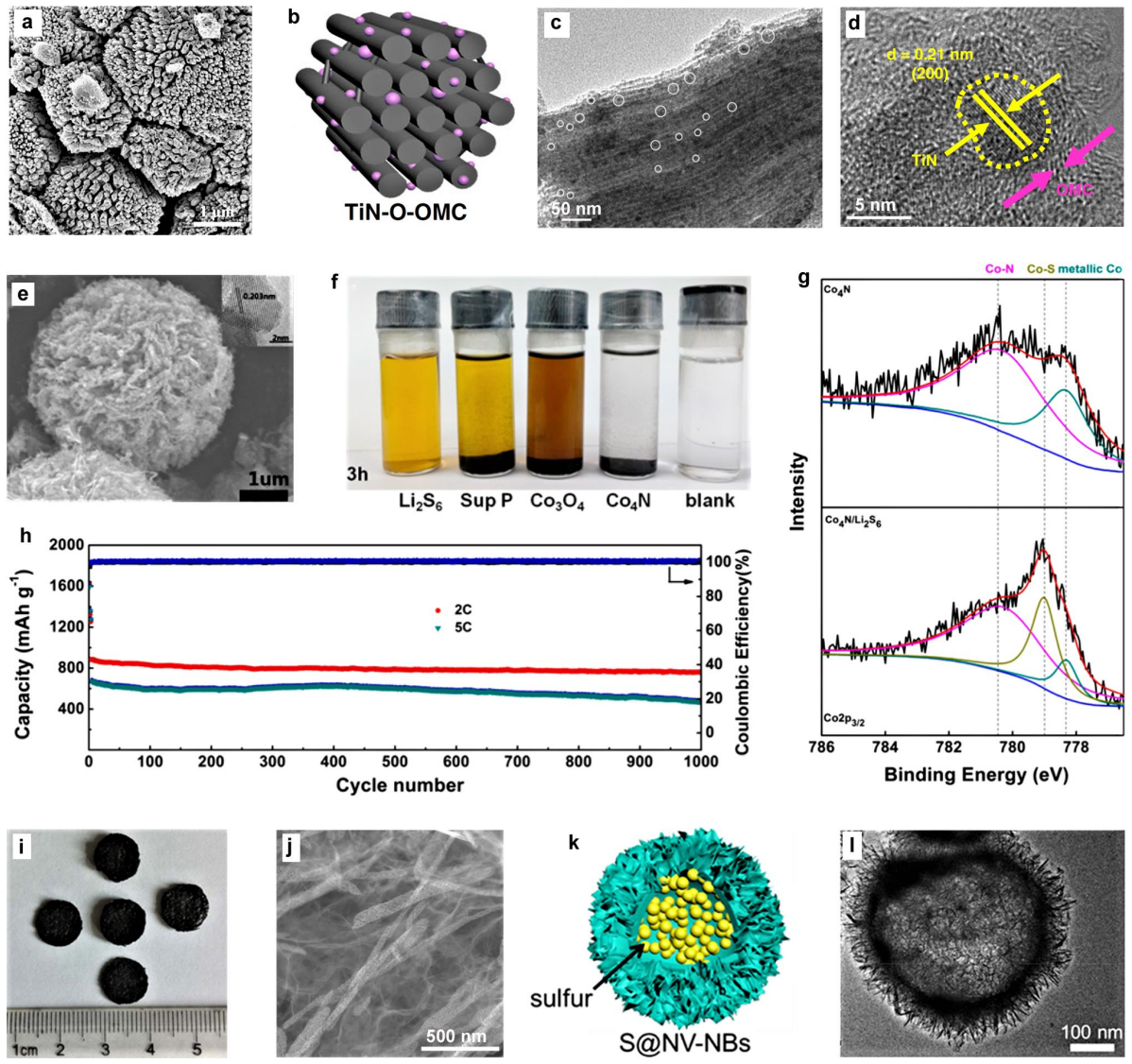

Figure 1.19 (a) SEM image of mesoporous TiN. Reproduced from reference[241]. Copyright 2016, Wiley-VCH. (b) Schematic of the mesoporous TiN-O-OMC. (c) TEM and (d) HR-TEM images of mesoporous TiN-O-OMC. (b-d) Reproduced from reference[244]. Copyright 2019, Nature Publishing Group. (e) SEM image of Co_4N nanosheets assembled mesoporous sphere. (f) Optical images of Li_2S_6 solutions after adding equal amounts of super P, Co_3O_4 and Co_4N, respectively. (g) Co $2p_{3/2}$ XPS spectra of CoN_4 phase and Co_4N/Li_2S_6, respectively. (h) Cycling performances and Coulombic efficiencies of Co_4N/S cathodes at 2C

and 5C, respectively. (e-h) Reproduced from reference[246]. Copyright 2017, American Chemical Society. (i) Optical image of VN/G composite foams. (j) TEM image of VN/G composite. (i,j) Reproduced from reference[247]. Copyright 2017, Nature Publishing Group. (k) Schematic of sulfur loaded-VN nanobubble. (l) TEM image of a single VN nanobubble. (k,l) Reproduced from reference[248]. Copyright 2017, American Chemical Society.

Co_4N was also used as polar and conductive host for Li-S batteries. Dong and co-workers reported a kind of Co_4N nanosheets assembled mesoporous spheres as the matrix for ultrahigh sulfur content Li-S batteries (**Figure 1.19**e).[246] Mesoporous Co_4N spheres were prepared by thermal treatment of mesoporous Co_3O_4 spheres at 400 °C for 4h in an NH_3 atmosphere. To evaluate the affinity of Co_4N for polysulfides, equal amounts of Sup P, Co_3O_4 and Co_4N were added into different vials with the same Li_2S_6 solution. After waiting for 3h, the vial with Co_4N has completely turned colorless, and the yellow color of Li_2S_6 solution with Co_3O_4 became lighter but was not completely obliterated, whereas that after adding Sup P still remained yellow (**Figure 1.19**f). This indicates that Co_4N has much stronger chemical adsorption capability for polysulfides compared to Co_3O_4. In order to elucidate the chemical interactions between Co_4N and Li_2S_6, XPS measurements were performed before and after Co_4N interacted with Li_2S_6 (**Figure 1.19**g). The spectrum shows that Co $2p_{3/2}$ of Co_4N can be divided into two characteristic peaks including Co-N bond and metallic Co, confirming the existence of Co with 0 valency. After adsorbing Li_2S_6, an additional peak at 778.9 eV appeared, indicative of a Co-S bond, and the intensity of the peak at 778.5 eV has declined a lot. This suggestes that cobalt with low valency in Co_4N has a strong affinity for sulfur in lithium polysulfides. With the mesoporous structure for sulfur

accommodation and unique surface properties of Co_4N to chemically anchor the polysulfides, the Co_4N/S composite showed very stable cycling performance at 2C and 5C for 1000 cycles (**Figure 1.19**h). Moreover, even the sulfur content in Co_4N/S composite increased to 95%, it still showed superior cycling performance with a high reversible capacity of above 540 mA h g^{-1} after 800 cycles at 2C. Recently, Co_4N nanoparticles/N-doped carbon composite were also developed to improve the polysulfide adsorption and redox kinetics in Li-S batteries.[249]

Vanadium nitride (VN) with a metallic conductivity of 1.17×10^6 S m^{-1} has also been used as a polar host for Li-S batteries.[247] The Li group reported a freestanding and porous VN/graphene foam as current collector for Li-S batteries (**Figure 1.19**i).[247] VO_x/G composite aerogel was prepared by the hydrothermal reaction between GO and NH_4VO_3, followed by the freeze-drying process. After heating the VO_x/G composite aerogel at 550 °C for 3 h in an NH_3 atmosphere, VN/G composite aerogel was obtained. Finally, freestanding VN/G composite electrodes (**Figure 1.19**i) were obtained by cutting and compressing the VN/G composite aerogel. The SEM image in **Figure 1.19**j showed that the VN nanoribbons penetrate through the continuous graphene networks. The 3D interconnected graphene frameworks can facilitate the transport of lithium ions and electrons, while the polar and conductive VN nanoribbons can not only trap the polysulfides but also promote the redox reaction kinetics. After dropping an appropriate amount of Li_2S_6 solution into the freestanding VN/G composite electrodes, a high initial capacity of 1471 mA h g^{-1} was delivered and it retained a high capacity of 1252 mA h g^{-1} after 100 cycles at 0.2C.

In order to enable more efficient physical confinement of sulfur species by VN, Jin's group has designed vanadium nitride nanobubbles to encapsulate sulfur (**Figure 1.19**k).[248] To

obtain this novel structure, a two-step organometallic compound conversion and thermal nitridation process was developed. Uniform carbon nanospheres were first prepared as the template, followed by coating with a layer of vanadium-based precursor. Then carbon nanospheres were removed by heating under air, and vanadium-based precursor was simultaneously converted into V_2O_5 nanobubbles. Finally, the VN nanobubbles were obtained by annealing V_2O_5 nanobubbles at 600 °C in NH_3/Ar atmosphere. The TEM image in **Figure 1.19**l shows that the as-prepared VN nanobubbles have a highly porous-shell structure with large internal void space. This unique nanoarchitecture can not only provide efficient physical confinement for sulfur species, but also provide strong chemical affinity for polysulfides. Moreover, the high conductivity of VN ensures the effective utilization and fast redox kinetics of polysulfides. Benefiting from the above merits, the sulfur-filled VN nanobubbles demonstrated impressive high areal capacity of 5.81 mA h cm^{-2} with good stability at a high areal sulfur loading of 5.4 mg cm^{-2}.

1.2.8 Metal carbides as host

Metal carbides are another kind of polar and conductive materials that have demonstrated potential applications for Li-S batteries. However, due to the rigorous conditions required to produce metal carbides, the use of metal carbides as sulfur substrate is just in its early stage. In this section, typical metal carbides, such as TiC, W_2C, Mo_2C, B_4C, NbC and MXene, will be discussed as efficient sulfur substrates to improve the performance of Li-S batteries.

In 2016, Zhang's group reported that the TiC substrate can effectively enhance the electrochemical kinetics of Li-S batteries.[250] EIS spectra of the Li_2S_6 symmetric cells

indicated that the charge transfer resistance at the interface between carbon-fiber paper supported TiC (CP-TiC) and lithium polysulfides was much lower compared to that of CP-TiO_2 and CP (**Figure 1.20**a). Such enhanced charge transfer kinetics can be attributed to the strong interfacial affinity of TiC for polysulfides. Besides the enhanced chemical interaction, the TiC also promoted the dynamic polysulfide conversion, as evidenced by the increased redox current of CP-TiC in Li_2S_6 symmetric cells (**Figure 1.20**b). To give more insight on the transformation from liquid lithium polysulfide to solid Li_2S, potentiostatic discharge curves of a Li_2S_8/tetraglyme solution at 2.05 V on different substrates were show in **Figure 1.20**c. The capacities of Li_2S precipitated on CP, CP-TiO_2 and CP-TiC were 54, 45 and 97 mA h g^{-1}, respectively. This suggests that TiC can facilitate the nucleation and growth of Li_2S, which is a vital process in Li-S batteries. **Figure 1.20**d-f show morphologies of the initial nucleation of Li_2S on different substrates. The CP shows very clean surface with invisible Li_2S nuclei (**Figure 1.20**d). This can be ascribed to the poor affinity between polar lithium polysulfides and nonpolar carbon, which needs to overcome a substantial energy barrier for Li_2S nucleation on CP. Due to the smaller surface energy difference between polar TiO_2 and Li_2S, TiO_2 increased the initial nucleation of Li_2S (**Figure 1.20**e). However, the semiconducting TiO_2 inevitably restrained the lateral growth of Li_2S once they came into contact, resulting in a low overall precipitated capacity. Only TiC, both polar and conductive, promoted uniform distribution of nucleation sites and full surface coverage of Li_2S films (**Figure 1.20**f). Benefiting from the promoted electrochemical kinetics by TiC, the TiC@G/S electrode demonstrated better electrochemical performance compared to TiO_2@G/S (**Figure 1.20**g).

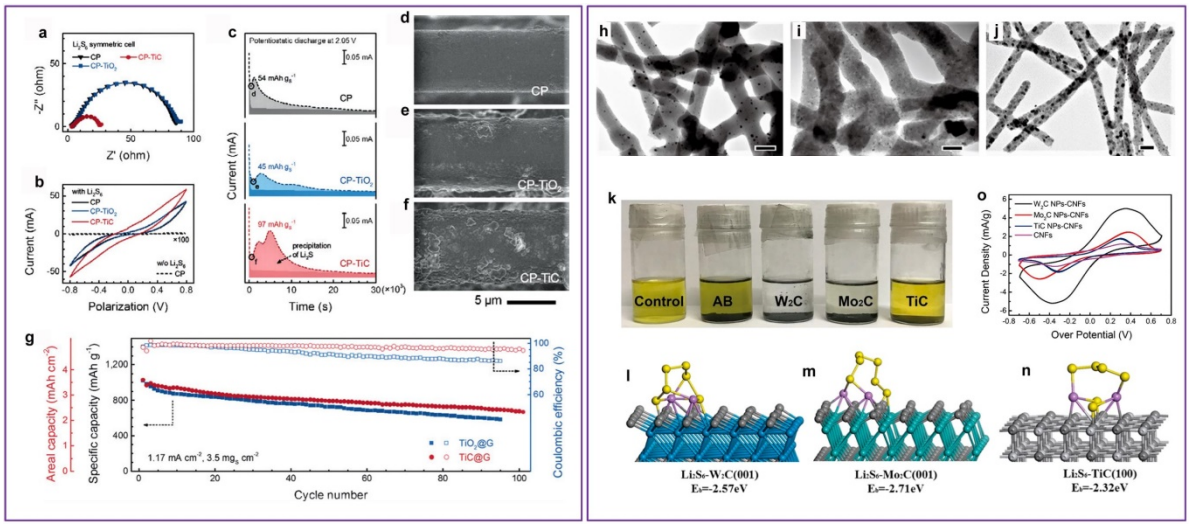

Figure 1.20 (a) EIS and (b) CV of Li_2S_6 symmetric cells with different working electrodes. (c) Potentiostatic discharge curves of a Li_2S_8/tetraglyme solution at 2.05 V on different substrates. The lighter and darker colors represent the precipitation of Li_2S and reduction of Li_2S_8/Li_2S_6, respectively. (d-f) SEM images of the precipitated Li_2S on different substrates as indicated in c. (g) Cycling performances of TiC@G/S and TiO_2@G/S electrodes at 0.2C. (a-g) Reproduced from reference[250]. Copyright 2016, Wiley-VCH. TEM images of (h) W_2C NPs-CNFs, (i) Mo_2C NPs-CNFs and (j) TiC NPs-CNFs, respectively (scale bars=200 nm). (k) Photographs of the Li_2S_6 adsorption by different powders in DOL/DME (1:1, v/v) solution. Optimized geometries of Li_2S_6 adsorbed on (001) planes of (l) W_2C, (m) Mo_2C and (n) TiC, respectively. (o) CV curves of Li_2S_6 symmetric cells using W_2C NPs-CNFs, Mo_2C NPs-CNFs, TiC NPs-CNFs and CNFs as electrodes. (h-o) Reproduced from reference[251]. Copyright 2018, American Chemical Society.

Yu's group has developed a strategy to load different kinds of metal carbide nanoparticles on carbon nanofibers (CNFs) *via* facile metal oxide coating and a following carbonization process.[251] **Figure 1.20**h-j show the TEM images of the as-synthesized W_2C NPs-CNFs, Mo_2C NPs-CNFs and TiC NPs-CNFs, respectively, indicating ultrafine metal carbide nanoparticles have distributed uniformly on the CNFs. To probe the capability of these metal carbides for absorbing lithium polysulfides, W_2C, Mo_2C, TiC and acetylene black with the

same total surface area were added into equal amounts of Li_2S_6 solution. As shown in **Figure 1.20**k, the color of Li_2S_6 solution after the addition of W_2C and Mo_2C is much lighter than that of TiC, indicating the strong chemical adsorption capability of W_2C and Mo_2C to polysulfides. DFT calculations were further performed to simulate the chemical interactions between Li_2S_6 and these metal carbides (**Figure 1.20**l-n). The calculated binding energies of Li_2S_6 on W_2C and Mo_2C are higher than that for TiC, which is in accordance with the adsorption measurements. The catalytic performances of these metal carbides for polysulfide conversion were studied *via* the Li_2S_6 symmetric cells (**Figure 1.20**o) and W_2C NPs-CNFs showed the best catalytic performance towards polysulfide conversion. When evaluated as sulfur host for Li-S batteries, the W_2C NPs-CNFs/S electrode also demonstrated the best electrochemical performance compared to that of Mo_2C NPs-CNFs/S and TiC NPs-CNFs/S. This suggests that the moderate chemical adsorption ability for sulfur species is vital for the diffusion and conversion of polysulfides. It was believed that the competition between adsorption and diffusion of sulfur species on the surface of the electrode plays a vital role on the electrochemical performance of Li-S batteries.[148] In particular, if the binding energy is too low, the electrode can only capture a little amount of sulfur species, leading to seriously shuttle effect of polysulfides and capacity fading. When the binding energy is too high, the diffusion of sulfur species on the electrode is difficult, thus the electrochemical reaction of sulfur species and the deposition of solid Li_2S or S would be limited. This study provides rational guidance for the future design of polar materials with moderate chemical binding with polysulfides.

Boron carbide (B_4C), by virtue of its low density (≈2.5 g cm^{-3}),[252] good conductivity (1.25-3.33 S cm^{-1}),[253] and superior catalytic effect,[253-255] was also developed as a bifunctional sulfur substrate for Li-S batteries by Manthiram's group.[256] B_4C nanowires were prepared *via* a catalyst-assisted strategy in which excess CNF acted both as a template and carbon source to react with boron powder, and nickel functioned as the catalyst to direct the tip-growth of B_4C nanowires (**Figure 1.21**a). **Figure 1.21**b,c showed the SEM images of vertical-aligned B_4C nanowires grown on the self-standing CNF substrate. The B_4C nanowires can not only chemically anchor the lithium polysulfides, but also catalysis their redox reaction. When B_4C-CNF was used as a current collector for Li-S batteries, a high capacity retention of 815 mA h g^{-1} was achieved after 500 cycles at 1C, which was much better than that of CNF (**Figure 1.21**d). Moreover, even at ultrahigh areal sulfur loadings of 6.1 and 10.3 mg cm^{-2}, the B_4C-CNF still delivered high discharge capacities of 1017 and 860 mA h g^{-1} at 0.2C with superior cycling stability (**Figure 1.21**e). Encouraged by the impressive performance of coin-cells, pouch cells were further assembled to evaluate the potential of B_4C-CNF for practical batteries. EIS spectra of the pouch cells indicated that the B_4C nanowires can effectively accelerate the charge transfer at the interface between the electrode and electrolyte **(Figure 1.21**f). When 40 mg sulfur mass was loaded in a 12 cm^{-2} current collector, the pouch cell employing B_4C-CNF still exhibited better cycling performance compared to that of CNF (**Figure 1.21**g). Moreover, even 200 mg sulfur mass was loaded to a larger substrate area of 40 cm^{-2}, the pouch cell with B_4C-CNF also displayed high discharge capacity of 625 mA h g^{-1} after 50 cycles (**Figure 1.21**h), demonstrating promising application for practical Li-S batteries.

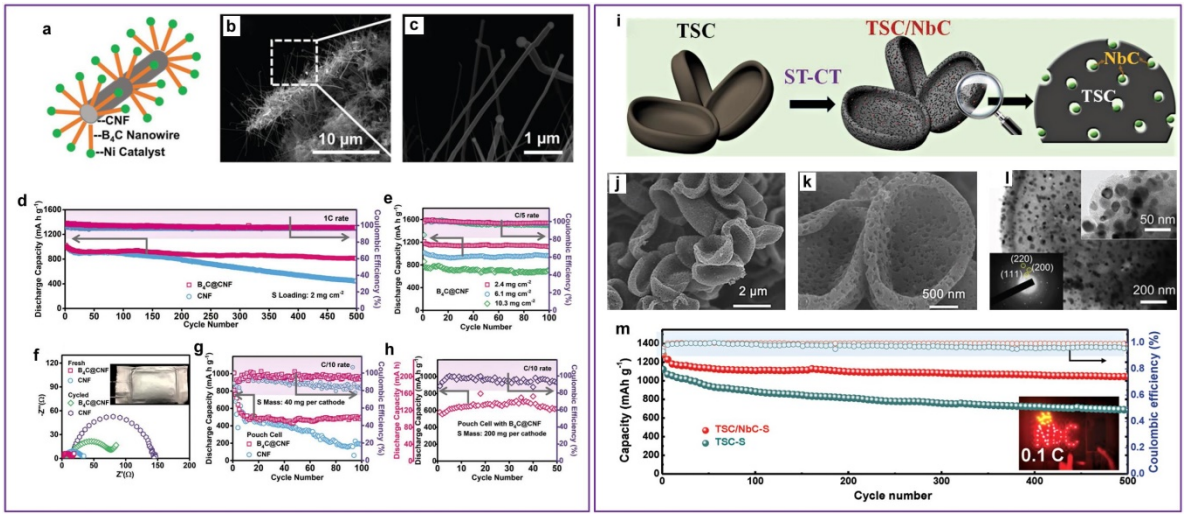

Figure 1.21 (a) Schematic structure of B_4C@CNF. (b,c) SEM images of B_4C@CNF. Electrochemical performances of coin-cells: (d) Cycling performances of B_4C@CNF/S and CNF/S cathodes at 1C over 500 cycles, (e) Cycling performances of B_4C@CNF/S cathodes at 0.2C with higher sulfur loadings. Electrochemical performances of pouch-cells: (f) EIS spectra of B_4C@CNF/S and CNF/S cathodes before and after cycling, (g) Cycling performances of B_4C@CNF/S and CNF/S electrodes with sulfur mass of 40 mg per cathode at 0.1C, (h) Discharge capacities of B_4C@CNF/S with sulfur mass of 200 mg per cathode. (a-h) Reproduced from reference[256]. Copyright 2018, Wiley-VCH. (i) Schematic of the synthesis process for TSC/NbC composite. (j,k) SEM and (l) TEM images of TSC/NbC composite. The insets in l show the SAED pattern and enlarged TEM image. (m) Cycling performances of TSC/NbC-S and TSC-S at 0.1C for 500 cycles. The inset demonstrates the LEDs powered by the battery. (i-m) Reproduced from reference[257]. Copyright 2019, Wiley-VCH.

Recently, Xia's group reported the implanting of highly conductive niobium carbide (NbC) nanoparticles into trichoderma spore carbon (TSC) as an efficient sulfur host for Li-S batteries (**Figure 1.21**i).[257] The TSC/NbC hybrids show a highly porous structure with pore size of 30-50 nm (**Figure 1.21**j,k). It has a high specific surface area of 555 m^2 g^{-1}. TEM images indicate that the NbC nanoparticles with diameters of 25-30 nm have distributed

uniformly in the TSC substrate (**Figure 1.21**l). The porous TSC scaffold can provide sufficient space for sulfur accommodation and increase the utilization of active materials, while the polar and conductive NbC nanoparticles can not only enhance the overall conductivity of the electrode but also perform strong chemical interaction effect with polysulfides. As a result, the TSC/NbC-S composite showed long-cycling performance of 937.9 mA h g^{-1} after 500 cycles, which was much better than that of TSC-S cathode (**Figure 1.21**m).

As an emerging kind of 2D nanomaterials, MXene has attracted great research interests in energy storage and conversion since its first discovery by Gogotsi and co-workers in 2011.[258-262] MXene is a family of early-transition metal carbides or carbonitrides. Nazar's group pioneered the use of MXene phase Ti_2C as sulfur host (**Figure 1.22**a).[263] Owing to the carbon-deficient characteristic of Ti_2C, the under-coordinated titanium atoms can form strong Lewis acid-base bonding with the sulfur atoms in sulfur species (**Figure 1.22**b). XPS measurements confirmed the existence of Ti-S bonds between Ti_2C and sulfur species (**Figure 1.22**c,d). By virtue of the high conductivity and strong chemical trapping ability of Ti_2C for polysulfides, the Ti_2C/S composite exhibited a high discharge capacity of about 1200 mA h g^{-1} at 0.2C and a capacity retention of 80% was achieved after 400 cycles at 0.5C. In order to prevent the stacking of the MXene nanosheets, the Nazar group further integrated the carbon nanotubes into the layer of MXene nanosheets to form the interwoven MXene/CNTs composite host to improve the performance of Li-S batteries.[264]

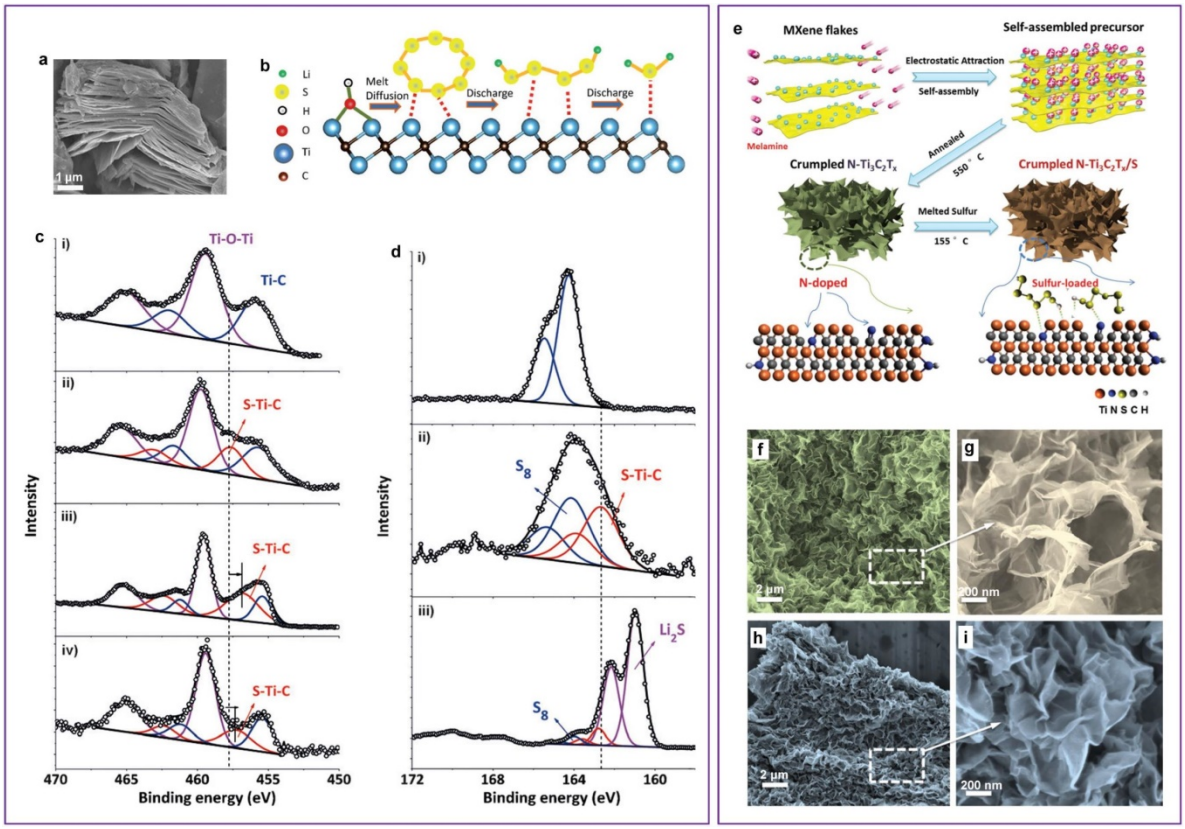

Figure 1.22 (a) SEM image of MXene phase Ti_2C. (b) Illustration of the interactions between MXene and sulfur species. (c) Ti 2p XPS spectra of i) Ti_2C and ii) S/Ti_2C, iii) Li_2S_4-Ti_2C and iv) S/Ti_2C electrode after discharged to 1.8 V at C/20, respectively. (d) S 2p XPS spectra of i) S, ii) S/Ti_2C, and iii) S/Ti_2C electrode after discharged to 1.8 V at C/20, respectively. (a-d) Reproduced from reference[263]. Copyright 2015, Wiley-VCH. (e) Schematic of the synthesis process for N-$Ti_3C_2T_x$/S composite. SEM images of crumpled porous N-$Ti_3C_2T_x$ nanosheets (f,g) before and (h,i) after sulfur loading. (e-i) Reproduced from reference[265]. Copyright 2018, Wiley-VCH.

Despite MXene nanosheets can generate strong chemical interaction with polysulfides and improve the overall conductivity of the electrode, the intrinsic 2D structure can not provide sufficient space to bind all of the sulfur species at the interfaces, especially when the sulfur content is higher than a certain level. To this end, our group developed a 3D hierarchical nitrogen-doped $Ti_3C_2T_x$ nanosheets as sulfur host.[265] MXene flakes were first mixed with

melamine via the electrostatic interaction process to form self-assembled MXene/melamine composite, followed by annealing at 550 °C to produce the nitrogen-doped $Ti_3C_2T_x$ (N-$Ti_3C_2T_x$) nanosheets with 3D hierarchical porous structure (**Figure 1.22**e). Finally, crumpled N-$Ti_3C_2T_x$/S was obtained by the melt-diffusion strategy. **Figure 1.22**f,g showed the SEM images of N-$Ti_3C_2T_x$, indicating that ultrathin MXene nanosheets were assembled into a highly porous structure, which would provide additional physical confinement for sulfur species. After loading sulfur, the N-$Ti_3C_2T_x$/S still maintained the highly porous architecture (**Figure 1.22**h,i). When evaluated as cathodes for Li-S batteries, a high reversible capacity of 1144 mA h g^{-1} was delivered at 0.2C and a retained capacity of 610 mA h g^{-1} after 1000 cycles was achieved at 2C. Inspired by this work, a flower-like porous $Ti_3C_2T_x$ matrix has been developed recently for high areal capacity Li-S batteries.[266]

1.2.9 Metal phosphides as host

Transition metal phosphides are a kind of polar materials that have higher conductivity compared to their oxides and sulfides. Moreover, compared to conductive metal nitrides and carbides, the synthesis of metal phosphides is facile and gentle. Great progress has been made on metal phosphides for electrocatalytic water splitting.[267-270] With the same demand for metal phosphides with high conductivity and superior catalytic property, the metal phosphides have swarmed into Li-S batteries recently. In this section, typical metal phosphides will be discussed as sulfur host materials to improve the performance of Li-S batteries.

Wang's group first reported the use of metal phosphides as efficient host materials for high performance Li-S batteries.[271] By integrating MoP nanoparticles-decorated carbon nanotubes with S deposited on graphene oxide, a substantially improved cycling performance with capacity decay rates as low as 0.017% per cycle over 1000 cycles was realized.[271] The authors also found that MoP can not only effectively adsorb the lithium polysulfides but also promote their redox reaction. As the surface of metal phosphides was readily to be oxidized under ambient conditions, the actual binding mechanism between MoP and lithium polysulfides was not completely clear. To elucidate the chemical interactions between metal phosphides and lithium polysulfides, the Wang group further conducted XPS measurements for both the CoP and CoP-R nanoparticles after they were soaked in a lithium polysulfide solution.[272] Here the CoP-R represents the CoP that has been reduced at 500 °C in an Ar/H_2 atmosphere to eliminate the oxidation layer on metal phosphides. As shown in **Figure 1.23**a,c, both the Co $2p_{3/2}$ and P 2p spectra of natural CoP nanoparticles show obvious oxidized Co and P species. After CoP interacted with lithium polysulfides, the intensity of the Co-O component greatly reduced, while the Co-P/S component increased markedly (**Figure 1.23**a). These spectra changes were attributed to the formation of Co-S bonding between Co atoms in the surface oxidation layer of CoP with S atoms in lithium polysulfides. This was consistent with the observed growth of the component at 161.5 eV in the S 2p spectrum, which was ascribed to the terminal S-Co bonding (**Figure 1.23**e). The P 2p spectrum showed a minor decrease in the P-O component and a minor increase in the P-Co component, indicative of a slight reduction of the oxidized P species, possibly due to its reaction with lithium polysulfides. In contrast, the Co and P species in CoP-R exhibited no observable spectra

changes after interacted with lithium polysulfides, suggesting the CoP-R surface was unable to chemically bind with lithium polysuldfides. This was also experimentally verified by the Li_2S_6 adsorption measurements. Based on the XPS analysis, a convincing binding scheme between CoP and lithium polysulfides was proposed as shown in **Figure 1.23**f. The natural oxidation can generate a surface oxidation layer dominated by Co-O-P species. The highly electronegative O created high-valence Co sites which can react with lithium polysulfide species to form Co-S bonding and leave Li-O-P species on the surface (**Figure 1.23**f). By virtue of the surface oxidation layer capable of anchoring polysulfides and an inner core for conducting electrons, the CoP-CNT/S cathode demonstrated improved electrochemical performance compared to CoP-R-CNT/S and CNT/S cathode.

Tao's group has studied a series of metal phosphides (Ni_2P, Co_2P and Fe_2P) as effective additives to enhance the performance of Li-S batteries.[273] By using DFT calculations, it was found that metal phosphides can not only entrap the polysulfides but also catalyze the decomposition of Li_2S to accelerate the kinetics in Li-S batteries. As a result, the cathodes with the addition of Ni_2P, Co_2P or Fe_2P all delivered higher reversible capacity and much more stable cycling performance compared to the cathodes without metal phosphides. In particular, the Ni_2P based cathode delivered a high reversible capacity of about 1100 mA h g^{-1} after 300 cycles at 0.2C, corresponding to an average capacity decay rate of only 0.01% per cycle.

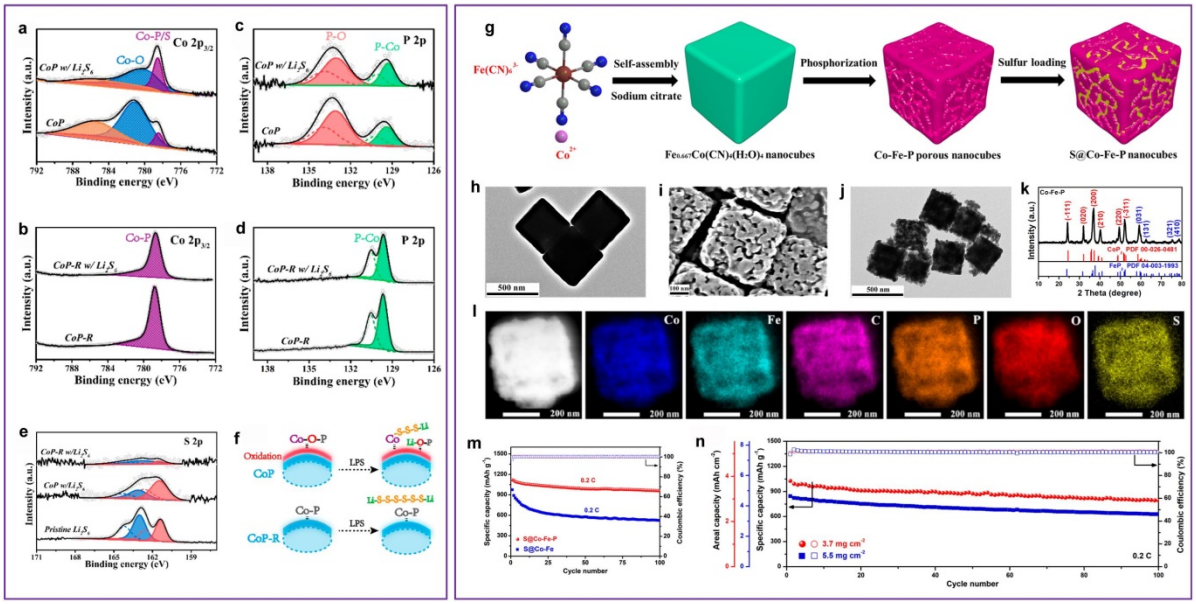

Figure 1.23 (a,b) Co $2p_{3/2}$, (c,d) P 2p, and (e) S 2p XPS spectra of (a,c) CoP and (b,d) CoP-R nanoparticles before and after interacting with Li_2S_6. (f) Proposed binding mechanism of lithium polysulfides on CoP and CoP-R surfaces. (a-f) Reproduced from reference[272]. Copyright 2018, American Chemical Society. (g) Schematic illustration of the synthesis process for S@Co-Fe-P nanocubes. (h) TEM image of $Fe_{0.667}Co(CN)_4(H_2O)_4$ nanocubes. (i) SEM and (j) TEM image of porous Co-Fe-P nanocubes. (k) XRD pattern of Co-Fe-P nanocubes. (m) Cycling performances of S@Co-Fe-P and S@Co-Fe electrodes at 0.2C. (n) Cycling performances of S@Co-Fe-P cathodes at 0.2C with higher areal sulfur loadings. g-n) Reproduced from reference[274]. Copyright 2019, American Chemical Society.

In order to increase the sulfur utilization during the electrochemical reaction in Li-S batteries, our group recently developed Co-Fe mixed metal phosphide (Co-Fe-P) nanocubes with hierarchically interconnected-pore architecture to encapsulate active sulfur (**Figure 1.23**g).[274] Crystalline $Fe_{0.667}Co(CN)_4(H_2O)_4$ nanocubes (**Figure 1.23**h) were first synthesized via the self-assembly strategy between $Fe(CN)_6^{3-}$ and Co^{2+}, followed by the phosphorization process to create abundant interconnected pore structures (**Figure 1.23**i,j). The XRD pattern indicated that the as-synthesized Co-Fe-P composed of a mixture of CoP_2 and FeP_2 (**Figure**

1.23k). After sulfur loading, the S@Co-Fe-P still maintained its nanocube morphology and the sulfur was distributed uniformly into the pores of the nanocubes (**Figure 1.23**l). Benefiting from highly-interconnected pore architecture, superior conductivity, and strong polysulfide trapping as well as catalytic effect for the redox reaction, the S@Co-Fe-P cathode demonstrated much stable cycling performance compared to the S@Co-Fe cathode (**Figure 1.23**m). Moreover, the S@Co-Fe-P displayed high areal capacities of 3.8 and 4.6 mA h cm^{-2} at high sulfur loadings of 3.7 and 5.5 mg cm^{-2}, respectively. Subsequently, double-shelled Ni-Fe-P nanoboxes,[275] carbon cloth@CoP/C[276] and carbon cloth@FeP/C[277] were also developed as sulfur host materials and showed impressive electrochemical performance.

Although much progress has been made on the metal phosphide based host materials for Li-S batteries in the past two years, the research on them is still in its early stage. Because of the many intrinsic advantages of metal phosphides, more complicated nanostructured metal phosphides are generally needed to enable abundant interfaces and tunable exposed surfaces to bind with polysulfides to further improve the performance of Li-S batteries.

1.2.10 Metal borides as host

Recently, metal borides with high metallic conductivity have also been used as host materials for Li-S batteries. Xu's group first reported the use of titanium diboride (TiB_2) as sulfur host.[278] TiB_2 has an excellent theoretical conductivity of about 10^6 S cm^{-1}.[278] The schematic of the (001) surface of TiB_2 is illustrated in **Figure 1.24**a and it shows a high density of coordinatively unsaturated Ti atoms, which provides abundant active sites to anchor sulfur species. The TiB_2 nanoparticles (**Figure 1.24**b,c) were synthesized *via* a metal

hydrolysis-assisted strategy using TiO_2 and B powder as precursor materials. When heated to 150 °C, the Mg hydrolysis reaction occurred and released a great deal of heat. With the presence of Mg and B, the TiO_2 can be easily transformed into the TiB_2. Sulfur was then incorporated onto the TiB_2 substrate *via* a melt-diffusion process (**Figure 1.24**d). The EDX mapping of a single TiB_2/S nanoparticle indicated that sulfur was distributed uniformly onto the TiB_2 substrate. When evaluated as the cathode for Li-S batteries, the TiB_2/S electrode delivered a high initial discharge capacity of 1232 mA h g^{-1} and retained a capacity of 842.3 mA h g^{-1} after 150 cycles at 0.2C (**Figure 1.24**f). As the pore volume of the as-synthesized TiB_2 nanoparticles was negligible (0.032 cm^{-3} g^{-1}), the physical confinement played a negligible role in trapping the polysulfides. In this regard, the superior performance can be largely attributed to the excellent conductivity and effective chemical entrapment of TiB_2 for polysulfides.

In order to increase the sulfur utilization and further improve the electrochemical performance of Li-S batteries, Sun's group integrated cobalt boride (Co_2B) nanoparticles with porous graphene nanosheets to improve the performance of Li-S batteries.[279] The polar Co_2B nanoparticles can provide strong chemical interaction with polysulfides, while the porous graphene can not only act as the 3D conductive network to transport electrons but also relive the volume change of sulfur upon cycling. As a result, the CoB_2-G/S composite had a very high sulfur utilization efficiency with a high capacity of 1543 mA h g^{-1} at 0.1C. Moreover, the CoB_2-G/S electrode showed very stable cycling performance with a capacity of 758 mA h g^{-1} after 450 cycles at 1C, corresponding to an ultralow capacity decay rate of only 0.029% per cycle.

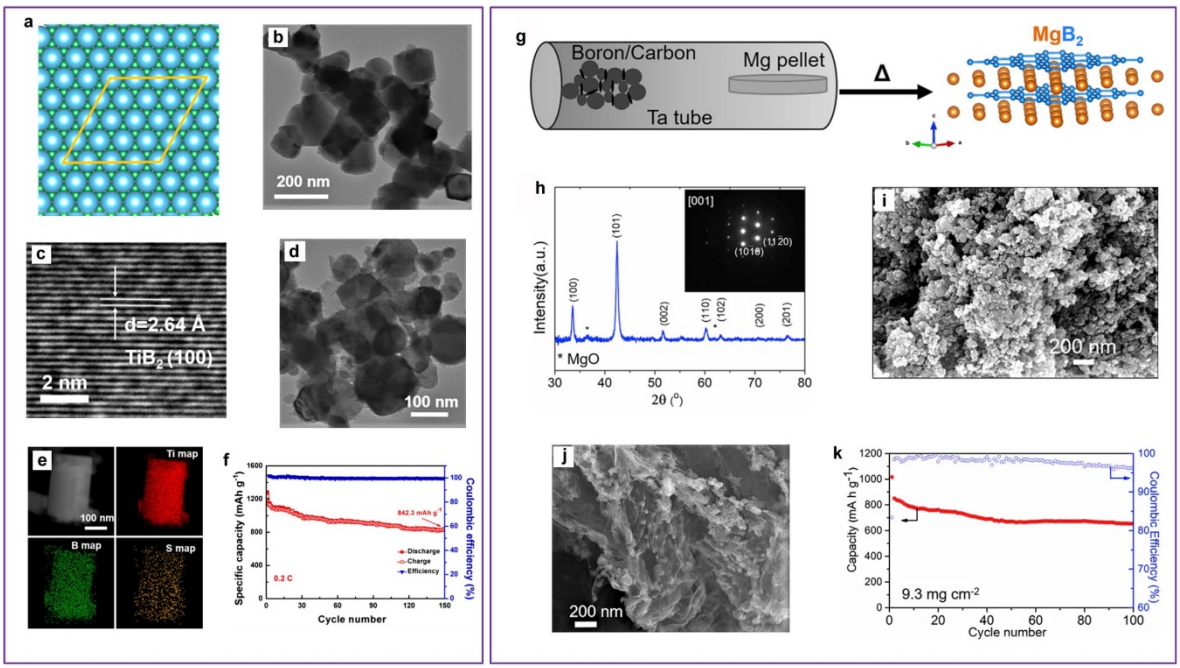

Figure 1.24 (a) Schematic of TiB_2 (001) surface. (b) TEM and e) HRTEM images of TiB_2 nanoparticles. (d) TEM image of TiB_2/S composite. (e) Scanning TEM image of a single TiB_2/S nanoparticle and corresponding EDX mapping. (f) Cycling performance and Coulombic efficiencies of TiB_2/S cathode at 0.2C for 150 cycles. (a-f) Reproduced from reference[278]. Copyright 2018, American Chemical Society. (g) Schematic of the synthesis strategy for MgB_2. (h) XRD pattern of MgB_2.The inset shows the SAED pattern. (i) SEM image of MgB_2 nanoparticles. (j) SEM image of MgB_2-graphene composite. (k) Cycling performance and Coulombic efficiencies of MgB_2-graphene/S cathode with a high sulfur loading of 9.3 mg cm^{-2} at 0.2C. The first cycle was at 0.05C. (g-k) Reproduced from reference[280]. Copyright 2019, Cell Press.

Besides TiB_2 and CoB_2, metallic and polar MgB_2 was also developed as sulfur host material by Nazar and co-workers.[280] The MgB_2 has a very similar band structure as graphite (**Figure 1.24**g), which makes it a metallic hole-type compound that exhibits high electronic conductivity as high as 10^4 S cm^{-1}.[281] The MgB_2 nanoparticles were synthesized by a vapor-solid reaction between vaporized Mg and boron powder (**Figure 1.24**g). The XRD and SAED patterns confirmed that MgB_2 was the primary crystalline phase (**Figure 1.24**h). The

particle size of the as-synthesized MgB_2 was about 100 nm (**Figure 1.24**i). When evaluated as the sulfur host material, the MgB_2/S composite demonstrated much improved cycling performance compared to MgO/S and C/S composites. This can be attributed to the higher conductivity and stronger chemical bonding between MgB_2 and polysulfides compared to that of MgO. It is well known that the chemical interaction between metal oxides/sulfides and lithium polysulfides mainly relies on the O/S-Li bonding, which would potentially impede the direct electron transfer to the active S_x^{2-} anions and likely delay the Li^+ diffusion, thus retarding the electrochemical reaction kinetics. Nevertheless, by using DFT calculations, the authors proposed that both B- and Mg-terminated surfaces in MgB_2 bonded exclusively with S_x^{2-} anions and thus accelerated the redox reaction kinetics. To further increase the sulfur utilization efficiency at high sulfur loading, MgB_2 nanoparticles were sandwiched between graphene layers to increase the surface area (**Figure 1.24**j). When the sulfur loading was increased to 9.3 mg cm^{-2}, the MgB_2-G/S electrode still exhibited stable cycling performance with high capacity (**Figure 1.24**k).

1.2.11 Other emerging metal compounds as host

Apart from the typical transition metal compounds summarized above, some emerging metal compounds have also shown promise to improve the performance of Li-S batteries. This section will discuss some emerging metal compound hosts for high performance Li-S batteries.

Gao's group reported the use of cobalt oxyhydroxide (CoOOH) as sulfur immobilizer for Li-S batteries.[282] CoOOH shows a half-metallic behavior with high conductivity of 5 S

cm^{-1}.[283] The CoOOH nanosheets were prepared by the oxidation of $Co(OH)_2$ sheets using NaClO as oxidant. The morphology of the as-synthesized CoOOH nanosheets was shown in **Figure 1.25**a,b. The hexagon CoOOH nanosheets composed of small cubic nanocubes with diameter of about 100 nm, which can provide abundant adsorption and catalytic sites to trap and power the polysulfide conversion. The specific surface area of the CoOOH sheets was as high as 214.4 m^2 g^{-1}. Sulfur nanoparticles were then mixed with the CoOOH sheets via an ultrasonic process to obtain S@CoOOH sheets (**Figure 1.25**c). Even at a high sulfur loading of 91.8%, the S@CoOOH still retained its original sheet morphology (**Figure 1.25**c). The EDX mapping indicated that sulfur nanoparticles were distributed uniformly in the nanosheets (**Figure 1.25**d-f). When used as cathodes for Li-S batteries, the S@CoOOH composite showed high gravimetric and volumetric capacities of 1199 mA h $g^{-1}_{composite}$ and 1511 mA h cm^{-3} at 0.1C. Meanwhile, satisfactory cycling performance over 500 cycles with a low capacity decay rate of 0.09% per cycle was achieved, which can be attributed to the strong Lewis acid-base interaction between CoOOH and polysulfides as well as the superior conductivity of CoOOH sheets.

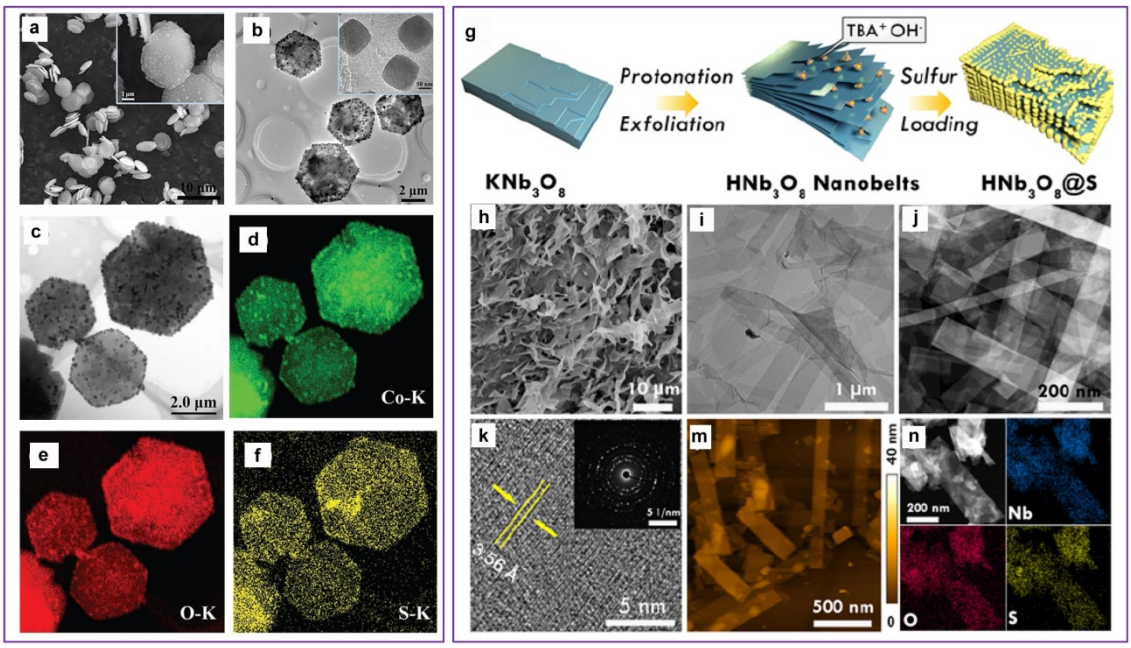

Figure 1.25 (a) SEM and (b) TEM images of CoOOH sheets. (c) TEM image and (d-f) corresponding EDX mappings of S@CoOOH sheets. (a-f) Reproduced from reference[282]. Copyright 2019, Wiley-VCH. (g) Schematic illustration of the synthesis process of HNb_3O_8@S. h) SEM and (i,j) TEM images of HNb_3O_8 nanobelts. (k) HRTEM image of HNb_3O_8 nanobelts. The inset shows the SAED pattern. m) AFM image of HNb_3O_8 nanobelts. (n) Scanning TEM image of HNb_3O_8@S nanobelts and corresponding EDX mappings. (g-n) Reproduced from reference[284]. Copyright 2019, Wiley-VCH.

Xu et al. reported the use of ultrathin niobic acid (HNb_3O_8) nanobelts to promote the polysulfide adsorption and conversion process.[284] The HNb_3O_8 nanobelts were synthesized by proton-exchange from KNb_3O_8 nanobelts followed by the chemical exfoliation process as illustrated in **Figure 1.25**g. **Figure 1.25**h-m shows the morphology of the as-synthesized HNb_3O_8 nanobelts, indicating its ultrathin nanostructure. Oxygen-deficient HNb_3O_8 (HNb_3O_8-v) nanobelts were also synthesized by annealing in reducing atmosphere. EDX mappings of the sulfur-loaded HNb_3O_8 nanosheets confirmed the homogeneous loading of sulfur on the HNb_3O_8@S nanobelts (**Figure 1.25**n). The ultrathin nanostructure was an

excellent model to study the adsorption and conversion behavior of lithium polysulfides due to its sufficient electroactive sites. By using both experimental and theoretical methods, the authors found that the oxygen deficiency in HNb_3O_8 nanobelts can lead to inferior catalytic performance for polysulfide conversion and the decrease in electrochemical performance for Li-S batteries. The inferior performance can be mainly attributed to the decrease in conductivity as well as weakened polysulfide adsorption on the catalyst surface. Unlike many previous reports that defect and vacancy engineering can enhance the catalytic performance for polysulfide conversion; this study shows us that defect-engineering can impact many factors that play vital roles in polysulfide conversion, which would be a valuable reference for the future rational design of redox mediators for Li-S batteries.

1.2.12 Using metal to mediate polysulfide redox

Besides metal compounds, pure metal materials have also been used as sulfur host to mediate the polysulfide redox. Amine and co-workers first reported the employ of a pure metal-Mo as a sulfur host.[285] The authors found that the Mo surface can not only effectively entrap the polysulfides, but also catalytically decompose polysulfides and Li_2S. Even with a 80% high sulfur content, the Mo/S composite displayed a high discharge capacity of 1003 mA h g^{-1} after 130 cycles at 0.1C and 786 mA h g^{-1} after 100 cycles at 5C. Following this work, Peng and co-workers reported that Co_xSn_y alloy can also possess strong chemisorption and superior electrocatalytic activity for polysulfide conversion. By using the Co_xSn_y alloys modified hollow N-doped carbon nanoboxes as sulfur host, a high reversible capacity of 1006 mA h g^{-1}

after 100 cycles at 0.2C and long-term cycling performance with a capacity retention of 81.2% after 500 cycles at 1C were realized.

Besides using micrometer and nanometer metal particles to mediate polysulfide redox, single metal atoms have also swarmed into the area of Li-S batteries owing to their higher atomic utilization efficiency for catalysis. Yang and co-workers pioneered the work of using single-atom catalyst to boost the polysulfide conversion in Li-S batteries.[286] They synthesized a kind of single iron atomic sites in porous N-doped carbon (Fe-PNC) to use as sulfur host. Aymmetric Li_2S_6 cells and EIS spectra suggested that the Fe-PNC electrode showed high electrocatalytic activity for polysulfide conversion and lower charge transfer resistance compared to that of PNC. Moreover, the authors also found that the Fe-PCN/S had a smaller phase nucleation overpotential for the formation of nanoscale Li_2S as revealed by the ex situ SEM image of the discharged product, which can thus enhance the lithium ion diffusion in Li_2S. As a result, the Fe-PCN/S exhibited improved electrochemical performance compared to that of PCN/S. Besides this work, the Zhang group also reported the use of single iron atoms supported on nitrogen-rich carbon matrix to accelerate the electrochemical conversion kinetics in Li-S batteries.[287] By using both experimental and theoretical methods, the authors found that the atomically dispersed single iron atoms can effectively reduce the Li_2S decomposition energy barrier and thus promote its delithiation process, which is a vital step during the electrochemical reactions in Li-S batteries. By virtue of these benefits, an ultrahigh rate performance of 588 mA h g^{-1} at 12C and long-cycling performance over 1000 cycles with a capacity decay rate of only 0.06% per cycle at 5C were realized.

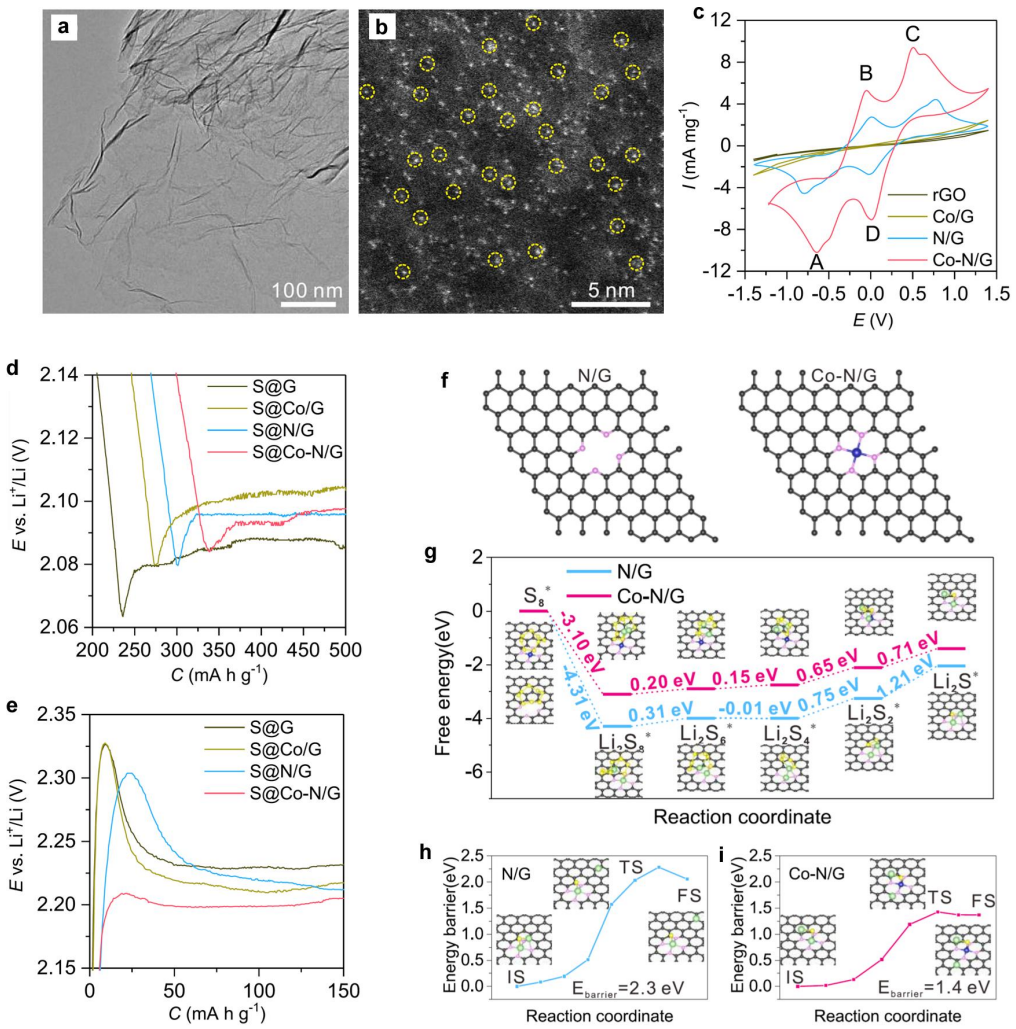

Figure 1.26 (a) TEM and b) HAADF-STEM images of single Co atoms on nitrogen-doped graphene (Co-N/G). (c) CVs of Li_2S_6 symmetric cells with different electrodes. (d) Discharge and (e) charge profiles of S@Co−N/G, S@N/G, S@Co/G, and S@rGO electrodes showing the overpotentials for conversion between soluble lithium polysulfides and insoluble Li_2S_2/Li_2S. (f) Atomic structures of N/G and Co-N/G used in the first-principle calculations. (g) Gibbs free energy profiles for the reduction of lithium polysulfides on N/G and Co-N/G substrates, respectively. The insets show the optimized adsorption geometries of intermediate sulfur species on N/G and Co-N/G substrates, respectively. Energy profiles of Li_2S decomposition on (h) N/G and i) Co-N/G. The insets show the initial, transition, and final structures. The black, pink, dark blue, green and yellow balls represent C, N, Co, Li and S atoms, respectively. Reproduced from reference[288]. Copyright 2019, American Chemical Society.

Recently, Wan and co-workers reported that monodisperse cobalt atoms anchored on nitrogen-doped graphene (Co-N/G) can accelerate the electrochemical conversion reactions in Li-S batteries.[288] The TEM image of the as-synthesized Co-N/G indicated that no nanoparticles were detected on the nanosheets (**Figure 1.26**a). Atomic-resolution aberration-corrected HAADF-STEM image suggested that abundant individual Co atoms were randomly dispersed on the Co-N/G nanosheets (**Figure 1.26**b). The CV curve of Li_2S_6 symmetric cells using Co-N/G as working and counter electrodes showed four distinct peaks (**Figure 1.26**c), corresponding to the two-stage transformation process between S_8 and Li_2S_2/Li_2S. The much higher peak current densities of Co-N/G indicated the much favorable redox kinetics. Since both Co-N/G and N/G had very similar nitrogen content, the Co-N-C center should be the major active sites responsible for propelling the electrochemical reaction kinetics. The improved electrochemical kinetics of Co-N/G was also confirmed by the lower overpotentials during both the discharge and charge process (**Figure 1.26**d,e). To understand the mechanism for the enhanced redox kinetics of S@Co-N/G cathode during discharge and charge process, first-principle calculations were further performed on the possible reactions of lithium polysulfides on Co-N/G and N/G, respectively. Two models of N-doped graphene with and without Co atoms were employed for the simulation (**Figure 1.26**f). During discharge, S_8 undergoes several steps to successively form Li_2S_8, Li_2S_6, Li_2S_4, Li_2S_2 and finally Li_2S. The optimized geometries of sulfur species and Gibbs free energy profiles were shown in **Figure 1.26**g. It is obvious that after the spontaneous exothermic conversion from S_8 to Li_2S_8, the subsequent formation of Li_2S_6, Li_2S_4, Li_2S_2 and Li_2S are either endothermic or nearly thermoneutral. The transformation from Li_2S_2 to Li_2S owns the largest positive Gibbs

free energy, suggesting that this is the rate-determining step during the whole discharge process. This value is 0.71 eV on Co-N/G and 1.21 eV on N/G. The much lower Gibbs free energy on Co-N/G for the reduction of Li_2S_2 to Li_2S indicates the more thermodynamically favorable on Co-N/G substrate. During the charge process, the calculated energy barriers for the decomposition of Li_2S on N/G and Co-N/G were 2.29 and 1.43 eV, respectively (**Figure 1.26**h,i), which suggested that Co-N-C center can act as an efficient active site to propel the Li_2S oxidation process. Based on the above analysis, the Co-N/G host can effectively boost the electrochemical conversion reactions during both discharge and charge process, thus leading to the improved electrochemical performance. The S@Co-N/G cathode with a high sulfur content of 90% delivered a high capacity of 1210 mA h g^{-1} and a high areal capacity of 5.1 mA h cm^{-2} with a high sulfur loading of 6 mg cm^{-2}.

1.3 Separator modification and interlayer engineering

In 2012, the Manthiram group pioneered the work of inserting an interlayer between the separator and cathode for improving the cycling performance of Li-S batteries (**Figure 1.27** a,b).[41] They proposed that the carbon interlayer can serve two roles: (i) helping confine lithium polysulfides in the cathode side to suppress their shuttle effect and (ii) acting as another current collector to increase sulfur utilization. With the inserted carbon interlayer, the charge transfer resistance largely decreased, indicating the enhanced reaction kinetics. By combining the carbon interlayer with just a pure sulfur cathode, a stable capacity of over 1000 mA h g^{-1} after 100 cycles at 1C was achieved. This represents a very promising result because of its simple and commercially feasible means of fabrication process.

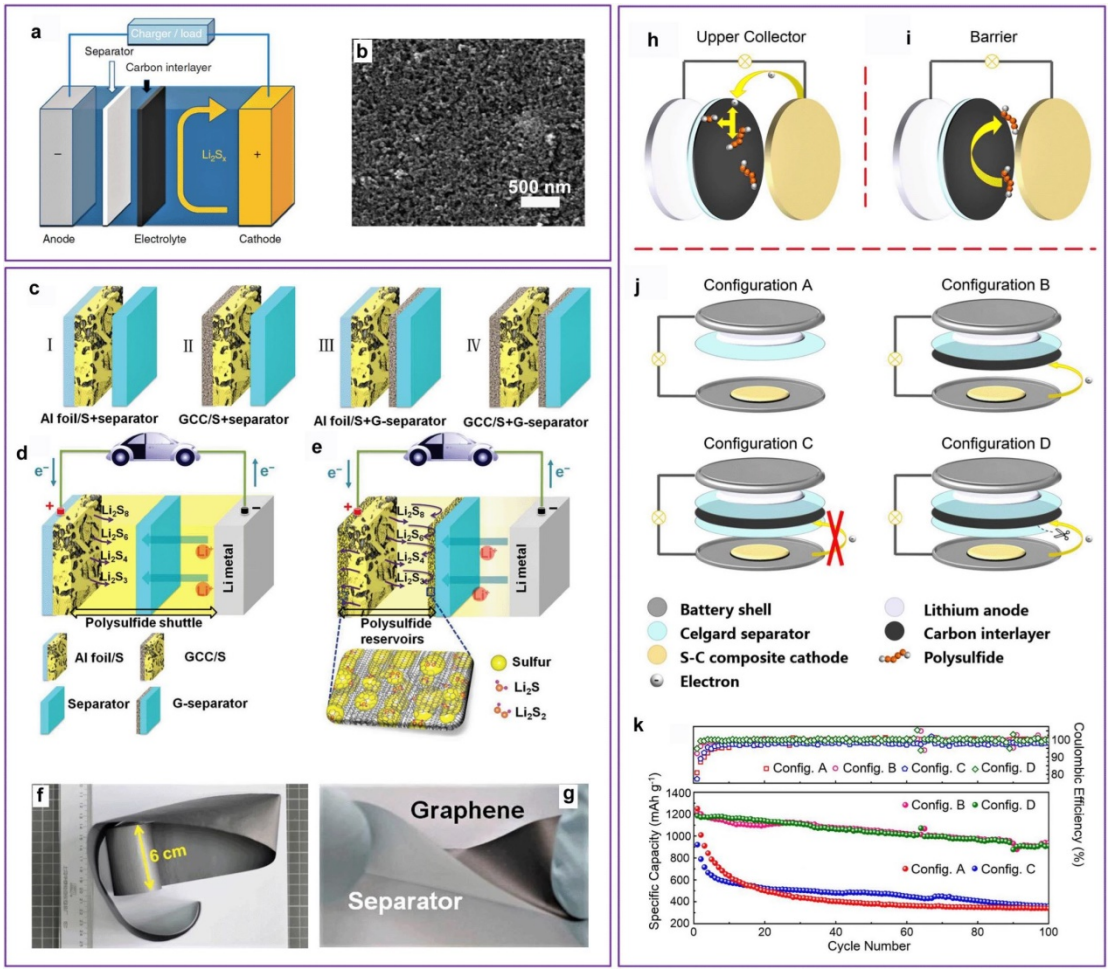

Figure 1.27 (a) Schematic configiration of a Li-S battery with an additional carbon interlayer. b) SEM image of the microporous carbon paper. (a,b) Reproduced from reference[41]. Copyright 2012, Nature Publishing Group. (c) Schamatic of four different electrode configurations. Schematics of Li-S batteries with (d) electrode configuration I and (e) electrode configuration IV. Photographs of f) large-area graphene current collector strip and g) G-separator. (c-g) Reproduced from reference[289]. Copyright 2014, Wiley-VCH. (h,i) Schematic illustrations of two hypothetical functions of carbon interlayer in Li-S batteries. (j) Schematic illustrations of four different battery configurations. (k) Cycling performances and Coulombic efficiencies of Li-S batteries with four different battery configurations. (h-k) Reproduced from reference[290]. Copyright 2018, The Electrochemical Society.

To gain more understanding on the role of carbon interlayer (**Figure 1.27**h,i), Huang and co-workers designed a series of battery configurations to further analyze the function

mechanism in Li-S batteries (**Figure 1.27**j).[290] Configuration A shows the routine Li-S battery without carbon interlayer. Configuration B shows a carbon interlayer inserted between the cathode and Celgard separator, in which the carbon interlayer has an electrical contact with the cathode. In comparison with configuration B, an additional Celgard separator was inserted between carbon interlayer and cathode, which disconnects the electron transfer between the cathode and carbon interlayer, thus the function of carbon interlayer as an upper current collector is eliminated and the physical block effect for polysulfides is isolated during discharge-charge process. Configuration D is similar to configuration C except that a corner of the additional Celgard separator has been cut out, thus the electron transfer between the cathode and carbon interlayer is well maintained, which means the carbon interlayer can also act as an upper current collector. By comparing the electrochemical performances of these configurations, both configuration B and D exhibited much better cycling performances and higher capacities compared to configuration A and C (**Figure 1.27**k). This suggests that the carbon interlayer as an upper current collector plays the key role on the improvement of Li-S battery performance, which further facilitates the redox reactions from dissolved lithium polysulfides to Li_2S/S_8. This comprehensive study provides valuable insight on the rational design of interlayers to improve the performance of Li-S batteries.

To avoid sacrificing the energy density of a practical Li-S battery, it is more advisable to modify the separator with an ultralight and thin carbon layer instead. To this end, Cheng and co-workers coated a 10 μm thin layer of graphene film on one side of the Celgard separator (G-separator) via a filtration process (**Figure 1.27**g).[289] The battery with the G-separator showed much improved electrocehmcial performance compared to the unmodified one. To

further increase the energy density of the battery, a lightweight graphene film (1.3 mg cm^{-2}) was used to replace the Al foil (5.4 mg cm^{-2}) as current collector (**Figure 1.27**e,f). By coupling both the graphene current collector and graphene-coated separator, a high specific capacity of about 1000 mA h g^{-1} was achieved with 70% capacity retention after 300 cycles at the current density of 1500 mA g^{-1}. In order to further reduce the inactive part in the battery and simplify the fabrication process, this group further designed a sulfur-graphene-PP separator integrated electrode as shown in **Figure 1.28**.[291] Instead of coating active sulfur on another graphene current collector, the sulfur slurry was directly coated on the graphen-coated separator to fabricate an integrated electrode. After paired with lithium metal, the S-G@PP separator cell exhibited a high initial discharge capacity of about 950 mA h g^{-1} and stable cycling performance over 500 cycles with a capacity decay rate of only 0.064% per cycle at the current density of 1500 mA g^{-1}.

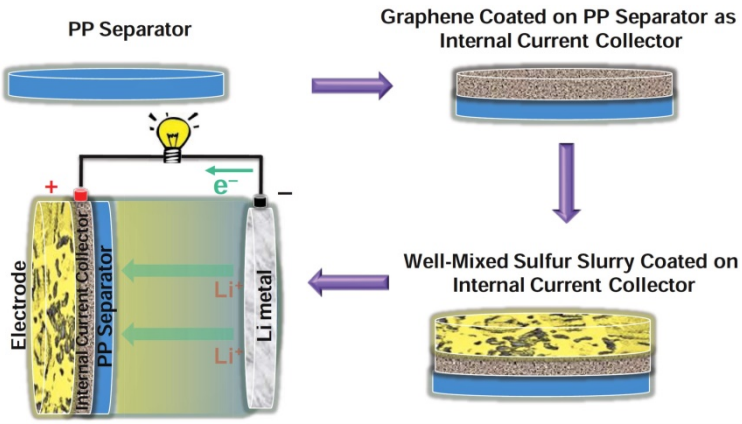

Figure 1.28 Schematic of the fabrication process of sulfur-graphene-PP separator integrated electrode and the corresponding battery assembly. Reproduced from reference[291]. Copyright 2015, Wiley-VCH.

In another report to reduce the thickness and weight of the interlayer, Wan and co-workers coated the PP separator with a two atomical layer CVD-graphene film (**Figure 1.29**a).[292] The bilayer graphene film has a thickness of only about 0.6 nm and areal density of about 0.15 μg cm^{-2}, which is negligible to the pristine PP separator. The top-view of the bilayer graphene coated PP separator indicates that the macropores in the original PP separator have been effectively covered by the atomic layer graphene (**Figure 1.29**b,c). The high relolution TEM image and Raman spectra confirmed the existence of two-layer graphene (**Figure 1.29**d,e). The two-layer CVD-graphene on separator represents the thinnest and lightest interlayer up to date. The interlayer can effectively increase the sulfur utilization during the redox reaction and supress the shuttle effect of polysulfides. As a result, the Li-S cell with the two-layer CVD-graphene coated PP separator demonstrated a very good cycling performance over 1500 cycles at 0.5C with a low capacity decay rate of only 0.026% per cycle, compared to a decay rate of 0.05% per cycle with the bare PP separator.

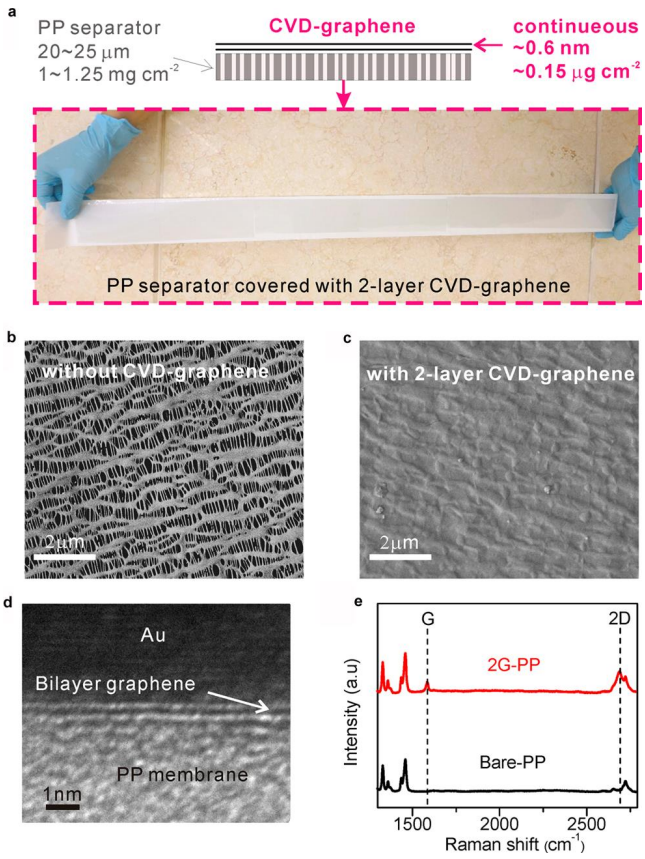

Figure 1.29 (a) Schematic and photograph of PP separator covered with 2-layer CVD-graphene with an areal of 5 × 60 cm^2. SEM images of the surface of PP separator (b) with and c) without 2-layer CVD-graphene. (d) Cross-sectional TEM image of PP separator coated with 2-layer CVD-graphene. (e) Raman spectra of bare-PP and 2G-PP. Reproduced from reference.[292] Copyright 2017, American Chemical Society.

Instead of using nonpolar and compact carbon film as interlayer to physically block the shuttle effect of polysulfides, the utilization of polymetric materials with negatively-charged functional groups as interlayer to allow the hopping of positive lithium ions yet repel polysulfide anions electrostatically is another strategy. To this end, a thin layer of Nafion with negatively-charged sulfonate groups was coated onto the Celgard separator as the ion selective membrane to allow the hopping of positive lithium ions and prevent the shuttle of negative polysulfides due to the Coulombic interactions (**Figure 1.30**b,c,e).[293] Using this

Nafion-coated Celgard membrane as separator, the Li-S battery showed much enhanced cycling performance compared to that of routine membrane (**Figure 1.30**f). Besides Nafion, other polymetric materials such as poly(allylamine hydrochloride) (PAH) and poly(acrylic acid) (PAA) were also assembled on polyethylene (PE) separator via a layer-by-layer assembly.[294] The movement of polysulfide anions was significantly supressed due to the Coulombic repulsion effect originated from the negatively charged groups on PAA, while the movement of Li cations was not affected. Using this ion-permselecive membrane modified PE separators in Li-S batteries, improved Coulomic efficiency and cycling performance were ahieved compared to that with the prinstine PE separator. In another report, the Manthiram group modified the PP separator with negatively charged carboxyl functional groups via a sequence of hydroxylating, grafting, and hydrolyzing process.[295] The resulted carboxyl-functionalized PP separator not only promoted the transport of lithium ions but also inhibited the migration of polysulfide anions from cathode to anode side. As a result, the Li-S batteries with the carboxyl-functionalized PP separator demonstrated much enhanced electrochemical performance compared to the unmodified one.

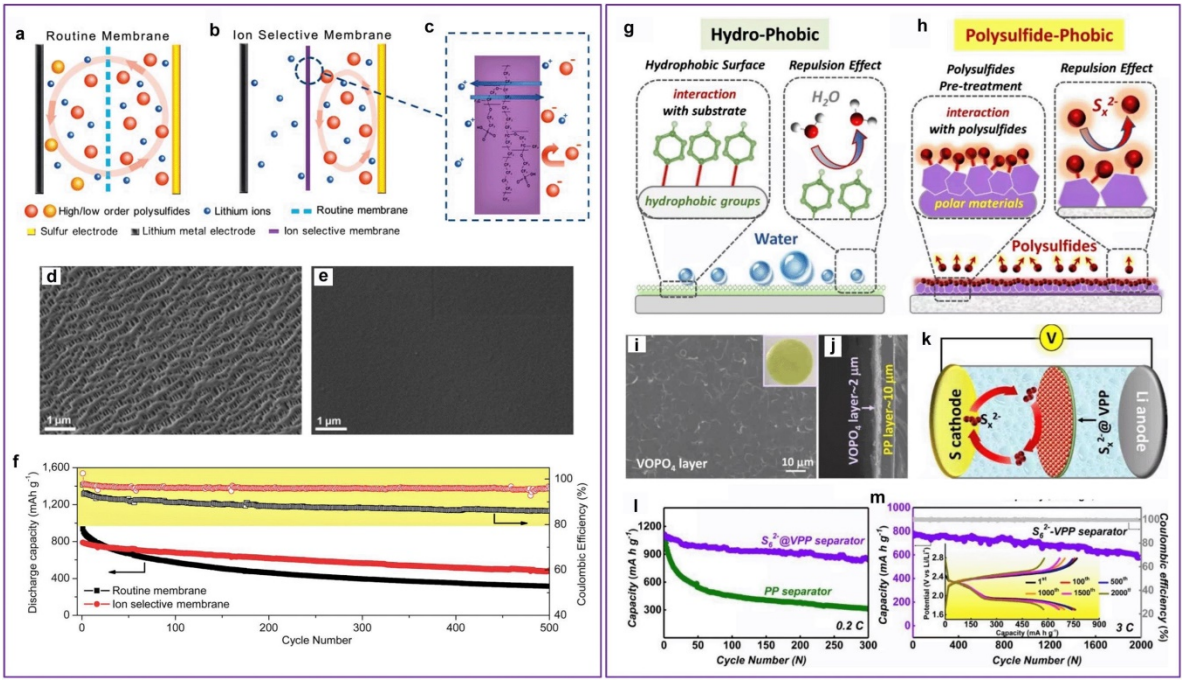

Figure 1.30 Schematic illustrations of Li-S battery configurations using (a) routine membrane and (b) ion selective membrane. (c) Enlarged microstructure of the ion selective membrane. SEM images of (d) routine PP/PE/PP membrane and (e) ion selective Nafion-PP/PE/PP membrane. (f) Cycling performances of Li-S batteries with routine membrane and ion selective membrane at 1C, respectively. (a-f) Reproduced from reference[293]. Copyright 2014, Royal Society of Chemistry. Schematics of (g) a hydro-phobic interface and (h) a polysulfide-phobic interface. (i) Top-view and (j) side-view of $VOPO_4$/PP membrane. The inset in i shows the photograph of $VOPO_4$/PP membrane. (k) Schematic illustration of suppressing polysulfide shuttle by using a S_6^{2-}-$VOPO_4$/PP separator. (l) Cycling performances of Li-S cells with different separators. (m) Long-cycling performance of the Li-S battery with S_6^{2-}-$VOPO_4$/PP separator at 3C for 2000 cycles. The inset shows the voltage profiles at selective cycles. (g-m) Reproduced from reference[296]. Copyright 2019, Wiley-VCH.

Instead of utilizing externally functional groups to repel the polysulfides, Zhou's group recently proposed a "self-defense" mechanism by constructing a "polysulfide-phobic" interface on the separator to suppress the shuttle effect of polysulfides (**Figure 1.30**g-m).[296]

As illustrated in **Figure 1.30**h, with polysulfides pre-treatment on the polar $VOPO_4$-coated separator, the surface of separator can act as a "polysulfide-phobic" interface to suppress the shuttle effect of polysulfides. The time/space-resolved operando Raman spectra was performed to confirm the adsorption-induced "self-defense" effect against polysulfides. The "polysulfide-phobic" separator was fabricated by coating a thin layer of $VOPO_4$ nanosheets (about 2 μm) on PP separator, followed by immersing it into a Li_2S_6 DME/DOL solution to anchor polysulfides to form a "polysulfide-phobic" surface (**Figure 1.30**i,j). Using S_6^{2-}-$VOPO_4$/PP as separator for Li-S batteries, it showed much enhanced cycling performance compared to the routine PP separator (**Figure 1.30**l). Moreover, the Li-S battery with the S_6^{2-}-$VOPO_4$/PP separator delivered a high capacity of 578 mA h g^{-1} even after 2000 cycles at a high rate of 3C, corresponding to a very low capacity decay rate of only 0.012% per cycle (**Figure 1.30**m).

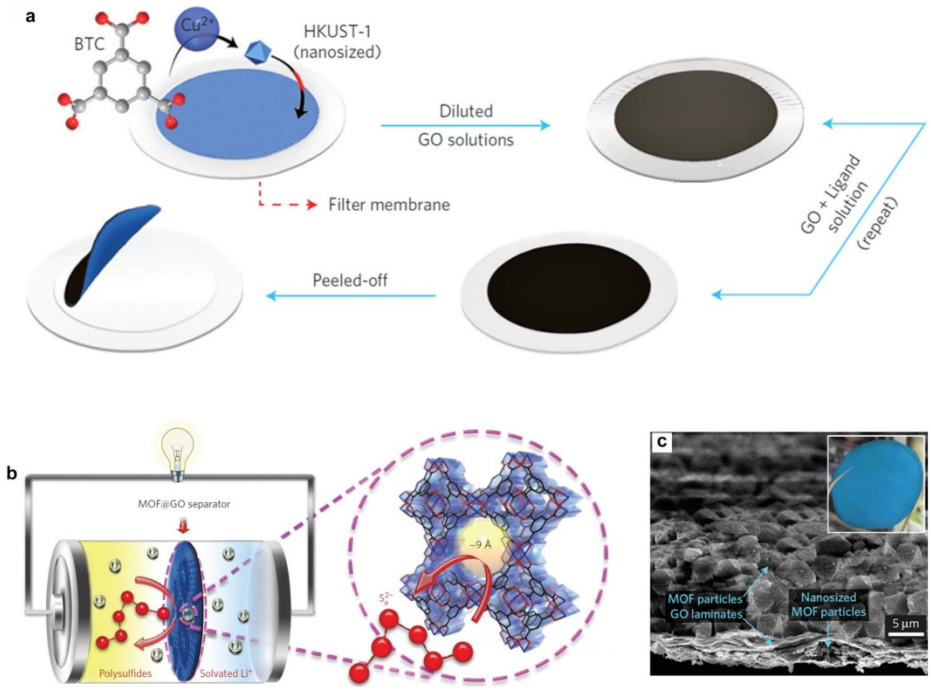

Figure 1.31 (a) Schematic of the fabrication process for artificial MOF@GO separator. (b)

Schematic of MOF@GO separator acting as ionic sieve towards polysulfides. The enlarged image illustrates the pore size of the HKUST-1 (about 0.9 nm) is much smaller than that of polysulfides. (c) Cross-sectional SEM image of the MOF@GO separator. The inset shows a photograph along the MOF side. Reproduced from reference[297]. Copyright 2016, Nature Publishing Group.

Beside using the polymetric Celgard separators, MOF-based materials were also used to fabricate the separator for Li-S batteries. Zhou's group first reported the use of MOF@GO membrane as the separator for Li-S batteries.[297] The fabrication process was illustrated in **Figure 1.31**a. The initial MOF layer was grown in situ. Then a thin GO layer was covered on the MOF layer via the filtration process. The filtration process was repeated two or three times to give a better fabrication. As the pore window of HKUST-1 is about 0.9 nm, which is much smaller than that of lithium polysulfides (**Figure 1.31**b), the HKUST-1@GO film can be acted as an ionic sieve to mitigate the shuttle effect of polysulfides while the transportation of lithium ions was not affected. As a result, when a sulfur-containing mesoporous carbon was used as the cathode without intricate synthesis or surface modification, the Li-S battery with MOF@GO separator showed long-term cycling performance over 1500 cycles with an ultralow capacity decay rate of 0.019% per cycle.

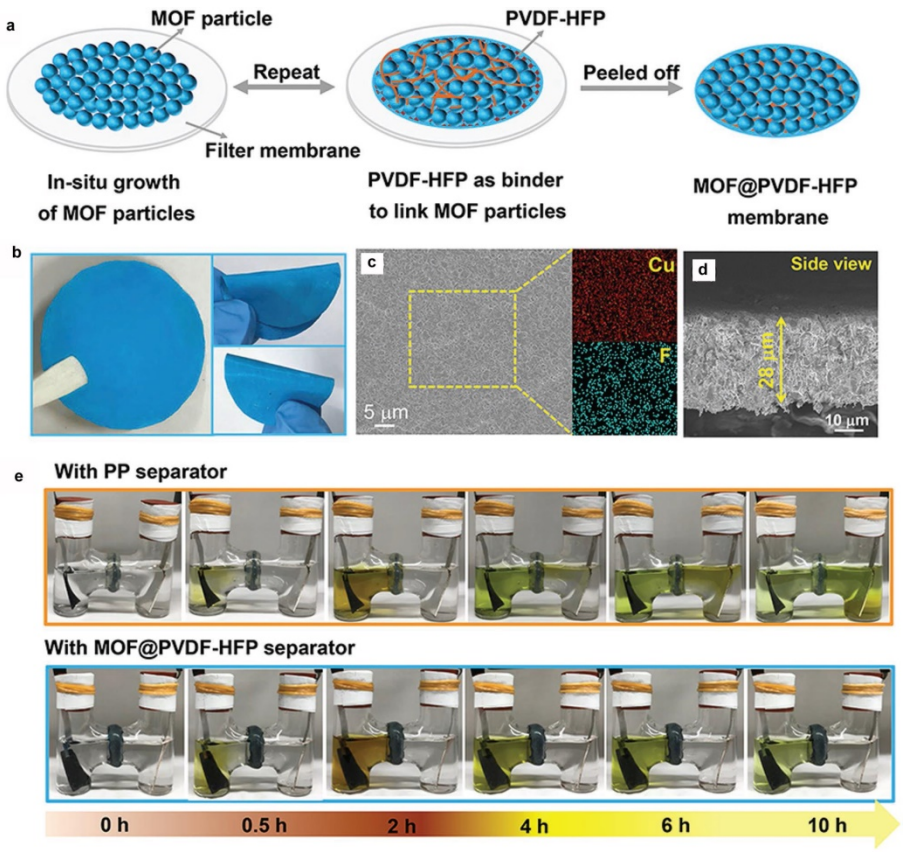

Figure 1.32 (a) Schematic of the fabrication process for MOF@PVDF-HFP membrane. (b) Digiutal photos of the flexible MOF@PVDF-HFPs separator. c) TOP-view SEM image of the MOF@PVDF-HFP separator and the corresponding elemental mappings of Cu and F. (d) Side-view of the MOF@PVDF-HFP separator. (e) Digital photos of visible H-type Li-S cells with different separators during a discharging process. Reproduced from reference[298]. Copyright 2018, Wiley-VCH.

Although MOF@GO membrane was a promising separator for Li-S batteries, the electronic conductivity of GO nanosheets may cause self-discharge of the battery or even the risk of short circuit. To this end, this group further replace the GO with Poly(vinylidene fluoride-co-hexafluoropropylene) (PVDF-HFP) binder to link the MOF particles to form the MOF@PVDF-HFP membrane as separator (**Figure 1.32**a).[298] The photographes of the obtained MOF@PVDF-HFP membranes were shown in **Figure 1.32**b, indicating their great

flexibility. The SEM image and corresponding elemental mappings of the membrane showed that MOF particles were distributed uniformly in the separator (**Figure 1.32**c). The corss-sectional SEM image showed that the membrane had a thickness of about 28 μm (**Figure 1.32**d). To study the effect of MOF@PVDF-HFP membrane on the difussion of polysulfides, visual H-type Li-S glass cell measurements were performed **(Figure 1.32**e). After discharge for 0.5h, both of the left chambers in the glass cells turned into yellow colour, indicating the formation of lithium polysulfides. Upon the continuous discharging process, the right chamber of glass cell with PP separator also turned into yellow colour, suggesting that the polysulfides diffused from the cathode to the anode side. However, the right chamber of the glass cell with the MOF@PVDF-HFP separator remained its original colour, indicating that the MOF@PVDF-HFP can efficiently inhibit the shuttle effect of polysulfides. Using the MOF@PVDF-HFP membrane as the separator for a flexible Li-S pouch cell with a high sulfur loading of 5.8 mg cm^{-2}, a high initial discharge capacity of 1269 mA h g^{-1} and a retained capacity of 936 mA h g^{-1} after 200 cycles were achieved at a high sulfur loading of 5.8 mg cm^{-2}, demonstarting its great potential for practical applications.

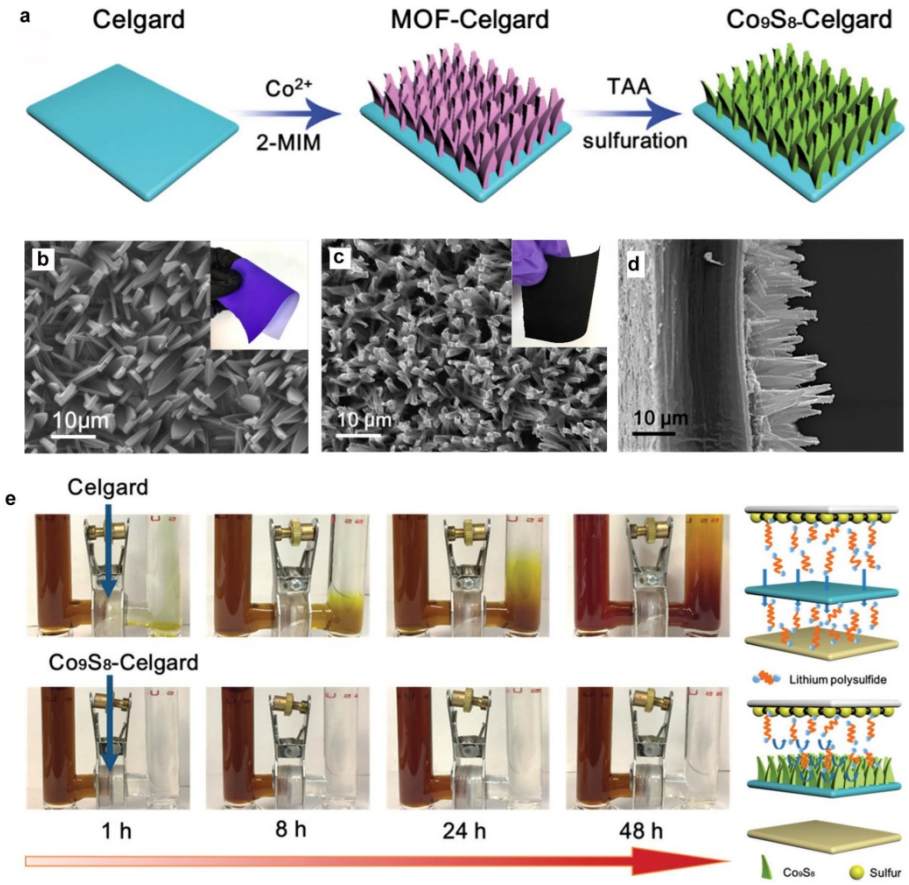

Figure 1.33 (a) Schematic of the in-situ growth of Co_9S_8 arrays on Celgard separator. Surface SEM images of (b) MOF-Celgard and (c) Co_9S_8-Celgard separators. The insets show the corresponding digital photos. (d) Cross-sectional SEM image of Co_9S_8-Celgard separator. (e) Photographs of glass cells with Li_2S_6 in DOL/DME solution and pure DOL/DME solvent in the left and right chambers, respectively, separated by Celgard (top panel) and the Co_9S_8-Celgard separator (bottom panel) and the improvement mechanism of the Co_9S_8-Celgard separator during the charge/discharge processes. Reproduced from reference[299]. Copyright 2018, Royal Society of Chemistry.

As most of the interlayers are fabricated by the vacume filtration method, this can make the materials easily stack together and thus form a thick interlayer. Although the shuttle effect of polysulfides could be largely supressed by the stacked thick interlayer, the transport of lithium ions would also be limited to some extent. In this regard, it is more desirable to

design porous and lightweight interlayers, which can not only allow fast lithium ion transport, but also provide abundant polar interfaces and conductive interafces to adsorb the intermidiate lithium polysulfides for high electrochemical utilization. To this end, the Manthiram group pioneeringly in situ grew well-aligned and hollow Co_9S_8 arrays on the Celgard separator as an efficient polysulfide barrier for Li-S batteries (**Figure 1.33**).[299] MOF-Celgard was fabricated by fixing a piece of Celgard on the beaker wall and immersing in a mixture of aqueous soulution containing 2-methylimidazole and $Co(NO_3)_2$ $6H_2O$ for 5h. The morphology of the in situ grown MOF-Celgard was shown in **Figure 1.33**b, showing the well-aligned array structure. After that, a piece of the MOF-Celgard was immersed into an aqueous solution containing thioacetamide (TAA), followed by the hydrothermal reaction at 100 °C for 6h to produce the Co_9S_8-Celgard. The Co_9S_8 nanowalls were grown uniformly on the Celgard separator with an areal density of about 0.16 mg cm^{-2} (**Figure 1.33**c,d). Glass cells were further assembled to confirm that the Co_9S_8 nanowalls can effectively supress the difussion of polysulfides (**Figure 1.33**e). As a result, the Li-S cell with Co_9S_8-Celgard separator exhibited a high capacity of 1385 mA h g^{-1} with a retention of 1190 mA h g^{-1} after 200 cycles.

Modification of separators is of wide interest in the area of Li-S batteries owing to its simplified fabrication procerdure. Many other materials, such as InN nanowires,[300] MoS_2,[301, 302] GO@MoS_2,[303] MoS_2/graphene,[304] N,S-codoped graphene,[305, 306] CNTs,[307-309] GO/CNTs,[310] Ni foam,[311] CNFs,[312-315] Fe_3C/CNF,[316] V_2O_5/CNF,[317] MoS_2/CNTs,[318] MXene,[319, 320] VS_4-CNFs,[321] red phosphorus,[322] Co/mSiO_2-NCNTs,[323] MoS_2/TiN,[324] MoS_2/PDDA/PAA,[325] Prussian blue,[326] MnO_2,[327] MnO_2/graphene,[328] MnO_2/GO/CNT,[329] laponite nanosheets,[330]

MoP/rGO,[331] polypyrrole,[332-334] CNT/N-doped carbon quantum dot,[40] BN,[335] silica nanoparticles,[336] $Li_4Ti_5O_{12}$/graphene,[337] $BaTiO_3$,[338] Nb_2O_5/RGO,[339] Sb_2Se_{3-x}/rGO,[340] MoN/graphene,[341] black phosphorus,[342] BN/graphene,[343] TiO_2,[344] TiO_2/graphene,[345] TiO_2@CNFs,[346] CoB_2@CNT,[347] carbonized cellulose,[348] hollow carbon spheres,[349] Co-embedded carbon nanosheets,[350] and single atom-coordinated N-doped carbon[351-353] have also been explored as interlayers for Li-S batteries. In order to realize a high-performance Li-S battery, a perfect interlayer should have the following merits: (i) lightweight and thin architecture that would not compromise the energy density of the battery; (ii) high conductivity to increase the active material utilization; (iii) abundant interfaces and polar active sites that can facilitate trapping and catalytic conversion of lithium polysulfides. These principles should be taken into consideration for the rational design of interlayers for Li-S batteries in the future.

1.4 Binder improvement

As an important component in rechargeable batteries, the basic functions of binders are to bind active materials and conductive additives onto current collectors, and to maintain the structural and mechanical integrity of the electrode upon cycling.[49, 354, 355] Owing to its strong adhesion, good thermal stability and wide electrochemical window, polyvinylidene fluoride (PVDF) binder has been widely used in the rechargeable batteries today.[49] However, some intrinsic characteristics of PVDF, such as low mechanical ductility, weak affinity to polar active sulfur species and insulating property make it not a perfect binder for Li-S battery system. Accordingly, multifunctional binders have been developed to improve the

performance of Li-S batteries in recent years. The principles of designing multifunctional binders for Li-S batteries should mainly consider (i) the high mechanical strength to withstand volume fluctuation upon cycling, (ii) the strong affinity to polysulfides for alleviating the shuttle effect, and (iii) overcoming the insulating nature of sulfur and its discharged products.

1.4.1. Mechanical strength

In Li-S batteries, the sulfur cathode undergoes huge volume expansion upon lithiation, which can lead to the structure instability and collapse of the electrode. In addition, to pursue a high specific energy of a practical Li-S battery, fabricating thick electrode with high sulfur loading is a prerequisite.[356] However, the thick electrodes usually suffer from the cracking and pulverization issues that the active material can easily delaminate from the current collector.[357] Accordingly, developing multifunctional binders with strong adhesion and high mechanical strength to afford long-term structure integrity of the electrode is vital for the practical application of Li-S batteries. Nevertheless, traditional linear polymer binders such as PVDF are not capable of affording high mechanical strength to accommodate the frequent volume change upon long-term cycling due to their facile swelling and dissolution into organic electrolyte as well as the weak interchain interactions. By contrast, the polymer binders with 3D network structure provide new opportunities for strengthening the mechanical properties and maintaining the integrity of the electrode with high sulfur loading owing to their robust interchain interactions. For example, Nazar's group synthesized the cross-linked carboxymethyl cellulose- citric acid (CMC-CA) binder via the esterification

reaction between the –OH groups in CMC and the –COOH groups in CA at 150 °C (**Figure 1.34**a).[358] When the cross-linked CMC-CA binder was used to fabricate the thick electrode with high sulfur loading of 5.2 mg cm^{-2}, the obtained electrode showed very flat morphology without cracks (**Figure 1.34**c). In contrast, the electrode fabricated with PVDF binder showed obvious cracks (**Figure 1.34**b). This indicates that the cross-linked CMC-CA binder has great advantage in fabricating robust thick electrode compared to the linear PVDF binder.

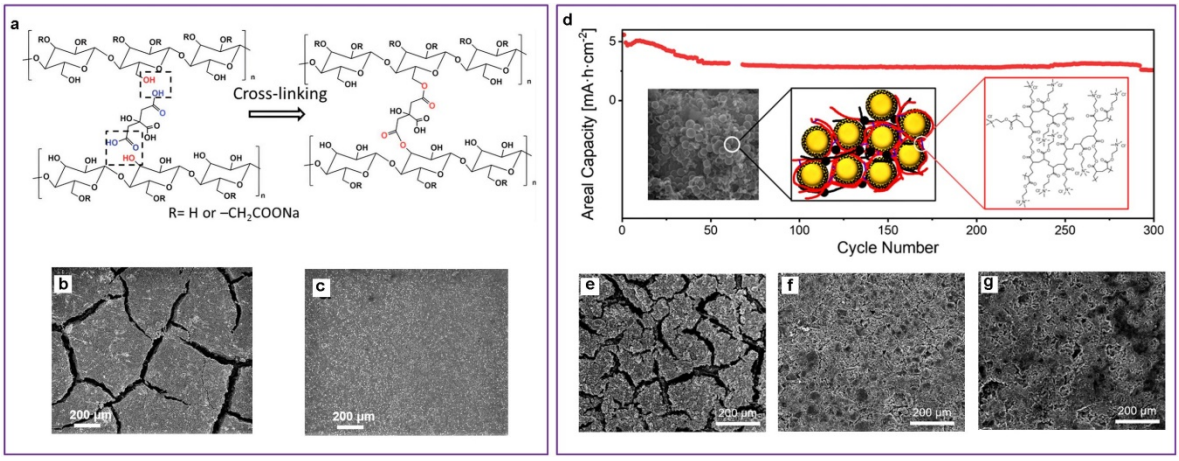

Figure 1.34 (a) Schematic of the cross-linking of CMC binder with CA as linker. SEM images of the surface of thick sulfur cathodes with high sulfur loading of 5.2 mg cm^{-2} using (b) PVDF binder and (c) cross-linked CMC-CA binder. (a-c) Reproduced from reference[358]. Copyright 2016, Wiley-VCH. (d) Cycling performance of the sulfur cathode using poly(AETMAC-co-EGDA) as binder. The insets show the SEM image of sulfur@porous hollow carbon sphere cathode, the illustration of S@carbon spheres linked by the poly(AETMAC-co-EGDA) binder and the structure of the binder. SEM images of the surface of sulfur cathodes after 100 cycles fabricated with (e) PVDF binder, (f) poly(DADMAC-co-EGDA) binder and (g) poly(AETMAC-co-EGDA) binder. (d-g) Reproduced from reference[359]. Copyright 2019, American Chemical Society.

Recently, the Nazar group further developed two highly cross-linked polymer binders through the radical copolymerization between ethylene glycol diacrylate (EGDA) and

[2-(acryloyloxy)ethyl]-trimethylammonium chloride (AETMAC) or diallyldimethylammonium chloride (DADMAC).[359] Using the obtained cross-linked poly(AETMAC-co-EGDA) and poly(DADMAC-co-EGDA) polymer binders to fabricate thick electrodes with high sulfur loading of 6 mg cm^{-2}, both of the electrodes kept intact after deep cycling for 100 cycles (**Figure 1.34**f,g). In contrast, the PVDF-based electrode showed large cracks upon deep cycling. This indicates that the cross-linked polymer can afford higher mechanical strength and toughness to the electrode.

1.4.2. Polysulfide regulation

Despite prior tremendous efforts on the design of sulfur host and interlayer to alleviate the shuttle effect of polysulfides, the contribution of binder on the immobilization of polysulfides cannot be ignored. In 2013, the Cui group used *ab initio* simulations to elucidate the interactions between common functional groups in binders with Li_2S and lithium polysulfides.[360] It was found that carbonyl functional groups had much stronger chemical binding energy towards sulfur species compared to other functional groups such as -C-F- group in PVDF routine binder. The group further screened PVP with carbonyl groups as a proof-of-concept binder for Li-S batteries. The *ab initio* simulations showed that PVP has higher binding energies with sulfur species compared to that of PVDF (**Figure 1.35**a,b). To compare the effectiveness of PVP and PVDF binders as dispersion agents for Li_2S cathodes, electrode slurries were prepared by mixing Li_2S, carbon and PVP/PVDF in NMP solution. As shown in **Figure 1.35**c, the electrode slurry using PVP as binder exhibited homogeneous dispersion without aggregations. However, the electrode slurry using PVDF as binder showed

large aggregates (**Figure 1.35**d). The two kinds of electrodes with different binders were further evaluated by electrochemical tests and the Li_2S cathode with PVP binder showed much improved cycling performance compared to that of PVDF binder. This work spurred numerous interests on the rational design of multifunctional binders with polar functional groups to trap the polysulfides. For example, Xiao and co-workers used polyamidoamine (PAMAM) dendrimers as multifunctional binders for sulfur cathodes.[361] The abundant functional groups in PAMAM can effectively adsorb the intermediate polysulfides. Guo and co-workers found that the copolymer poly(vinylidenedifluoride-trifluoroethylene) (P(VDF-TRFE)) has higher adhesion strength and stronger chemical interaction with polysulfides compared to PVDF.[362] As a result, the sulfur cathode with P(VDF-TRFE) binder showed much improved cycling performance compared to the corresponding cathode with PVDF binder. Yan and co-workers developed a kind of amino functional group (AFG) binder via the polymerization of hexamethylene diisocyanate (HDI) with polyethylenimine (PEI) polymer.[363] Owing to the strong affinity of amino groups to polysulfides, the sulfur cathode with AFG binder exhibited impressive cycling performance with a capacity retention of 91.3% over 600 cycles at 2C. Cui's group utilized ammonium polyphosphate (APP) as a multifunctional binder for sulfur cathode.[364] APP can effectively trap the polysulfides through the strong chemical interaction. The coupling of APP with lithium ions facilitates the ion transfer and propels the redox reaction kinetics. Moreover, the APP can act as a flame retardant to ensure the safety of the cathode. The sulfur cathode with APP binder exhibited superior rate performance of 520 mA h g^{-1} at 4C and impressive cycling performance for 400 cycles with a capacity decay rate of 0.038% per cycle. Xiong and co-workers developed a

kind of hydrophilic and hyperbranched binder (denoted as PPA binder) via the crosslink between poly(ethylene glycol) diglycidyl ether and polyethylenimine (**Figure 1.35**g).[48] As illustrated in **Figure 1.35**e, the polysulfide dissolution process occurred after several cycles due to the poor affinity of PVDF to polysulfides. In contrast, the abundant polar functional groups in PPA can effectively anchor the polysulfides (**Figure 1.35**f). XPS analysis and DFT calculations were also further performed to confirm the multidimensional Li-O, Li-N and S-O interactions between lithium polysulfides and PPA binder. As a result, the sulfur cathode with PPA binder demonstrated much improved cycling performance compared to the cathode with routine PVDF binder.

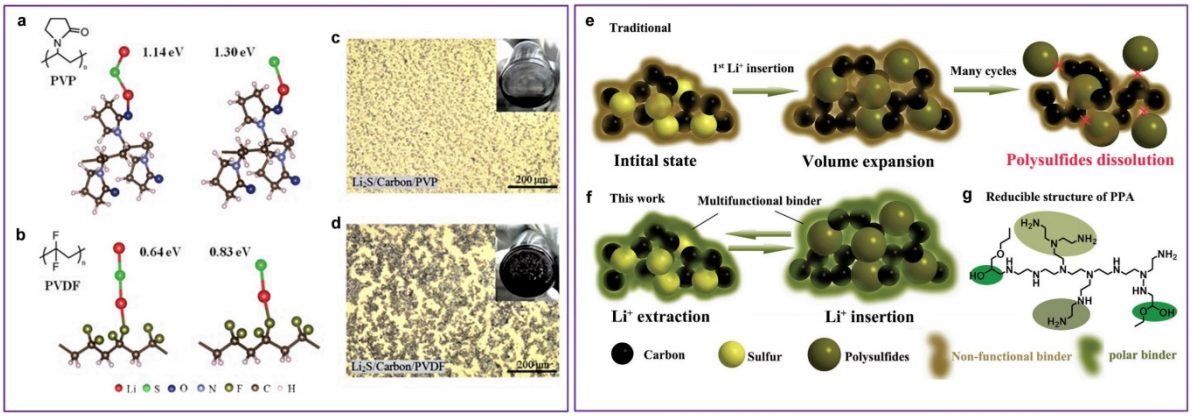

Figure 1.35 The optimized binding geometries of Li_2S and LiS species on (a) PVP and (b) PVDF binders. Optical microscopy images of electrode slurries of (c) Li_2S/Carbon/PVP and (d) Li_2S/Carbon/PVDF in NMP (60:35:5 by weight in both cases). The insets show the corresponding digital images. (a-d) Reproduced from reference[360]. Copyright 2013, Royal Society of Chemistry. (e) Schematic of electrode construction using (e) traditional PVDF binder and f) polar polymer with abundant amino and amide groups. (g) The reducible molecular structure PPA binder. (e-g) Reproduced from reference[48]. Copyright 2018, Wiley-VCH.

1.4.3 Conductivity

Besides mechanical strength and polar characteristic, the conductivity of the binder is also important for a Li-S battery. By using conductive binders, the amount of conductive additives can be reduced, which is vital to improve the specific energy of a practical Li-S battery. To this end, Liu and co-workers used four kinds of binders with different functionalities and conductivity to study how the interface properties affect the battery performance (**Figure 1.36**).[365] It was found that more solid-state sulfur species precipitation was observed with binders that have carbonyl functional groups, like poly(9, 9-dioctylfluorene-co-fluorenone-co-methylbenzoic ester) (PFM) and poly(vinylpyrroli-done) (PVP). Additionally, the introducing of conductive binders can also promote the Li_2S precipitation. As a result, the sulfur cathode with the PFM binder showed the best electrochemical performance among these four different binders (**Figure 1.36**b).

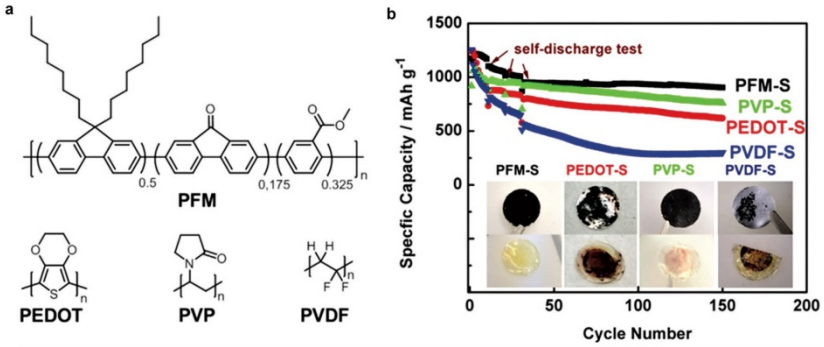

Figure 1.36 (a) Molecule structures of four different binders. (b) Cycling performances at 0.1C and self-discharge tests of cathodes with different binders. Reproduced from reference[365]. Copyright 2015, Elsevier.

Manthiram's group adopted the conductive and elastic nanocomposite of polypyrrole and polyurethane (PPyPU) as the binder for sulfur cathode.[366] The conjugated polypyrrole can

improve the overall conductivity of the electrode, while the polyurethane acts as an elastic matrix for flexible electrodes. When this binder was used with a simple carbon/sulfur composite, the resulted flexible Li-S batteries demonstrated impressive electrochemical performance even at high areal sulfur loading.

1.5 Electrolyte optimization

As an important component in the battery system, electrolytes function as the ion transport pathway between the anode and cathode. The electrolytes used in Li-S batteries can be classified into liquid electrolytes and solid electrolytes. The liquid electrolytes with relatively high solubility and mobility of polysulfides can definitely afford faster redox kinetics.[35, 367-376] However, the polysulfide shuttle is inescapable in liquid electrolytes. In this regard, the solvent-free solid-state electrolytes are promising to physically block the shuttle of polysulfides.[377-379] Additionally, solid-state electrolytes can also protect lithium metal anodes against corrosion by polysulfides and minimize the dendrite formation, improving the safety of Li-S batteries.[380] However, the solid-state electrolytes usually suffer from the low ionic conductivity due to the large interfacial resistance between the electrode and electrolyte as well as the slow lithium ion transport through the solid-state electrolyte.[381, 382]

1.5.1 Liquid electrolytes

1.5.1.1 Ether-based electrolytes

Ether solvents have been widely used in Li-S battery electrolytes due to their high mobility for polysulfides as well as good chemical stability against polysulifides.[367, 383, 384] Among various ether-based solvent systems, the electrolytes containing 1,3-dioxolane (DOL) and

1,2-dimethoxy ethane (DME) with a volume ratio of 1:1 provide a balance between the solubility, ionic conductivity and mobility for polysulfides, as well as the formation of a SEI layer on the lithium anode. DME has higher polysulfide solubility and better kinetics for its redox reaction, while DOL owns lower polysulfide solubility but promotes the formation of a more stable SEI layer on the lithium metal anode surface.[367, 368]

Except for solvent, lithium salt, which plays roles in conducting lithium ions, is another important component in Li-S electrolytes. Among various lithium salts, lithium bis(trifluoromethane sulfonel) imide (LiTFSI) is most widely used in Li-S electrolytes owing to its balanced properties in electrochemical stability, ionic conductivity and compatibility with the intermediate polysulfides.[367] The concentration of lithium salt in electrolytes also affects the performance of Li-S batteries.[385] A higher lithium salt concentration can definitely restrain the dissolution of polysulfides owing to the dissolution equilibrium mechanism. However, it decreases the speed of lithium ion transport and induces large polarization of the batteries due to the increased viscosity of electrolytes. The cost of the batteries can also increase with the raised lithium salt concentration. Accordingly, a medium concentration of 1 M lithium salt is commonly used in most of the Li-S electrolytes because it can balance the ionic conductivity, viscosity and salt solubility.

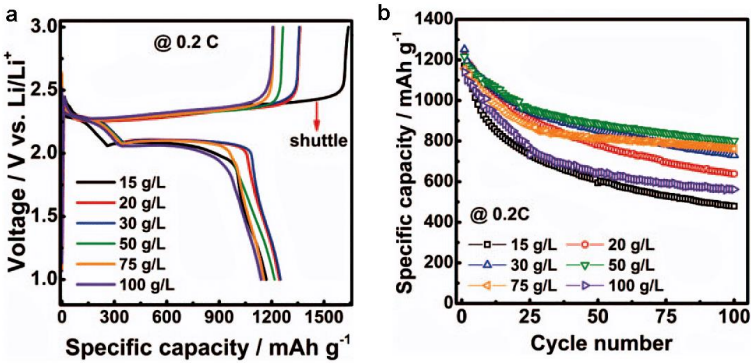

Figure 1.37 (a) Voltage profiles and (b) cycling performances of Li-S batteries at different sulfur/electrolyte ratios. Reproduced from reference[386]. Copyright 2013, The Electrochemical Society.

Besides the lithium salt concentration, the electrolyte amount also influences the electrochemical performance of Li-S batteries. A lower electrolyte amount leads to the decreased dissolution of polysulfides. However, the lower electrolyte amount can also result in the sluggish lithium ion transport and low sulfur utilization efficiency due to the poor wettability of the electrode by electrolyte. A higher electrolyte amount leads to the increased dissolution of polysulfides and also the decreased energy density of a practical Li-S battery. Therefore, an optimized electrolyte amount is vital to the performance of Li-S batteries. Xiao and co-workers studied the effect of electrolyte-to-sulfur (E/S) ratio on the performance of Li-S batteries and they found that an optimized E/S ratio of 20 μL/mg (corresponding to 50 g/L in **Figure 1.37**) showed a good balance between the electrode wetting ability and polysulfide dissolution.[386] Nevertheless, this value is relatively high and not beneficial to realize a high specific energy. Accordingly, more work needs to be done to improve the electrochemical performance of Li-S batteries under lean electrolyte conditions.

The introduction of additives with small amounts to ether-based electrolytes was found to be an effective way to enhance the performance of Li-S batteries.[383] A major breakthrough was achieved in 2008 when Mikhaylik found that lithium nitrate ($LiNO_3$) can effectively protect the lithium metal anode by forming a stable SEI layer on the surface.[387] To understand the chemical composition of the SEI layer, Aurbach and co-workers systematically studied the surface component of the lithium metal anode in the presence of $LiNO_3$ using Fourier

transform infrared (FTIR) spectra and XPS.[388] It was found that $LiNO_3$ can be reduced by lithium to form Li_xNO_y species, and it can also oxidize sulfides to produce Li_xSO_y species, both of which can passivate the lithium metal surface and thus alleviate the undesirable side reactions between lithium and polysulfides. Owing to its great benefit, $LiNO_3$ additive is adopted in most of the Li-S electrolytes today.

Besides forming protective layer on lithium anode, the addition of suitable additives into electrolytes can also assist to create a protective layer on the cathode surface to retard the out diffusion of polysulfides into electrolytes. For example, Yang et al. found that the addition of pyrrole into the electrolyte can lead to the formation of a barrier layer of polypyrrole on the sulfur cathode via the in situ polymerization process, which can effectively trap the polysulfides and block the out diffusion of polysulfides.[389] As a result, the Li-S cells with 5 wt% pyrrole in the electrolyte exhibited a high discharge capacity of 607 mA h g^{-1} after 300 cycles at 1C.

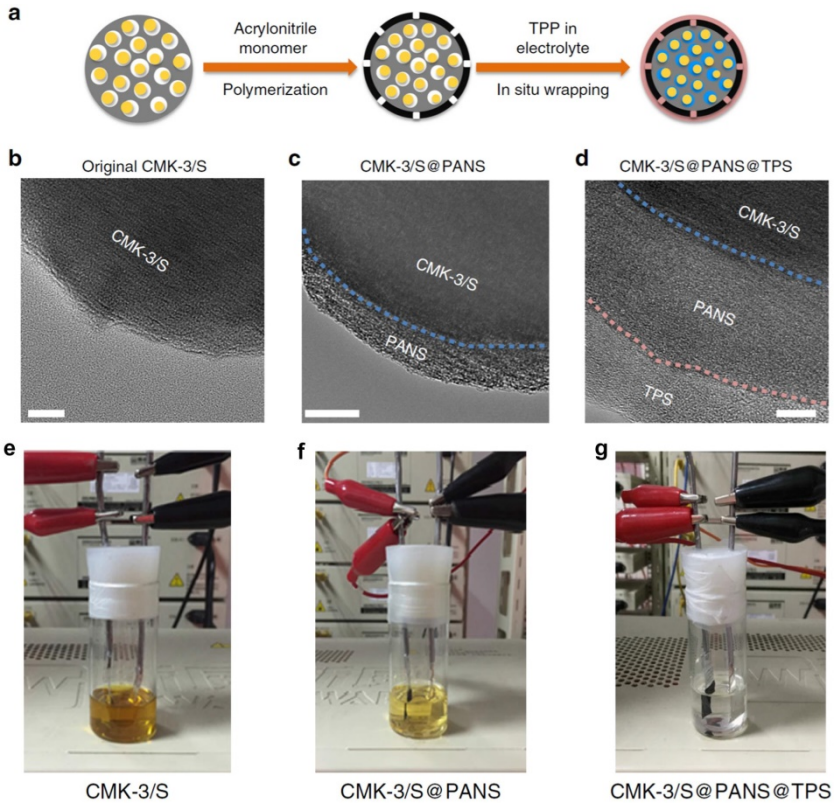

Figure 1.38 (a) Schematic for in situ wrapping a TPS layer on the cathode. TEM images of (b) CMK-3/S, (c) CMK-3/S@PANS and (d) CMK-3/S@PANS@TPS. The scale bars are all 10 nm. Digital photos of glass cells with (e) CMK-3/S, (f) CMK-3/S@PANS and (g) CMK-3/S@PANS@TPS cathodes after 20 cycles at 0.1C. Reproduced from reference[390]. Copyright 2017, Nature Publishing Group.

Chen and co-workers reported that the addition of triphenylphosphine (TPP) into the DOL/DME electrolyte can react with the sulfur intermediates to produce a protective triphenylphosphine sulfide (TPS) layer on the preassembly wrapping surface (**Figure 1.38**).[390] This compact and tight TPS coating layer can allow the transport of lithium ions into the wrapped C/S composite cathode while block the out diffusion of polysulfides. The sealed glass cell with CMK-3/S@PANS@TPS cathode showed colorless feature even after 20 cycles at 0.1C (**Figure 1.38**g), suggesting the polysulfides were effectively confined in the

C/S cathode by the TPS layer. By virtue of this unique structural advantage, the Li-S cell with CMK-3/S@PANS@TPS cathode demonstrated greatly improved Coulombic efficiency and cycle life with an ultralow capacity decay rate of 0.03% per cycle over 1000 cycles at 1C.

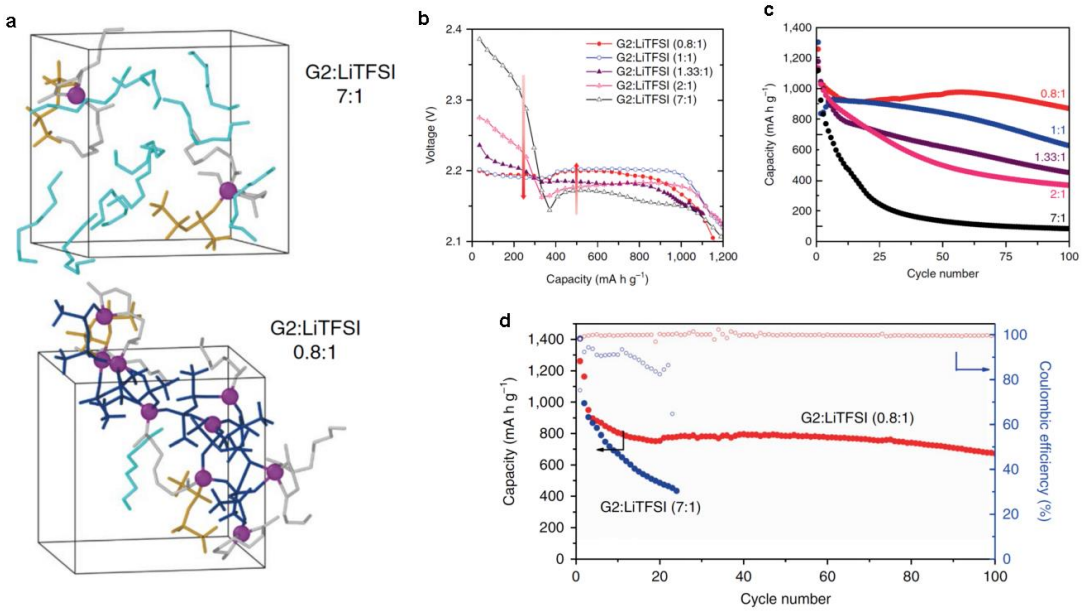

Figure 1.39 (a) Ab initio calculations of the two electrolyte systems with different electrolyte/lithium salt ratios. The purple, cyan, grey, gold and blue color represent Li^+ cations, free diethylene glycol dimethyl ether (G2) molecules, coordinated G2 molecules, contact-ion-pair of $TFSI^-$ anions and aggregates of $TFSI^-$ anions, respectively. The cubic box represents the supercell for the calculated system. (b) Discharge profiles and (c) cycling performance of Li-S cells using G2:LiTFSI electrolytes with different molar ratios. (d) Cycling performances and Coulombic efficiencies of Li-S cells using an low E/S ratio of 5 μL/mg at 0.2C with different G2:LiTFSI electrolytes. Reproduced from reference[391]. Copyright 2018, Nature Publishing Group.

Recently, Nazar's group found that by decreasing the solvent/salt molar ratio in a diethylene glycol dimethyl ether system (G2:LiTFSI), the sulfur reaction pathway transitioned from a dissolution-precipitation route to a quasi-solid state conversion process.[391]

Ab initio calculations suggested that the chain length of G2 was the right dimension to fully wrap around the $TFSI^-$ anions to form an extended 3D network structure at a low solvent/salt molar ratio of 0.8:1 (**Figure 1.39**a). In **Figure 1.39**b, the first discharge plateau decreased upon decreasing G2:LiTFSI and increased in the second stage. The lower first plateau voltage indicates an earlier transformation into low-order polysulfides. Thus the authors deem this a quasi-solid conversion process when decreasing G2:LiTFSI to a molar ratio of 0.8:1. Owing to the effect of sparing solubility, the Li-S cells using G2:LiTFSI with lower molar ratio demonstrated higher capacity retention (**Figure 1.39**c). Moreover, the electrolyte enabled dendrite-free Li plating and showed a 20-fold reduction in parasitic reactions with metallic Li, which largely decreased electrolyte consumption and increased the capacity retention at an ultralow E/S ratio of 5 μL/mg (**Figure 1.39**d). This work provides a new avenue to improve the performance of Li-S batteries by tuning the electrolyte network structure.

1.5.1.2 Carbonate-based electrolytes

Carbonate solvents such as propylene carbonate (PC), ethylene carbonate (EC), diethyl carbonate (DEC) and dimethyl carbonate (DMC) have been widely used in commercial lithium ion battery electrolytes for nearly 30 years due to their high ionic conductivity as well as wide operation voltage and temperature window.[392-395] However, they are incompatible with most of the sulfur cathodes due to the strong nucleophilic reactivity between polysulfides and carbonate solvents,[396] which leads to sudden capacity fading during the initial several cycles.[397, 398] Nevertheless, carbonate-based electrolytes can occasionally work if the sulfur is covalently immobilized on a polymeric composite,[112, 399-404] or strongly

confined in a microporous host material[78, 79, 405-409] or fully encapsulated by a molecular layer deposited coating[395, 410]. The discharge voltage profiles of these cathodes in carbonate electrolytes usually display a continuously decreasing profile instead of two typical discharge plateaus as in the cases of ether electrolytes, indicating the direct reduction of sulfur to insoluble Li_2S_2 or Li_2S without the formation of high-order lithium polysulfides or the polysulfide life is too short to deliver a discharge voltage plateau. This eliminates the undesirable nucleophilic reactions between polysulfide anions with carbonate solvents and the intractable polysulfide shuttle problem in ether based electrolytes can also be excluded. As a result, these cathodes coupled with carbonate electrolytes usually demonstrate much stable cycling performance compared to the conventional sulfur cathodes in ether electrolytes. However, due to the rigorous structure requirements of these cathodes, the sulfur contents (mostly <40% in the whole electrode) are usually very low. In addition, the discharge voltage of these cathodes (normally <2.0V) is not as high as that in the cases of ether electrolytes. These factors can decrease the energy density of a practical Li-S battery in carbonate electrolytes. Therefore, much effort should be done to improve the sulfur active material content in these cathodes and the mechanism during the discharge process in carbonate electrolytes needs further investigated.

1.5.2 Solid-state electrolytes

Instead of using liquid electrolytes, the use of solid electrolytes was believed to be a promising approach to physically block the polysulfide shuttle and lithium dendrite growth in Li-S batteries.[380, 411-414] However, the solid-state electrolytes usually suffer from low ionic

conductivity and large interfacial resistance, limiting their practical applications. The solid electrolytes can be generally sorted into solid polymer electrolytes and inorganic solid electrolytes. In the following, we will discuss some approaches to improve the properties of solid electrolytes for all-solid-state Li-S batteries.

1.5.2.1 Solid polymer electrolytes

Solid polymer electrolytes are normally prepared by dissolving a lithium salt into high-molecule weight polymer host, such as polyethylene oxide (PEO), polyacrylonitrile (PAN), poly(methyl methacrylate) (PMMA), and poly(vinylidenefluoridecohexafluoropropylene) (PVDF-HFP).[367, 415-422] Solid polymer electrolytes have the benefits of good flexibility and high mechanical strength.[415, 417, 423] Among various solid polymer electrolytes, polyethylene oxide (PEO) is most widely used in Li-S batteries.[33] Nevertheless, the ionic conductivities of PEO-based solid polymer electrolytes are relatively low (below 10^{-5} S cm^{-1}) at room temperature, which is difficult to satisfy the practical requirement. Therefore, many efforts have been devoted to increase the ionic conductivity of solid polymer electrolytes. For example, Hicham et al. found that cross-linking of PEO-based solid electrolytes can effectively increase the ionic conductivity.[424] Zhang et al. found that the lithium salt in the solid polymer electrolytes plays a key role in the ionic conductivity and PEO-LiFSI complex shows higher ionic conductivity compared to that of PEO-LiTFSI.[425] Some researchers found that the ionic conductivities of PEO-based solid electrolytes can also be improved by incorporating inorganic fillers, which includes both inactive inorganic particles such as TiO_2[426] and lithium ion conducting

materials such as $Li_7La_3Zr_2O_{12}$[427]. Although the ionic conductivity of the PEO-based solid electrolytes can be improved to some extent through the above methods, the large interfacial resistance between the electrolyte and electrode also limits the electrochemical performance of Li-S batteries. The ball-milling method was found to be an effective strategy to decrease the interfacial resistance between the electrolyte and lithium anode.[428, 429]

1.5.2.2. Inorganic solid electrolytes

Inorganic solid electrolytes that can permselectively allow the transport of lithium ions while physically block the dissolution and diffusion of polysulfides are also used in Li-S batteries.[383] Because of the high mechanical strength of inorganic solid electrolytes, they can also effectively inhibit the formation of lithium dendrites, improving the safety of Li-S batteries. Various inorganic lithium ion conductors such as Li_2S-P_2S_5,[430-434] Li_2S-SiS_2,[435] Li_3PS_4,[436-439] $Li_{1.5}PS_{3.3}$,[440] $Li_7P_{2.9}S_{10.85}Mo_{0.01}$,[441] $Li_7P_{2.9}Mn_{0.1}S_{10.7}I_{0.3}$,[442] $Li_{10}GeP_2S_{12}$,[437, 443] $Li_{3.25}Ge_{0.25}P_{0.75}S_4$,[439] $Li_{1.5}Al_{0.5}Ge_{1.5}(PO_4)_3$,[444, 445] $Li_{1.3}Al_{0.3}Ti_{1.7}(PO_4)_3$,[446, 447] thio-LISICONs,[448, 449] and $LiBH_4$[450-452] have been explored as solid electrolytes for all-solid-state Li-S batteries. To improve the ionic conductivity and decrease the interfacial resistance of the solid elelctrolytes, Hu and co-workers designed an integrated bilayer solid-state framework with controllable thickness and smaller interface resistance (**Figure 1.40**). In this bilayer architecture, the porous layer provides continuous and efficient pathways for lithium ions and electrons transport while integrating high sulfur loading, and the thin dense garnet layer with high mechanical strength blocked the diffusion of

polysulfides and formation of lithium dendrites. This integrated cathode can achieve a high sulfur loading of 7 mg cm^{-2} and demonstrated superior cycling stability.

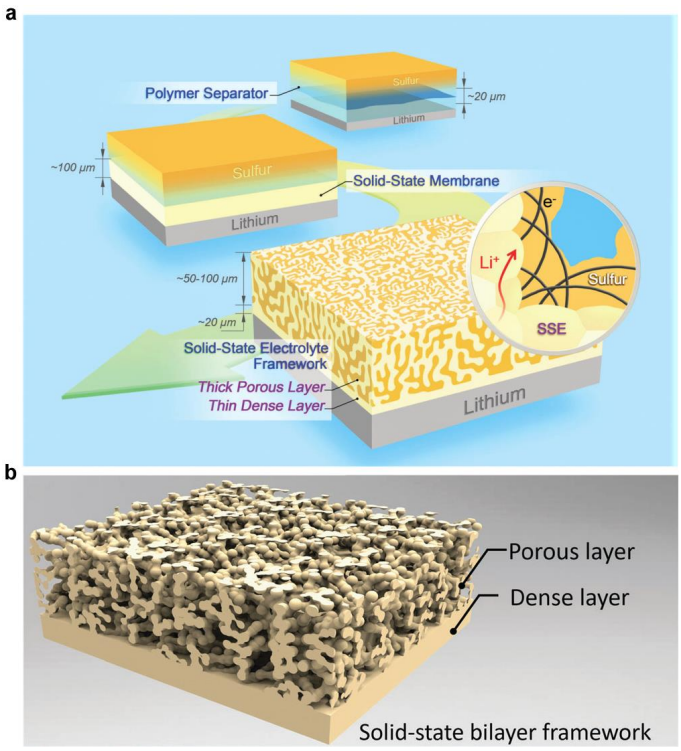

Figure 1.40 Schematic of the garnet bilayer solid-state electrolyte. Reproduced from reference[453]. Copyright 2017, Royal Society of Chemistry.

1.5.3 Gel polymer electrolytes

Gel polymer electrolytes consist of solid polymer electrolytes and plasticizers which combine the advantages of both solid and liquid electrolytes.[402, 454-464] In gel polymer electrolytes, a suitable amount of liquid electrolytes are immobilized by the polymer matrix, thus they show higher ionic conductivity compared to the solid polymer electrolytes as well as afford mechanical strength to block the diffusion of polysulfides and formation of lithium dendrites.[367, 383, 465-474] The polymer matrix are typically based on PEO,[369, 456, 459, 461, 462] PVDF,[458, 463] PVDF-HFP,[460, 475-480] PMMA,[457, 481-483] PVDF-HFP/PMMA,[484, 485]

PAN/PMMA,[486] and PVDF/PEO[487], while the commonly used plasticizers are based on ether solvents. To overcome the solubility of ether solvents for polysulfides as well as safety risks caused by the flammable solvent, ionic liquids have also been employed as attractive plasticizer in gel polymer electrolytes.[479, 486, 488-490] However, increased interfacial resistance between ionic liquid based gel polymer electrolytes and lithium metal anode was also induced at the same time, which led to the large polarization and fast capacity decay.[367, 489]

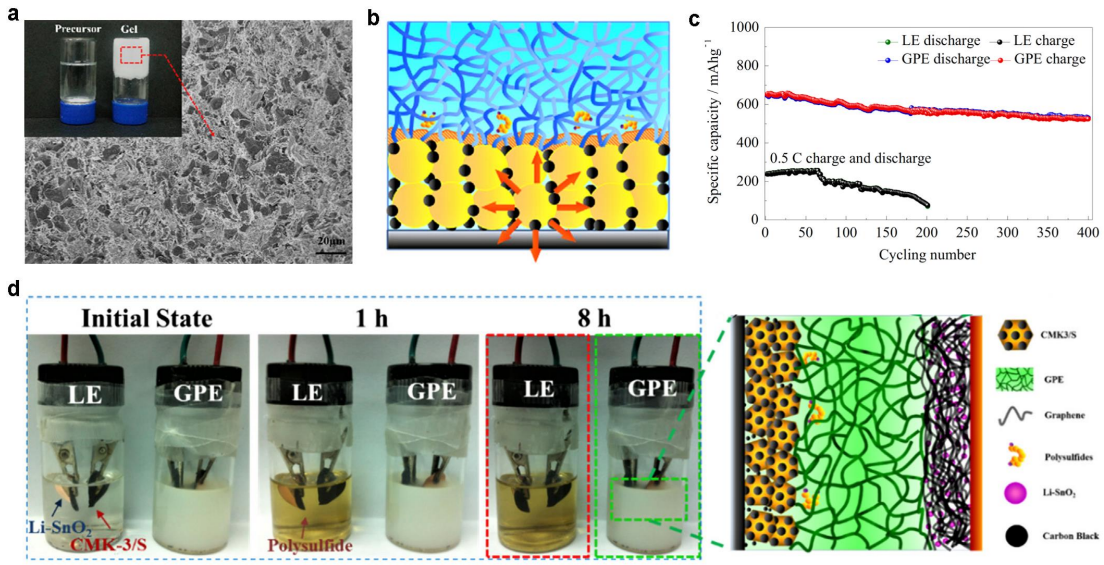

Figure 1.41 (a) SEM image of the PETEA-based gel polymer electrolyte. The inset shows the photographs of the gel electrolyte and its precursor solution. (b) Illustration of the formation of a passivation layer on the sulfur cathode surface. (c) Cycling performances of Li-S cells with PETEA-based gel polymer electrolyte and liquid electrolyte. (a-c) Reproduced from reference[491]. Copyright 2016, Elsevier. (d) Visual glass cells of SnO_2/LE/S and SnO_2/GPE/S. Reproduced from reference[492]. Copyright 2016, Elsevier.

Recently, Kang's group reported a pentaerythritol tetraacrylate (PETEA)-based gel polymer electrolyte with impressive electrochemical performance for Li-S batteries (**Figure 1.41**a).[491] It was believed that a stable passivation layer was formed at the interface between

the gel polymer electrolyte and the sulfur electrode (**Figure 1.41**b), which decreased the interfacial resistance. Even coupled with a bare sulfur cathode, the Li-S cell with the PETEA-based gel polymer electrolyte showed a capacity retention of 81.9% after 400 cycles at 0.5C, which was much higher than that of the liquid electrolyte based Li-S cell (**Figure 1.41**c). This group also combined the PETEA-based gel polymer electrolyte with a SnO_2 anode to make a lithium ion sulfur cell.[492] The visual cells showed that the polysulfides can be easily dissolved into the liquid electrolyte but hardly dissolved into the gel polymer electrolyte (**Figure 1.41**d). A lithium ion sulfur cell with the PETEA-based gel polymer electrolyte and the SnO_2 anode demonstrated impressive electrochemical performance with 82.1% capacity retention after 500 cycles at 1C.

1.6 Lithium metal anode protection in Li-S batteries

Owing to the high solubility and reactivity of lithium polysulfides, the lithium metal anode is vulnerable to be attacked by the polysulfide species, resulting in the shuttle effect and low Coulombic efficiency.[493-495] In addition, the formation of lithium dendrites can cause safety issues of lithium metal-based rechargeable batteries. In this section, we will highlight the strategies to protect lithium metal anode against polysulfide corrosion as well as suppress the lithium dendrite growth in Li-S batteries. The strategies can be classified into two aspects: passivation of the lithium metal surface by a protective layer or hosting metallic Li in a prepared matrix, which will be discussed in the following parts.

1.6.1 Lithium metal interface design

One common strategy to stabilize lithium anode is to create a bifunctional protective layer on lithium metal surface to block lithium polysulfides as well as regulate homogenous lithium ion flux.[28, 494, 495] The construction of protective layers can be classified into in situ method via electrolyte additives and ex situ strategy via building artificial anode/electrolyte interface.

1.6.1.1 Forming intrinsic passivation SEI layer via electrolyte additives

Because of the highly negative electrochemical potential of Li^+/Li, virtually any electrolyte component can be reduced at the Li surface.[26, 392] Accordingly, selecting appropriate electrolyte additives that can decompose, polymerize or adsorb on the Li surface, and thus modifying the physic-chemical properties of the SEI layer against polysulfides is a promising strategy to protect lithium metal anode. A major breakthrough in this area was the discovery of lithium nitrate ($LiNO_3$) as a powerful electrolyte additive by Mikhaylik in 2008.[387] It was found that the addition of $LiNO_3$ can effectively alleviate the shuttle effect of polysulfides and improve the performance of Li-S batteries by promoting the formation of a stable SEI layer on the lithium metal surface.

Besides $LiNO_3$, some other additives were also developed to improve the performance of Li-S batteries. Xiong and co-workers reported that the addition of (lithium bis(oxalato) borate) LiBOB in the liquid electrolyte can passivate the lithium surface to inhibit its side reaction with polysulfides, thus a higher discharge capacity and better cycling performance were realized.[496] Liang and co-workers reported the use of phosphorus pentasulfide (P_2S_5) as an additive in electrolyte can not only passivate the lithium metal surface against polysulfides,

but also act as a redox mediator to promote the dissolution of Li_2S and thus alleviate the capacity loss caused by the precipitation of Li_2S.[497] Yushin and co-workers reported that the lithium iodide (LiI) additive in electrolyte induced a protective layer on both the Li_2S based cathode and lithium anode, which inhibited the dissolution of polysulfides in the cathode side and reduction of polysulfides on the anode side.[498] In addition, the overpotential of the first charge was reduced and improved cycling performance was achieved with the LiI additive. This indicates that the LiI additive can also act as a redox mediator to propel Li_2S oxidation. Besides LiI, Zhao and co-workers found that indium triiodide (InI_3) additive can also function as a redox mediator to reduce the activation barrier of Li_2S cathode as well as passivate the lithium metal surface against polysulfide corrosion.[499] Armand and co-workers reported the use of lithium azide (LiN_3) as an electrolyte additive to improve the performance of all solid state Li-S batteries.[45] LiN_3 can promote the formation of a uniform and highly ionic conductive passivation layer on lithium metal to inhibit polysulfide corrosion and lithium dendrite growth. It significantly improved the cycling performance and Coulombic efficiency of the all solid state Li-S batteries, even outperforming the state-of-the-art $LiNO_3$ additive.

1.6.1.2 Building artificial anode/electrolyte interface

Besides constructing an intrinsic SEI passivation layer on lithium metal anode through electrolyte additives, another strategy is to build a protective layer on the lithium metal anode before battery assembly, which provides more options to manipulate the components of the protective layer and control the reaction conditions.[495] Since this protective layer built outside the battery owns similar properties compared to the intrinsic SEI layer, they are also

described as “artificial SEI”.[500] The fabrication methods of these artificial SEI mainly involve two strategies: direct surface coating or chemically reacting with lithium foil.[500] In this section, some typical “artificial SEI” fabricated through these two strategies will be discussed.

In 2014, Wen and co-workers reported that ex situ formed conductive polymers on lithium metal anodes such as poly(3,4-ethylenedioxythiophene)-co-poly(ethylene glycol) (PEDOT-co-PEG) can effectively inhibit the corrosion reaction between polysulfides and lithium anodes as well as restrain the growth of lithium dendrites.[501] The lithium metal was directly immersed into the polymer solution for several times to obtain a polymer coated layer on the metal surface with a thickness of about 10 μm. The Li-S battery with the polymer-coated lithium metal anode exhibited much improved cycling performance and higher Coulombic efficiency compared to that of the unmodified one, suggesting the polysulfide shuttle effect was effectively restricted. In addition, the SEM image of the lithium anode without polymer-coated layer showed serious dendrite growth and corrosion after 100 cycles, while the lithium anode with polymer-coated layer showed very smooth morphology. This indicates that the polymer-coated layer on lithium anode can effectively inhibit the reaction between lithium metal and polysulfides as well as suppress the growth of lithium dendrites, which can be attributed to the physical protection and high mechanical properties of the robust polymer layer on the lithium metal surface.

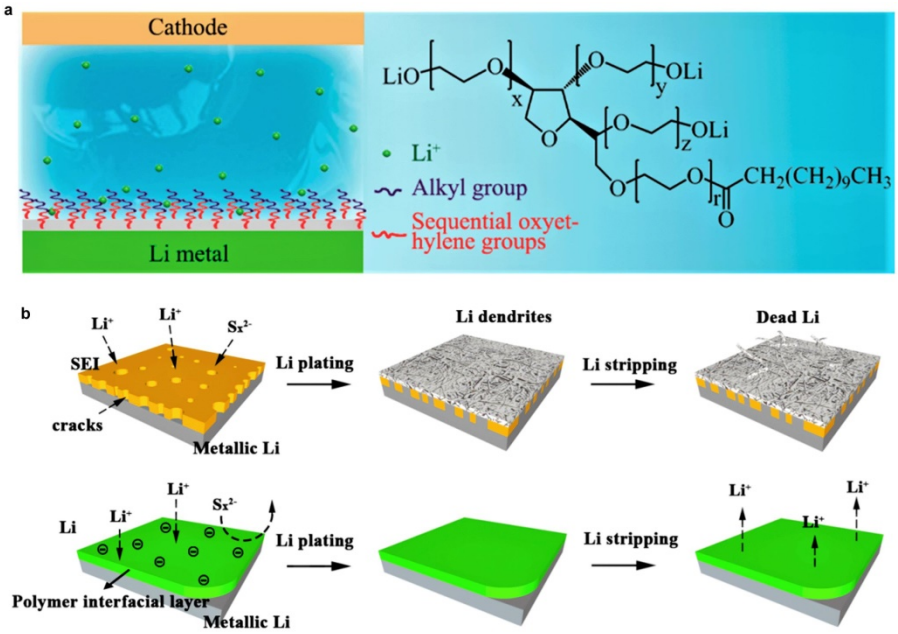

Figure 1.42 (a) Schematic of tween polymer-grafted lithium metal. (b) Schematic of lithium plating and stripping process on bare lithium metal and tween polymer-grafted lithium metal. Reproduced from reference[502]. Copyright 2018, American Chemical Society.

Yan and co-workers reported that the tween polymer can be grafted on the lithium metal surface to protect the lithium metal (**Figure 1.42**).[502] It was found that the sequential oxyethylene groups improved the lithium ion conductivity and the compatibility of the lithium metal/electrolyte interface, while the alkyl chains refused polysulfides from going near the lithium metal surface. The tween polymer layer can also effectively inhibit the lithium dendrite growth during charge-discharge process. When tween-grafted Li was used in an all solid state Li-S battery, a high reversible capacity of 1051 mA h g^{-1} was attained at 0.2C and stable cycling performance over 500 cycles at 2C with a low capacity decay rate of 0.058% per cycle was realized.

Besides polymer layer, inorganics have also been coated on the lithium metal surface against dissolved polysulfides. For example, a porous Al_2O_3 layer was coated on the lithium

metal surface through a spin-coating strategy for Li-S batteries by Gao and co-workers.[503] The Al_2O_3 coated lithium metal can effectively improve the performance of Li-S batteries compared to the uncoated one. Additionally, the SEM images of the cycled cells indicated that the Al_2O_3 coating layer can facilitate the homogeneous Li deposition on the anode due to the even distribution of lithium ion flux via the Al_2O_3 coating layer. Moreover, the authors also found that the thickness of Al_2O_3 layer was vital to the electrochemical performance of Li-S batteries and a moderate coating of 0.58 mg cm^{-2} showed the best performance. When the coating amount was too low (0.23 mg cm^{-2}), the Al_2O_3 layer cannot effectively restrain the direct contact between polysulfides and lithium metal. If the coating amount was too high (0.73 mg cm^{-2}), the thick Al_2O_3 layer can block the penetration of electrolyte and diffusion of lithium ions.

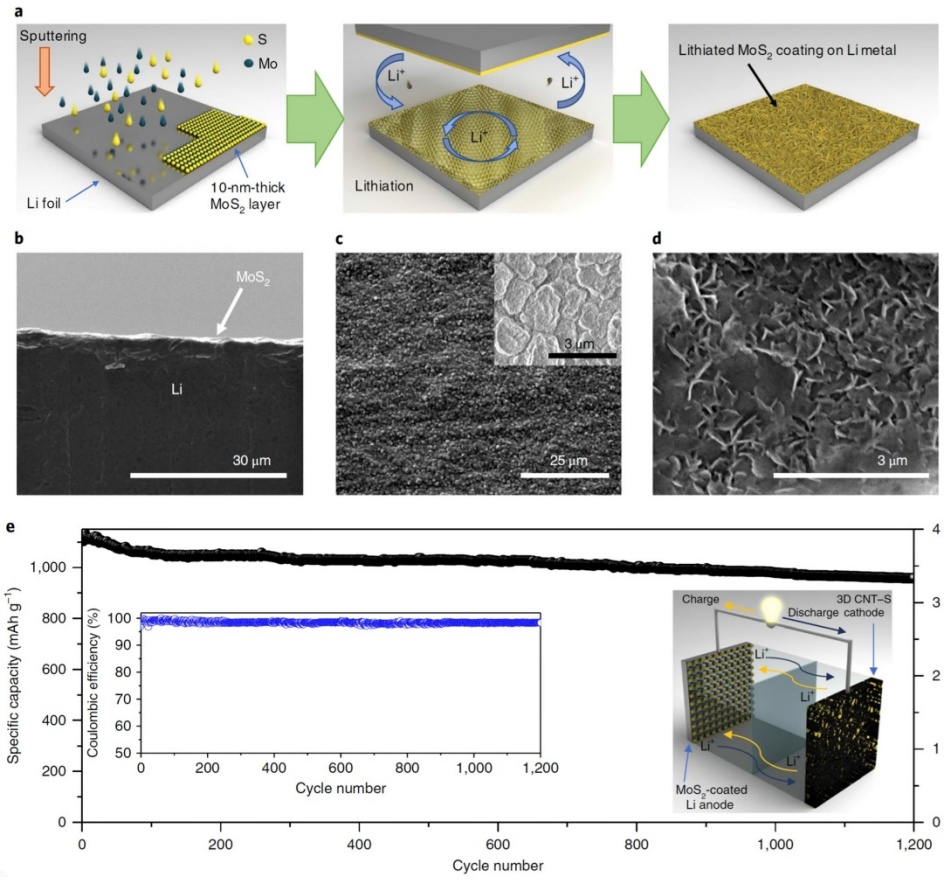

Figure 1.43 (a) a) Schematic of the fabrication process of MoS_2-coated Li metal anode via the sputtering and subsequent lithiation. (b) Side and (c) top view SEM images of as-deposited MoS_2 on lithium metal. The inset in c shows the enlarged image. (d) Top-view SEM image of lithiated MoS_2 on lithium metal surface. (e) Cycling performance of a Li-S battery with MoS_2-coated Li metal as anode and CNT-sulfur as cathode for 1200 cycles at 0.5C. The inset illustrates the configurations of the as-assembled battery. Reproduced from reference[504]. Copyright 2018, Nature Publishing Group.

To avoid compromising the energy density of the battery, the protective layer on lithium metal should be as thin as possible. To this end, an ultrathin layer of MoS_2 with a thickness of only 10 nm was coated on the lithium foil via the sputtering and subsequent lithiation process (**Figure 1.43**).[504] The MoS_2 layer showed tight adhesion to the surface of lithium metal and facilitated uniform flow of lithium ions into and out of bulk lithium metal. Thus, the symmetric MoS_2-coated lithium metal cell exhibited stable lithium plating and stripping with low voltage hysteresis compared to that using bare lithium metal. When MoS_2-coated lithium metal anode was coupled with carbon nanotube-sulfur cathode, a high specific capacity of 940 mA h g^1 after 1200 cycles was achieved at 0.5C, corresponding to an average capacity decay rate of only 0.013% per cycle.

Besides, some in situ formed protective layers on lithium metal show more homogeneous and compatible interfaces. Wen and co-workers fabricated a layer of Li_3N on the surface of lithium metal via the in situ reaction between Li and N_2.[505] The in situ formed Li_3N protective layer had a conformal coating on the lithium metal, thus can act as an effective shield against polysulfides. In addition, the superior ionic conductivity of Li_3N (10^{-3} S cm^{-1}) can allow fast lithium ion transport. When the Li_3N protected lithium metal was used in the Li-S batteries, a

high average Coulombic efficiency of 92.3% over 500 cycles was obtained even without the addition of $LiNO_3$ in the electrolyte, which was much higher than the case of unprotected one (about 80%). SEM images of the cycled batteries also showed a much thinner Li_2S_2/Li_2S layer of about 10 μm in the Li_3N protected lithium metal surface compared to a thicker surface of Li_2S_2/Li_2S layer of 100 μm in the pristine lithium metal, which indicated the corrosive reaction between lithium metal and polysulfides was effectively suppressed.

1.6.2 Lithium metal host design

Due to the "hostless" nature of pristine 2D Li foil, lithium metal anodes suffer from intrinsic volume change upon cycling, which leads to the poor mechanical stability of the SEI layer and low utilization of active materials.[506] Accordingly, it is necessary to design a 3D matrix with lithiophilic property to host metallic Li. The fabrication methods of infiltrating Li into a 3D host can be classified into melt infusion strategy and electrodeposition approach using sacrificing cells.

1.6.2.1 Hosts with pre-stored lithium via molten infusion

In 2016, Cui's group pioneered the work of using 3D layered rGO with nanoscale gaps to host metallic Li via the molten infusion strategy (**Figure 1.44**a-d).[507] GO films were first prepared via the filtration method. Then the sparked rGO film with nanoscale gaps was obtained by partially putting GO film into contact with molten Li. Finally, the layered Li-rGO film was fabricated by putting the edge of the rGO film into contact with molten Li, during which the molten Li was infused into the nanogaps of the layered rGO via capillary force. This layered Li-rGO has several benefits: first, the layered rGO host can minimize the

volume change by dividing dense Li into smaller domains; second, the increased accessible Li active sites can reduce the effective current density, thus homogenizing the lithium ion flux and further inhibiting the dendrite growth.

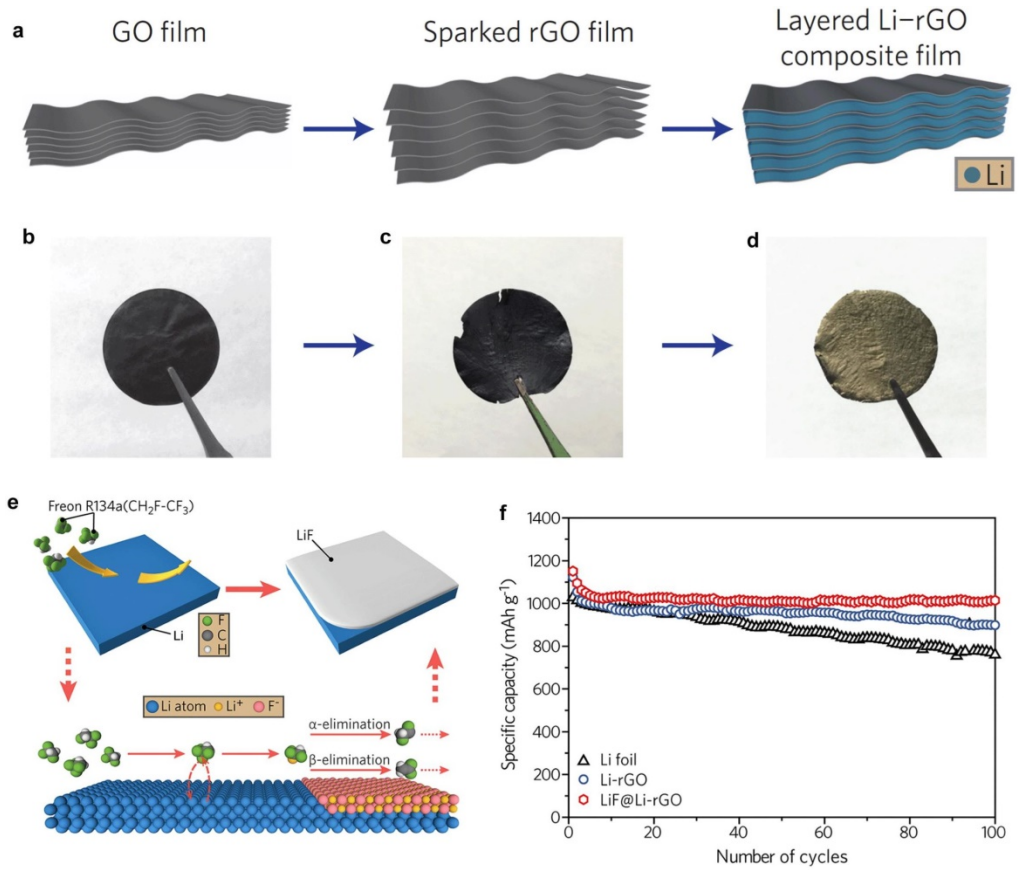

Figure 1.44 (a) Schematic of the fabrication process for layered Li-rGO film. (b) Digital photos of (b) GO film, (c) sparked rGO film and d) layered Li-rGO film. (a-d) Reproduced from reference[507]. Copyright 2016 Nature Publishing Group. (e) Schematic of the lithium metal coated by a thin layer of LiF. (f) Cycling performances of Li-S prototype cells with Li foil, Li-rGO and LiF-coated Li-rGO as anodes. (e,f) Reproduced from reference[508]. Copyright 2017, American Chemical Society.

To eliminate the corrosion of Li by polysulfides, the Cui group further coated a thin LiF layer on the 3D Li-rGO foil through the in situ reaction between lithium and commercial Freon R134a (**Figure 1.44**e).[508] The solid-gas interfacial reaction showed well-controlled

reactivity and excellent permeability that enabled a uniform and conformal coating of LiF layer on the lithium surface. When LiF-protected Li-rGO was used in the Li-S battery, improved cycling performance was achieved compared to the unprotected one (**Figure 1.44**f).

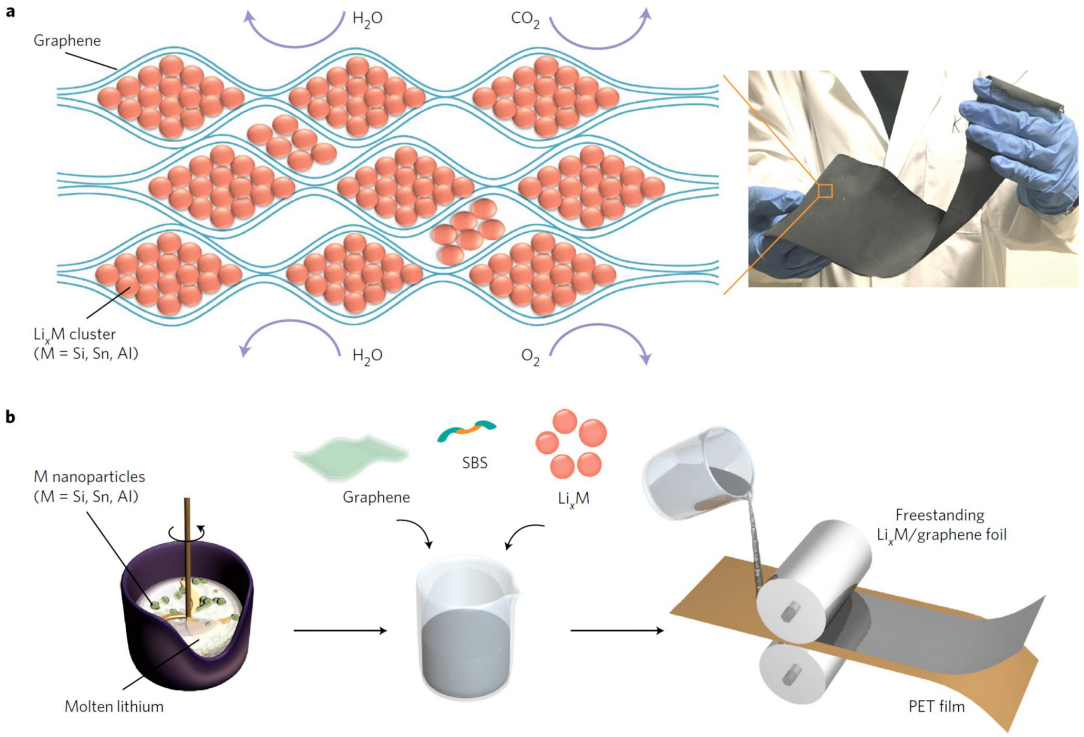

Figure 1.45 (a) Schematic of the microstructure of Li_xM/graphene film. b) Schematic of the fabrication process for Li_xM/graphene film. Reproduced from reference[509]. Copyright 2017, Nature Publishing Group.

In order to realize the large-scale application of lithium metal based anodes, Cui's group further developed an air-stable and self-standing lithium alloy/graphene foil as anode for Li-S batteries (**Figure 1.45**a).[509] The fabrication process of Li_xM/graphene foil (M=Si, Sn, Al) is illustrated in **Figure 1.45**b. Thin graphene layers were coated on both sides of the Li_xM/graphene film to insure that the Li_xM nanoparticles on the surface were also protected

by the graphene layers. Owing to the conformal coating of Li_xSi by graphene layers, the large Li_xSi/graphene foil can be stable in air conditions, which is beneficial for large-scale production. When Li_xSi/graphene foil was used as anodes for Li-S batteries, much improved cycling performance was achieved compared to that with the pristine Li foil. XPS analysis was further performed on the cycled anodes. It was found that much lower Li_2S_2/Li_2S peaks were detected on the cycled Li_xSi/graphene foil compared to that of pristine Li foil. This suggests that graphene sheets can effectively alleviate the polysulfide shuttle and Li_2S_2/Li_2S deposition on the anodes.

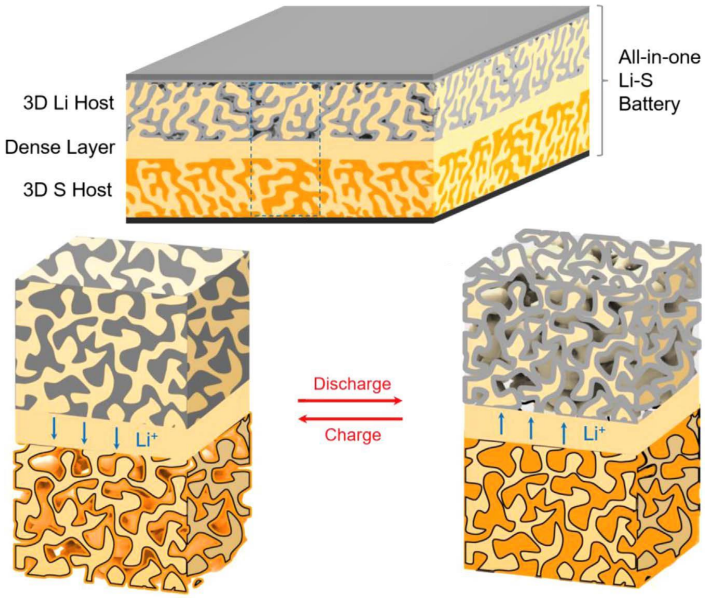

Figure 1.46 Schematic of an all-in-one solid-state Li-S battery based on trilayer garnet electrolyte. Reproduced from reference[510]. Copyright 2018, Elsevier.

Recently, Hu's group designed an all-in-one Li-S battery enabled by a porous-dense-porous trilayer garnet electrolyte (**Figure 1.46**).[510] Both lithium metal anode and sulfur cathode were melt-diffusion into the solid and porous garnet framework, while the thin dense ceramic electrolyte acted as a separator. Owing to the unique all solid-state

frameworks, the polysulfide shuttle and lithium dendrite growth can be effectively eliminated. As a result, the all-in-one solid-state Li-S battery achieved a high reversible capacity of over 1200 mA h g^{-1} with a Coulombic efficiency of nearly 100%.

1.6.2.2 Hosts without pre-stored lithium

This type of host structures can also be regarded as three-dimensional current collectors. In this case, lithium metal is deposited into a well-designed 3D high surface area scaffold instead of planar Li or Cu foils. For example, Wu's group reported the use of cobalt-embedded N-doped porous carbon nanosheets (Co/N-PCNSs) as a two-in-one host for both the sulfur cathode and lithium metal anode in Li-S batteries.[511] Li@Co/N-PCNSs anodes were prepared by pre-plating a certain amount of metallic Li onto the Co/N-PCNSs coated Cu foil and S@Co/N-PCNSs cathodes were prepared via the melt-diffusion strategy. After coupling the Li@Co/N-PCNSs anode with the S@Co/N-PCNSs cathode, the full Li-S battery exhibited superior cycling performance and stable Coulombic efficiency.

Hu and co-workers reported the use of 3D hierarchically and continuously porous nickel photonic crystal (NPC) as a dual host for both sulfur cathode and lithium anode (**Figure 1.47**a).[512] PS opal template was first synthesized by the self-assembly of PS spheres on a tungsten foil. Metallic nickel was then electrodeposited into the void space of PS opal template. After removing the opal template by immersing PS@Ni into the toluene, the 3D hierarchical porous NPC was obtained. Finally, sulfur and metallic Li were respectively loaded into the nanopores of NPC to fabricate the 3D NPC@S cathode and 3D NPC@Li anode. The conductive 3D NPC network can not only provide efficient electron and lithium

ion transport to facilitate the redox reaction kinetics in the cathode, but also inhibit the lithium dendrite growth and volume change in the anode. As a result, 3D NPC@Li/3D NPC@S full cell exhibited improved rate performance and cycling performance compared to the 3D NPC@S/Li half-cell. The use of two-in-one host in Li-S batteries is of wide interests and there are some other reports. Tao's group used the rice husk derived porous carbon as host for both lithium anode and sulfur cathode.[513] Zhu and co-workers developed nitrogen-doped mesoporous honeycomb-like carbon spheres to simultaneously boost the performance of sulfur cathode and Li anode.[514]

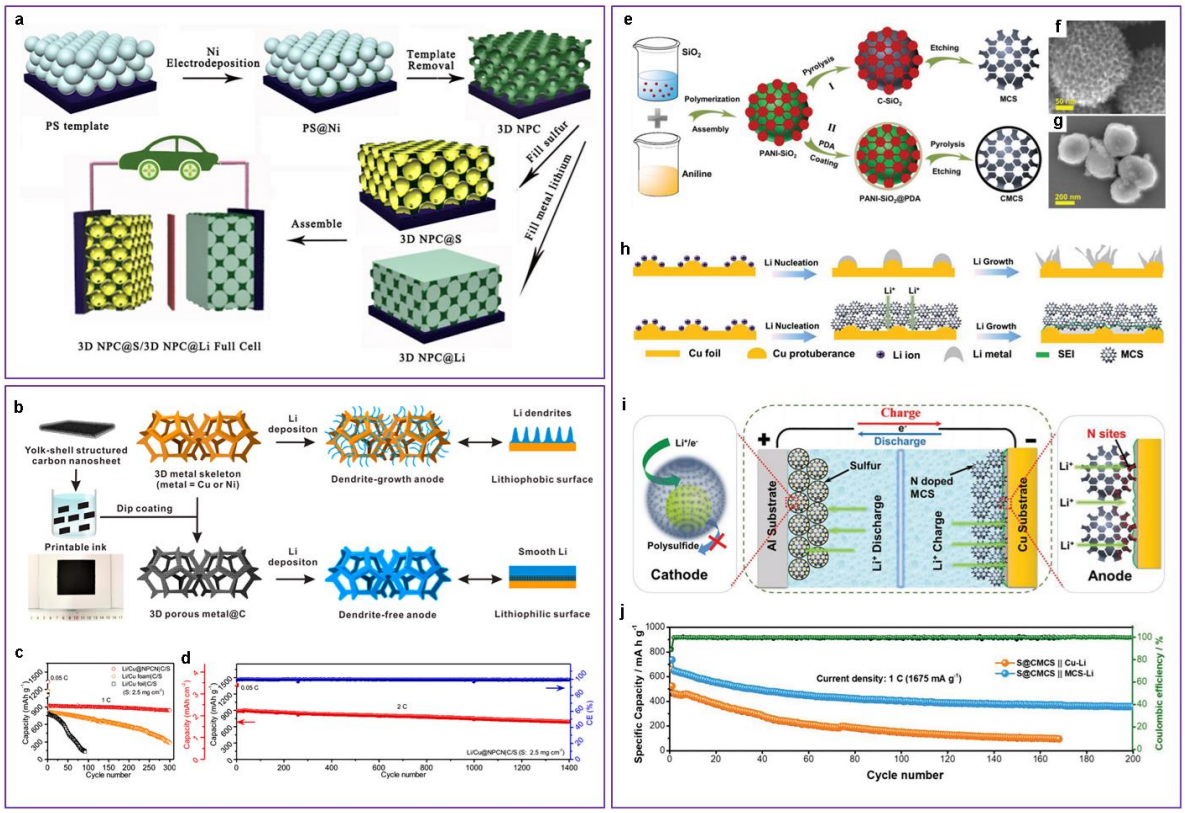

Figure 1.47 (a) Schematic of the fabrication process for 3D NPC@S/3D NPC@Li full cell. Reproduced from reference[512]. Copyright 2018, Wiley-VCH. (b) Schematic for the fabrication of dendrite-free lithium anode by designing NPCN-wrapped 3D metal foam as the current collector. (c) Cycling performances of Li/Cu foil|C/S, Li/Cu foam|C/S, and Li/Cu@NPCN|C/S full cells at 1C. (d) Cycling performance of Li/Cu@NPCN|C/S full cell at

2C. (b-d) Reproduced from reference[515]. Copyright 2019, American Chemical Society. (e) Schematic of the synthesis process MCS and CMCS. SEM images of f) MCS and (g) CMCS. h) Schematic of lithium deposition on Cu foil directly and through MCS. (i) Schematic of the Li-S full cell with S@CMCS as cathode and Li@MCS as anode. (j) Cycling performances of S@CMCS cathodes coupled with Li@MCS and Li@Cu anodes respectively at 1C. e-j) Reproduced from reference[514]. Copyright 2019, Wiley-VCH.

Recently, Zheng and co-workers designed a 3D lithiophilic current collector by modifying 3D Cu foam with yolk-shell structured N-doped porous carbon nanosheets (NPCN) (**Figure 1.47**b).[515] The Li/Cu@NPCN anode was prepared by pre-plating a certain amount of metallic Li onto the NPCN@Cu foam. After pairing the Li/Cu@NPCN anode with a C/S cathode, the resulted Li-S full cell demonstrated remarkable cycling stability (**Figure 1.47**c,d). Zhu's group designed a kind of bifunctional and tunable mesoporous carbon spheres (MCS) that simultaneously improve the performance of sulfur cathode and lithium anode (**Figure 1.47**e-i).[514] Owing to its honeycomb structure with high surface area and abundance of nitrogen sites, the MCS homogenize the lithium ion flux and inhibit the lithium dendrite growth. Upon covering one layer of amorphous carbon on the MCS (CMCS), the obtained carbon cages can encapsulate sulfur inside and reduce the polysulfide shuttle (**Figure 1.47**e,g), which can enhance the cycling performance of Li-S batteries. As a result, the full Li-S battery assembled with S@CMCS as cathode and Li@MCS/Cu as anode exhibited much higher capacity compared to the cell with Li@Cu as anode and S@CMCS as cathode (**Figure 1.47**j).

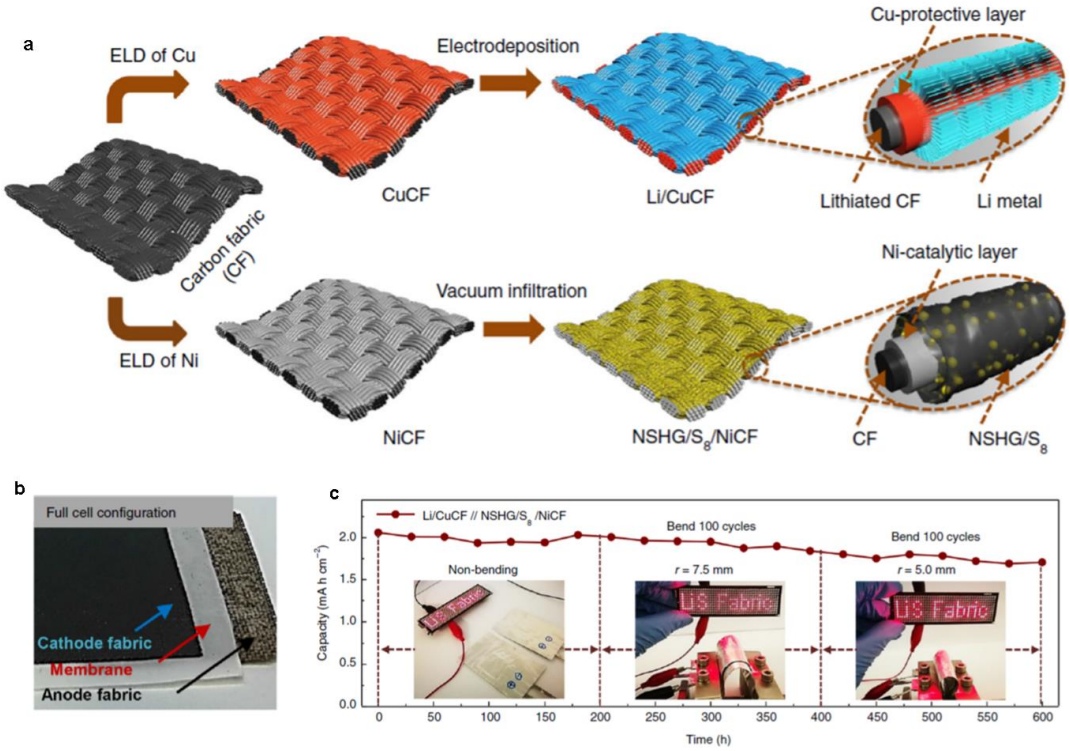

Figure 1.48 (a) Schematic of the fabrication process for Cu-coated and Ni-coated carbon fabrics as hosts for lithium and sulfur, respectively. (b) Photograph of the inner configuration of a Li-S full battery. (c) Cycling performance of Li-S fabric full cells under non-bending and bending conditions. Reproduced from reference[516]. Copyright 2018, Nature Publishing Group.

Zheng's group reported the use of Cu-coated and Ni-coated carbon fabrics as freestanding hosts for lithium and sulfur, respectively (**Figure 1.48**a).[516] To achieve this, a certain amount of lithium metal was electrochemically deposited on the Cu-coated carbon fabric (CuCF) to form the Li/CuCF anode. On the other hand, a slurry mixture containing S_8, nitrogen and sulfur co-doped graphene (NSHG), super P was coated on the NiCF to yield the NSHG/S_8/NiCF cathode. Finally, the two pieces of fabric electrodes were assembled with a Celgard membrane to produce a soft-package Li-S full cell (**Figure 1.48**b). The carbon fabrics can not only endow mechanical flexibility of the electrodes but also effectively reduce

the local current density of the electrodes. The Cu coating on the anode side renders uniform lithium plating and stripping without dendrite formation, while the Ni coating on the cathode side efficiently catalyze the polysulfide conversion. As a result, the soft Li-S fabric full cell showed stable cycling performance over 600 cycles with high areal sulfur loading (**Figure 1.48**c), indicating potential for practical applications.

Chapter 2 General Experimental Methods and Characterizations

2.1 Overview

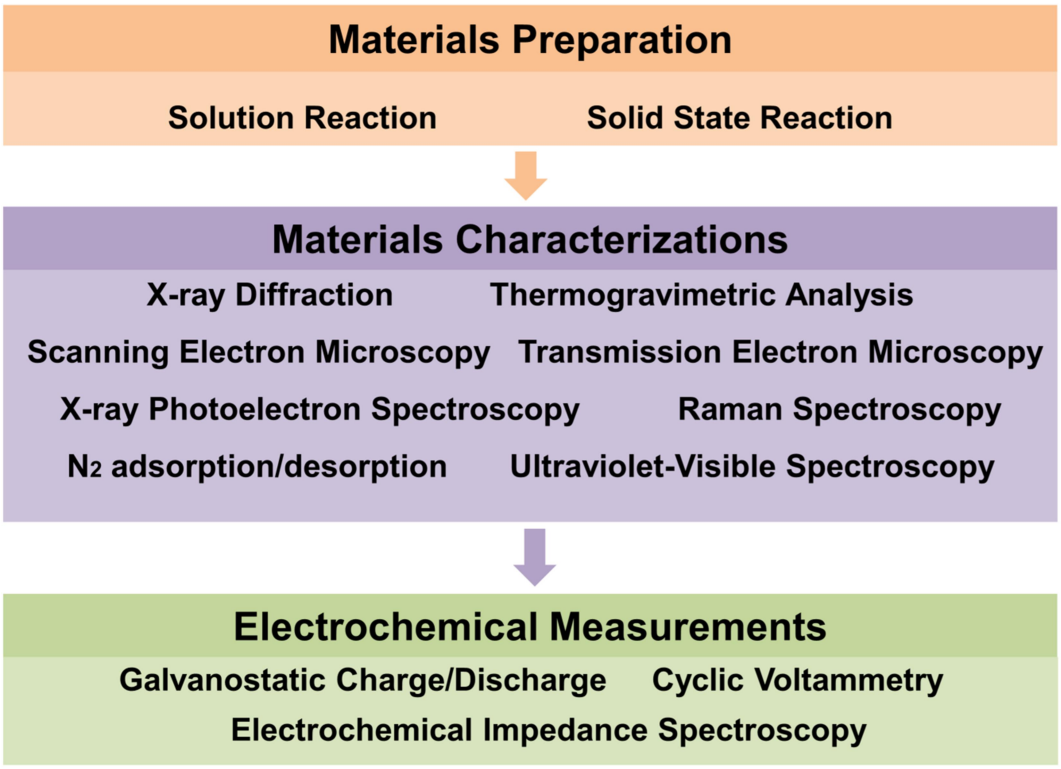

Figure 2.1 Framework of the experiments

Figure 2.1 presents the process of application of nanomaterials for battery applications, which mainly includes three steps:

(i) Design and synthesis of nanomaterials by solution reaction, solid reaction or chemical vapor deposition method. All chemicals and materials used in this thesis are list below in **Table 2.1**.

(ii) Characterization of the morphology and physical properties of the as-synthesized materials by using different electron microscopes and spectroscopy tools, such as Scanning Electron Microscopy (SEM), Transmission Electron Microscopy (TEM), X-ray Diffraction

(XRD), Thermogravimetric Analysis (TGA), X-ray Photoelectron Spectroscopy (XPS), Raman Spectroscopy, N_2 adsorption/desorption and Ultraviolet-Visible Spectroscopy.

(iii) Test the electrochemical performance of the as-synthesized materials by Galvanostatic Charge/Discharge measurements, Cyclic Voltammetry and Electrochemical Impedance Spectroscopy.

Table 2.1 Chemicals/materials used in the thesis

Chemicals	Formular	Purity	Supplier
Titanium(IV) oxide	TiO_2	99.5%	Sigma-Aldrich
Styrene	$C_6H_5CH=CH_2$	99%	Sigma-Aldrich
Potassium persulfate	$K_2S_2O_8$	99%	Sigma-Aldrich
Sodium dodecyl sulfate	$CH_3(CH_2)_{11}OSO_3Na$	98.5%	Sigma-Aldrich
Sulfur	S	99%	Sigma-Aldrich
Carbon disulfide	CS_2	99%	Sigma-Aldrich
Lithium sulfide	Li_2S	99.98%	Sigma-Aldrich
1,2-Dimethoxyethane	$CH_3OCH_2CH_2OCH_3$	99.5%	Sigma-Aldrich
1,3-Dioxolane	$C_3H_6O_2$	99%	Sigma-Aldrich
Lithium nitrate	$LiNO_3$	99.99%	Sigma-Aldrich
Potassium hexacyanoferrate(III)	$K_3Fe(CN)_6$	99%	Sigma-Aldrich
Cobalt nitrate hexahydrate	$Co(NO_3)_2 \cdot 6H_2O$	98%	Sigma-Aldrich
Sodium citrate	$HOC(COONa)(CH_2COOH)_2$	99.5%	Sigma-Aldrich
Sodium hypophosphite	$NaPH_2O_2$	98%	Sigma-Aldrich

Carbon black	C	100%	Sigma-Aldrich
Polyvinylidene fluoride	$(CH_2CF_2)_n$	-	Sigma-Aldrich
N-methylpyrrolidone	C_5H_9NO	99.5%	Sigma-Aldrich
Ethanol	CH_3CH_2OH	95%	Sigma-Aldrich
LiTFSI	$CF_3SO_2NLiSO_2CF_3$	99%	Sigma-Aldrich
Graphite	C	75%	Sigma-Aldrich
Lithium foil	Li	99.99%	Hohsen Corparation

2.2 Materials preparation

2.2.1 Solution reaction

Solution based reaction is the most widely used method for the preparation of uniform nanocrystals. It utilizes water or solvent as the reaction medium which can enable the uniform mixing of precursors. In this thesis, solution reaction method is used to prepare TiO_2 nanotubes and Prussian blue analogue nanocube precursors.

2.2.2 Solid state reaction

The solid state reaction is the widely used method for the preparation of polycrystalline solids by simply mixing of the solid precursor materials. In order to speed the reaction kinetics and enable the reaction process more adequate, the solid reaction normally requires a high temperature than 500 ^{o}C. In this thesis, solid state reaction is used to prepare porous TiO-Graphene composite and Co-Fe-P nanocubes.

2.3 Materials characterizations

2.3.1 X-ray Diffraction

X-ray Diffraction is a very powerful method for the determination of materials' crystal structures. The XRD rely on the Bragg's Law ($n\lambda=2d$ sin θ). This law connects the relationship between the wavelength of electromagnetic radiation, diffraction angle and lattice spacing of a crystal material. The crystal phase of the materials can be identified by using the standard JCPDS cards. The XRD measurements in this thesis are performed on a Bruker D8 Discover XRD instrument.

2.3.2 Thermogravimetric analysis

Thermogravimetric analysis is a method of thermal analysis to measure the mass of sample when increasing the temperature at a constant increasing rate. It can provide the physical and chemical properties of the materials. It is a useful tool to characterize the decomposition characteristic of a material. This measurement usually performs in air or nitrogen atmosphere. In this thesis, we mainly use TGA to determine the sulfur content in the cathodes by increasing temperature to 500 °C at 10 °C/min under nitrogen atmosphere. The TGA data in this thesis was recorded on a TG-DTA (SDT 2960) system.

2.3.3 Scanning electron microscope

Scanning electron microscope (SEM) is a type of electron microscopy that relies on a focused beam of electrons to scan the surface of the sample to produced images. Compared to light microscope using visible light, SEM can have much higher magnification. SEM is a useful

tool to characterize the 3D microstructure of the materials. An energy dispersive X-ray spectrometer (EDS) is connected with the SEM to determine the qualitative and quantitative elemental information of the materials. The SEM and EDS are characterized on field-emission electron microscopy (FESEM, Zeiss Supra 55VP) and electron microscopy (Zeiss Evo SEM).

2.3.4 Transmission electron microscope

Transmission electron microscopy is a microscopy technique that relies on a beam of electrons to transmit through the specimen to form the image. The specimen is usually a piece of ultrathin solids with thickness less than 100 nm or a suspension on the grid. The image is formed through the interaction of the electrons with the specimen when a beam electrons transmit through the sample. TEM has much higher resolution than the light microscope due to the much smaller de Broglie wavelength of electrons. TEM also usually has higher magnification than SEM. In this thesis, the morphology and chemical composition of the samples were characterized by transmission electron microscopy (TEM, Model JEM2010, JEOL).

2.3.5 X-ray photoelectron spectroscopy

X-ray photoelectron spectroscopy (XPS) is a quantitative spectroscopic technique which relies on the photoelectric effect. It can not only identify the composition of a material but also the chemical state. XPS works by irradiating a sample with a beam of X-rays, so it can only obtain the surface properties of a material. XPS technique is widely used in the area of materials, chemistry and physics. In this thesis, XPS was performed on an ESCALAB250Xi

(Thermo Scientific, UK) equipped with monochromated Al K alpha (energy 1486.68 eV).

2.3.6 Raman spectroscopy

Raman spectroscopy is often used to study the molecule vibrations and crystal structures. It works on irradiating a sample with a laser light source. Raman spectroscopy is widely used to determine the properties of graphene based materials, such as the defects and layers. In this thesis, Raman spectra were collected from a Renishaw inVia Raman spectrometer system (Gloucestershire, UK) equipped with a Leica DMLB microscope (Wetzlar, Germany) and a Renishaw He-Ne laser source producing 17 mW at 633 nm.

2.3.7 N_2 adsorption/desorption

The N_2 adsorption/desorption method is a useful tool to determine the specific surface area, pore size and pore volume of the as-prepared samples. The sample was dried in nitrogen for 24h before the measurement. The Brunauer-Emmet-Teller (BET) surface area and pore information were characterized on a Micromeritics 3 Flex analyzer using physical adsorption/desorption of nitrogen gas at the liquid-nitrogen temperature. The calculation is based on the Barret-Joyner-Halenda (BJH) method.

2.3.8 Ultraviolet-visible spectroscopy

Ultraviolet-visible spectroscopy refers to the adsorption or reflectance spectroscopy in the range of ultraviolet and visible light. Samples containing bonding and non-bonding electrons absorb energy from ultraviolet or visible light to excite their electrons to higher molecule orbitals. This technique is widely used in the field of analytic chemistry. In this thesis,

Ultraviolet-visible spectroscopy was used to study the concentration of Li_2S_6 in the adsorption measurements. The Ultraviolet-visible spectroscopy was performed on a Carry 300 UV/vis spectrophotometer.

2.4 Electrochemical measurements

2.4.1 Cell assemble

The working electrode was made by blending and grinding sulfur or the composite material, carbon black and polyvinylidene fluoride (PVDF) with the weight ratio of 8:1:1 in N-methylpyrrolidone, then the homogeneous slurry was casted on the Al foil and dried at 55 °C overnight under vacuum. The electrolyte was 1 M of lithium bis(trifluoromethanesulfonyl) imide in DME and DOL (1:1 in volume) solvent with 1% $LiNO_3$ as additive. The 2032-type coin-cells were assembled by using the working electrode, the Celgard separator and lithium metal anode in an Ar-filled glove box. As for assemble of Li-S batteries with freestanding electrode, it can directly act as the working electrode without the use of carbon black and PVDF binder.

2.4.2 Galanostatic charge and discharge

Galanostatic charge and discharge tests are major tools for evaluating the electrochemical performance of rechargeable batteries, including specific capacity, cycling performance, Coulombic efficiency and rate performance. For Li-S batteries, each cell is charged and discharged at constant current in the voltage range of 1.7-2.8V. The charge/discharge capacities of electrode materials can be determined based on the formula Q=I*t, where I

refers to the current and t represents the charge/discharge time. The specific capacity of the electrode material is calculated based on the mass of sulfur. The cycling performance is evaluated after a certain times of cycles. The Coulombic efficiency is calculated based on charge capacity/discharge capacity. The rate performance is evaluated by gradually increasing the current density and then dropping back to the initially current rate. In this thesis, galanostatic charge and discharge tests were performed on Neware battery testing system and Land battery testing machine.

2.4.3 Cyclic voltammetry

Cyclic voltammetry (CV) is an electrochemical measurement that used to trace the relation between current and voltage. It contains the anodic scan process and cathodic scan process. It is a widely used electroanalytical technique to study the redox process of electrode materials. In Li-S batteries, the cathodic scan represents the discharge process, that is the reduction of S_8 to long-chain lithium polysulfides and then to short-chain lithium sulfides. So it usually has two reduction peaks. During the anodic scan process, the lithium sulfide is oxidized to produce S_8. The CV can be cycled for several times to evaluate the stability of the electrode. In this thesis, CV tests were tested on a Bio-Logic VMP3 electrochemistry workstation at a 0.1 mV s^{-1}.

2.4.4 Electrochemical impedance spectroscopy

Electrochemical impedance spectroscopy is an electrochemical technique to test the impedance of an electrochemical system within short time. EIS is powerful method to study the charge transfer properties at the interface of the electrodes. For Li-S batteries, the EIS is

an effective tool to test the charge transfer properties between the electrode and electrolyte. EIS is measured by applying an AC potential to a battery and then testing the current through the battery. EIS has wide applications in corrosion, sensors, electrocatalysis, batteries and fuel cells. In this thesis, EIS measurements were tested on a Bio-Logic VMP3 electrochemistry workstation at an amplitude of 5 mV in the frequency range of 0.01 Hz-100 kHz.

Chapter 3 Self-standing Sulfur Cathodes Enabled by 3D Hierarchically Porous Titanium Monoxide-Graphene Composite Film for High-Performance Lithium-Sulfur Batteries

3.1 Introduction

Conventional lithium-ion batteries based on lithium intercalation chemistry, with a theoretical energy density of about 400 Wh/kg, have been unable to meet the ever-increasing demand for high-energy storage applications such as vehicle electrification and grid electrical storage.[517] Among emerging advanced battery technologies, lithium-sulfur (Li-S) batteries show extraordinary promise for next-generation energy storage due to their high theoretical energy density, environmental benignity and the abundance of sulfur in nature. Li-S batteries possess a high theoretical specific energy of 2500 Wh kg^{-1}, which is more than five times higher than that of traditional lithium-ion batteries.[17]

Despite these intriguing advantages, the commercialization of Li-S batteries has been impeded by three main issues: (a) the inherent poor electronic and ionic conductivity of sulfur and its discharged product Li_2S or Li_2S_2, (b) the dissolution and shuttle effect of intermediate lithium polysulfides, and (c) large volumetric expansion of nearly 80% upon the lithiation process. These problems result in low specific capacity, low Coulombic efficiency and fast capacity degradation upon cycling. Accordingly, strenuous efforts have been devoted to enhance the electrochemical performance of Li-S batteries, including incorporating sulfur into conductive matrix,[518-521] constructing polysulfide blocking interlayers,[345, 522, 523] applying functional binders[524] and developing new electrolytes or additives.[525, 526] Among these

strategies, compositing sulfur with carbonaceous materials is considered to be the most popular method owing to the excellent conductivity of carbon materials. In 2009, Nazar's group pioneered the work of using highly-ordered mesoporous carbon (CMK-3) as a sulfur host and it shows a reversible capacity over 800 mAh g^{-1} after 20 cycles.[519] Inspired by this concept, various carbon nanostructures including hollow carbon spheres,[527, 528] carbon nanotubes,[529] and porous graphene[36, 530, 531] have been developed as sulfur hosts for Li-S batteries. However, as the nonpolar carbon materials can only provide weak physical adsorption of the polar polysulfides, the carbon/sulfur composite cathodes still suffer from severe capacity decay over long-time cycling.

Recently, host materials owning strong chemical interactions with polysulfides have become more promising.[532, 533] For instance, heteroatom doping and functionalization of nonpolar carbon materials lead to much improvement of chemical adsorption ability for polysulfides.[84, 534, 535] Owing to strong Lewis acid-base interactions with polysulfides, metal organic frameworks[179, 182] and MXene nanosheets[263, 536] have been developed as efficient sulfur hosts for improving the electrochemical performance of Li-S batteries. Polar metal oxides,[121, 518, 537-540] metal sulfides,[541-545] metal nitrides[241, 247, 546, 547] and metal carbides[548] have also been employed as sulfur hosts owing to their capability to adsorb polysulfides more tightly than carbon materials. However, most of these polar metallic compounds have intrinsically poor electronic and ionic conductivity, resulting in relatively low sulfur utilization and rate performance. In this regard, it's crucial to design electrodes with both high conductivity and a polar nature in one host.

In spite of the great progresses achieved in terms of specific capacity and cycling

performance, the practically available energy density of current Li-S batteries is still limited. The main reason is that the inclusion of inactive components in cathodes generally reduces the sulfur content and weakens the advantages of Li-S batteries (**Table 3.1** compares the weight percentage of each component in two types of batteries). The traditional aluminum foil current collector that is used to fabricate the sulfur cathode has a density of about 5 mg cm^{-2} and accounts for approximately 15% weightage of a battery.[255] In addition, the conventional slurry-coating process needs to use toxic solvents (e.g., NMP), and the addition of binders and carbon black additives to electrodes will definitely lead to low overall specific energy of a full battery. Furthermore, when the areal sulfur loading is increased for achieving an attractive energy density, the thick material coating can easily generate cracks and peel from the Al foil, which hinders the lithium ion and electron transport during the cycling process. Therefore, in order to reduce inactive parts of a battery and construct more reliable Li-S batteries with high specific energy, the most elegant strategy is to design freestanding and binder-free conductive matrix to host sulfur as a cathode.

Table 3.1 The weight percentage of different components of a typical cathode for different types of Li-S batteries.

Traditional sulfur cathode				**The self-standing sulfur cathode in this work**			
Al foil	Composite	Additive	Binder	Al foil	Composite	Additive	Binder
5mg cm^{-2}	1 mg cm^{-2}	0.125 mg cm^{-2}	0.125 mg cm^{-2}	0	1 mg/cm^{-2}	0	0
Total weight: 6.25 mg cm^{-2}				Total weight: 1 mg cm^{-2}			

In conventional lithium sulfur cathode, Al foil and other inactive parts take up most of the weight of the cathode part (>80%), which will largely weaken the energy density of a full battery.

Hence, combining the above-mentioned two aspects, it is ideal to design a porous self-standing host with polar characteristic that can strongly adsorb the polysulfides while keeping the overall electrode highly conductive, and thereby improving specific energy of the full battery. Although a variety of sulfur host materials based on these concepts has been successfully developed, the design of an ideal sulfur host matrix simultaneously possessing high conductivity, high porosity, polar characteristic and a self-standing property remains an enormous challenge. And most reportded cathode host materials can only meet one or two of the criteria, which can not fulfill the great potential of Li-S batteries.

Herein, for the first time, we innovate a new sulfur host material enabled by Magnéli phase titanium monoxide nanoparticle-graphene composite (TiO-G) film to combine the merits of a self-standing property, high conductivity, polar characteristic and high porosity in one host. The freestanding interconnected graphene scaffold with three-dimensional (3D) architecture provides excellent electron transport properties, and its hierarchically porous structure facilitates electrolyte wettability and rapid lithium ion transport throughout the entire electrode architecture. Furthermore, the highly polar and ultrafine TiO nanoparticles throughout the graphene networks not only show strong chemical entrapment for the intermediate polysulfides, but also accelerate the redox reaction kinetics. Benefiting from this attractive architecture, the TiO-G/S cathode delivered a high specific capacity of 1350 mAh g^{-1} at 0.1C, a Coulombic efficiency approaching 100%, and a high rate performance of 832

mAh g^{-1} at 2C. In addition, when the areal sulfur loading was increased to 5.2 mg cm^{-2}, the TiO-G/S electrode delivered a high areal capacity of 3.2 mAh cm^{-2} after 300 cycles at 0.2C, demonstrating excellent cycling stability compared with other recently reported sulfur cathodes with high areal sulfur loadings.

3.2 Experimental section

3.2.1 Synthesis of polystyrene (PS) sphere templates

PS nanospheres were prepared by a traditional emulsion polymerization method. Typically, 200 mg of potassium persulfate and 151.1 mg of sodium dodecyl sulfate were dissolved in 140 mL of deionized water, followed by stirring under argon atmosphere protection for 30 minutes. The solution was then transferred into an oil bath and heated to 70 °C. After that, 8 mL styrene monomer was dropped into the solution under vigorous stirring. After reaction for 10 hours at 70 °C, monodisperse PS nanospheres were obtained by dialysis for 3 days in order to remove any impurities.

3.2.2 Preparation of TiO_2 nanotubes

TiO_2 nanotubes were prepared by a previously reported method.[549] The detailed procedure is as follows. 2.0 g of commercial TiO_2 particles were dispersed in 30 mL of 10 M NaOH under stirring for 30 min. It was then transferred into a Teflon-lined autoclave and heat treated at 120 °C for 24 h. After being cooled down to room temperature, the white powders were obtained after centrifuged and washed with deionized water. The product was then dipped

into 0.1 M HCl solution under stirring for 12 h. Finally, TiO_2 nanotubes were obtained after washed with a large amount of deionized water.

3.2.3 Preparation of 3D porous TiO-G film and other control host materials

Graphene oxide was synthesized via a modified Hummer's method.[53] Porous TiO-G film was prepared by a hard template strategy. Typically, 15 mg of TiO_2 nanotube powder was firstly dispersed into 5 mL of deionized water by sonication for 30 min. Then 10 mL of GO dispersion (3.5 mg/mL) and 5 mL of PS sphere dispersion (30 mg/mL) were added into the TiO_2 dispersion under vigorous stirring. After stirring for 1 hour, the resulting dispersion was poured into a small cylindrical mold and then frozen in a refrigerator for 2 h. Then the cylindrical PS-TiO_2-GO aerogel was formed by freeze drying of the ice solid in a lyophilizer for 24 h. Then the PS-TiO_2-GO aerogel was compressed and punched into several small disks with diameter of 12 mm. Finally, self-standing and porous TiO-G film was obtained by annealing the small PS-TiO_2-GO disks under a reducting atmosphere of Ar/H_2 (95:5) mixture gas at 1000 °C for 4 h with a heating rate of 5 °C/min. For comparison, porous TiO_2-G film was prepared by annealing the same precursor of PS-TiO_2-GO at 900 °C for 2 h under Ar atmosphere. Porous G film was also synthesized by annealing precursor of PS-GO at 900 °C for 2 h under Ar atmosphere. Thicker electrodes can be prepared easily by raising the precursor material amounts.

3.2.4 Preparation of porous TiO-G/S electrode and other control electrodes

A 100 mg/ml sulfur/CS_2 solution was first prepared by dissolving sublimed sulfur in CS_2 solvent. A certain amount of the obtained solution was dropped into the porous TiO-G film

by a pipette and left under a fume hood overnight for CS_2 evaporation. Then the sulfur contained film was heat treated in a sealed vial at 155 °C for 12 h under Ar protection. After that the film was further heated to 200 °C and kept for 1 hour under Ar protection to evaporate the excess sulfur on the surface. The product was denoted as TiO-G/S. The sulfur loading amount was controlled by the dropping volume of S/CS_2 solution, and obtained by weighing the TiO-G film before and after sulfur loading. The areal sulfur loading was controlled by the thickness of the TiO-G film and the dropping volume of S/CS_2 solution. Typically, the sulfur loading amount was about 1 mg cm^{-2} and the sulfur content was about 65%. However, higher sulfur loading of about 5.2 mg cm^{-2} was also achieved by simply increasing the thickness of the film and the dropping volume of S/CS_2 solution. For comparison, TiO_2-G/S and G/S electrodes were also prepared following the same procedure.

3.2.5 Preparation of Li_2S_6 solution

A certain amount of sulfur and lithium sulfide (Li_2S) with a molar ratio of 5:1 was added to an appropriate amount of 1,2-dimethoxyethane (DME) and 1,3-dioxolane (DOL) (1:1 in volume) under vigorous stirring at 50 °C overnight until sulfur was fully dissolved.

3.2.6 Structure characterization

The morphology of the material was analyzed by field emission scanning electron microscopy (FESEM, Zeiss Supra 55VP) and transmission electron microscopy (TEM, JEOL JEM-2011). The crystal structure was characterized by X-ray diffraction (XRD, Siemens D5000) using Cu Kα radiation with a scanning step of 0.02° per second. Raman spectra were obtained from a Renishaw inVia Raman spectrometer system (Gloucestershire, UK) equipped

with a Leica DMLB microscope (Wetzlar, Germany) and a Renishaw He-Ne laser source producing 17 mW at 633 nm. Thermogravimetric analysis (TGA) was performed with a 2960 SDT system. N2 adsorption/desorption isotherms were collected from a Micromeritics 3Flex analyzer (Micromeritics Instrument Corporation, Norcross, GA, USA).

3.2.7 Electrochemical measurements

The electrochemical performance of the electrodes were measured in CR2032-type coin cells assembled in an Ar-filled glove box. The electrolyte was prepared by dissolving 1 M lithium bis(trifluoromethanesulfonyl) imide in a mixture of 1,3-dioxolane (DOL) and 1,2-dimenthoxyethane (DME) (1:1 in volume) with 1% $LiNO_3$ as additive. Typically, 10 μL of the electrolyte was dropped into the freestanding film. A "Celgard" separator was then placed on top of the electrode, followed by adding 20 μL of the electrolyte onto the separator. Finally, lithium metal foil was placed on top of the separator as the anode. For thicker electrode with areal sulfur loading of 5.2 mg cm^{-2}, 60 μL of electrolyte has been applied to ensure fully wetting the electrode. The galvanostatic charge/discharge measurements were performed in a voltage range of 1.7-2.8 V with current densities of 0.1C to 2C rate using a NEWARE battery tester. The capacities were calculated based on the mass of sulfur. The cyclic voltammetry study of the electrode was recorded by a CHI660C electrochemical workstation in the voltage range of 1.7-2.8 V versus Li/Li^+ at a scan rate of 0.1 mV s^{-1}. The electrochemical impedance measurements were carried out with an amplitude of 5 mV in the frequency range of 0.01 Hz-100 kHz.

3.3 Results and discussion

3.3.1 Materials synthesis and characterization

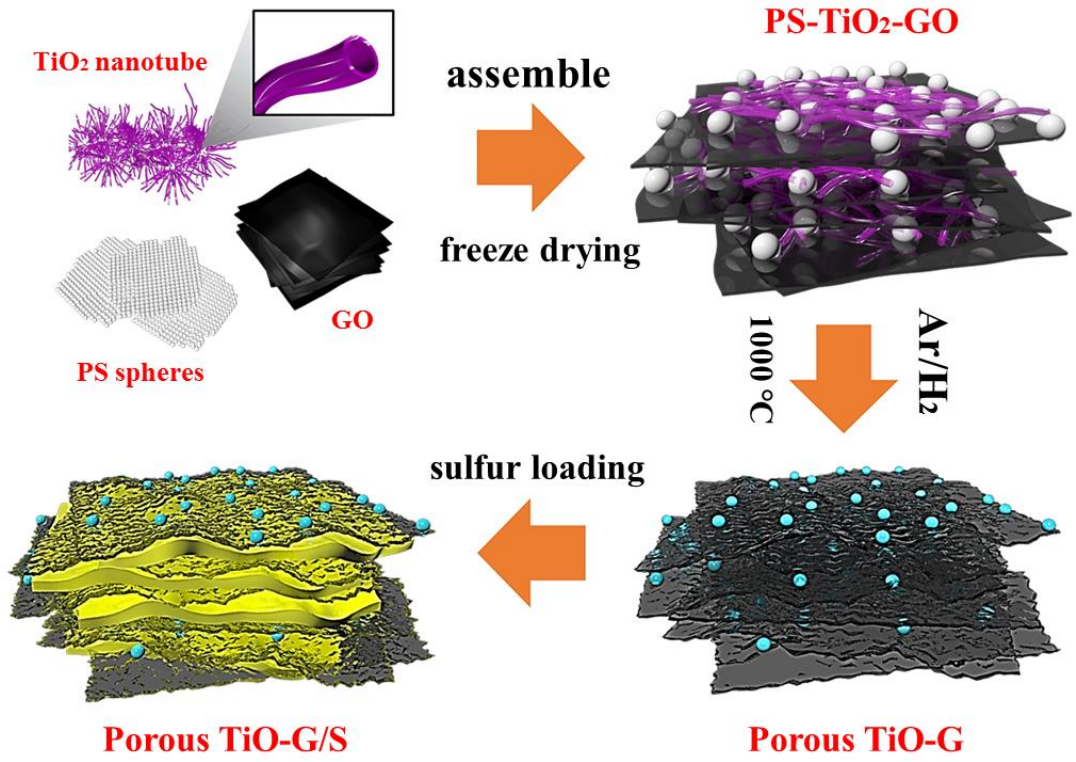

Figure 3.1 Schematic illustration of the synthesis procedure of 3D hierarchically porous TiO-G/S film. The grey and blue spheres represent the PS spheres and TiO nanoparticles, respectively.

The synthesis procedure of the porous and self-standing TiO-G/S composite film is illustrated in **Figure 3.1**. Polystyrene (PS) sphere templates were first synthesized by the traditional emulsion polymerization method. As shown in the scanning electron microscope (SEM) image (**Figure 3.2**a) and particle size distribution plot (**Figure 3.3**), the PS spheres are highly uniform and monodisperse with an average diameter of about 100 nm.

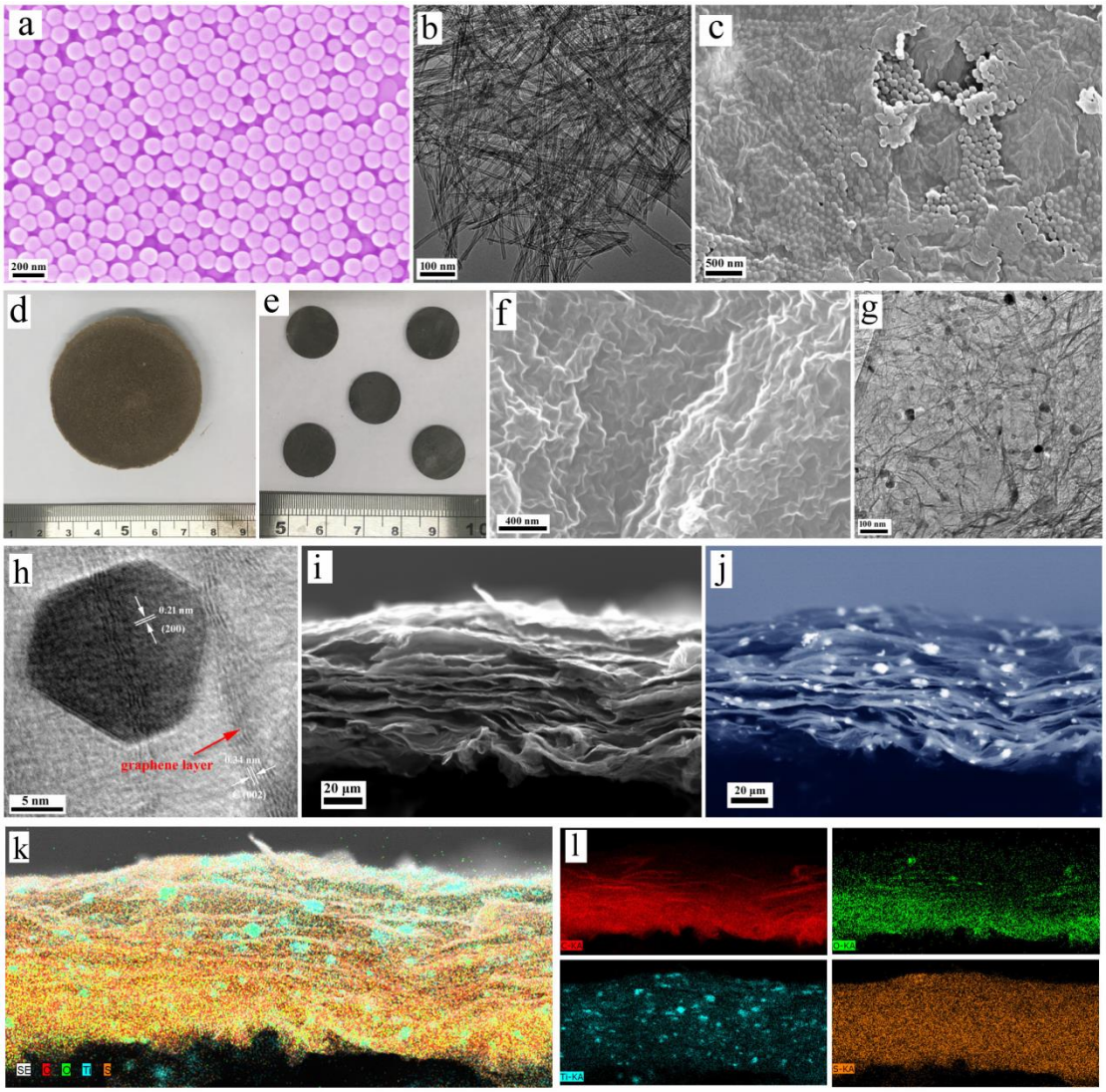

Figure 3.2 (a) SEM image of PS spheres. (b) TEM image of TiO_2 nanotube. (c) SEM image of the surface of PS-TiO_2-GO aerogel. Optical images of (d) PS-TiO_2-GO aerogel and (e) TiO-G film. (f) SEM image of the surface of porous TiO-G film. (g) TEM and (h) high-resolution TEM images of porous TiO-G composite. Cross-sectional (i) SEM image, (j) backscattered electron image and the corresponding (k, l) elemental mappings of the porous TiO-G/S film.

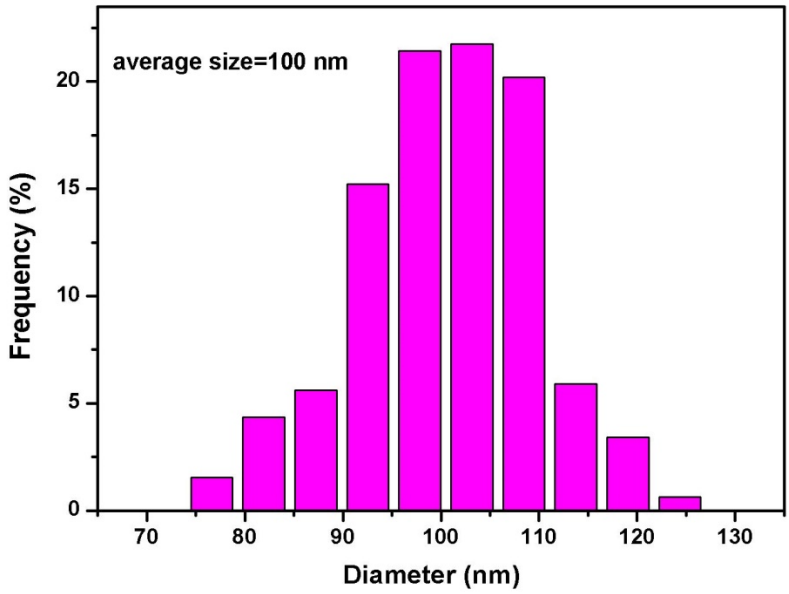

Figure 3.3 Size distribution of PS spheres.

Then a suspension of the PS spheres, TiO_2 nanotubes (**Figure 3.2**b) and graphene oxide (GO) nanosheets (**Figure 3.4**) was mixed together and self-assembled to form a hierarchical PS-TiO_2-GO aerogel after a freeze drying process (**Figure 3.2**d). The SEM image of the surface of the aerogel is shown in **Figure 3.2**c, indicating that most of the PS spheres are wrapped by the ultrathin graphene layer.

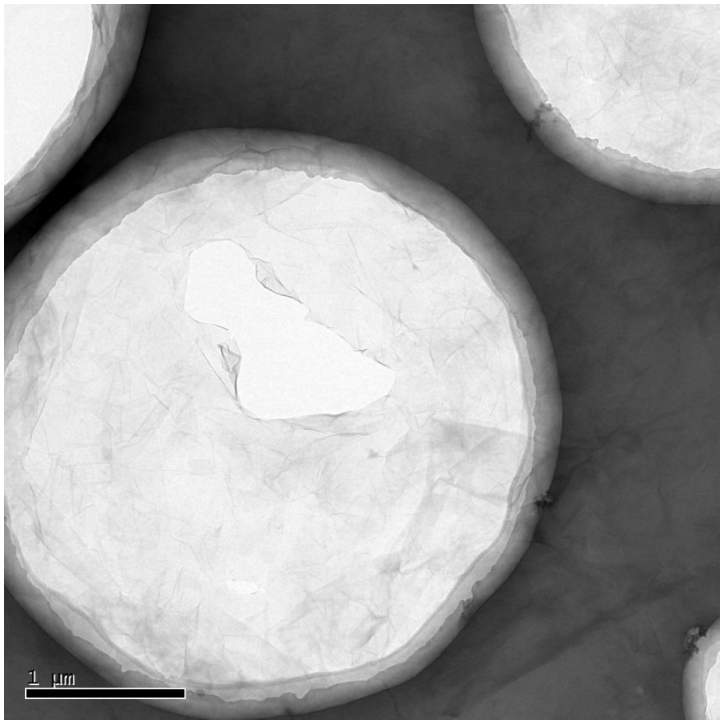

Figure 3.4 TEM image of graphene oxide.

Subsequently, the PS-TiO_2-GO aerogel was compressed and punched into several small disks with diameter of 12 mm. After this the small disks were calcinated in a reducing atmosphere of Ar/H_2 (95:5) mixed gases at 1000 °C for 4 h, during which the GO matrix and semi-conductive TiO_2 nanotubes were transformed into graphene matrix and conductive TiO nanoparticles, respectively. Meanwhile, numerous pores were generated in the film due to the decomposition of the PS spheres at high temperature. The optical images of the obtained porous TiO-G films are shown in **Figure 3.2**e, indicating that the self-standing nature of the films has not collapsed during the high-temperature annealing process, which can be attributed to the robust and interconnected network of the graphene skeleton.

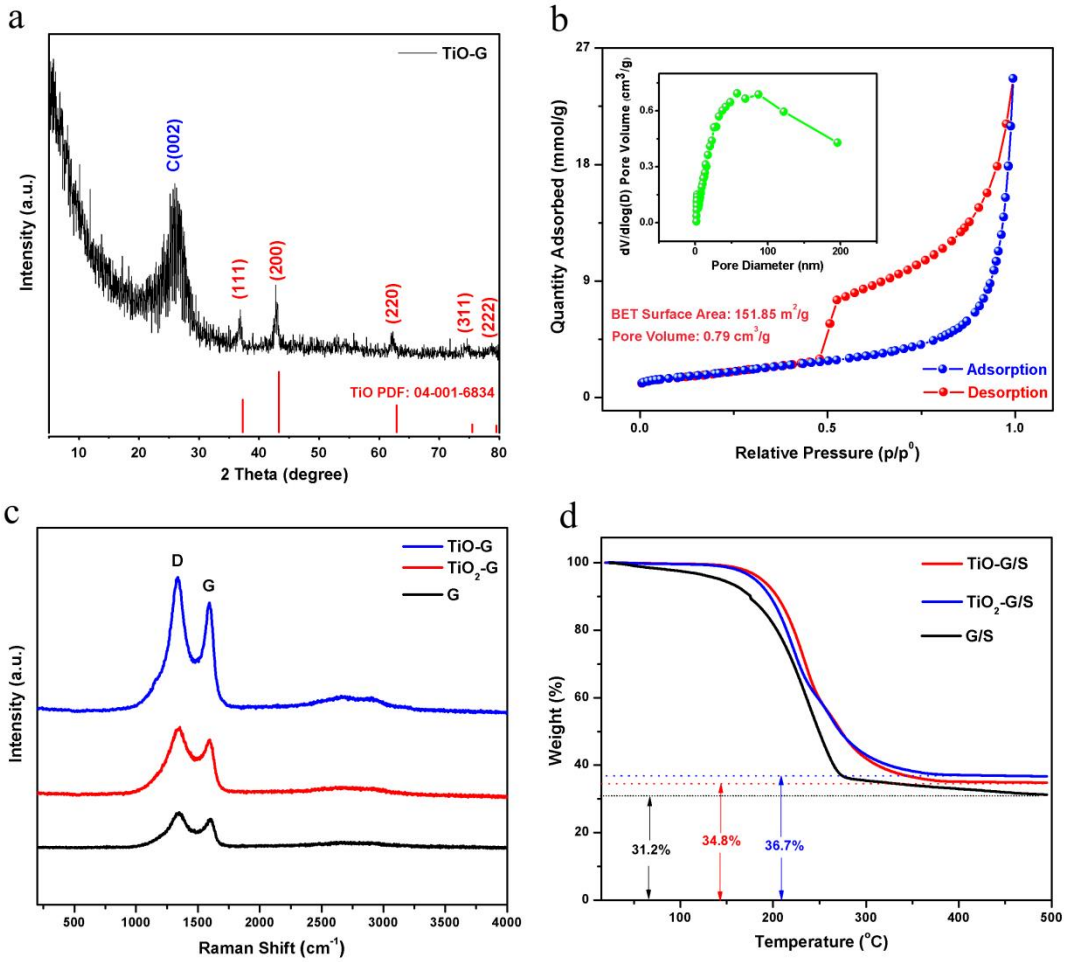

Figure 3.5 (a) XRD pattern of the porous TiO-G composite. (b) Nitrogen adsorption-desorption isotherm of the porous TiO-G composite. Inset shows the pore size distribution obtained using the BJH method. (c) Raman spectra of the porous TiO-G, TiO_2-G and graphene. (d) TGA curves of the porous TiO-G/S, TiO_2-G/S and G/S in N_2 atmosphere with a heating rate of 10 °C /min.

The crystal structure of the obtained porous TiO-G film was examined by X-ray diffraction (XRD) (**Figure 3.5**a). The peak at around 26° is ascribed to the graphene stacking, while the other peaks are assigned to the Magnéli TiO phase (TiO PDF card number: 04-001-6834). A typical SEM image of the surface of the hierarchically porous TiO-G film is shown in **Figure 3.2**f. It is easily discerned that numerous pores were generated in the graphene matrix. The

pore sizes are mainly distributed around 100 nm as measured by the Barrett-Joyner-Halenda method (the inset of **Figure 3.5**b), which is in accordance with the SEM observation (**Figure 3.2**f, **3.6**) and very close to the diameter of PS spheres in **Figure 3.2**a,c.

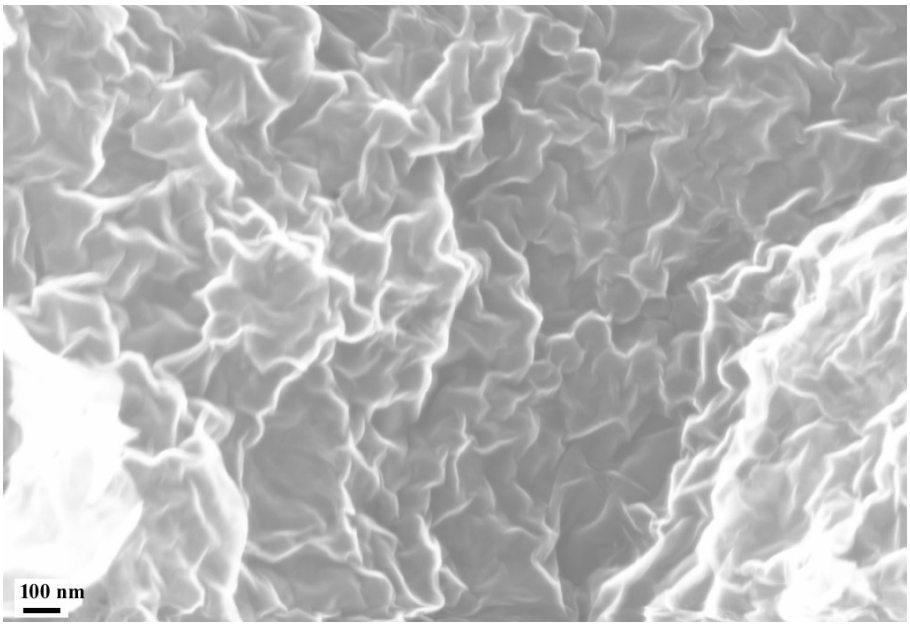

Figure 3.6 Magnified SEM image of the surface of porous TiO-G film.

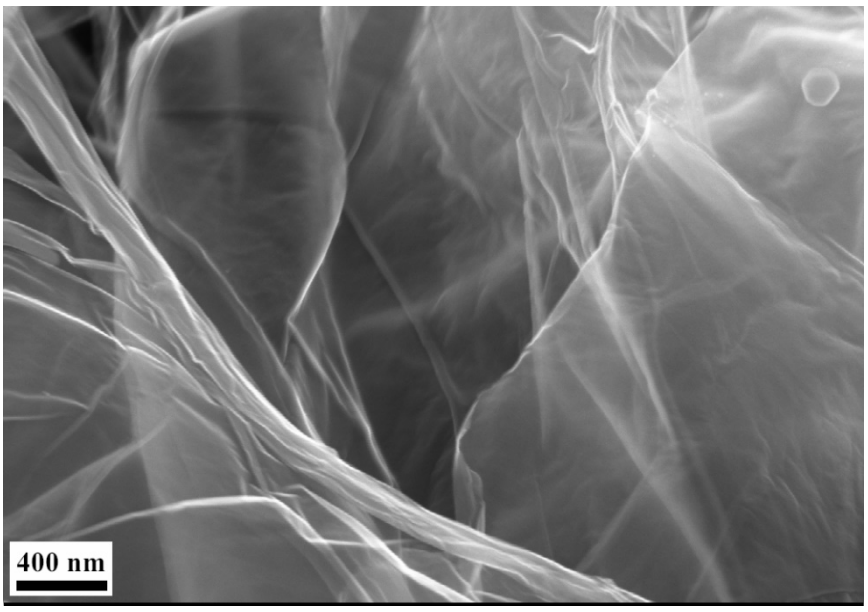

Figure 3.7 SEM image of the nonporous TiO-G without the use of PS sphere template.

For comparison, nonporous TiO-G film was also prepared via the same procedure but without the use of PS sphere templates. This showed very smooth characteristic and did not have pores in the graphene matrix (**Figure 3.7**). The cross-sectional SEM image of the porous TiO-G film is shown in **Figure 3.8** and the thickness of the film is around 102 μm. Numerous voids with several micrometers in size can be clearly observed, which are able to stockpile a large amount of sulfur and provide excellent penetration for the electrolyte. The Brunauer−Emmett−Teller (BET) specific surface area and pore volume of the porous TiO-G film are 151.85 m^2/g and 0.79 cm^3/g, respectively (**Figure 3.5**b). The high specific surface area and large pore volume not only can provide abundant pore structure to accommodate sulfur, but also supply numerous adsorption and catalytic sites for the polysulfides, thus significantly improving both the specific capacity and cycling performance of Li-S batteries. The highly interconnected graphene skeleton in the 3D porous TiO-G film provides excellent electron transport properties, and its hierarchically porous structure, with large-sized pores in the cross-sectional 3D network and middle-sized pores in the graphene sheets, facilitates rapid lithium ion transport and alleviates diffusion limitations throughout the entire electrode architecture. The porous and flexible characteristics of the graphene networks can also buffer the large volume expansion of sulfur during the lithiation process,[263, 536] which is otherwise one of the major obstacles in Li-S batteries. The elemental mappings of C, O and Ti further reveal the hybrid structure of the porous TiO-G composite (**Figure 3.8**).

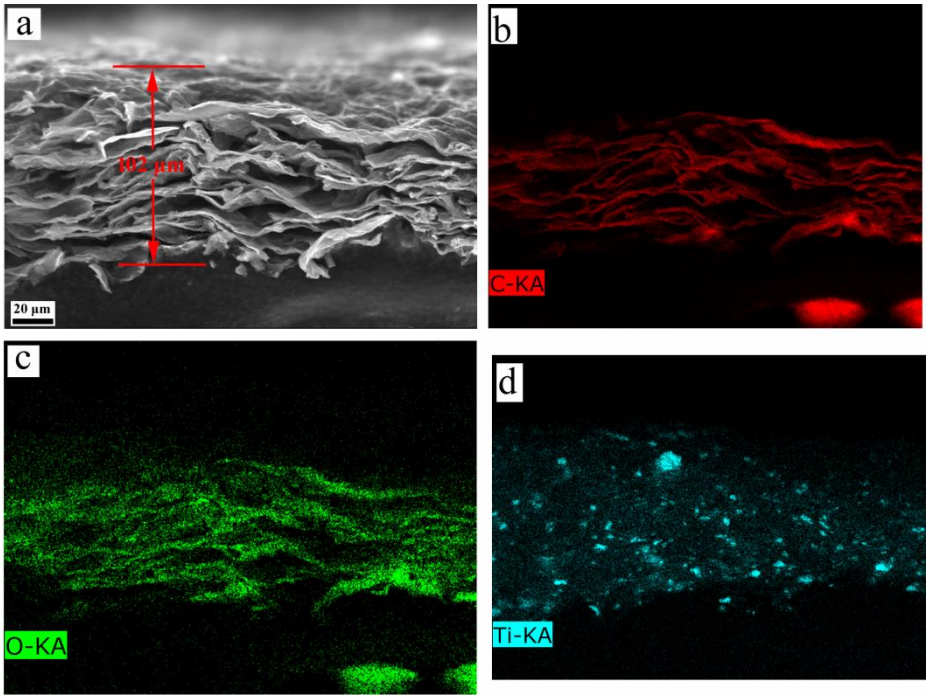

Figure 3.8 (a) Cross-sectional SEM image of the porous TiO-G film, and (b,c,d) the corresponding C-, O- and Ti-elemental mappings.

To identify the TiO phase more clearly, TEM and high-resolution TEM analysis were performed (**Figure 3.2**g,h). It is interesting to note that the TiO_2 nanotubes have transformed into ultrafine TiO nanoparticles during the annealing process (**Figure 3.2**g), which can be ascribed to the structural change at high temperature. The graphene networks provided a supporting substrate to prevent the aggregation of the TiO nanoparticles. The average size of the TiO nanoparticles is around 15 nm. A representative high-resolution TEM (HRTEM) image of an individual TiO nanoparticle is shown in **Figure 3.2**h, revealing lattice fringes with a d-spacing of 0.21 nm, which is in agreement with spacing of the (200) plane of TiO. The (002) plane of the multilayer graphene with a spacing of 0.34 nm can be also easily observed beside the TiO nanoparticle.

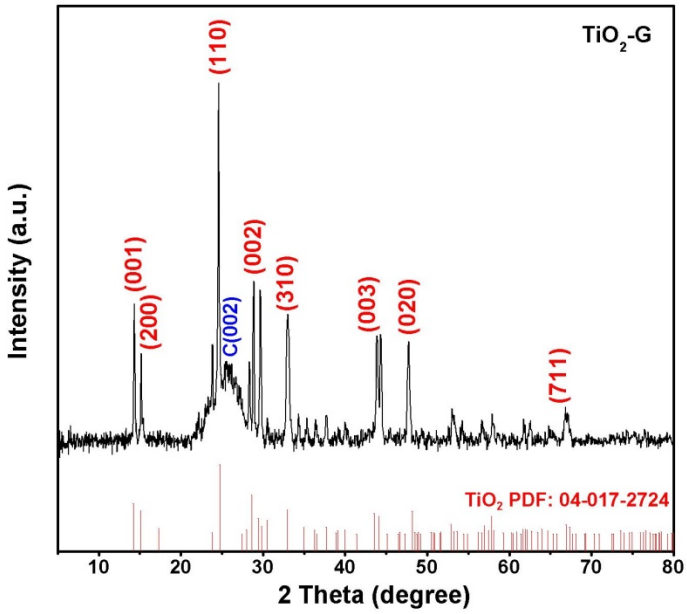

Figure 3.9 XRD pattern of TiO_2-G composite.

For comparison, TiO_2-G film and bare graphene film were also prepared. Porous TiO_2-G film was synthesized by annealing the same precursor of PS-TiO_2-GO aerogel at 900 °C for 2 h under Ar atmosphere. The crystal structure of the film was examined by XRD (**Figure 3.9**). The major peaks are assigned to TiO_2 (TiO_2 PDF card No. 04-017-2724) with a wide peak at around 26° corresponding to graphene stacking. TEM images of the obtained TiO_2-G composite are shown in **Figure 3.10**, indicating that TiO_2 nanotubes have turned into TiO_2 nanoparticles during the annealing process and their morphology is similar to that of the TiO nanoparticles mentioned above (**Figure 3.10**a). A representative HR-TEM image of a single TiO_2 nanoparticle reveals lattice fringes with a d-spacing of 0.31 nm, which is in agreement with the (002) plane spacing of TiO_2 (**Figure 3.10**b).

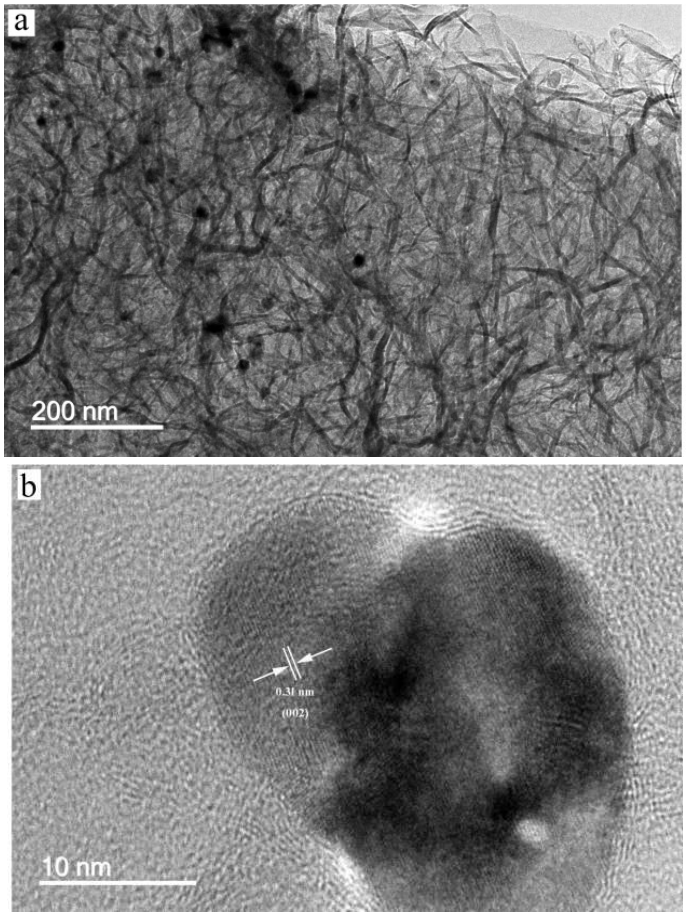

Figure 3.10 (a) TEM and (b) high-resolution TEM images of TiO_2-G composite.

Pure graphene film was also prepared as another comparison sample by annealing the PS-GO aerogel at 900 °C for 2 h under Ar atmosphere (**Figure 3.11**). Raman spectra were performed to characterize these materials as indicated in **Figure 3.5**c. The two distinct peaks located at about 1345 cm^{-1} and 1594 cm^{-1} are easily observed, which are attributed to the D band and G band of carbon, respectively. The D band is related to lattice defects and disorder, whereas the G band is associated with the ordered structure of graphitic crystallites. The porous TiO-G (I_D/I_G=1.218) and TiO_2-G (I_D/I_G=1.208) has a slightly higher I_D/I_G than the pure graphene (I_D/I_G=1.204) film. This indicates that porous TiO-G and TiO_2-G have more

defect density when composited with graphene materials, which is beneficial for polysulfide adsorption.

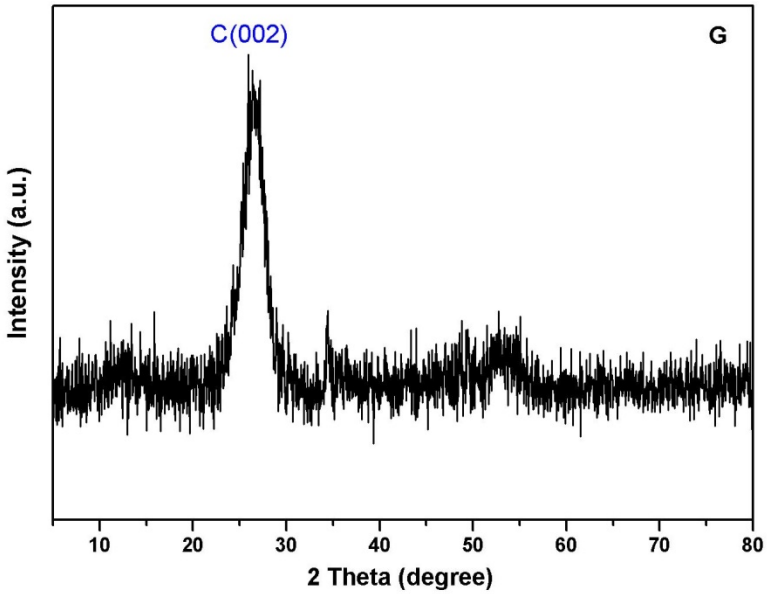

Figure 3.11 XRD pattern of the graphene film.

Sulfur was loaded by infiltrating sulfur/CS_2 solution into these freestanding films, drying under a fume hood, then keeping at 155 °C for 12 h to let sulfur distribute uniformly in the pores of the film, and afterwards heating at 200 °C for 1 h to evaporate the excess sulfur from the surface of the film. The morphology of the porous TiO-G film remains well after sulfur loading without obvious sulfur aggregation (**Figure 3.2**i). To identify TiO nanoparticles more clearly in the obtained porous TiO-G/S film, cross-sectional backscattered electron image analysis was carried out (**Figure 3.2**j). The white dots in **Figure 3.2**j represent the signal of Ti element due to the different contrast between the metal and nonmetal elements, indicating that the ultrafine TiO nanoparticles distribute uniformly in the 3D hierarchically porous TiO-G/S film. This distribution plays a key role in chemically adsorbing the intermediate

polysulfides and accelerating the redox reaction kinetics during the discharge-charge processes. The cross-sectional elemental mapping images of the porous TiO-G/S film demonstrate that sulfur is homogeneously distributed in the self-standing TiO-G host (**Figure 3.2**k, l). To make a fair comparison, the sulfur contents in TiO-G/S, TiO_2-G/S and G-S films were all controlled to be about 65% (**Figure 3.5**d).

3.3.2 Electrochemical performances

A series of electrochemical measurements were performed to evaluate the electrochemical performances of the porous TiO-G film and other comparison host materials. The self-standing films were directly used as cathodes and the areal sulfur loadings were all controlled to be about 1.0 mg cm^{-2}. To probe the structural effect of the different host materials on the charge transport kinetics of the cathodes, an electrochemical impedance spectra (EIS) technique was first carried out. As shown in the Nyquist plots of **Figure 3.12**a, the spectra consist of two parts, a semicircle in the high-frequency region representing the charge transfer resistance with a straight line in the low-frequency region associated with the mass transfer process. It can be easily observed that the porous TiO-G/S cathode has the smallest semicircle in the high-frequency region, suggesting the lowest charge transfer resistance compared to the TiO_2-G/S and G/S cathodes. Since the three samples have approximately the same sulfur contents and areal sulfur loadings, the different charge transfer resistance can be attributed to the different conductivity of the host materials. Benefitting from the oxygen deficient characteristic, the Magnéli phase TiO shows a metallic nature and high conductivity, which would play a vital role in facilitating the interfacial charge transfer

kinetics for surface reactions. On the contrary, the TiO_2-G/S cathode shows the biggest semicircle, indicating the highest charge transfer resistance, which can be ascribed to the relatively poor conductivity of TiO_2. **Figure 3.12**b shows the 1^{st} to 6^{th} cyclic voltammetry (CV) profiles of the TiO-G/S cathode at a scan rate of 0.1 mV s^{-1} in the voltage range of 1.7-2.8 V. The two peaks located at about 2.35 V and 2.05 V in the cathodic region correspond to the reduction of S_8 to long-chain lithium polysulfides (Li_2S_x, $4 \leq x \leq 8$) and the transformation from long-chain lithium polysulfides to short-chain Li_2S_2/Li_2S, respectively. In the other half of the cycle, the two anodic peaks are attributed to the oxidation of Li_2S_2/Li_2S to lithium polysilfides and then to S_8, respectively. The high repeatability of the CV curves from the 1^{st} to 6^{th} cycles indicates the excellent reversibility and low polarization of the electrode.

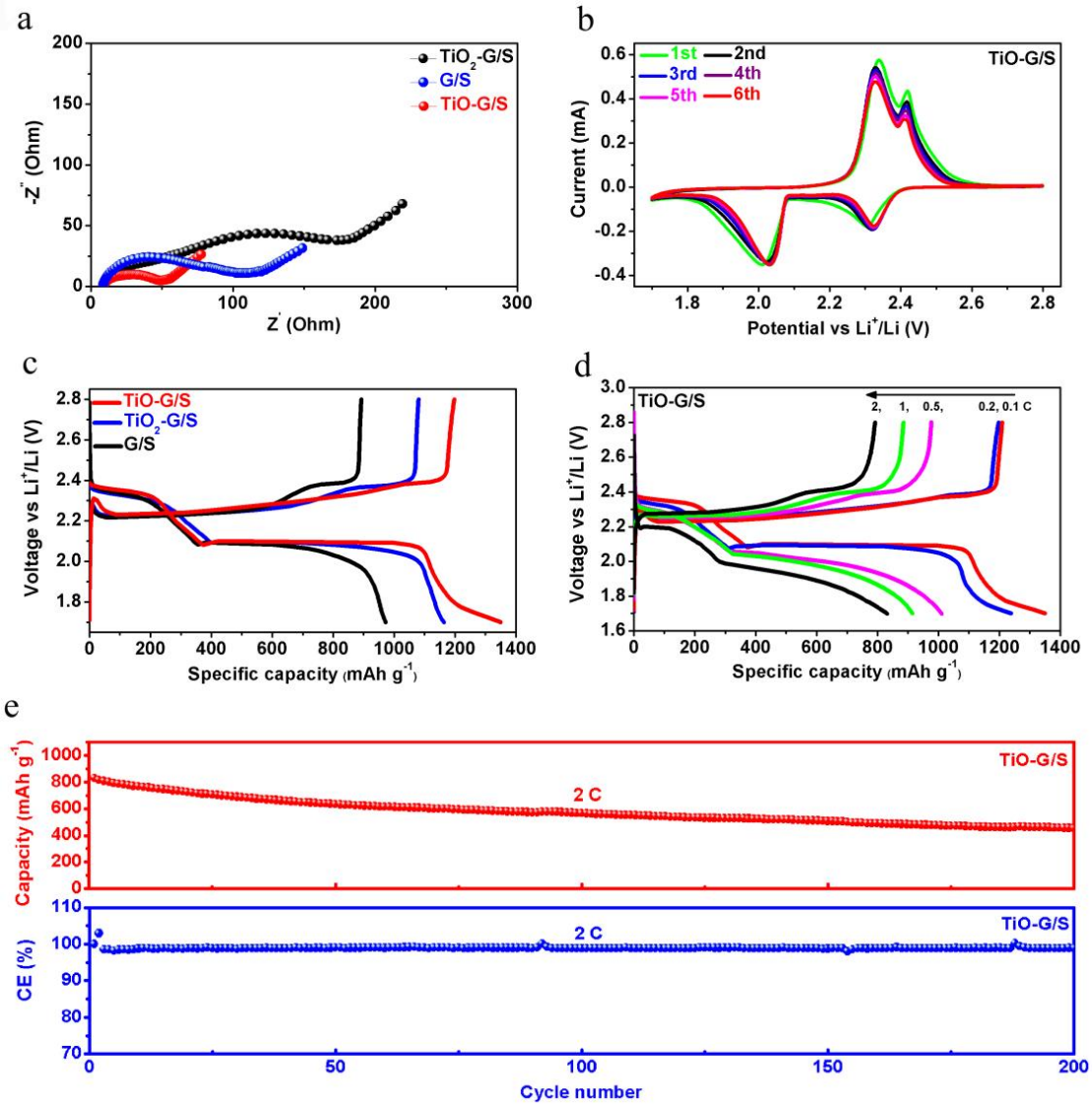

Figure 3.12 (a) Nyquist plots of the porous TiO-G/S, TiO_2-G/S and G/S cathodes before cycling from 0.01 Hz-100 kHz. (b) The 1st to 6th CV profiles of the porous TiO-G/S cathode at a scan rate of 0.1 mV s^{-1} in the voltage range of 1.7-2.8 V. (c) The first-cycle galvanostatic charge-discharge voltage profiles of the porous TiO-G/S, TiO_2-G/S and G/S cathodes at 0.1 C in the potential window from 1.7 to 2.8 V. (d) Galvanostatic charge-discharge voltage profiles of the porous TiO-G/S cathode at various current densities from 0.1 to 2 C. (e) Cycling performance and Coulombic efficiency of the porous TiO-G/S cathode at 2 C for 200 cycles.

Figure 3.12c shows the first-cycle galvanostatic charge-discharge voltage profiles of the porous TiO-G/S, TiO_2-G/S and G/S cathodes at 0.1 C (1C=1675 mA g^{-1}) in the potential

window from 1.7 to 2.8 V. The charge-discharge profiles of the porous TiO-G/S consist of two discharge plateaus at about 2.35 V and 2.1 V, and two charging plateaus between 2.2 and 2.4 V, respectively, which are in accordance with the CV curves. Among the three samples, the TiO-G/S cathode shows the longest second discharge plateau and the lowest polarization, indicating better redox reaction kinetics and more efficient sulfur utilization. **Figure 3.13** demonstrates the cycling performance and Coulombic efficiency of the porous TiO-G/S, TiO_2-G/S and G/S cathodes at 0.5 C. The TiO-G/S cathode delivers an initial discharge capacity of 1019 mAh g^{-1}, higher than that of the TiO_2-G/S (870 mAh g^{-1}) and G/S (699 mAh g^{-1}) cathodes. More importantly, it showed better cycling performance with a Coulombic efficiency approaching 100% in the subsequent cycles, suggesting that the polysulfides dissolution was effectively mitigated in the porous TiO/G host, which can be attributed to the better chemical trapping ability of the ultrafine TiO nanoparticles in the film. In contrast, the pure G/S film shows the fastest capacity fading, which could be due to the nonpolar characteristic and ineffective lithium polysulfides confinement of the pure graphene film.

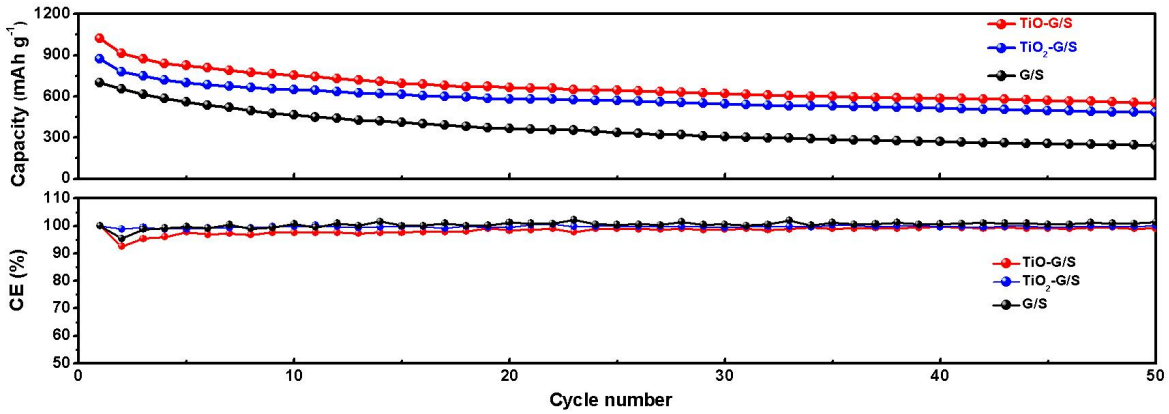

Figure 3.13 Cycling performance and Coulombic efficiencies of the porous TiO-G/S, TiO_2-G/S and G/S cathodes at 0.5 C for 50 cycles.

Figure 3.12d shows the first-cycle galvanostatic charge-discharge voltage profiles of the porous TiO-G/S cathodes at various current densities from 0.1 to 2 C. The TiO-G/S cathodes delivered a high initial discharge capacity of 1350 mAh g^{-1}, 1238 mAh g^{-1}, 1011 mAh g^{-1}, 915 mAh g^{-1} and 831 mAh g^{-1} at current densities of 0.1 C, 0.2 C, 0.5 C, 1 C and 2 C, respectively, indicating excellent rate performance. Although higher polarization occurs at higher current densities due to the slower dynamics of lithium reaction with sulfur, the charge-discharge voltage profiles still contain two plateaus at the high current rate of 2 C. The TiO-G/S cathode was further cycled with the current rate increasing from 0.2 to 2 C (**Figure 3.14**). It shows relatively good cycling stability except for the initial few cycles at 0.2 C. More importantly, when the current density was reduced back to 0.2 C, the discharge capacity is recovered to 988 mAh g^{-1}, suggesting relatively good cycling stability after the high rate charge and discharge tests. **Figure 3.12**e demonstrates the long-term cycling performance of the porous TiO-G/S cathode at 2 C. It delivered a high initial discharge capacity of 831 mAh g^{-1} and retained a discharge capacity of 455 mAh g^{-1} after 200 cycles at 2 C. The Coulombic efficiencies of the porous TiO-G/S cathode are > 98% during the cycling process.

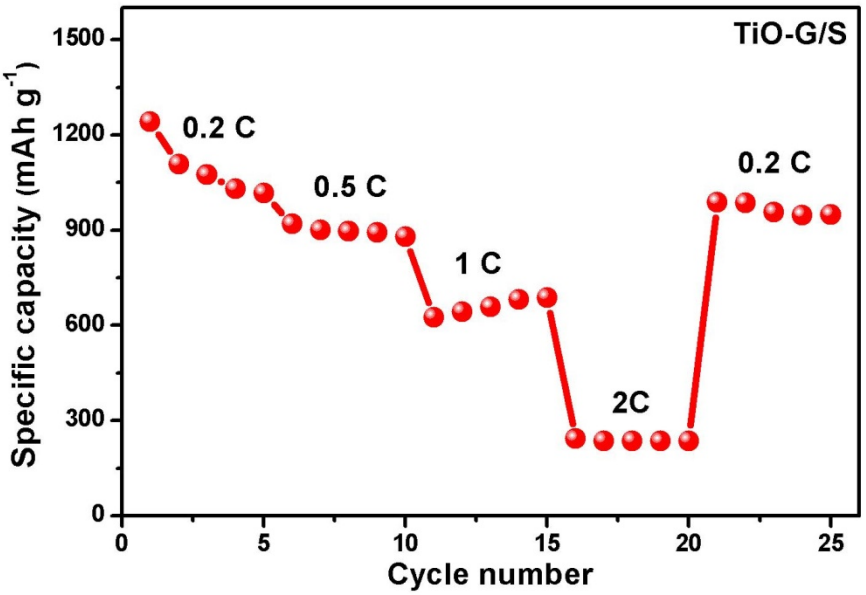

Figure 3.14 Rate performance of the porous TiO-G/S cathode at different current densities.

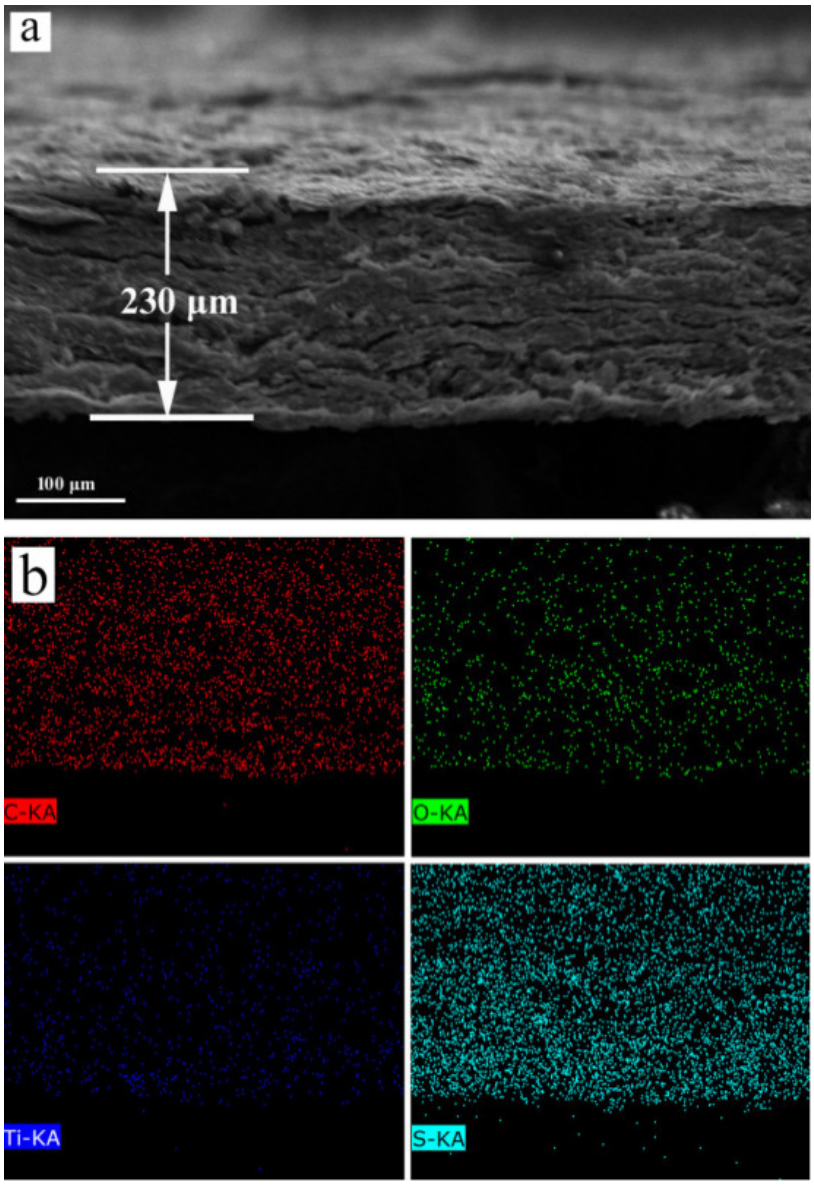

Figure 3.15 Cross-sectional (a) SEM image and (b) elemental mappings of C, O, Ti and S of the thicker TiO-G/S electrode.

Since high areal sulfur loading and high areal capacity are two important factors for achieving high specific energy of a practical Li-S battery, porous TiO-G film with higher areal sulfur loading of about 5.2 mg cm^{-2} was prepared by increasing the thickness of the film from 102 to 230 µm (**Figure 3.15**) and the dropping volume of S/CS_2 solution. As indicated in **Figure 3.16**a, the areal capacity of the thicker electrode soon reaches 4.1 mAh cm^{-2}

(corresponding to a specific capacity of 786 mAh g^{-1}) after the activation in the initial few cycles. And it retains a discharge capacity of 3.15 mAh cm^{-2} (equal to a specific capacity of 606 mAh cm^{-2}) after 300 cycles at 0.2 C, which is higher than that of the commercial lithium-ion batteries (about 3.0 mAh cm^{-2}). **Figure 3.16**b shows the comparison of the performances of many recently reported sulfur host materials, it should be noted that the porous TiO-G/S film of this work demonstrates much enhanced areal capacity as well as improved cycling performance with a high areal sulfur loading compared with most of the recent works. Good cycling performance of a high areal sulfur loading electrode requires good conductivity of the host material as well as efficient confinement of the lithium polysulfides. All above results demonstrate that the freestanding TiO-G film is a promising sulfur host material for achieving stable cyclability and high energy density of a practical Li-S battery.

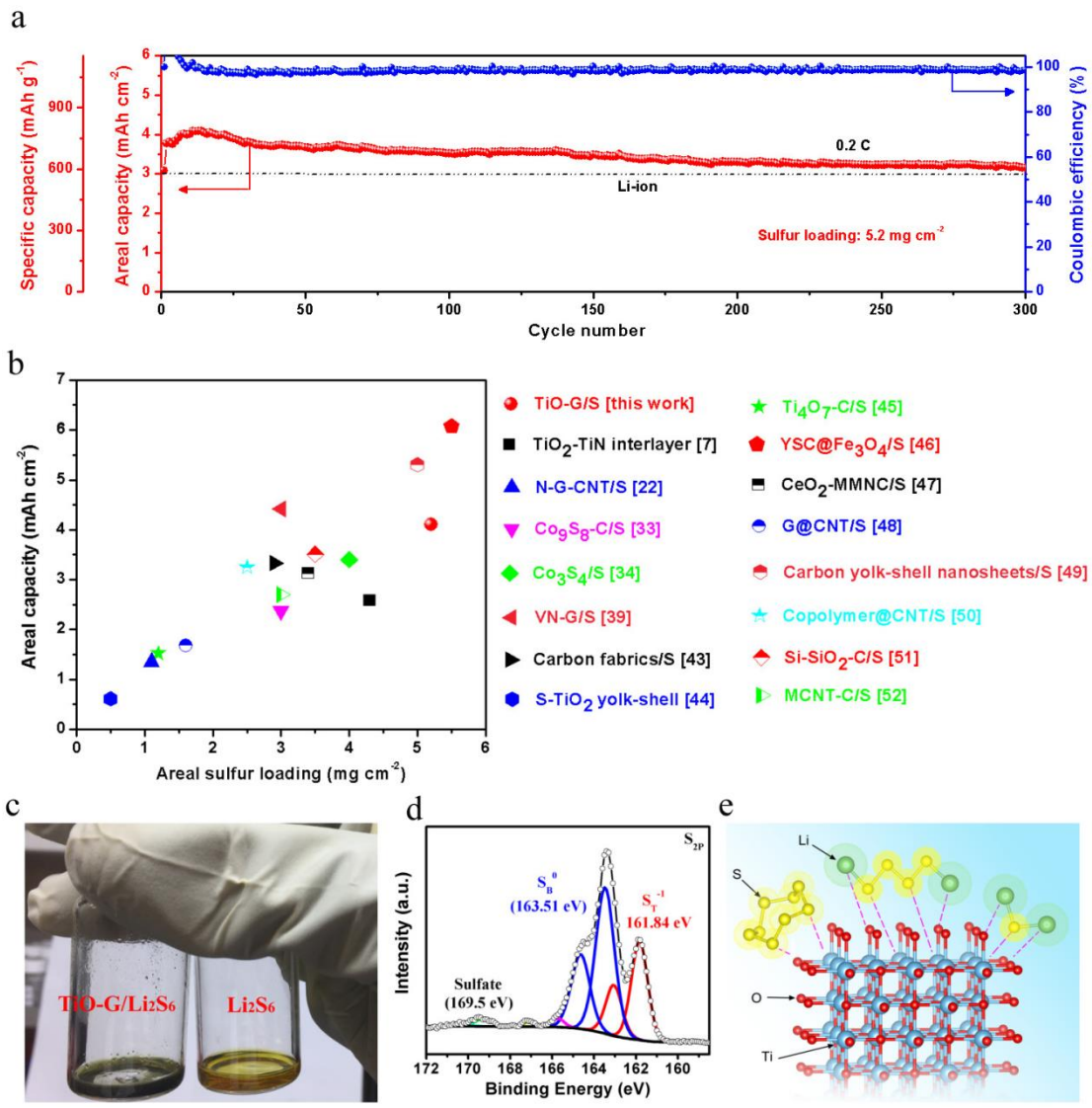

Figure 3.16 (a) Cycling stability and Coulombic efficiency of porous TiO-G/S cathode at 0.2 C for 300 cycles with high areal sulfur loading of about 5.2 mg cm^{-2}. (b) Comparison of the electrochemical performance of this work with some recent publications. (c) Optical images of a Li_2S_6 solution before and after the addition of TiO-G powder. (d) High-resolution S 2p spectra of TiO-G/Li_2S_6. (e) Demonstration of the chemical interaction between TiO and sulfur species. The Ref. in Figure b refer to: [7] *Energy Environ. Sci.* 2017, 10, 1694-1703; [22] *Adv. Energy Mater.*, 2017, 7, 1602014; [33] *Nano Energy*, 2017, 38, 239-248; [34] *Nano Energy*, 2017, 37, 7-14; [39] *Nat. Commun.*, 2017, 8, 14627; [43] *ACS Nano*, 2017, 11, 4694–4702; [44] *Nat. Commun.,* 2013, 4, 1331; [45] *Adv. Funct. Mater.,* 2017, 27, 1701176; [46] *Adv. Mater.,* 2017, 29, 1702707; [47] *ACS Nano*, 2017, 11, 7274–7283; [48] *Adv. Energy Mater.,* 2017, 7, 1602543; [49] *Nat. Commun.*, 2017, 8, 482; [50] *Adv. Mater.*, 2017, 29, 1603835; [51] *Adv.*

Mater., 2016, 28, 3167–3172; [52] *Adv. Funct. Mater.,* 2016, 26, 1225-1232.

In order to elucidate the advantageous architecture of the porous TiO-G film and verify the strong chemical interaction between TiO-G and lithium polysulfides, a polysulfide adsorption test was performed by adding appropriate amount of TiO-G powder into Li_2S_6 solution. As shown in **Figure 3.16**c, upon adding the TiO-G powder, the original colour of the Li_2S_6 solution immediately faded away, demonstrating the strong chemical adsorption ability of the porous TiO-G for polysulfides. Furthermore, in order to quantitatively probe the strong chemical interaction between TiO-G and lithium polysulfides, X-ray photoelectron spectroscopy (XPS) analysis was performed on the solid TiO-G/Li_2S_6 powder after the DME/DOL solvent is volatilized. As shown in **Figure 3.16**d, the high-resolution S 2p spectra of TiO-G/Li_2S_6 exhibits two main sulfur contributions located at 161. 84 eV and 163.51 eV, which are attributed to the terminal sulfur(S_T^{-1}) and bridging sulfur (S_B^0) element, respectively [121]. Moreover, compared with pure Li_2S_6 in the previous work [550], both the S_T^{-1} and S_B^0 in TiO-G/Li_2S_6 shift to a higher binding energy, suggesting a decrease in electron density of the S_T^{-1} and S_B^0 [550, 551]. All of these results evidently demonstrate the strong chemical interaction between TiO-G and lithium polysulfides. **Figure 3.16**e illustrates the detailed binding mechanism of TiO with sulfur species. As the surfaces of Magnéli phase TiO nanocrystals have abundant low coordinated Ti sites which have unsaturated chemical binding, they are easily accessible for external chemical interactions with the sulfur species [549]. According to previous theoretical calculations, the TiO host can provide very strong chemical adsorption energy for lithium polysulfides due to the formation of both Ti-S and

Li-O bonds [518]. As a result, it is rational to assume that the excellent electrochemical performance of the TiO-G/S cathode mainly originates from the unique surface chemical properties of TiO.

3.4 Conclusions

In summary, we have proposed a novel strategy to fabricate the self-standing and highly conductive polar TiO-G/S film with 3D hierarchically porous architecture for Li-S batteries. The highly interconnected porous graphene matrix not only can facilitate rapid lithium ion and electron transport, but also provide sufficient spaces for sulfur accommodation and cushion of the volume expansion during the lithiation process. In addition, the ultrafine and polar TiO nanoparticles distributed over the entire graphene networks provided strong chemical entrapment for lithium polysulfides and their high conductivity also accelerated the redox reaction kinetics. Benefiting from this delicate architecture, the freestanding TiO-G/S film delivered a high initial discharge capacity of 1350 mAh g^{-1} at 0.1 C and a high rate performance of 832 mAh g^{-1} at 2 C. Furthermore, when the areal sulfur loading was increased to 5.2 mg cm^{-2}, the TiO-G/S cathode can deliver a high areal capacity of 3.2 mAh cm^{-2} after 300 cycles at 0.2 C, demonstrating excellent cycling stability at high areal sulfur loading. This work opens up the avenue for constructing more efficient nanoarchitectures with the merits of a self-standing property, high conductivity, polar characteristic and high porosity in one host. Only by using such efficient sulfur hosts, can high energy density Li-S batteries be developed for practical applications.

Chapter 4 Co-Fe Mixed Metal Phosphide Nanocubes with Highly Interconnected-Pore Architecture as an Efficient Polysulfide Mediator for Lithium-Sulfur Batteries

4.1 Introduction

The past decades have witnessed great success of lithium-ion batteries in the field of portable electronics since their first commercialization by Sony in the 1990s.[552] However, the energy density of current lithium-ion batteries relying on lithium intercalation mechanism is approaching its limit (~400 Wh kg^{-1}).[13] Thus, it is difficult to satisfy the mounting energy requirement for many emerging applications, such as electrical vehicles and smart grids. Among alternative battery technologies, lithium-sulfur (Li-S) batteries, based on a multi-electron conversion chemistry, demonstrate extraordinary promise for next-generation energy storage owing to their overwhelming specific energy (~2500 Wh kg^{-1}).[16, 31] Additionally, sulfur is environmentally benign, cheap and abundant in nature, making Li-S batteries more intriguing. In spite of these attractive benefits, the practical implementation of Li-S batteries is plagued with several bottlenecks, including the poor conductivity of sulfur and lithium sulfide, the dissolution and shuttle effect of polysulfides, and the huge volume change upon cycling.[33, 35] These dilemmas lead to low sulfur utilization efficiency and rapid capacity decay upon cycling. Therefore, various methods have been developed to solve these problems, including melting sulfur into the conductive matrix,[31, 36, 37] modification of separators,[38-40] appending interlayers,[41, 42] developing new electrolytes or additives,[43-46] and applying functionalized binders.[44, 47-51] Among these strategies, infiltrating sulfur into porous

carbon materials is the most popular method due to their superior conductivity, large surface area and diversity in nanostructures.[31, 37, 52, 53] Nevertheless, because the nonpolar carbon can only serve as the physical barrier for the polar polysulfides, the sulfur/carbon composites still suffer from severe capacity decline upon long-term cycling.[60]

Recently, polar materials have become more effective in moderating the diffusion of intermediate polysulfides owing to their strong chemical binding with lithium polysulfides. For instance, surface functionalization and heteroatom doping of carbonaceous materials could effectively strengthen the chemical trapping ability to polysulfides.[82, 84, 553] Metal organic frameworks and MXene nanosheets were found to be effective matrix to chemically immobilize polysulfides due to the strong Lewis acid-base interactions between them.[182, 183, 265, 319, 554-556] Polar metal oxides,[115, 121, 135, 145, 557] metal sulfides,[205, 216, 558-561] metal nitrides[241, 247, 248, 562, 563] and metal carbides[251, 564] can also generate strong chemical interactions with polysulfides. However, most of metal oxides and sulfides have inherently poor conductivity, leading to the low sulfur utilization efficiency and sluggish redox reaction kinetics upon cycling.

Transition metal phosphides, with superior conductivity compared to their oxides and sulfides counterparts, have been largely studied in recent year, as efficient electrocatalysts for water splitting.[267] The metal phosphides show metallic characteristic and even superconductivity,[273] which would be very beneficial to facilitate the redox reaction kinetics and increase the sulfur utilization efficiency for Li-S batteries. Additionally, because of the facile and gentle synthesis procedure of metal phosphides by compared with conductive metal nitrides and carbides, making them to be attractive candidates for the electrochemical

applications. Yet the study of polar and conductive metal phosphides as sulfur hosts is just in its early stage and rare reports are regarding this. Moreover, as the porosity and conductivity of the transition metal compounds are usually contradictory and difficult to be simultaneously satisfied, the previously reported metal phosphides were applied just in the irregular particle form without adequate porosity, which could only adsorb polysulfides near the surface. This results in another problem one cannot avoid. Specifically, when the sulfur content is higher than a certain value, the polar material would not be able to supply sufficient interfaces to immobilize all of the polysulfides in the electrode. The amount of areal sulfur loading is another crucial parameter for practical applications of Li-S batteries, which directly determines the energy density of a Li-S battery.[54] However, most of the previous works reported the low areal sulfur loading (normally below 3 mg cm^{-2}) and low areal capacity (below 3 mAh cm^{-2}), which cannot satisfy the high energy demand for emerging applications.[115, 131, 251] It is thus crucial to explore polar yet conductive host materials with high porosity to restrain the shuttle effect and increase the sulfur utilization efficiency for high sulfur loading Li-S batteries.

Herein, we report the synthesis of uniform Co-Fe mixed metal phosphide (Co-Fe-P) nanocubes with highly interconnected-pore architecture as an efficient polysulfide mediator for Li-S batteries. The obtained Co-Fe-P nanocubes have several pivotal advantages as sulfur host materials for Li-S batteries. Firstly, the abundant and interconnected-pore architecture provides sufficient space for sulfur loading and buffers the volume change upon cycling. Secondly, the polar Co-Fe-P nanocubes with interconnected-pore architecture can supply adequate interfaces to chemically anchor the intermediate polysulfides and further promote

the kinetics of polysulfide conversion, thus suppressing the shuttle effect. Thirdly, the inherently metallic conductivity facilitates the redox reaction kinetics and maximizes the sulfur utilization efficiency. Benefiting from the above merits, the sulfur-loaded Co-Fe-P (S@Co-Fe-P) nanocubes exhibited high specific capacity, superior rate performance and excellent cycling stability for Li-S batteries. Moreover, the S@Co-Fe-P electrode showed high areal capacity with good stability at a high areal sulfur loading of 5.5 mg cm^{-2}. Impressively, the commercial size soft-package Li-S batteries based on S@Co-Fe-P cathodes also demonstrated superior cycling stability with good flexibility, indicating their great potential for practical applications.

4.2 Experimental section

4.2.1 Preparation of $Fe_{0.667}Co(CN)_4(H_2O)_4$ nanocubes

First, 200 mL of deionized (DI) water was added into 1.31704 g of potassium hexacyanoferrate(III) powder to form a homogeneous solution. The obtained solution was then poured into 200 mL solution containing 1.31418 g of cobalt nitrate hexahydrate and 2.6469 g of sodium citrate under stirring. After the reaction proceed for 24 h at room temperature, the product was centrifuged and rinsed with water for several times to remove the soluble impurities. Finally, $Fe_{0.667}Co(CN)_4(H_2O)_4$ nanocubes were obtained by drying at 60 °C under vacuum overnight.

4.2.2 Preparation of Co-Fe-P nanocubes and Co-Fe particles

In a typical procedure, 50 mg $Fe_{0.667}Co(CN)_4(H_2O)_4$ nanocubes and 500 mg sodium hypophosphite were first put at two porcelain boats. The two porcelain boats were then

transferred into a tube furnace with the sodium hypophosphite at the upstream side. The samples were then annealing at 600 °C for 2 h under the Ar atmosphere. For comparison, Co-Fe-P were also prepared at the annealing temperature of 500, 650 and 700 °C, respectively. Co-Fe particles were prepared by the same method as Co-Fe-P except without adding the sodium hypophosphite.

4.2.3 Preparation of S@Co-Fe-P and S@Co-Fe

A certain mass ratio of Co-Fe-P nanocubes and sulfur powder were mixed and grind together for 30 min. Then the mixed powder was sealed in a vial and heated at 155 °C for 12 h to allow the diffusion of sulfur into the interconnected-pore structure of Co-Fe-P nanocubes. For comparison, S@Co-Fe was also prepared *via* the same procedure except Co-Fe was used as the host material instead of Co-Fe-P.

4.2.4 Preparation of Li_2S_6 solution and adsorption test

Lithium sulfide (Li_2S) and sulfur powders with a molar ratio of 1:5 were added into a certain amount of 1,3-dioxolane (DOL) and 1,2-dimethoxyethane (DME) (1:1 in volume) solvent. Then the mixture was stirred at 50 °C until the solid was fully dissolved to obtain the homogeneous Li_2S_6 solution. For the polysulfide adsorption test, 20 mg of Co-Fe-P and Co-Fe powder were added into two vials with 2 mL of 3 mM Li_2S_6 solution, respectively. All the steps were completed in the glovebox.

4.2.5 Symmetric cell assembly and measurements

The working electrodes for symmetric cells were fabricated without the presence of elemental sulfur. Typecially, Co-Fe-P (or Co-Fe) powder and PVDF powders with the weight ratio of

4:1 were mixed and grinded together in NMP solvent, then the homogeneous slurry was coated onto the Al foil and dried in the oven under vacume overnight. After that, the electrode was punched into circualr disks with a diameter of 12 mm. The areal sulfur laoding for the electrodes were about 1 mg cm^{-2}. Then the symmetric cell was assembled using the prepared electrodes both as working and counter electrodes. The electrolyte was 1 M Li_2S_6 in the conventional Li-S electrolyte containing 1M lithium bis(trifluoromethanesulfonyl) imide in DME and DOL (1:1 in volume) solvent with 1% $LiNO_3$ as additive. The cyclic voltammetry (CV) tests were performed in the voltage range of -0.7-0.7 V with a scan rate of 50 mV s^{-1}. The electrochemical impedance spectroscopy (EIS) spectra were measured in the frequency range of 200 kHz to 10 mHz with the amplitude of 10 mV. The electrochemical tests were carried out on a Bio-Logic VMP3 electrochemistry workstation.

4.2.6 Materials characterization

Field-emission SEM (Zeiss Supra 55VP) and TEM (JEOL JEM-2011) were used to study the morphology of the materials. The crystalline structure of the product was examined by using a Bruker D8 Discovery X-ray diffractometer. XPS analysis was performed to investigate the surface chemistry information of the materials by using a Kratos Axis 165 spectrometer. Thermogravimetric analysis (TGA) curves were collected from a 2960 SDT system. UV spectra were recorded on Agilent Cary 7000 UMS. N_2 adsorption-desorption isotherms were acquired using a Micromeritics 3Flex analyzer relying on the BET method. The pore size was obtained according to the BJH method.

4.2.7 Electrochemical measurements

The working electrode was made by blending and grinding S@Co-Fe-P (or S@Co-Fe), carbon black and polyvinylidene fluoride (PVDF) with the weight ratio of 8:1:1 in N-methylpyrrolidone, then the homogeneous slurry was casted on the Al foil and dried at 55 °C overnight under vacuum. The electrolyte was 1 M of lithium bis(trifluoromethanesulfonyl) imide in DME and DOL (1:1 in volume) solvent with 1% $LiNO_3$ as additive. The 2032-type coin-cells were assembled by using the S@Co-Fe-P (or S@Co-Fe) electrode, the Celgard separator and lithium metal anode in an Ar-filled glove box. The electrolyte amount was controlled about 20 μL per 1 mg of sulfur mass for the sulfur loading of about 1 mg cm^{-2} electrode. For the higher sulfur loading of about 3 and 3.7 mg cm^{-2} electrode, the electrolyte volume was controlled about 10 μL per 1 mg of sulfur. For the high sulfur loading of 5.5 mg cm^{-2}, the electrolyte amount was about 8 μL per 1 mg of sulfur. For pouch-cell level, the working electrode area was about 30 cm^2 and the areal sulfur loading was about 1 mg cm^{-2}. The galvanostatic charge-discharge tests were conducted at different current rates in the voltage window of 1.7-2.8 V by using the NEWARE battery tester. The cyclic voltammetry (CV) tests were performed at the current density of 0.1 mV s^{-1} by using a Bio-Logic VMP3 electrochemistry workstation. The electrochemical impedance spectroscopy (EIS) spectra were collected in the frequency range of 100 kHz to 0.01 Hz with the amplitude of 5 mV by using a Bio-Logic VMP3 electrochemistry workstation.

4.2.8 Computational methods

The first-principle calculations were conducted by using the CASTEP package.[565] The Perdew-Burke-Ernzerhof (PBE)[566] functional was applied to study the exchange-correlation potentials. Ultrasoft pseudopotentials[567] and Generalized Gradient Approximation were used to study the energy and geometry of the system. The adsorption energies (E_{ads}) of Li_2S_6 on the host material surface are defined as: $E_{ads} = E_{total} - E_{species} - E_{substrate}$, where E_{total}, $E_{species}$ and $E_{substrate}$ represent the total energy of the adsorption system, the energy of Li_2S_6, and the energy of CoP_2 (-111) or FeP_2 (101) or $FeCo_3$ (111) surface, respectively.

4.3 Results and discussion

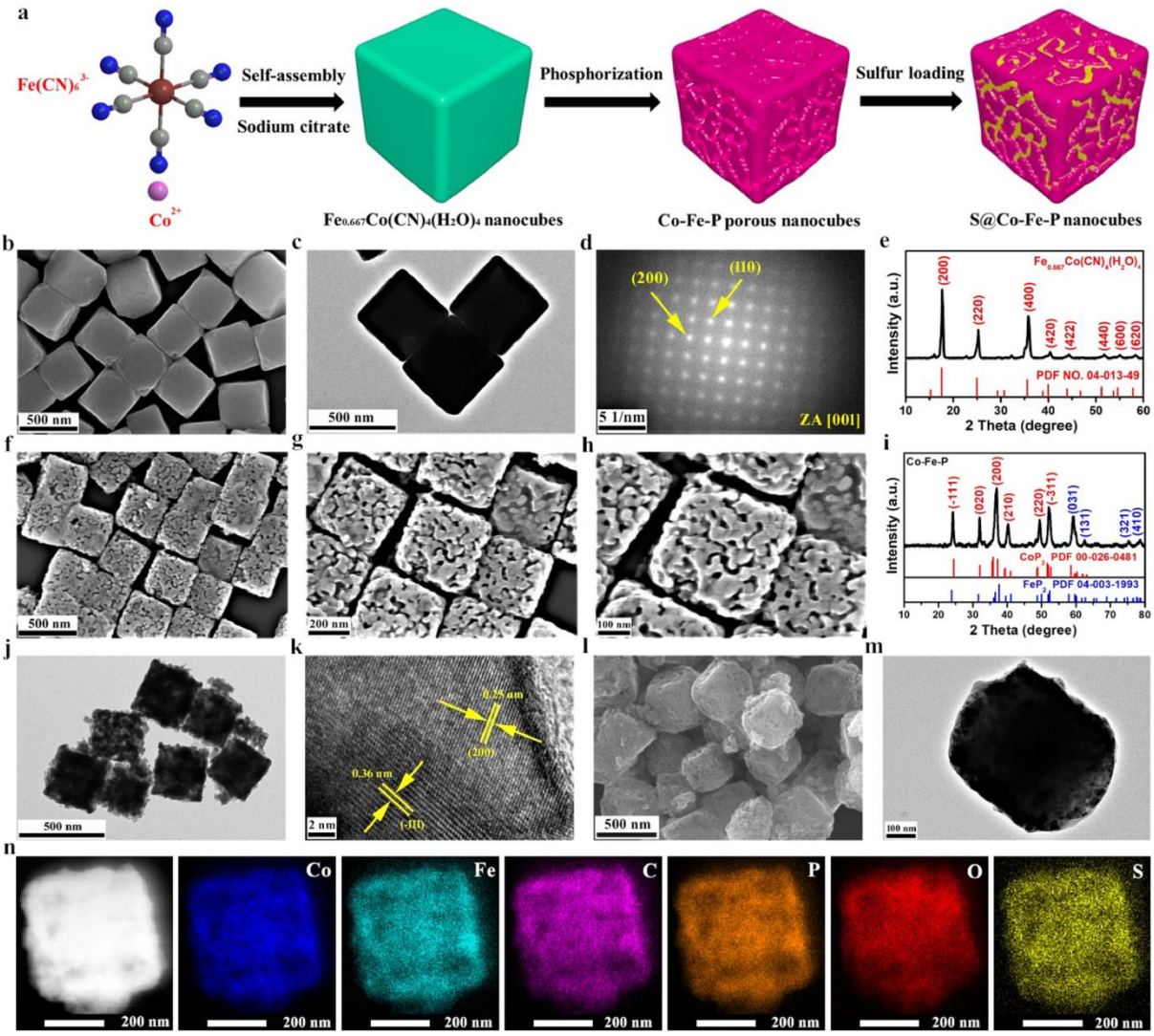

Figure 4.1 (a) Schematic illustration of the synthesis process for S@Co-Fe-P nanocubes. (b) SEM and (c) TEM images of $Fe_{0.667}Co(CN)_4(H_2O)_4$ nanocubes. (d) The SAED pattern of a single $Fe_{0.667}Co(CN)_4(H_2O)_4$ nanocube. (e) XRD pattern of $Fe_{0.667}Co(CN)_4(H_2O)_4$ nanocubes. (f-h) SEM images of Co-Fe-P nanocubes. (i) XRD pattern of Co-Fe-P nanocubes. (j) TEM and (k) HR-TEM images of Co-Fe-P nanocubes. (l) SEM and (m) TEM images of S@Co-Fe-P nanocubes. (n) STEM and corresponding elemental mappings (Co, Fe, C, P, O and S elements) of a single S@Co-Fe-P nanocube.

The synthesis process of S@Co-Fe-P nanocubes is schematically illustrated in **Figure 4.1**a and the detailed procedure is presented in the experimental section. Crystalline $Fe_{0.667}Co(CN)_4(H_2O)_4$ nanocubes were first prepared by a self-assembly approach using $Fe(CN)_6^{3-}$ and Co^{2+} as precursors. The obtained nanocubes are highly uniform with a very smooth surface (**Figure 4.2**a and **Figure 4.1**b, c). The average size is about 395 nm (**Figure 4.2**b).

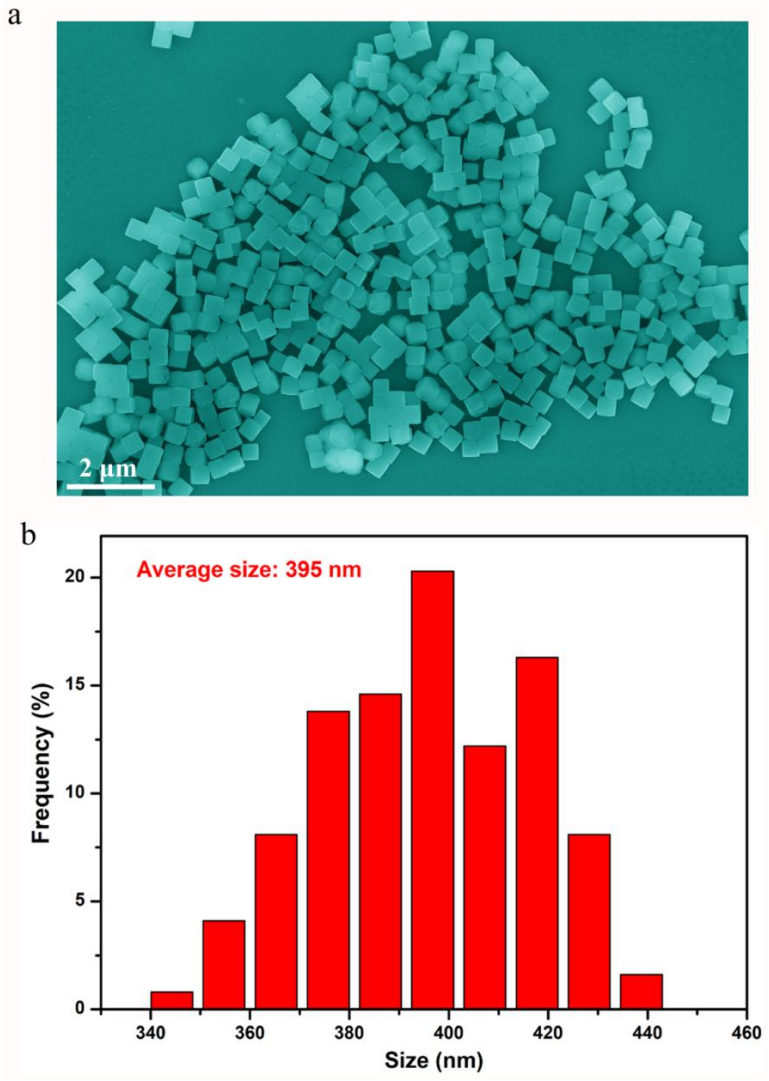

Figure 4.2 (a) Low resolution SEM image and (b) corresponding size distribution of $Fe_{0.667}Co(CN)_4(H_2O)_4$ nanocubes.

X-ray diffraction (XRD) analysis indicates that $Fe_{0.667}Co(CN)_4(H_2O)_4$ (PDF card No. 04-013-49) is the primary crystalline phase of the product (**Figure 4.1**e). The selected area electron diffraction (SAED) pattern (**Figure 4.1**d) of a single $Fe_{0.667}Co(CN)_4(H_2O)_4$ nanocube (**Figure 4.3**) can be indexed to the (200) and (110) crystal planes along the [001] zone axis, confirming their good single crystalline feature.

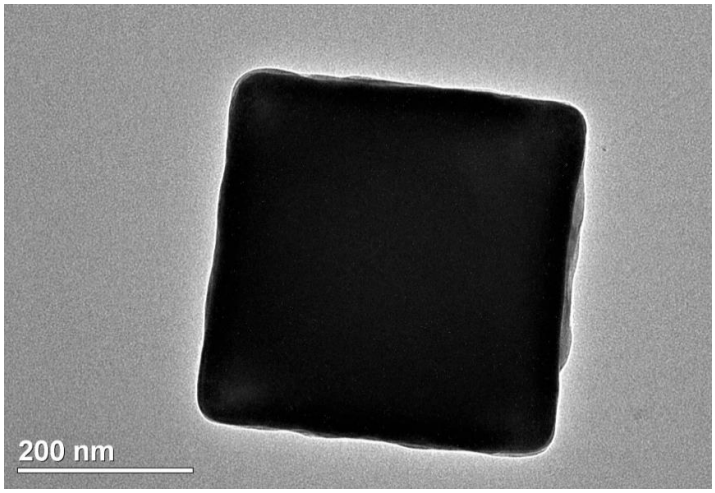

Figure 4.3 TEM image of a single $Fe_{0.667}Co(CN)_4(H_2O)_4$ nanocube.

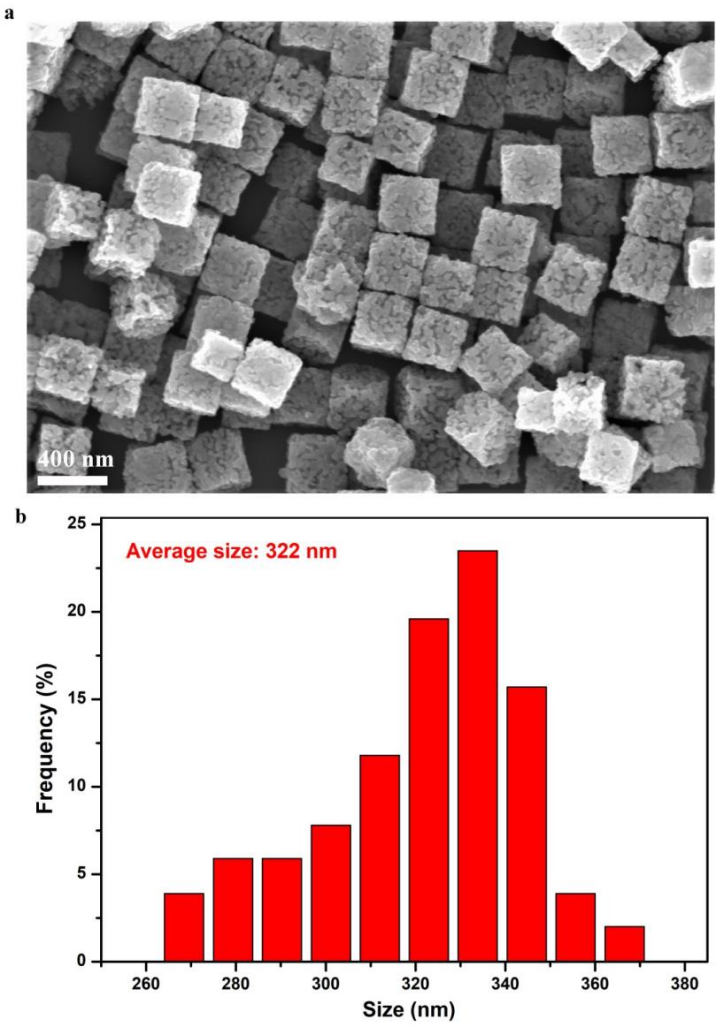

Figure 4.4 (a) Low resolution SEM image and (b) corresponding size distribution of Co-Fe-P nanocubes.

Then, the $Fe_{0.667}Co(CN)_4(H_2O)_4$ nanocubes were subjected to the phosphorization process at 600 °C for 2 h in Argon atmosphere, during which the PH_3 gas released from the NaH_2PO_2 reacted with them to generate the Co-Fe-P nanocubes. As shown in SEM images (**Figure 4.4**a and **Figure 4.1**f-h), the Co-Fe-P nanocubes maintain the uniform cubic morphology, whereas the average size of the nanocubes has decreased to about 322 nm (**Figure 4.4**b). This was ascribed to the structure shrink during the annealing and phosphorization process. Impressively, abundant interconnected-pore architecture were created throughout the

Co-Fe-P nanocubes, which would be highly beneficial for sulfur loading as well as providing sufficient electrical contact and adsorption sites for polysulfide conversion, thus significantly increasing the sulfur utilization efficiency and moderating the diffusion of intermediate polysulfides upon cycling.

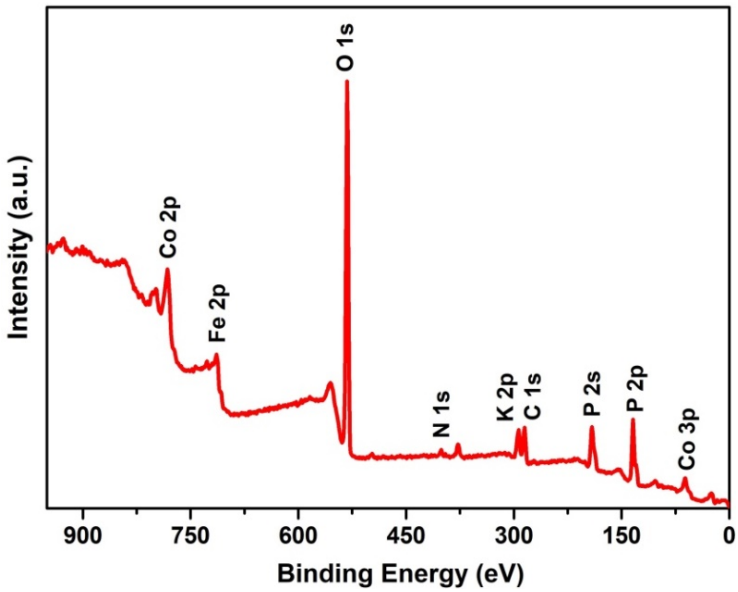

Figure 4.5 XPS survey spectrum of Co-Fe-P nanocubes.

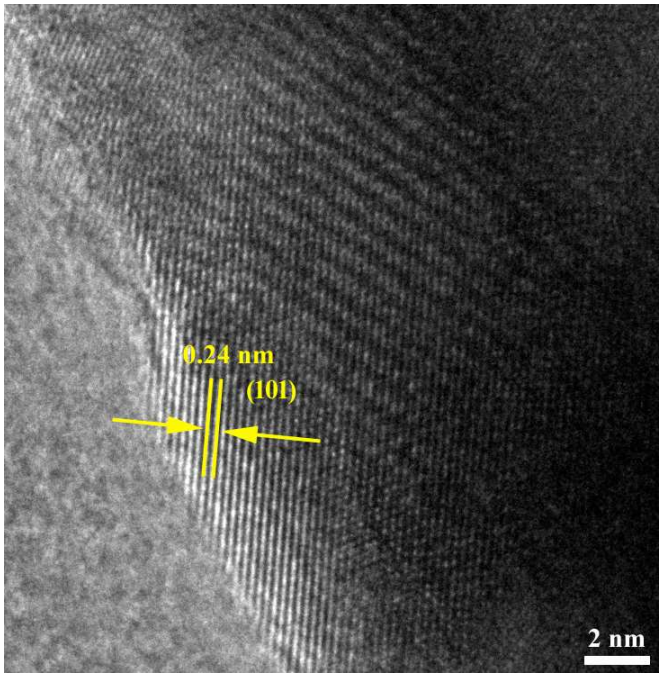

Figure 4.6 HR-TEM image of Co-Fe-P nanocubes. The lattice fringe is attributed to the (101) plane of FeP_2.

The TEM image further certifies the highly porous structure of the Co-Fe-P nanocubes (**Figure 4.1**j). The XRD analysis indicates that CoP_2 (PDF card No. 00-026-0481) and FeP_2 (PDF card No. 04-003-1993) are the main phase of the product (**Figure 4.1**i). The X-ray photoelectron spectroscopy (XPS) measurement further confirms the coexistence of Co, Fe, K, P, C, N and O elements in Co-Fe-P nanocubes (**Figure 4.5**). The high-resolution TEM (HRTEM) images in **Figure 4.1**k and **Figure 4.6** show three distinct fringes with spacings of 0.25 nm, 0.36 nm and 0.24 nm, which are in accordance with the (200), (-111) facets of CoP_2 and (101) plane of FeP_2 crystals, respectively. The specific surface area and pore information of Co-Fe-P nanocubes were studied by nitrogen adsorption-desorption isotherms (**Figure 4.7**). The Brunauer-Emmett-Teller (BET) specific surface area and pore volume are 93.5 m^2/g and 0.68 cm^3/g, respectively. The pore size distribution of Co-Fe-P nanocubes was further analyzed as shown in the inset of **Figure 4.7**, revealing abundant mesopores centred at 47 nm.

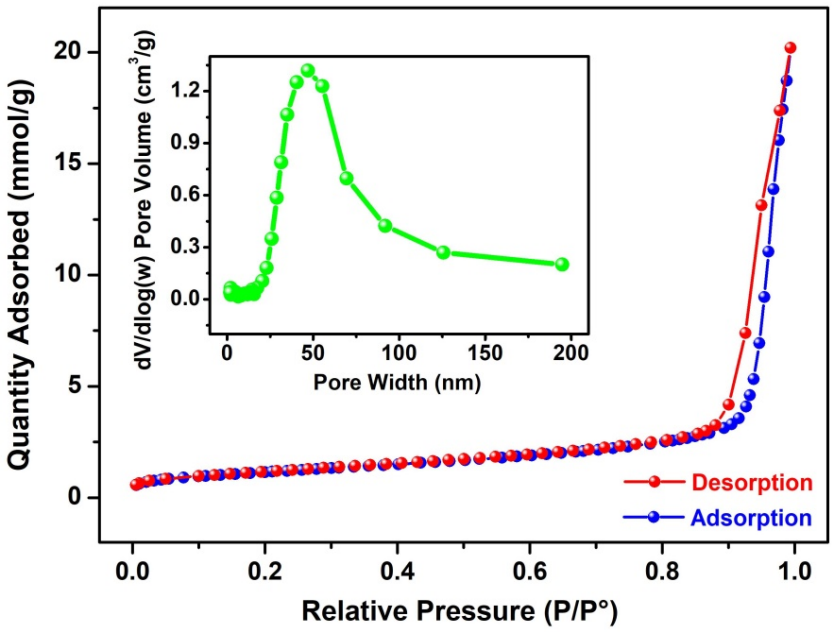

Figure 4.7 Nitrogen adsorption-desorption isotherm of the Co-Fe-P nanocubes. The inset shows the pore size distribution acquired using the BJH method.

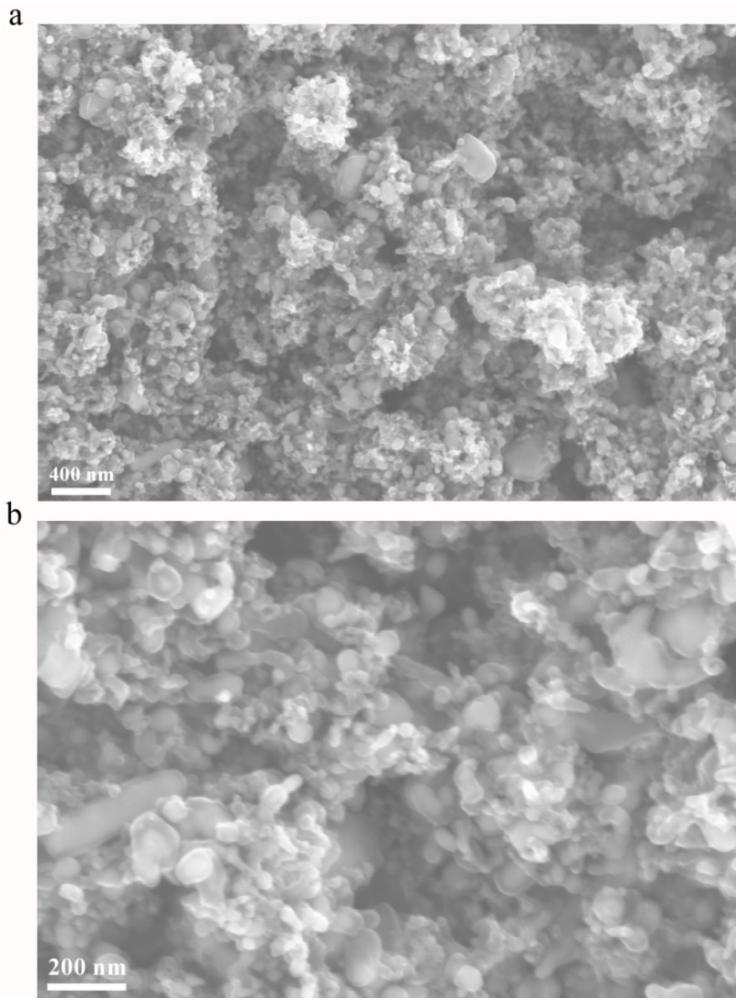

Figure 4.8 SEM images of Co-Fe nanoparticles.

It was interesting to note that, without the phosphorization process, the $Fe_{0.667}Co(CN)_4(H_2O)_4$ nanocubes were transformed into irregular particles after the same temperature annealing process, and the cubic morphology was completely destroyed (**Figure 4.8**). The XRD analysis indicates that the as-obtained product mainly contains $Fe_{0.25}Co_{0.75}$ (PDF card No. 04-003-3891) alloy phase, along with a small amount of oxides such as Fe_2O_3 (**Figure 4.9**). Here, "Co-Fe" is just used to denote the as-prepared particles without the phosphorization process. The BET specific surface area and pore volume of the Co-Fe

particles are 56.4 m^2/g and 0.25 cm^3/g, respectively, which are lower than that of Co-Fe-P nanocubes (**Figure 4.10**).

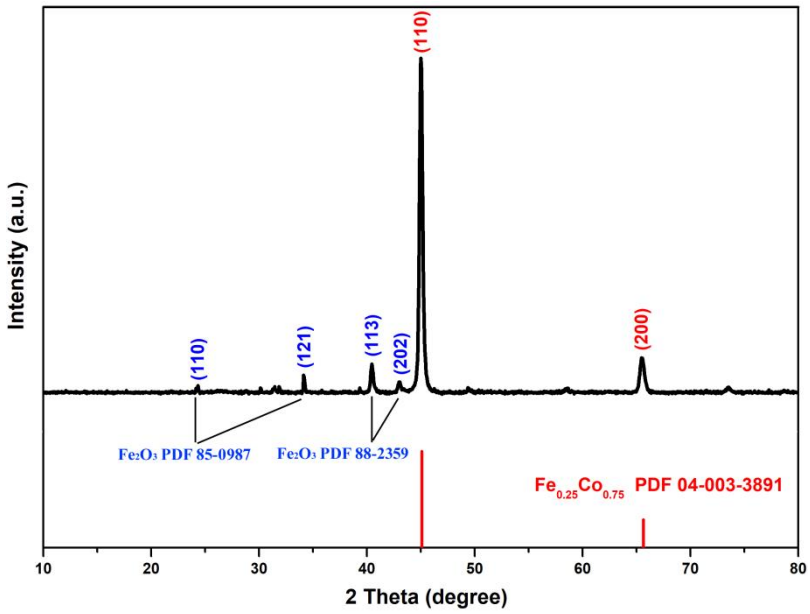

Figure 4.9 XRD pattern of Co-Fe nanoparticles.

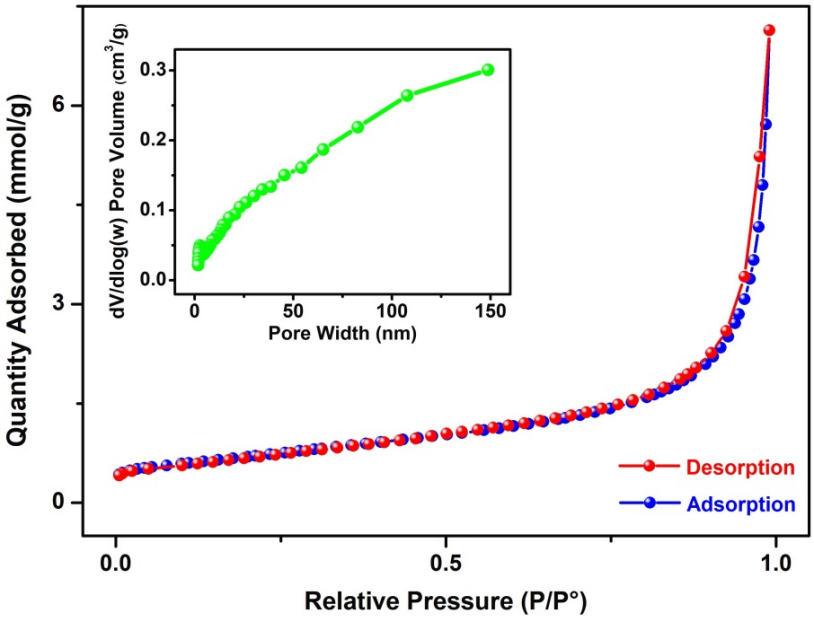

Figure 4.10 Nitrogen adsorption-desorption isotherm of the Co-Fe nanoparticles. The inset shows the pore size distribution obtained using the BJH method.

Furthermore, it was noticed that when the annealing temperature was decreased from 600 to 500 °C, the interconnected-pore architecture was partly disappeared although the cubic morphology was maintained (**Figure 4.11**). However, when the annealing temperature increased from 600 to 650 °C, the cubic morphology was partly collapsed and the size also largely shrunk (**Figure 4.12**). Further increasing the annealing temperature to 700 °C, the cubic morphology was totally collapsed and transformed into irregular particles (**Figure 4.13**). This indicates that the appropriate annealing temperature is crucial for the formation of uniform Co-Fe-P nanocubes with interconnected-pore architecture.

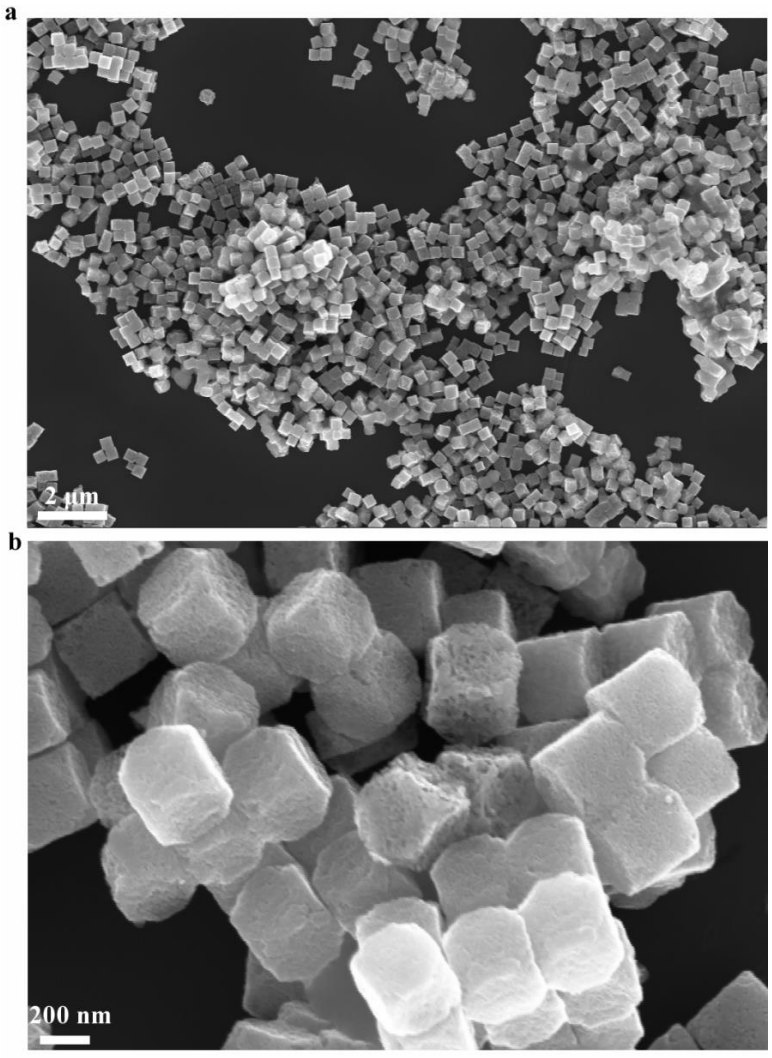

Figure 4.11 SEM images of Co-Fe-P nanoparticles synthesized at 500 °C.

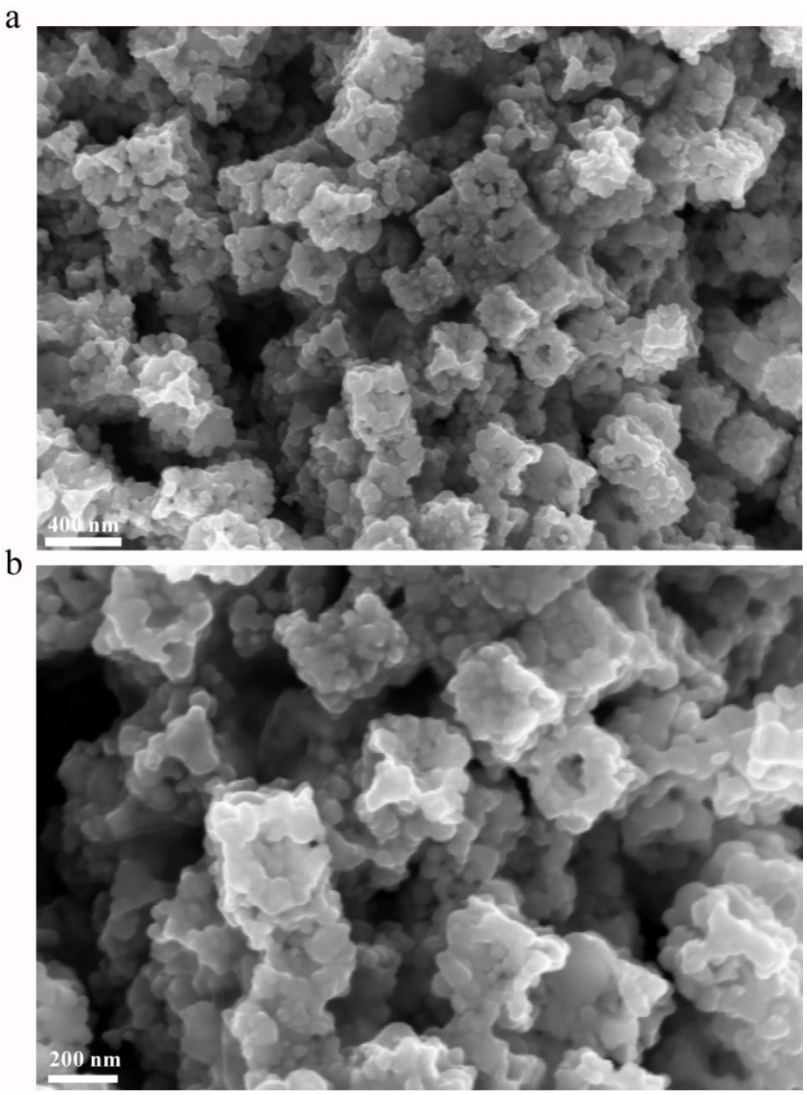

Figure 4.12 SEM images of Co-Fe-P nanoparticles synthesized at 650 °C.

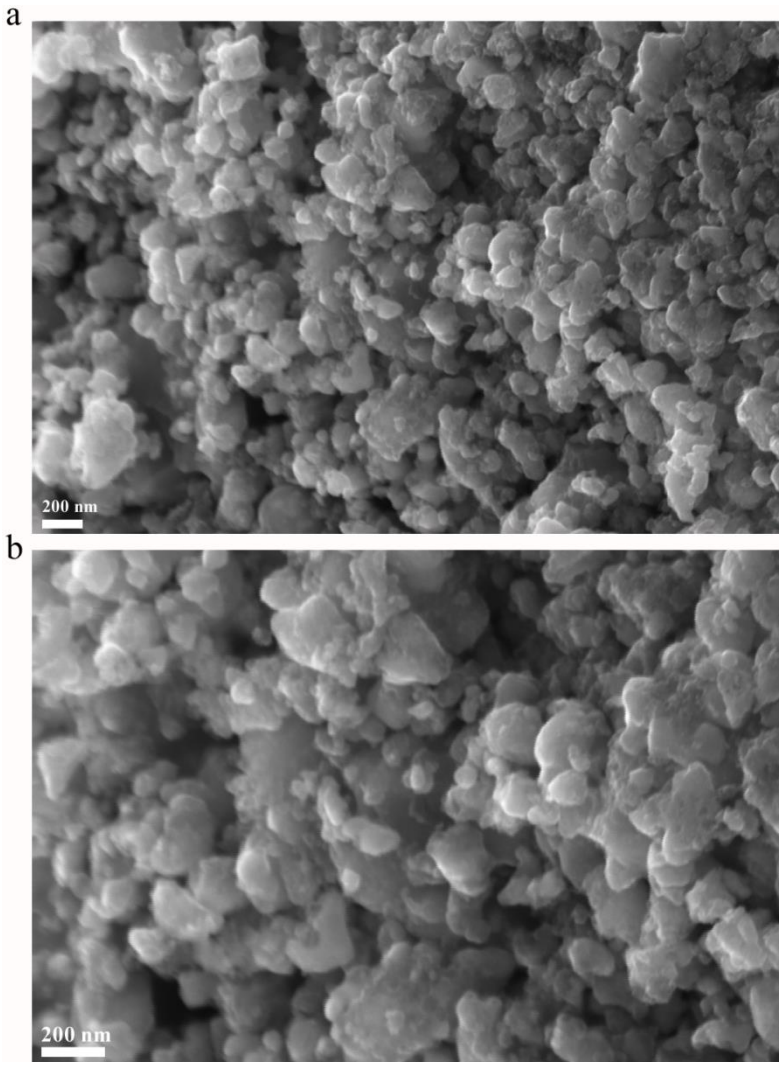

Figure 4.13 SEM images of Co-Fe-P nanoparticles synthesized at 700 °C.

The polar Co-Fe-P nanocubes with interconnected-pore architecture motivated us to load sulfur into them and apply as cathodes for Li-S batteries. **Figure 4.1**l shows the SEM image of sulfur-loaded Co-Fe-P nanocubes, which maintained their original cubic shape. **Figure 4.1**m demonstrates the TEM image of an individual S@Co-Fe-P nanocube and it shows a much darker contrast compared to the Co-Fe-P nanocubes in **Figure 4.1**j, manifesting that sulfur has been successfully encapsulated into the interconnected-pore structures. **Figure 4.1**n displays a scanning TEM (STEM) image and the corresponding elemental mappings of a

single S@Co-Fe-P nanocube. It reveals that sulfur has been homogeneously distributed in the porous architecture of Co-Fe-P nanocubes. For comparison, sulfur was also loaded into the Co-Fe particles by the same process. However, numerous sulfur aggregations can be easily discerned due to the low porosity of the Co-Fe particles (**Figure 4.14**). To make a fair comparison, both the sulfur contents in S@Co-Fe-P and S@Co-Fe were controlled at about 70% (**Figure 4.15**).

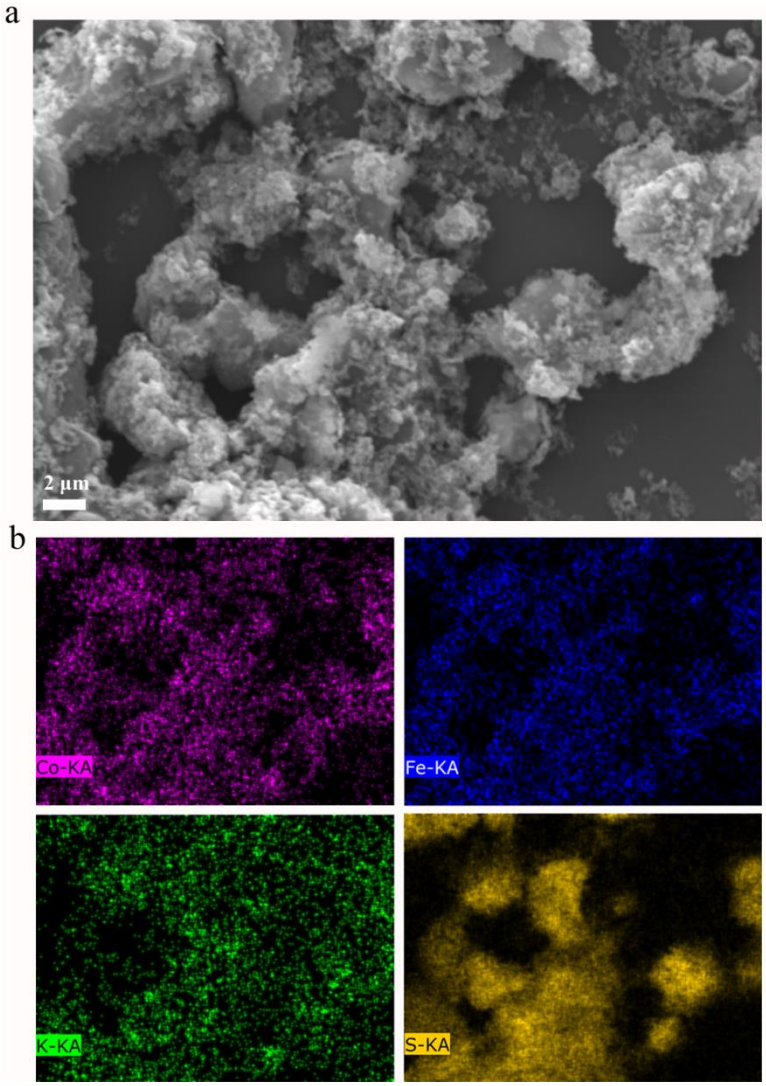

Figure 4.14 (a) SEM image and the (b) corresponding elemental mappings of the S@Co-Fe particles.

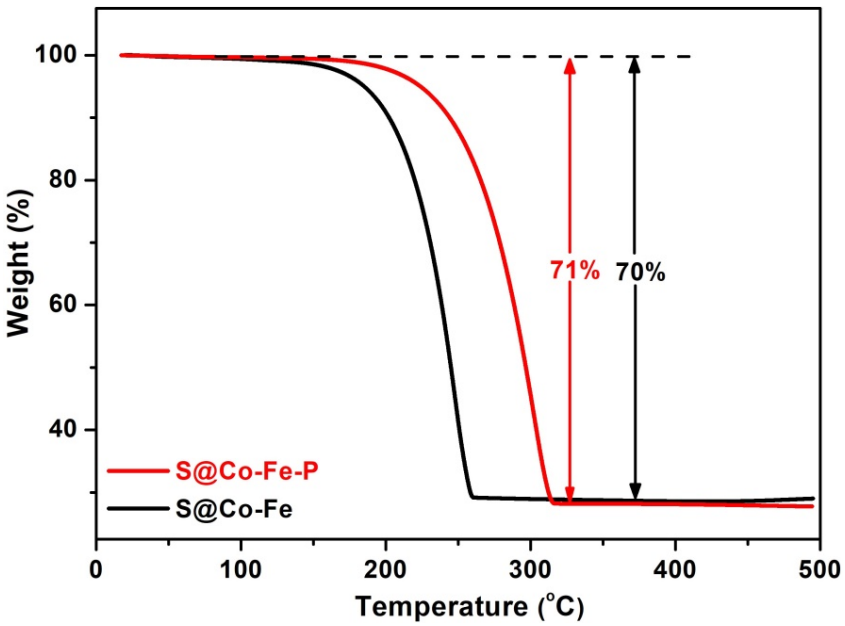

Figure 4.15 TGA curves of S@Co-Fe-P and S@Co-Fe nanocubes at a heating rate of 10 °C/min under Ar atmosphere.

Coin cells were then assembled to assess the electrochemical performances of S@Co-Fe-P nanocubes as cathodes for Li-S batteries. The cyclic voltammetry (CV) curves of both S@Co-Fe-P and S@Co-Fe cathodes (**Figure 4.16**a) display two representative cathodic peaks, which are ascribed to the transformation from S_8 to long-chain polysulfides followed by the further reduction to short-chain sulfides, respectively. The anodic peaks are attributed to the reverse oxidation process from short-chain sulfides to S_8. It is evident to note that the reduction peaks of the S@Co-Fe-P cathode are more positive and the oxidation peak is more negative compared to the S@Co-Fe cathode, suggesting the promoted polysulfide redox kinetics by Co-Fe-P nanocubes.

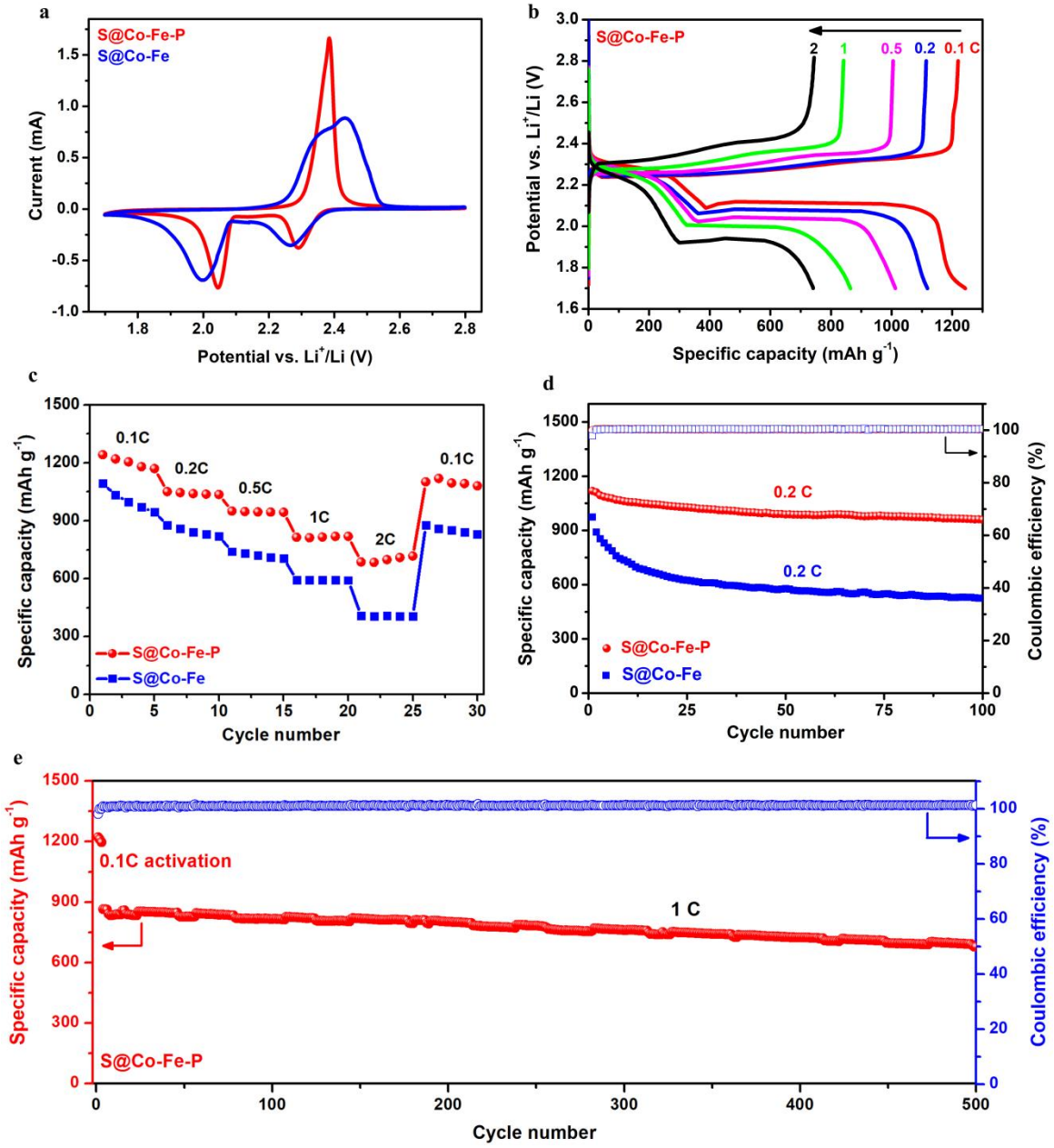

Figure 4.16 (a) The 2nd cycle CV curves of the S@Co-Fe-P and S@Co-Fe cathodes at 0.1 mV s^{-1}. (b) The 1st cycle charge-discharge voltage profiles of S@Co-Fe-P cathodes at current rates of 0.1, 0.2, 0.5, 1 and 2 C. (c) Rate performances of S@Co-Fe-P and S@Co-Fe cathodes. (d) Cycling performances and Coulombic efficiencies of S@Co-Fe-P and S@Co-Fe cathodes at 0.2 C. (e) Long cycling performance and Coulombic efficiency of the S@Co-Fe-P cathode at 1 C. The areal sulfur loading is about 1 mg cm^{-2}.

Figure 4.17 compares the first-cycle charge-discharge voltage profiles of S@Co-Fe-P and S@Co-Fe electrodes at 0.1 C. The voltage profiles of S@Co-Fe-P cathode consists of two typical discharge plateaus at around 2.3 and 2.1 V, which is consistent with the CV curve. In addition, the discharge plateaus of the S@Co-Fe-P cathode are longer and flatter with a higher specific capacity and a lower polarization compared to the S@Co-Fe cathode, suggesting the more efficient redox reaction kinetics promoted by Co-Fe-P nanocubes. The galvanostatic charge-discharge voltage profiles of S@Co-Fe-P electrodes at various current densities are presented in **Figure 4.16**b. The electrodes exhibited high initial specific capacities of 1243, 1118, 1012, 863 and 741 mAh g^{-1} at 0.1, 0.2, 0.5, 1 and 2 C rates, respectively. Even when the current rate was increased to 2 C, the charge-discharge voltage profiles of the S@Co-Fe-P electrode still contains two typical discharge plateaus, suggesting the low polarization characteristic even at high current rate. Next, the rate performances of the S@Co-Fe-P and S@Co-Fe cathodes were evaluated by successively increasing the current rate from 0.1 C to 0.2, 0.5, 1 and 2 C (**Figure 4.16**c). The S@Co-Fe-P electrode showed much higher discharge capacity and better stability under the different current rates compared to the S@Co-Fe electrode. When the current rate was returned back to 0.1 C, the specific capacity of the S@Co-Fe-P electrode was recovered to 1102 mAh g^{-1}, suggesting its good stability even after the high rate charge-discharge process.

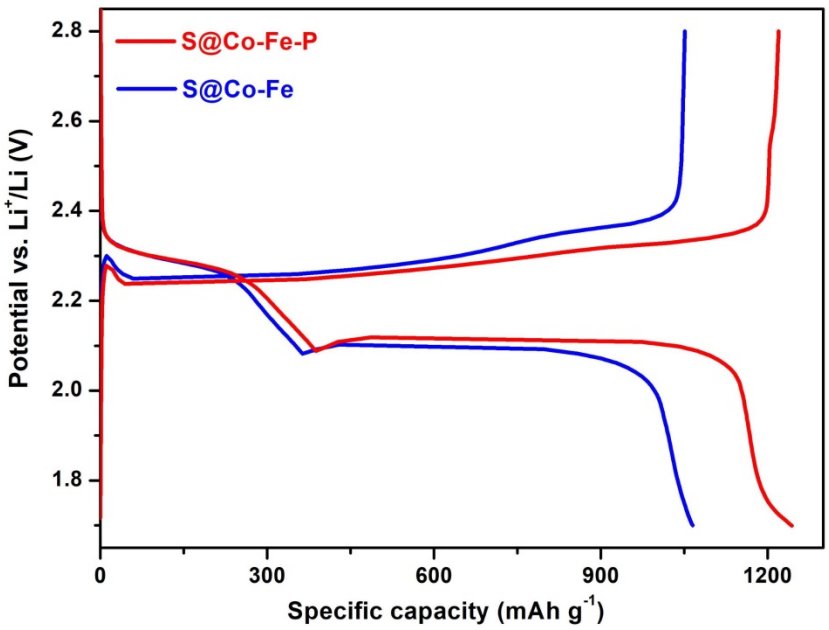

Figure 4.17 The galvanostatic charge-discharge voltage profiles of S@Co-Fe-P and S@Co-Fe cathodes at 0.1C.

To probe the charge transfer properties of S@Co-Fe-P and S@Co-Fe cathodes, electrochemical impedance spectroscopy (EIS) tests were performed (**Figure 4.18**). The S@Co-Fe-P electrode shows much lower charge transfer resistance (R_{ct}=56.81 Ω) compared to the S@Co-Fe electrode (205.8 Ω) (**Table 4.1**), which contributes to the enhanced rate performance and lower polarization.

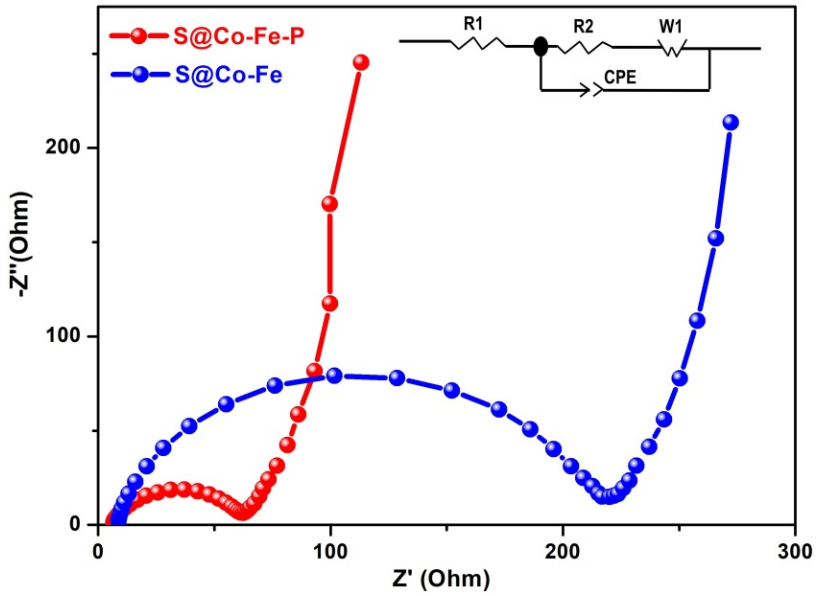

Figure 4.18 Nyquist plots of S@Co-Fe-P and S@Co-Fe electrodes before cycling. The inset shows equivalent circuit.

Table 4.1 Parameters identified by modeling the impedance spectra in **Figure 4.18**

Working Electrode	R_e (Ω)	R_{ct} (Ω)	Y1($\Omega^{-1}cm^{-2}s^{-n}$)	n1
S@Co-Fe-P	5.761	56.81	2.46×10^{-5}	0.74
S@Co-Fe	8.003	205.8	4.89×10^{-6}	0.85

The cycling performances of the S@Co-Fe-P and S@Co-Fe cathodes were then evaluated at a relatively low current rate of 0.2 C (**Figure 4.16**d). A high specific capacity of 1118 mAh g^{-1} was achieved for the S@Co-Fe-P electrode. After 100 cycles, it still remained at a high specific capacity of 958 mAh g^{-1}, indicating the polysulfide shuttle was effectively restrained by the Co-Fe-P nanocubes. Moreover, the Coulombic efficiency of the S@Co-Fe-P electrode approached 100% after the initial few cycles. In contrast, the S@Co-Fe electrode delivered an initial specific capacity of 973 mAh g^{-1}, and maintained a very low specific capacity of 524 mAh g^{-1} after 100 cycles, suggesting the low sulfur utilization and severe polysulfide shuttle upon cycling.

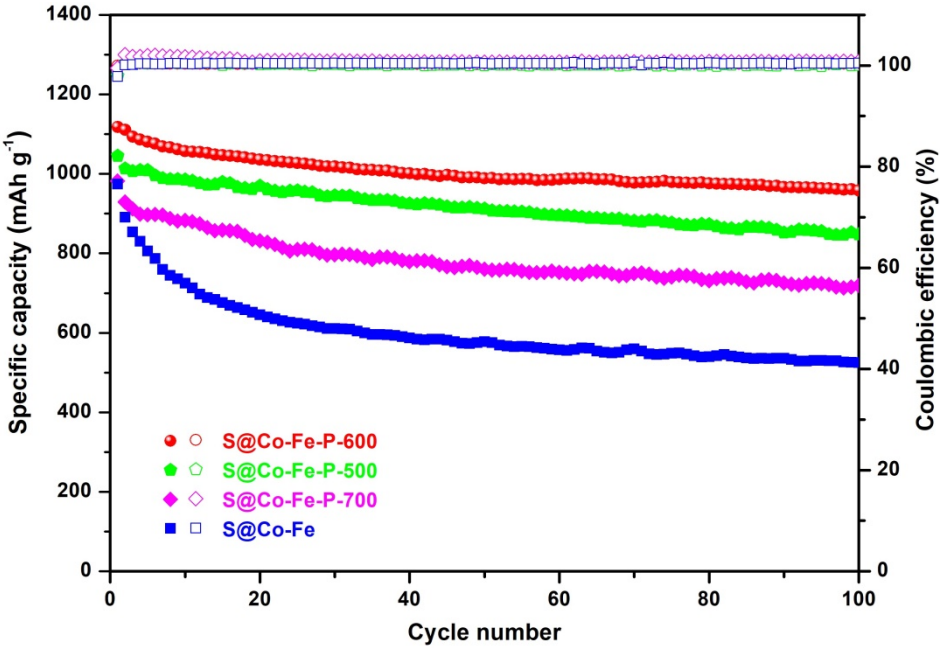

Figure 4.19 Cycling performances and Coulombic efficiencies of S@Co-Fe-P-600, S@Co-Fe-P-500, S@Co-Fe-P-700 and S@Co-Fe cathodes.

The cycling performances of Co-Fe-P with different annealing temperatures were also tested as shown in **Figure 4.19**. The Co-Fe-P host material synthesized at 600 °C demonstrated higher specific capacity and better cycling stability than that of Co-Fe-P samples prepared at 500 °C and 700 °C, respectively. This is because the Co-Fe-P synthesized at 600 °C contains more abundant interconnected-pore architectures, which can provide sufficient interfaces to trap and power the conversion of lithium polysulfides. In contrast, as the interconnected-pore structure of Co-Fe-P synthesized at 700 °C was totally collapsed, the S@Co-Fe-P-700 exhibited much lower discharge capacity and poorer cycling performance compared with S@Co-Fe-P-600 and S@Co-Fe-P-500. When the current density increased to 1 C, the S@Co-Fe-P electrode also demonstrated excellent cycling stability (**Figure 4.16**e). A high specific capacity of 863 mAh g^{-1} at 1 C was obtained after the initial activation process at 0.1 C for electrode wettability. After the long-term cycling for 500

cycles, it still maintained a high specific capacity of 678 mAh g^{-1}, accompanying with an average capacity decay rate of only 0.043% per cycle.

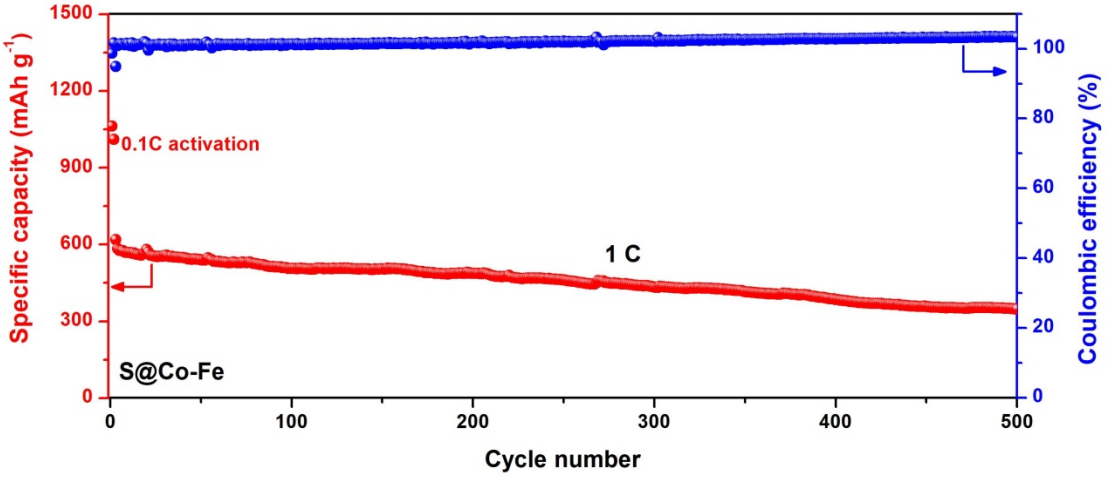

Figure 4.20 Cycling performance and Coulombic efficiency of the S@Co-Fe cathode at 1 C.

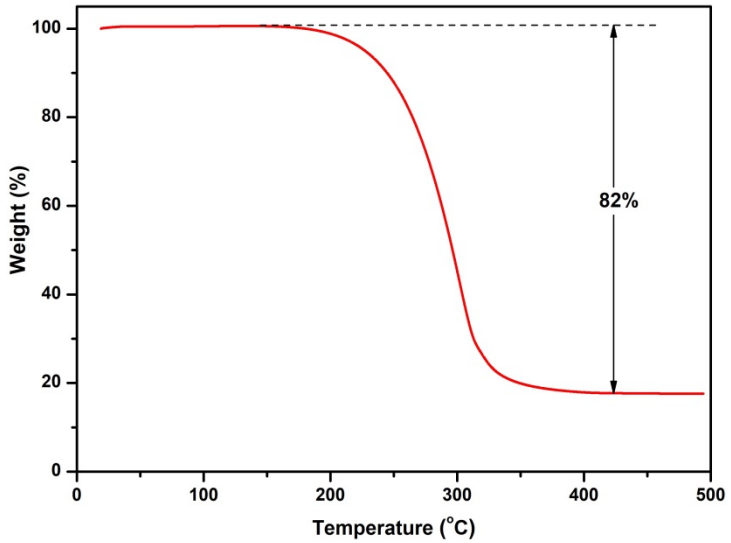

Figure 4.21 TGA curve of S@Co-Fe-P nanocubes with a higher sulfur content of about 82%.

On the contrary, the S@Co-Fe electrode displayed a lower initial specific capacity of 620 mAh g^{-1} at 1 C, and it showed inferior cycling performance with a retained capacity of only 348 mAh g^{-1} after 500 cycles (**Figure 4.20**). In addition, when the sulfur content in the

S@Co-Fe-P was increased to about 82% (**Figure 4.21**), the electrode also shows high specific capacity with superior cycling stability (**Figure 4.22**).

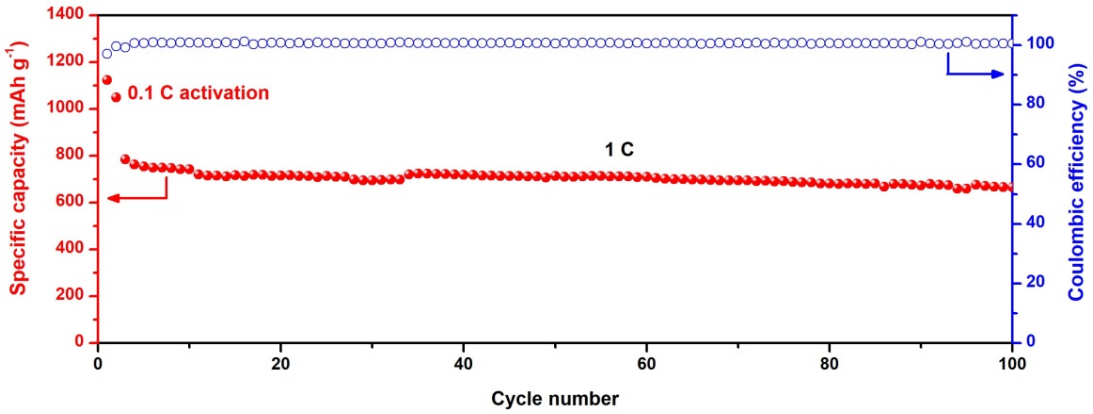

Figure 4.22 Cycling performance and Coulombic efficiency of S@Co-Fe-P cathode at 1C with a higher sulfur content of 82%. The areal sulfur loading is about 3 mg cm^{-2}.

Table 4.2 compares the cycling performances of this work with the recent reported metal compounds as sulfur host materials for Li-S batteries, demonstrating the great advantages of Co-Fe-P nanocubes.

Table 4.2 Comparison of the cycling performance of this work with other previously reported metal compounds as sulfur host materials for Li-S batteries.

Name	Initial capacity ($mAh\ g^{-1}$)	Cycle number	Current rate (C)	Capacity decay rate per cycle (%)
This work	**863**	**500**	**1**	**0.043**
S/WO_3[568]	769	100	0.2	0.56
$C@TiO_2@C–S$[117]	774	500	2	0.068
Ni_3S_2[212]	526	300	0.5	0.24
S/Ti_4O_7[128]	850	500	2	0.059

NbS_2@S@IG[230]	500	600	1	0.033
S/TiS_2[212]	700	300	0.5	0.073
S/TiO-Graphene[135]	831	200	2	0.226
a-Ti_3C_2−S/d-Ti_3C_2/PP[319]	800	200	2	0.248
S/FeS[212]	705	300	0.5	0.175
S/W_2C NPs-CNFs[251]	864	500	1	0.06
S/SnS_2[212]	610	300	0.5	0.229
S/TiN[241]	988	500	0.5	0.07
S/ VS_2[212]	830	300	0.5	0.052
S/WC[568]	843	100	0.2	0.18
S/MgO[150]	860	100	0.2	0.18
S/CoS_2[212]	684	300	0.5	0.05

The cells were then disassembled to analyze. **Figure 4.23** displayed digital photographs of the separators paired with S@Co-Fe-P and S@Co-Fe cathodes, respectively, after 500 cycles at 1 C. Bulky polysulfides can be easily discerned on the surface of the separator paired with the S@Co-Fe cathode, indicating that severe polysulfide dissolution and shuttle effect occurred in the S@Co-Fe based battery. In contrast, the separator paired with S@Co-Fe-P cathode was much cleaner and only a small amount of polysulfide residues could be visible, suggesting that the polysulfide dissolution and shuttle effect were effectively suppressed.

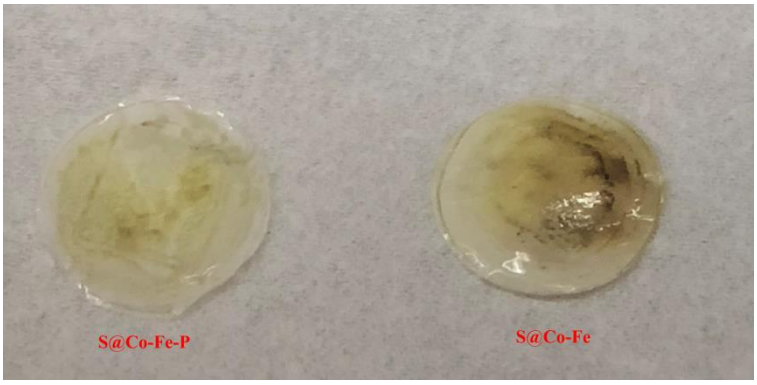

Figure 4.23 Digital photographs of the separators paired with S@Co-Fe-P and S@Co-Fe cathodes after 500 cycles at 1 C, respectively.

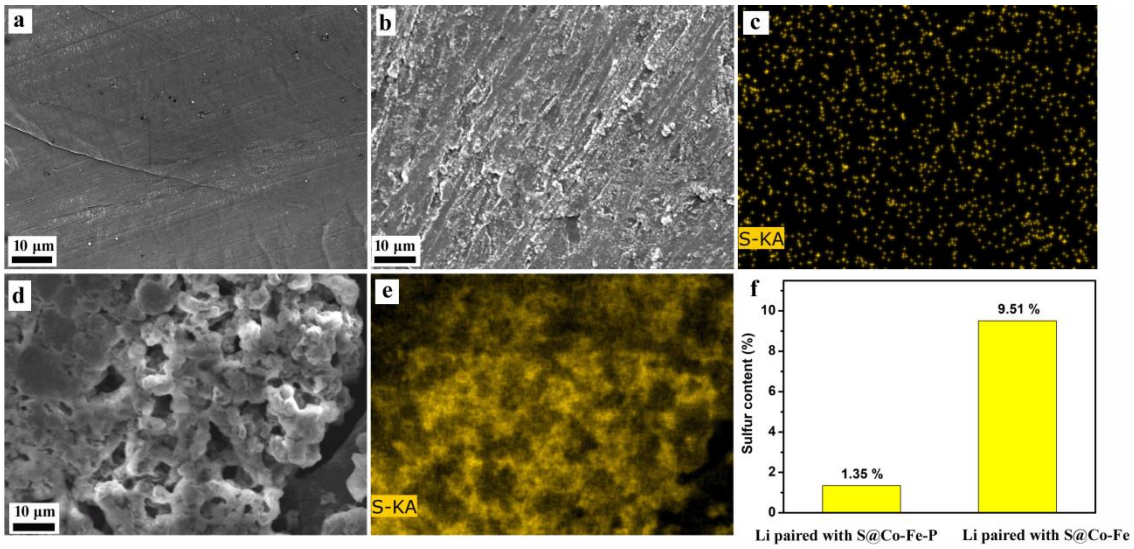

Figure 4.24 (a) SEM image of the lithium metal anode before cycling process. (b) SEM image and (c) corresponding sulfur mapping image of lithium metal anode paired with S@Co-Fe-P cathode after 500 cycles at 1 C. (d) SEM image and (e) corresponding sulfur mapping image of lithium metal anode paired with S@Co-Fe cathode after 500 cycles at 1 C. (f) The sulfur contents on the lithium metal anodes obtained from EDX analysis paired with S@Co-Fe-P and S@Co-Fe cathodes after 500 cycles at 1C, respectively.

To further reveal the suppression of the shuttle effect towards lithium metal anodes, the morphology of the lithium metal anodes were observed by SEM after cycling (**Figure 4.24**).

Abundant dendrite structures and significant corrosion of lithium metal were easily observed for the S@Co-Fe cathode, meanwhile the sulfur content on the lithium metal anode was as high as 9.51% (**Figure 4.24**d-f and **Figure 4.25**). In contrast, the surface of the lithium metal anode paired with the S@Co-Fe-P cathode was very smooth and uniform with a very low sulfur content of only 1.35% on the lithium metal anode (**Figure 4.24**b, c, f and **Figure 4.26**), again manifesting the polysulfide shuttle effect was efficiently restrained by the Co-Fe-P host. The superior cycling stability of the S@Co-Fe-P electrode should be attributed to the strong polar characteristic along with the highly interconnected-pore architecture that provided favorable microenvironments to immobilize lithium polysulfides.

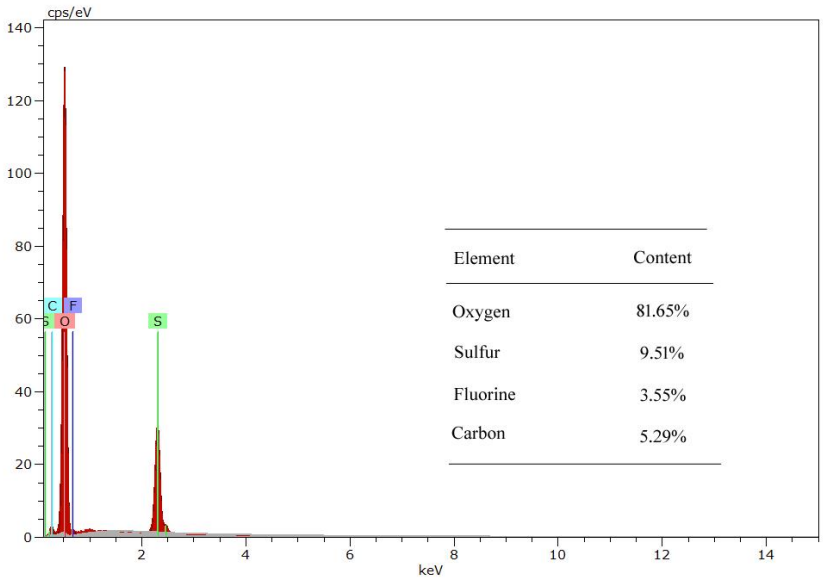

Figure 4.25 EDX spectrum of the lithium metal anode paired with the S@Co-Fe cathode after 500 cycles at 1 C. The inset shows the elemental contents and the carbon come from the nearby conducting substrate.

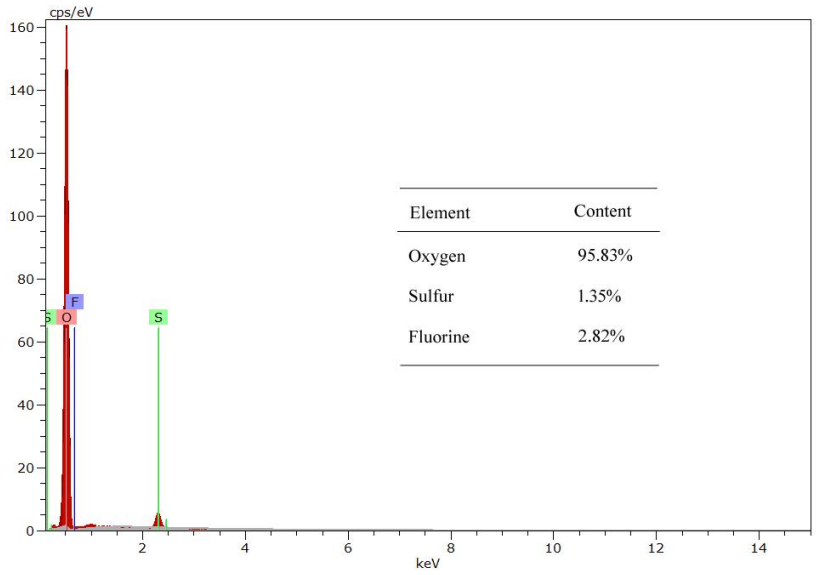

Figure 4.26 EDX spectrum of the lithium metal anode paired with the S@Co-Fe-P cathode after 500 cycles at 1 C. The inset shows the elemental contents.

Since the high areal sulfur loading is a crucial factor to achieve high energy density in practical Li-S batteries, we further investigated the feasibility of S@Co-Fe-P electrode at higher sulfur loading. High areal capacities of 3.8 and 4.6 mAh cm^{-2} were achieved when the areal sulfur loadings were further increased to about 3.7 and 5.5 mg cm^{-2}, respectively (**Figure 4.27**a). More importantly, even after 100 cycles, the S@Co-Fe-P electrode with an areal sulfur loading of 5.5 mg cm^{-2} still maintained a high areal capacity of 3.5 mAh cm^{-2}, demonstrating its superior cycling performance with high areal sulfur loading. **Figure 4.28** compares the areal capacity of this work with other previously reported metal compounds as sulfur host materials for Li-S batteries, demonstrating its superior electrochemical performance among existing sulfur host materials based on metal compounds.

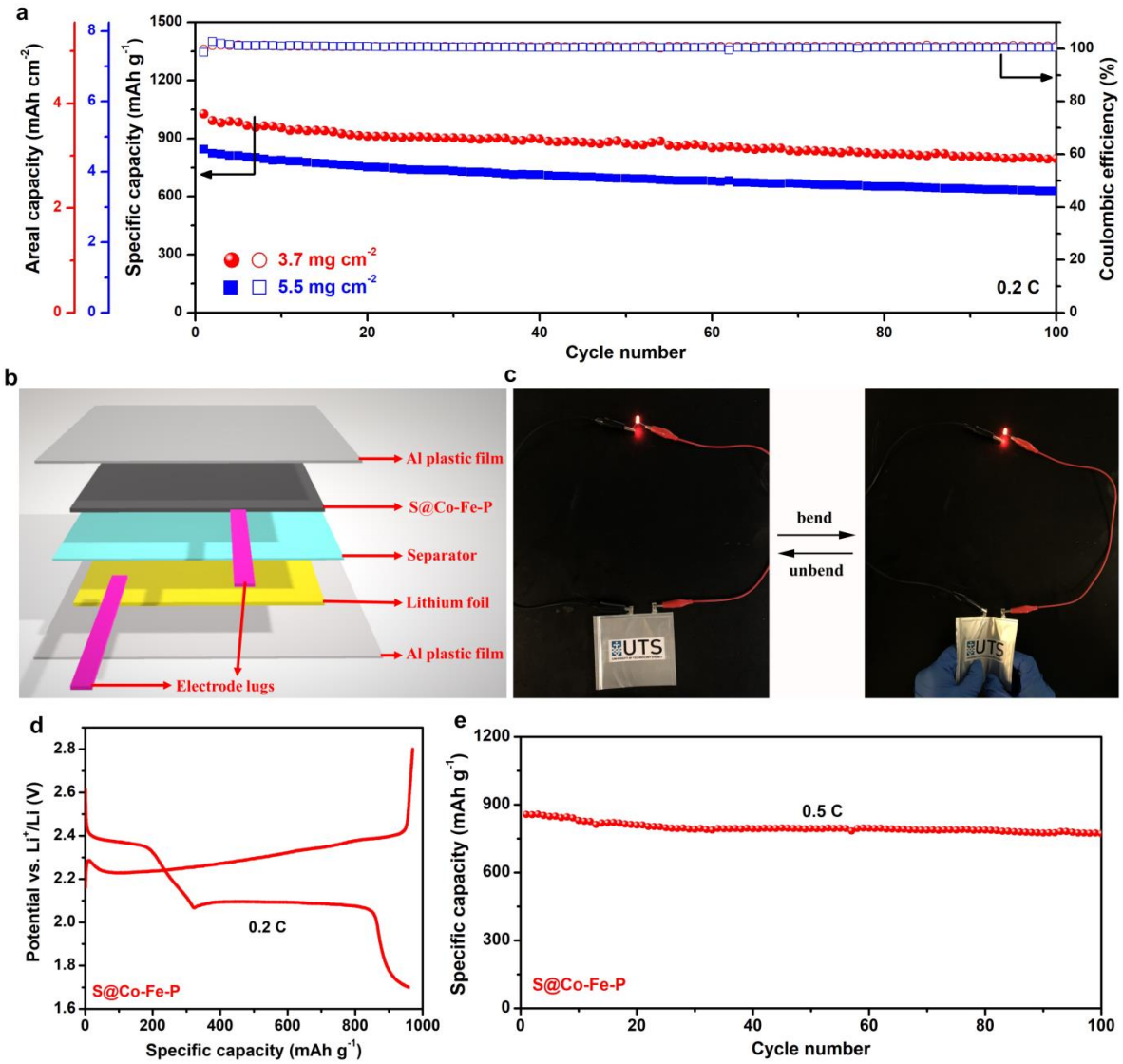

Figure 4.27 (a) Cycling performances and Coulombic efficiencies of S@Co-Fe-P cathodes at 0.2 C with high areal sulfur loadings of about 3.7 and 5.5 mg cm^{-2}, respectively. (b) Schematic diagram of the soft-package Li-S battery based on a S@Co-Fe-P cathode. (c) Photographs of a LED lighted by a S@Co-Fe-P based soft-package Li-S battery upon bending-unbending operations. Logo used with permission from University of Technology Sydney (UTS). (d) The first-cycle charge-discharge voltage profiles of S@Co-Fe-P based Li-S pouch-cell at 0.2 C. (e) Cycling performance of S@Co-Fe-P based Li-S pouch-cell at 0.5 C. The areal sulfur loading for the pouch-cell is about 1 mg cm^{-2}.

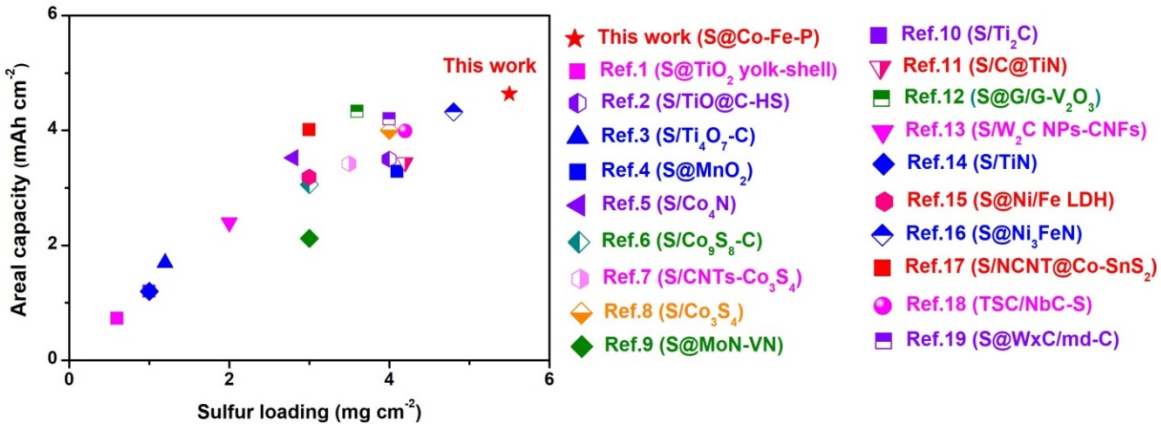

Figure 4.28 Comparison of the areal capacity of this work with other reported metal compounds as sulfur host materials for Li-S batteries. The Ref.1 to Ref.19 in the figure refer to: [1] *Nat. Commun.* 2013, *4*, 1331; [2] *Nat. Commun.* 2016, *7*, 13065; [3] *Adv. Funct. Mater.* 2017, *27*, 1701176; [4] *ACS Nano* 2016, *10*, 4192-4198; [5] *ACS Nano* 2017, *11*, 6031-6039; [6] *Nano Energy* 2017, *38*, 239-248; [7] *J. Am. Chem. Soc.* 2017, *139*, 12710-12715; [8] *Nano Energy* 2017, *37*, 7-14; [9] *Angew. Chem. Int. Ed.* 2018, *57*, 16703-16707; [10] *Angew. Chem. Int. Ed.* 2015, *54*, 3907-3911; [11] *Energy Storage Mater.* 2019, *16*, 228-235; [12] *Nano Energy* 2018, *53*, 432-439; [13] *Nano Lett.* 2018, *18*, 1035-1043; [14] *Adv. Mater.* 2016, *28*, 6926-6931; [15] *Angew. Chem. Int. Ed.* 2018, *57*, 10944-10948; [16] *Angew. Chem. Int. Ed.* 2019, *58*, 3779-3783; [17] *Adv. Funct. Mater.* 2019, 29, 1806724; [18] *Adv. Mater.* 2019, 1900009; [19] *Nano Energy* 2019, *59,* 636-643.

The impressive electrochemical performances of S@Co-Fe-P cathodes in coin cells encouraged us to further assess their practical applications in a commercially viable prototype. **Figure 4.27**b depicts a schematic diagram of the soft-package Li-S battery. The separator was sandwiched between the cathode and lithium foil. After the injection of electrolyte, the pouch cell was sealed by Al plastic film. **Figure 4.27**c demonstrated that a S@Co-Fe-P based soft-package Li-S battery could power a light-emitting diode (LED) with no visual disparity upon the bending-unbending operations, indicating its good flexibility. **Figure 4.27**d exhibits

the first-cycle charge-discharge voltage profiles of the Li-S pouch-cell based on the S@Co-Fe-P electrode at 0.2 C. It shows two typical discharge plateaus at around 2.35 and 2.1 V with a high discharge capacity of 958 mAh g^{-1}, suggesting the efficient sulfur redox reaction kinetics in the pouch-cell. **Figure 4.27**e presented the cycling performance of the assembled pouch-cell at 0.5 C. It showed an initial specific capacity of 857 mAh g^{-1} and retained a high specific capacity of 772 mAh g^{-1} after 100 cycles, demonstrating its superior cycling stability in the pouch-cell format. All the above results suggest that the S@Co-Fe-P cathodes hold great promise for potential practical applications in Li-S batteries.

In order to further reveal the superiority of Co-Fe-P nanocubes for moderating the diffusion of lithium polysulfides, the binding properties of Li_2S_6 with Co-Fe-P were systematically studied. The adsorption measurements were first performed by adding equal amounts of Co-Fe-P and Co-Fe powder into two aliquots of Li_2S_6 solution. As shown in the inset of **Figure 4.29**a, after resting for 4 h, the yellow Li_2S_6 solution with Co-Fe-P nanocubes completely turned colorless. In contrast, although the yellow color of the Li_2S_6 solution with Co-Fe particles became lighter, the yellow color was not completely obliterated, indicating that there were still some Li_2S_6 molecules in the solution. Ultraviolet-visible adsorption spectra measurements were also performed to monitor the concentration changes of Li_2S_6 solution after addition of Co-Fe-P or Co-Fe powders (**Figure 4.29**a). The adsorption peak of pristine Li_2S_6 solution is very strong in the visible light range. However, after adding Co-Fe-P or Co-Fe powder, the adsorption peak decreased substantially and almost completely disappeared for the Co-Fe-P/Li_2S_6 solution. These results clearly verify that the polar Co-Fe-P nanocubes have strong chemical adsorption capability towards lithium polysulfides.

To better clarify the chemical interactions between Co-Fe-P nanocubes and lithium polysulfides, XPS measurements were carried out before and after Co-Fe-P nanocubes soaked in Li_2S_6 solution. As shown in **Figure 4.29**b-d, the Co-Fe-P nanocubes show obvious oxidation states of Co $2p_{3/2}$ at 781.9 eV, Fe $2p_{3/2}$ at 713.1 eV and P 2p at 134.1 eV, respectively, indicating the surface oxidation of Co-Fe-P during the sample transportation/preparation process. Recently, it was reported that the superficial oxidation of CoP could effectively activate the surface metal sites for polysulfide binding by forming strong Co-S binding.[272] After Co-Fe-P nanocubes interacted with Li_2S_6, the intensities of both the Co-O and Fe-O components greatly decreased, while that of Co-P/S and Fe-P/S components increased concomitantly (**Figure 4.29**b, c). These distinct spectral changes can be attributed to the formation of strong Co-S and Fe-S bonds between the Co and Fe atoms in Co-Fe-P and S atoms in Li_2S_6.[272] The P 2p spectrum showed a decrease in the P-O component and an increase in the P-Co/Fe component (**Figure 4.29**d), indicating a slight reduction of the oxidized P species, likely induced by the lithium polysulfides.[272]

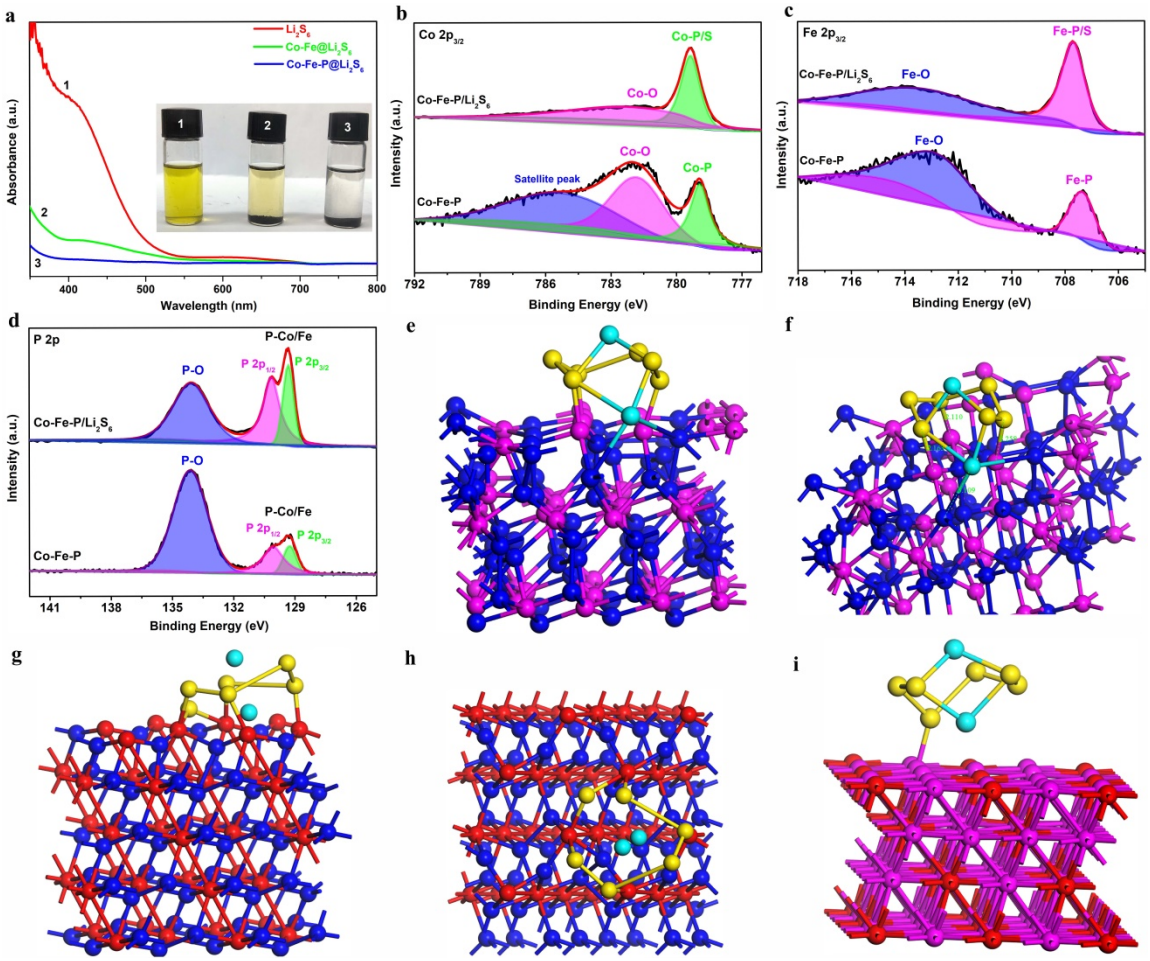

Figure 4.29 (a) Ultraviolet/visible adsorption spectra of a Li_2S_6 solution before and after the addition of Co-Fe or Co-Fe-P powder. The inset shows the digital photo of Li_2S_6 solution before and after the addition Co-Fe or Co-Fe-P powder. (b) Co $2p_{3/2}$, (c) Fe $2p_{3/2}$ and (d) P 2p XPS spectra of Co-Fe-P nanocubes before and after interacting with Li_2S_6. (e) Side (f) top view of a Li_2S_6 molecule adsorbed on the (-111) plane of CoP_2 using DFT calculations. (g) Side and (h) top view of a Li_2S_6 molecule adsorbed on the (101) plane of FeP_2 using DFT calculations. (i) Side view of a Li_2S_6 molecule adsorbed on the (111) plane of $Fe_{0.25}Co_{0.75}$ using DFT calculations. The pink, red, blue, yellow and light blue balls represent Co, Fe, P, S and Li atoms, respectively.

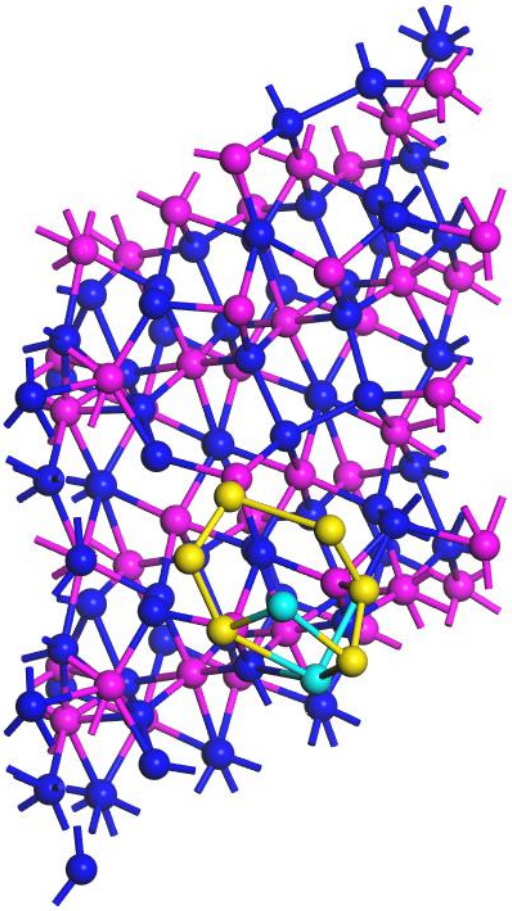

Figure 4.30 Top view of a Li_2S_6 molecule adsorbed on the (-111) plane of CoP_2 using DFT calculations. The pink, blue, yellow and light blue balls represent Co, P, S and Li atoms, respectively.

The strong chemical binding between Co-Fe-P and lithium polysulfides was further verified by the density functional theory (DFT) calculations. As Co-Fe-P mainly consists of CoP_2 and FeP_2 phases (**Figure 4.1**i), CoP_2 and FeP_2 were selected for DFT calculations, respectively. The (-111) plane of CoP_2 was selected for simulation. **Figure 4.29**e, f and **Figure 4.30** show the optimized binding geometry and bond lengths of a Li_2S_6 molecule adsorbed on the (-111) plane of CoP_2 in different views. The strong polar-polar interaction between Li_2S_6 and CoP_2 results in an obvious deformation of the Li_2S_6 molecule, forming

three Co-S and two Li-P bonds. The bond lengths of these Co-S bonds are 2.110-2.258 Å and Li-P bonds are about 3.109 Å. The binding energy between them was calculated to be -3.926 eV (**Figure 4.33**), which is much higher than with carbon materials,[84, 199, 247] indicating its strong chemical anchoring ability for polysulfides.

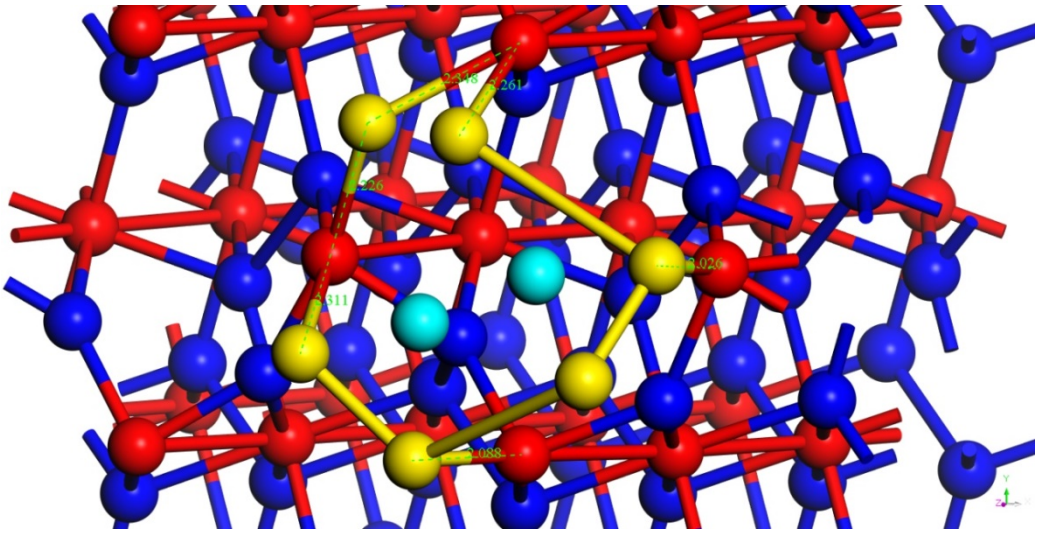

Figure 4.31 Top view of a Li_2S_6 molecule adsorbed on the (101) plane of FeP_2 using DFT calculations. The red, blue, yellow and light blue balls represent Fe, P, S and Li atoms, respectively.

Figure 4.29g, h and **Figure 4.31** show the binding geometry and bond lengths of a Li_2S_6 molecule adsorbed to the (101) facet of FeP_2 in different views. The Li-S bonds break and new bonds are subsequently formed between S and the surface Fe atoms of FeP_2. The binding energy between them is as high as -7.40 eV (**Figure 4.33**). Recently, Manthiram's group reported that the strong chemical interaction between boron carbide (B_4C) and Li_2S_4 molecules (binding energy ranged from 3.84 to 12.51 eV) resulted in the break of Li-S or S-S bonds in a Li_2S_4 molecule.[564] Our results are consistent with the above report.

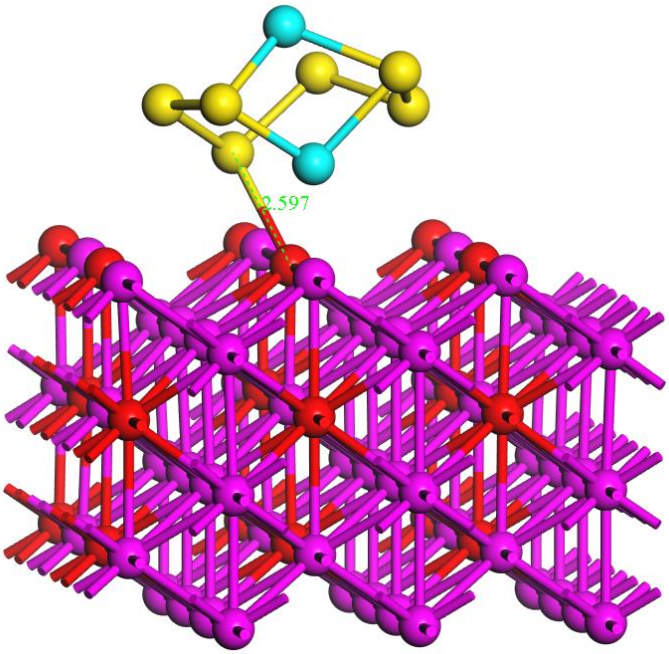

Figure 4.32 Side view a Li_2S_6 molecule adsorbed on the (110) plane of $Fe_{0.25}Co_{0.75}$ using DFT calculations. The binding energy is calculated to be -1.11 eV. The pink, red, yellow and light blue balls represent Co, Fe, S and Li atoms, respectively.

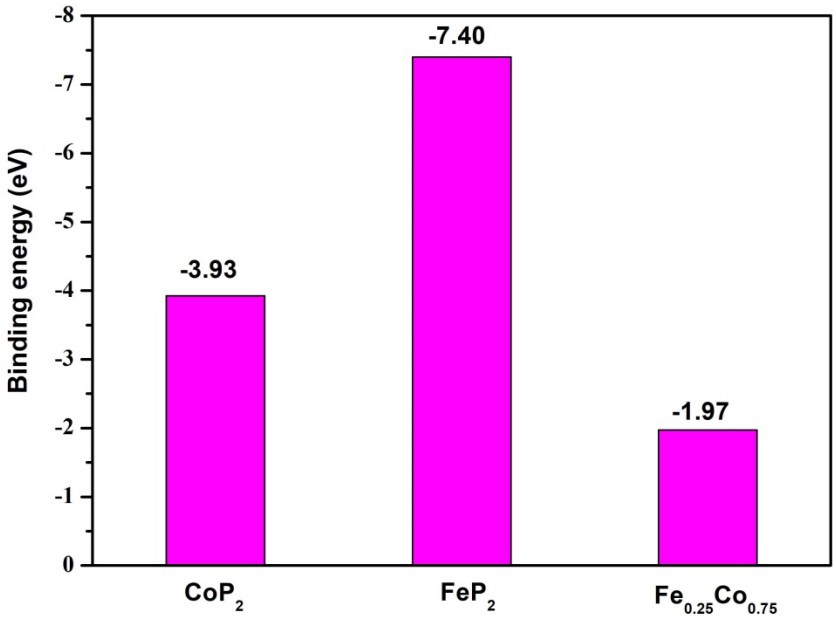

Figure 4.33 The calculated binding energies between Li_2S_6 and CoP_2, FeP_2 and $Fe_{0.25}Co_{0.75}$ (111).

For comparison, the binding property between Co-Fe and Li_2S_6 was also studied. As $Fe_{0.25}Co_{0.75}$ is the main phase of the Co-Fe product (**Figure 4.9**), here $Fe_{0.25}Co_{0.75}$ was selected for DFT calculations. As $Fe_{0.25}Co_{0.75}$ is a typical face-centred cubic structure and the (111) plane is the close-packed facet, the crystal naturally favors this facet during growth.[569, 570] Additionally, given that (110) is the strong peak in the XRD pattern (**Figure 4.9**), here (111) and (110) facets were selected as representative planes for DFT calculations. **Figure 4.29**i and **Figure 4.32** exhibit the optimized binding geometry of a Li_2S_6 molecule adsorbed on the (111) and (110) facets of $Fe_{0.25}Co_{0.75}$ surface in the side views, respectively. Because of the nonpolar property of $Fe_{0.25}Co_{0.75}$ crystal, the binding energy between Li_2S_6 molecule with (111) and (110) facets of $Fe_{0.25}Co_{0.75}$ were calculated to be only -1.97 eV and -1.11 eV. (**Figure 4.32** and **4.33**), which were much lower than that of CoP_2 and FeP_2. This is in accordance with the visual adsorption test in **Figure 4.29**a.

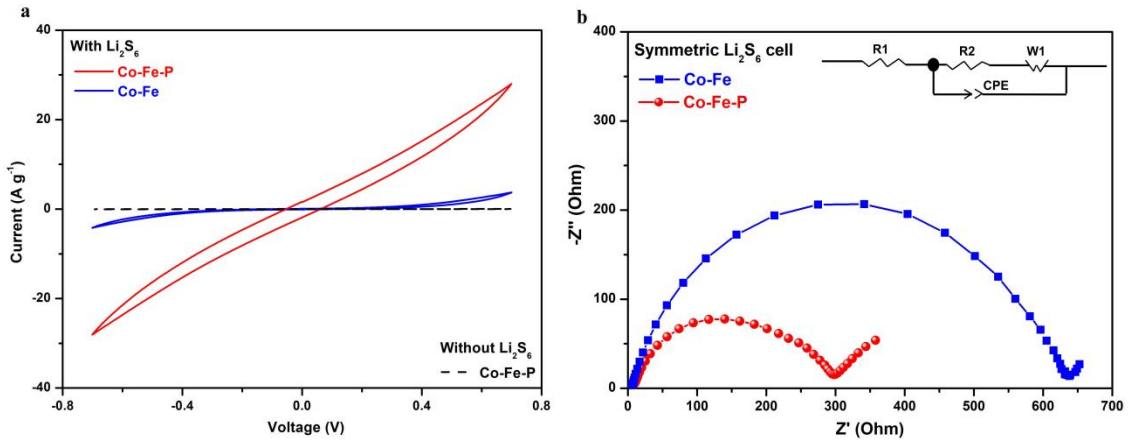

Figure 4.34 (a) CV curves of Li_2S_6 and Li_2S_6-free symmetric cells. (b) EIS spectra of symmetric Li_2S_6 cells. The inset in Figure b shows equivalent circuit.

Table 4.3 Parameters identified by modeling the impedance spectra of Li_2S_6 symmetric cells in **Figure 4.34**.

Working Electrode	R_e (Ω)	R_{ct} (Ω)	Y1($\Omega^{-1}cm^{-2}s^{-n}$)	n1
Co-Fe-P	4.352	352	3.86×10^{-5}	0.70
Co-Fe	5.356	613.3	1.89×10^{-5}	0.79

Besides the chemical trapping ability, the catalysis effect on the interfaces between the host material and polysulfides is also very important to propelling polysulfide redox and thus suppress the shuttle effect. The cyclic voltammetry (CV) in symmetric cell with identical working (Co-Fe-P or Co-Fe) and counter electrodes were performed (the detailed method is described in the experimental section). As shown in **Figure 4.34**a, the CV of the Li_2S_6-free symmetric cell shows minor contribution of capacitive current in the commercial Li-S battery electrolyte. However, when adding Li_2S_6 into the electrolyte, both the Li_2S_6 symmetric cells exhibit much higher current density, suggesting that the polysulfide redox reactions dominate the current response instead of the double-layer capacitance.[558] Moreover, the Li_2S_6 symmetric cell with Co-Fe-P electrodes demonstrates an order of magnitude higher current response compared to the Co-Fe electrodes, indicating that the interactions between Co-Fe-P and polysulfides not only statically exist but also dynamically accelerate the redox kinetics of polysulfide conversion.[199] Such substantially improved charge transfer is also verified by the EIS of the symmetric cell. As shown in **Figure 4.34**b, the symmetric Li_2S_6 cell with the Co-Fe-P electrodes exhibits much smaller semicircle in the Nyquist plots, indicating much smaller charge transfer resistance (R_{ct}) and enhanced redox reaction kinetics at the interfaces between Co-Fe-P and polysulfides (**Table 4.3**). Based on both the experimental and theoretical results, it is reasonable to conclude that the superior cycling performance of the S@Co-Fe-P cathode originates from the strong chemical interactions between Co-Fe-P nanocubes and polysulfides as well as the catalysis effect of the Co-Fe-P surface.

4.4 Conclusions

In summary, Co-Fe-P nanocubes were found to be an efficient polysulfide mediator for Li-S batteries. With the highly interconnected-pore architecture, superior electronic and ionic conductivity, and strong polysulfide trapping as well as catalysis capability, the S@Co-Fe-P cathode demonstrated high specific capacity, superior rate performance and long cyclability. Moreover, when the areal sulfur loading was increased to 5.5 mg cm^{-2}, the S@Co-Fe-P cathode showed high areal capacity with superior cycling stability. Impressively, the soft-package Li-S batteries based on S@Co-Fe-P cathodes also exhibited good electrochemical performance with great flexibility, suggesting the potential practical applications of S@Co-Fe-P cathodes for Li-S batteries. This work provides an efficient strategy for fabricating polar and conductive inorganic compounds with interconnected-pore architecture as effective polysulfide mediators for high-performance Li-S batteries.

Chapter 5 Summary and Future Perspective

5.1 Summary

In this thesis, we have first reviewed the mechanism, challenges and progress of Li-S batteries. To address the challenges of Li-S batteries, we then designed effective host materials to enhance the conductivity of sulfur cathode and suppress the polysulfide shuttle. The designed host materials all showed great advantages for using in Li-S batteries. They showed highly conductivity, strong chemical adsorption towards polysulfides and catalysis effect for polysulfide conversion. Following are detailed summary of the outcomes.

- **Self-standing sulfur cathodes enabled by 3D hierarchically porous titanium monoxide-graphene composite film for high-performance lithium-sulfur batteries.**

A novel strategy has been developed to fabricate the self-standing and highly conductive polar TiO-G/S film with 3D hierarchically porous architecture for Li-S batteries. The highly interconnected porous graphene matrix not only can facilitate rapid lithium ion and electron transport, but also provide sufficient spaces for sulfur accommodation and cushion of the volume expansion during the lithiation process. In addition, the ultrafine and polar TiO nanoparticles distributed over the entire graphene networks provided strong chemical entrapment for lithium polysulfides and their high conductivity also accelerated the redox reaction kinetics. Benefiting from this delicate architecture, the freestanding TiO-G/S film delivered a high initial discharge capacity of 1350 mAh g^{-1} at 0.1 C and a high rate performance of 832 mAh g^{-1} at 2 C. Furthermore, when the areal sulfur loading was increased to 5.2 mg cm^{-2}, the TiO-G/S cathode can deliver a high areal capacity of 3.2 mAh cm^{-2} after

300 cycles at 0.2 C, demonstrating excellent cycling stability at high areal sulfur loading. This work opens up the avenue for constructing more efficient nanoarchitectures with the merits of a self-standing property, high conductivity, polar characteristic and high porosity in one host. Only by using such efficient sulfur hosts, can high energy density Li-S batteries be developed for practical applications.

- **Co-Fe mixed metal phosphide nanocubes with highly interconnected-pore architecture as an efficient polysulfide mediator for lithium-sulfur batteries**

Co-Fe-P nanocubes were found to be an efficient polysulfide mediator for Li-S batteries. With the highly interconnected-pore architecture, superior electronic and ionic conductivity, and strong polysulfide trapping as well as catalysis capability, the S@Co-Fe-P cathode demonstrated high specific capacity, superior rate performance and long cyclability. Moreover, when the areal sulfur loading was increased to 5.5 mg cm^{-2}, the S@Co-Fe-P cathode showed high areal capacity with superior cycling stability. Impressively, the soft-package Li-S batteries based on S@Co-Fe-P cathodes also exhibited good electrochemical performance with great flexibility, suggesting the potential practical applications of S@Co-Fe-P cathodes for Li-S batteries. This work provides an efficient strategy for fabricating polar and conductive inorganic compounds with interconnected-pore architecture as effective polysulfide mediators for high-performance Li-S batteries.

5.2 Future perspective

After about 60 years' development, especially over the past decade, Li-S batteries have embraced great advances in terms of fundamental research. In the current stage, much more

attention should be transferred to making a commercially competitive Li-S full cell system a reality, and academic and industrial organizations need keep close communication. In this section, we will give some insight on the future development of Li-S batteries to bring it a step closer for large-scale practical applications.

5.2.1 Sulfur content in the cathode

Given the insulating nature of sulfur and Li_2S, the cathode electrode often contains a certain amount of inactive material, which usually occupies 40-60 wt% of the electrode. During the initial stage of academic research, the sulfur content is not that important. However, in the current stage, more attention should be paid into the sulfur content value when making a cathode electrode in order to achieve a commercially competitive energy density. In order to reduce the content of inactive part in the cathode, novel host materials with high conductivity should be developed. Another promising way is to develop novel sulfur host materials that are also electrochemically active in the voltage of Li-S batteries, so they do not contribute dead weight.

5.2.2 Areal sulfur loading

Over the past 3 years, although increasing attention has been paid to fabricate high sulfur loading electrodes, it compromised the sulfur utilization and cycling performance. In addition, the long-term cycling tests were normally evaluated with low areal sulfur loadings. Therefore, more work should be done to increase the electrochemical utilization with long-term cycling stability at high areal sulfur loading more than 5 mg cm^{-2}.

5.2.3 Lean electrolyte condition

The electrolyte amount is also an important parameter in a Li-S battery. In most of the literatures, the electrolyte-to-sulfur ratio is over 15 μL mg^{-1}, which cannot achieve a satisfied practical energy density. More work should be done with sulfur content more than 70%, areal sulfur loading more than 5 mg cm^{-2} and electrolyte/sulfur ratio lower than 10 μL mg^{-1}.

5.2.4 All solid-state Li-S batteries

Solid electrolytes with high mechanical modulus have the advantages of eliminating polysulfide dissolution and shuttle as well as inhibiting lithium dendrite growth basically, which represent a promising direction in the next-stage of research. As the study of all solid-state Li-S batteries is just in its infancy, some intractable obstacles such as low ionic conductivity and large interfacial resistance need to be resolved. The employ of theory-guided strategy such as DFT and machine learning can provide new opportunities in accelerating the screening of novel solid electrolytes with high lithium ion mobility and low interfacial resistance.[571, 572]

5.2.5 Prototype Li-S pouch cells

Over the past decade, the specific capacity and cycling performance of Li-S batteries based on coin-cells have improved a lot. Due to the different assemble process for coin cells and pouch cells, the good electrochemical performance in coin cells doesn't definitely mean superior performance in pouch cells. Therefore, more work should be done to evaluate the electrochemical performance in pouch cells with high sulfur content, high areal sulfur loading and low electrolyte/sulfur ratio. In addition, the lithium metal anode is always excessively

used in coin cells, which is not beneficial for realizing a high energy density. Thus, the matching between lithium anode and sulfur cathode should be taken into consideration when assembling a pouch cell to avoid the use of a large amount of excess lithium.

5.2.6 Safety

The use of lithium metal anodes can endow the Li-S batteries with high energy densities. However, the lithium dendrite growth can also bring about the safety issues, which needs to be absolutely resolved before the large-scale practical applications of Li-S batteries. There are two aspects of protecting the lithium metal anode: passivation of lithium metal surface or hosting metallic lithium in a prepared matrix. Among these methods, the use of solid electrolytes which can physically inhibit the lithium dendrite growth seems to be a promising approach that needs to be further studied.

5.2.7 Cost

In order to realize the large-scale practical application of Li-S batteries, the fabrication procedure needs to be simple and low cost. At present, most research studies are completed in laboratories which usually require complex synthetic process and harsh experimental conditions. In this case, attention needs to be paid to the materials synthesis and cell engineering with the capability to be large-scale produced.

By taking these principles into consideration, the practical application of Li-S batteries is probable to be realized in the near future!

APPENDIX: NOMENCLATURE

Abbreviations/Symbols	Full name
Ar	Argon
a.u.	Arbitrary unit
BET	Brunauer-Emmett-Teller
BJH	Barrett-Joyner-Halenda
CV	Cyclic Voltammetry
C-rate	Current rate
CNT	carbon nanotube
CB	Carbon black
DI	de-ionized
DMC	Dimethyl carbonate
EC	Ethylene carbonate
EV	Electric vehicle
EIS	Electrochemical Impedance Spectroscopy
FTIR	Fourier transform infrared spectroscopy
FESEM	Field-Emission Scanning Electron Microscopy
g	Gram
RGO	Graphene oxide
h	Hour
Hz	Hertz
HRTEM	High-resolution transmission electronic spectroscopy

Li	Lithium
LIBs	Lithium-ion Batteries
M	Molar concentration
mA h g^{-1}	Milli ampere hour per gram
min	Minute
mm	Millimeter
nm	Nanometer
NMP	1-methyl-2-pyrrolidinone
PC	Propylene carbonate
PVDF	Poly(vinylidene difluoride)
R_{ct}	Charge transfer resistance
SEM	Scanning electron microscopy
SAED	Selected area electron diffraction
SEI	Solid Electrolyte Interface
TEM	Transmission electron microscopy
TGA	Thermogravimetric analysis
XRD	X-ray diffraction
°	Degree
Ω	Ohm
°C	Degree Celsius
Z_W	Warburg impedance

REFERENCES

1. S. Chu and A. Majumdar, *Nature*, 2012, **488**, 294.
2. B. Obama, *Science*, 2017, **355**, 126-129.
3. S. Chu, Y. Cui and N. Liu, *Nat. Mater.*, 2017, **16**, 16.
4. B. Dunn, H. Kamath and J.-M. Tarascon, *Science*, 2011, **334**, 928-935.
5. Z. Yang, J. Zhang, M. C. Kintner-Meyer, X. Lu, D. Choi, J. P. Lemmon and J. Liu, *Chem. Rev.*, 2011, **111**, 3577-3613.
6. M. Armand and J.-M. Tarascon, *Nature*, 2008, **451**, 652.
7. J.-M. Tarascon and M. Armand, *Nature*, 2001, **414**, 359-367.
8. D. Larcher and J.-M. Tarascon, *Nat. Chem.*, 2015, **7**, 19.
9. M. Winter and R. J. Brodd, *Chem. Rev.*, 2004, **104**, 4245-4270.
10. M. Li, J. Lu, Z. Chen and K. Amine, *Adv. Mater.*, 2018, **30**, 1800561.
11. J. B. Goodenough and Y. Kim, *Chem. Mater.*, 2009, **22**, 587-603.
12. J. B. Goodenough and K.-S. Park, *J. Am. Chem. Soc.*, 2013, **135**, 1167-1176.
13. J. W. Choi and D. Aurbach, *Nat. Rev. Mater.*, 2016, **1**, 16013.
14. P. G. Bruce, B. Scrosati and J. M. Tarascon, *Angew. Chem. Int. Ed.*, 2008, **47**, 2930-2946.
15. A. Kwade, W. Haselrieder, R. Leithoff, A. Modlinger, F. Dietrich and K. Droeder, *Nat. Energy*, 2018, **3**, 290.
16. P. G. Bruce, S. A. Freunberger, L. J. Hardwick and J.-M. Tarascon, *Nat. Mater.*, 2012, **11**, 19.
17. Z. W. Seh, Y. Sun, Q. Zhang and Y. Cui, *Chem. Soc. Rev.*, 2016, **45**, 5605-5634.
18. M. Winter, B. Barnett and K. Xu, *Chem. Rev.*, 2018, **118**, 11433-11456.
19. M. S. Whittingham, *Chem. Rev.*, 2004, **104**, 4271-4302.
20. M. S. Whittingham, *Chem. Rev.*, 2014, **114**, 11414-11443.
21. M. S. Whittingham, *Science*, 1976, **192**, 1126-1127.
22. A. Grimaud, *Nat. Energy*, 2017, **2**, 17003.
23. S. A. Freunberger, *Nat. Energy*, 2017, **2**, 17091.
24. A. S. Arico, P. Bruce, B. Scrosati, J.-M. Tarascon and W. Van Schalkwijk, *Nat. Mater.*, 2005, 4, 366-377.
25. X.-B. Cheng, R. Zhang, C.-Z. Zhao and Q. Zhang, *Chem. Rev.*, 2017, **117**, 10403-10473.
26. D. Lin, Y. Liu and Y. Cui, *Nat. Nanotech.*, 2017, **12**, 194.
27. J. Liu, Z. Bao, Y. Cui, E. J. Dufek, J. B. Goodenough, P. Khalifah, Q. Li, B. Y. Liaw, P. Liu and A. Manthiram, *Nat. Energy*, 2019, **4**, 180-186.
28. W. Xu, J. Wang, F. Ding, X. Chen, E. Nasybulin, Y. Zhang and J.-G. Zhang, *Energy Environ. Sci.*, 2014, **7**, 513-537.
29. M. D. Tikekar, S. Choudhury, Z. Tu and L. A. Archer, *Nat. Energy*, 2016, **1**, 16114.
30. R. Chen, T. Zhao and F. Wu, *Chem. Commun.*, 2015, **51**, 18-33.
31. X. Ji, K. T. Lee and L. F. Nazar, *Nat. Mater.*, 2009, **8**, 500.
32. A. Manthiram, S. H. Chung and C. Zu, *Adv. Mater.*, 2015, **27**, 1980-2006.
33. A. Manthiram, Y. Fu, S.-H. Chung, C. Zu and Y.-S. Su, *Chem. Rev.*, 2014, **114**, 11751-11787.
34. A. Manthiram, Y. Fu and Y.-S. Su, *Acc. Chem. Res.*, 2012, **46**, 1125-1134.
35. Q. Pang, X. Liang, C. Y. Kwok and L. F. Nazar, *Nat. Energy*, 2016, **1**, 16132.
36. H. Wang, Y. Yang, Y. Liang, J. T. Robinson, Y. Li, A. Jackson, Y. Cui and H. Dai, *Nano Lett.*, 2011,

11, 2644-2647.
37. N. Jayaprakash, J. Shen, S. S. Moganty, A. Corona and L. A. Archer, *Angew. Chem. Int. Ed.*, 2011, **50**, 5904-5908.
38. J. He, Y. Chen and A. Manthiram, *Energy Environ. Sci.*, 2018, 11, 2560-2568.
39. Y. H. Lee, J. H. Kim, J. H. Kim, J. T. Yoo and S. Y. Lee, *Adv. Funct. Mater.*, 2018, 1801422.
40. Y. Pang, J. Wei, Y. Wang and Y. Xia, *Adv. Energy Mater.*, 2018, **8**, 1702288.
41. Y.-S. Su and A. Manthiram, *Nat. Commun.*, 2012, **3**, 1166.
42. G. Zhou, S. Pei, L. Li, D.-W. Wang, S. Wang, K. Huang, L.-C. Yin, F. Li, H.-M. Cheng, *Adv. Mater.*, 2014, **26**, 625-631.
43. Q. Pang, A. Shyamsunder, B. Narayanan, C. Y. Kwok, L. A. Curtiss and L. F. Nazar, *Nat. Energy*, 2018, **3**, 783-791.
44. W. Wahyudi, Z. Cao, P. Kumar, M. Li, Y. Wu, M. N. Hedhili, T. D. Anthopoulos, L. Cavallo, L. J. Li and J. Ming, *Adv. Funct. Mater.*, 2018, 1802244.
45. G. G. Eshetu, X. Judez, C. Li, O. Bondarchuk, L. M. Rodriguez-Martinez, H. Zhang and M. Armand, *Angew. Chem. Int. Ed.*, 2017, **56**, 15368-15372.
46. C.-C. Su, M. He, R. Amine, Z. Chen and K. Amine, *Angew. Chem. Int. Ed.*, 2018, **57**, 12033-12036.
47. J. Wang, Z. Yao, C. W. Monroe, J. Yang and Y. Nuli, *Adv. Funct. Mater.*, 2013, **23**, 1194-1201.
48. W. Chen, T. Lei, T. Qian, W. Lv, W. He, C. Wu, X. Liu, J. Liu, B. Chen and C. Yan, *Adv. Energy Mater.*, 2018, **8**, 1702889.
49. H. Chen, M. Ling, L. Hencz, H. Y. Ling, G. Li, Z. Lin, G. Liu and S. Zhang, *Chem. Rev.*, 2018, **118**, 8936-8982.
50. G. Li, M. Ling, Y. Ye, Z. Li, J. Guo, Y. Yao, J. Zhu, Z. Lin and S. Zhang, *Adv. Energy Mater.*, 2015, **5**, 1500878.
51. Y. Wang, X. Huang, S. Zhang and Y. Hou, *Small Methods*, 2018, 1700345.
52. G. Li, J. Sun, W. Hou, S. Jiang, Y. Huang and J. Geng, *Nat. Commun.*, 2016, **7**, 10601.
53. Y. Chen, J. Yang, Y. Yang, Z. Peng, J. Li, T. Mei, J. Wang, M. Hao, Y. Chen and W. Xiong, *Chem. Commun.*, 2015, **51**, 10490-10493.
54. R. Fang, S. Zhao, Z. Sun, D. W. Wang, H. M. Cheng and F. Li, *Adv. Mater.*, 2017, **29**, 1606823.
55. Y. He, Z. Chang, S. Wu and H. Zhou, *J. Mater. Chem. A*, 2018, **6**, 6155-6182.
56. X. Liu, J. Q. Huang, Q. Zhang and L. Mai, *Adv. Mater.*, 2017, **29**, 1601759.
57. S. Evers and L. F. Nazar, *Acc. Chem. Res.*, 2012, **46**, 1135-1143.
58. J. Schuster, G. He, B. Mandlmeier, T. Yim, K. T. Lee, T. Bein and L. F. Nazar, *Angew. Chem. Int. Ed.*, 2012, **51**, 3591-3595.
59. D. Su, D. Zhou, C. Wang and G. Wang, *Adv. Funct. Mater.*, 2018, **28**, 1800154.
60. J. Xu, T. Lawson, H. Fan, D. Su and G. Wang, *Adv. Energy Mater.*, 2018, **8**, 1702607.
61. Y. Yang, M. T. McDowell, A. Jackson, J. J. Cha, S. S. Hong and Y. Cui, *Nano Lett.*, 2010, **10**, 1486-1491.
62. L. Yu, X. Y. Yu and X. W. Lou, *Adv. Mater.*, 2018, **30**, 1800939.
63. A. Fu, C. Wang, F. Pei, J. Cui, X. Fang and N. Zheng, *Small*, 2019, **15**, 1804786.
64. L. Yu, H. B. Wu and X. W. D. Lou, *Acc. Chem. Res.*, 2017, **50**, 293-301.
65. J. Nai and X. W. D. Lou, *Adv. Mater.*, 2019, **31**, 1706825.
66. L. Zhou, Z. Zhuang, H. Zhao, M. Lin, D. Zhao and L. Mai, *Adv. Mater.*, 2017, **29**, 1602914.
67. L. Zhou, D. Zhao and X. Lou, *Angew. Chem. Inter. Ed.*, 2012, **51**, 239-241.

68. Z. Li, H. B. Wu and X. W. D. Lou, *Energy Environ. Sci.*, 2016, **9**, 3061-3070.
69. C. Zhang, H. B. Wu, C. Yuan, Z. Guo and X. W. Lou, *Angew. Chem. Inter. Ed.*, 2012, **51**, 9592-9595.
70. G. Zheng, Y. Yang, J. J. Cha, S. S. Hong and Y. Cui, *Nano Lett.*, 2011, **11**, 4462-4467.
71. F. Bonaccorso, L. Colombo, G. Yu, M. Stoller, V. Tozzini, A. C. Ferrari, R. S. Ruoff and V. Pellegrini, *Science*, 2015, **347**, 1246501.
72. Y. Chen, J. Li, T. Mei, X. g. Hu, D. Liu, J. Wang, M. Hao, J. Li, J. Wang and X. Wang, *J. Mater. Chem. A*, 2014, **2**, 20714-20722.
73. R. Raccichini, A. Varzi, S. Passerini and B. Scrosati, *Nat. Mater.*, 2015, **14**, 271.
74. V. Georgakilas, J. N. Tiwari, K. C. Kemp, J. A. Perman, A. B. Bourlinos, K. S. Kim and R. Zboril, *Chem. Rev.*, 2016, **116**, 5464-5519.
75. C. Wang, X. Wang, Y. Yang, A. Kushima, J. Chen, Y. Huang and J. Li, *Nano Lett.*, 2015, **15**, 1796-1802.
76. G. Tan, R. Xu, Z. Xing, Y. Yuan, J. Lu, J. Wen, C. Liu, L. Ma, C. Zhan and Q. Liu, *Nat. Energy*, 2017, **2**, 17090.
77. G. Zheng, Q. Zhang, J. J. Cha, Y. Yang, W. Li, Z. W. Seh and Y. Cui, *Nano Lett.*, 2013, **13**, 1265-1270.
78. B. Zhang, X. Qin, G. Li and X. Gao, *Energy Environ. Sci.*, 2010, **3**, 1531-1537.
79. S. Xin, L. Gu, N.-H. Zhao, Y.-X. Yin, L.-J. Zhou, Y.-G. Guo and L.-J. Wan, *J. Am. Chem. Soc.*, 2012, **134**, 18510-18513.
80. L. Ji, M. Rao, H. Zheng, L. Zhang, Y. Li, W. Duan, J. Guo, E. J. Cairns and Y. Zhang, *J. Am. Chem. Soc.*, 2011, **133**, 18522-18525.
81. Z. Wang, Y. Dong, H. Li, Z. Zhao, H. B. Wu, C. Hao, S. Liu, J. Qiu and X. W. D. Lou, *Nat. Commun.*, 2014, **5**, 5002.
82. C. Tang, Q. Zhang, M. Q. Zhao, J. Q. Huang, X. B. Cheng, G. L. Tian, H. J. Peng and F. Wei, *Adv. Mater.*, 2014, **26**, 6100-6105.
83. F. Pei, T. An, J. Zang, X. Zhao, X. Fang, M. Zheng, Q. Dong and N. Zheng, *Adv. Energy Mater.*, 2016, **6**, 1502539.
84. G. Zhou, E. Paek, G. S. Hwang and A. Manthiram, *Nat. Commun.*, 2015, **6**, 7760.
85. L. Chen, J. Feng, H. Zhou, C. Fu, G. Wang, L. Yang, C. Xu, Z. Chen, W. Yang and Y. Kuang, *J. Mater. Chem. A*, 2017, **5**, 7403-7415.
86. S. Yuan, J. L. Bao, L. Wang, Y. Xia, D. G. Truhlar and Y. Wang, *Adv. Energy Mater.*, 2016, **6**, 1501733.
87. X. Gu, C.-j. Tong, C. Lai, J. Qiu, X. Huang, W. Yang, B. Wen, L.-m. Liu, Y. Hou and S. Zhang, *J. Mater. Chem. A*, 2015, **3**, 16670-16678.
88. Y. Liang, Z. Tao and J. Chen, *Adv. Energy Mater.*, 2012, **2**, 742-769.
89. Z. Song and H. Zhou, *Energy Environ. Sci.*, 2013, **6**, 2280-2301.
90. J. Wang, J. Wang, Z. Kong, K. Lv, C. Teng and Y. Zhu, *Adv. Mater.*, 2017, **29**, 1703044.
91. J. Wang, J. Chen, K. Konstantinov, L. Zhao, S. Ng, G. Wang, Z. Guo and H. Liu, *Electrochim. Acta*, 2006, **51**, 4634-4638.
92. M. Sun, S. Zhang, T. Jiang, L. Zhang and J. Yu, *Electrochem. Commun.*, 2008, **10**, 1819-1822.
93. L. Qiu, S. Zhang, L. Zhang, M. Sun and W. Wang, *Electrochim. Acta*, 2010, **55**, 4632-4636.
94. F. Wu, S. Wu, R. Chen, J. Chen and S. Chen, *Electrochem. Solid-State Lett.*, 2010, **13**, A29-A31.
95. F. Wu, J. Chen, R. Chen, S. Wu, L. Li, S. Chen and T. Zhao, *J. Phys. Chem. C*, 2011, **115**,

6057-6063.
96. L. Xiao, Y. Cao, J. Xiao, B. Schwenzer, M. H. Engelhard, L. V. Saraf, Z. Nie, G. J. Exarhos and J. Liu, *Adv. Mater.*, 2012, **24**, 1176-1181.
97. W. Zhou, Y. Yu, H. Chen, F. J. DiSalvo and H. c. D. Abruña, *J. Am. Chem. Soc.*, 2013, **135**, 16736-16743.
98. W. Li, G. Zheng, Y. Yang, Z. W. Seh, N. Liu and Y. Cui, *Proc. Natl. Acad. Sci. U.S.A.*, 2013, **110**, 7148-7153.
99. W. Li, Q. Zhang, G. Zheng, Z. W. Seh, H. Yao and Y. Cui, *Nano Lett.*, 2013, **13**, 5534-5540.
100. Y. Yang, G. Yu, J. J. Cha, H. Wu, M. Vosgueritchian, Y. Yao, Z. Bao and Y. Cui, *ACS Nano*, 2011, **5**, 9187-9193.
101. W. J. Chung, J. J. Griebel, E. T. Kim, H. Yoon, A. G. Simmonds, H. J. Ji, P. T. Dirlam, R. S. Glass, J. J. Wie and N. A. Nguyen, *Nat. Chem.*, 2013, **5**, 518.
102. B. Q. Li, S. Y. Zhang, L. Kong, H. J. Peng and Q. Zhang, *Adv. Mater.*, 2018, **30**, 1707483.
103. G. Hu, Z. Sun, C. Shi, R. Fang, J. Chen, P. Hou, C. Liu, H. M. Cheng and F. Li, *Adv. Mater.*, 2017, **29**, 1603835.
104. K. Shen, H. Mei, B. Li, J. Ding and S. Yang, *Adv. Energy Mater.*, 2018, **8**, 1701527.
105. Z. Xiao, L. Li, Y. Tang, Z. Cheng, H. Pan, D. Tian and R. Wang, *Energy Storage Mater.*, 2018, **12**, 252-259.
106. Z. A. Ghazi, L. Zhu, H. Wang, A. Naeem, A. M. Khattak, B. Liang, N. A. Khan, Z. Wei, L. Li and Z. Tang, *Adv. Energy Mater.*, 2016, **6**, 1601250.
107. Y. Meng, G. Lin, H. Ding, H. Liao and C. Wang, *J. Mater. Chem. A*, 2018, **6**, 17186-17191.
108. X. Hu, J. Jian, Z. Fang, L. Zhong, Z. Yuan, M. Yang, S. Ren, Q. Zhang, X. Chen and D. Yu, *Energy Storage Mater.*, 2019, **22**, 40-47.
109. Y. Tsao, M. Lee, E. C. Miller, G. Gao, J. Park, S. Chen, T. Katsumata, H. Tran, L.-W. Wang and M. F. Toney, *Joule*, 2019, **3**, 872-884.
110. G. Li, X. Wang, M. H. Seo, M. Li, L. Ma, Y. Yuan, T. Wu, A. Yu, S. Wang and J. Lu, *Nat. Commun.*, 2018, **9**, 705.
111. J. Wang, J. Yang, J. Xie and N. Xu, *Adv. Mater.*, 2002, **14**, 963-965.
112. H. Yang, A. Naveed, Q. Li, C. Guo, J. Chen, J. Lei, J. Yang, Y. Nuli and J. Wang, *Energy Storage Mater.*, 2018, **15**, 299-307.
113. X. Wang, Y. Qian, L. Wang, H. Yang, H. Li, Y. Zhao and T. Liu, *Adv. Funct. Mater.*, 2019, 1902929.
114. H. Wang, W. Zhang, J. Xu and Z. Guo, *Adv. Funct. Mater.*, 2018, **28**, 1707520.
115. Z. W. Seh, W. Li, J. J. Cha, G. Zheng, Y. Yang, M. T. McDowell, P.-C. Hsu and Y. Cui, *Nat. Commun.*, 2013, **4**, 1331.
116. C. Zha, D. Wu, T. Zhang, J. Wu and H. Chen, *Energy Storage Mater.*, 2019, **17**, 118-125.
117. M. Fang, Z. Chen, Y. Liu, J. Quan, C. Yang, L. Zhu, Q. Xu and Q. Xu, *J. Mater. Chem. A*, 2018, **6**, 1630-1638.
118. G. Zhou, Y. Zhao, C. Zu and A. Manthiram, *Nano Energy*, 2015, **12**, 240-249.
119. S. B. Patil, H. J. Kim, H.-K. Lim, S. M. Oh, J. Kim, J. Shin, H. Kim, J. W. Choi and S.-J. Hwang, *ACS Energy Lett.*, 2018, **3**, 412-419.
120. J. Y. Hwang, H. M. Kim, S. K. Lee, J. H. Lee, A. Abouimrane, M. A. Khaleel, I. Belharouak, A. Manthiram and Y. K. Sun, *Adv. Energy Mater.*, 2016, **6**, 1501480.
121. X. Liang, C. Hart, Q. Pang, A. Garsuch, T. Weiss and L. F. Nazar, *Nat. Commun.*, 2015, **6**, 5682.

122. Z. Li, J. Zhang and X. W. Lou, *Angew. Chem. Int. Ed.*, 2015, **54**, 12886-12890.
123. S. Rehman, T. Tang, Z. Ali, X. Huang and Y. Hou, *Small*, 2017, **13**, 1700087.
124. J. Zhang, Y. Shi, Y. Ding, W. Zhang and G. Yu, *Nano Lett.*, 2016, **16**, 7276-7281.
125. X. Liang and L. F. Nazar, *ACS Nano*, 2016, **10**, 4192-4198.
126. L. Ma, R. Chen, G. Zhu, Y. Hu, Y. Wang, T. Chen, J. Liu and Z. Jin, *ACS Nano*, 2017, **11**, 7274-7283.
127. Y. Tao, Y. Wei, Y. Liu, J. Wang, W. Qiao, L. Ling and D. Long, *Energy Environ. Sci.*, 2016, **9**, 3230-3239.
128. Q. Pang, D. Kundu, M. Cuisinier and L. Nazar, *Nat. Commun.*, 2014, **5**, 4759.
129. X. Tao, J. Wang, Z. Ying, Q. Cai, G. Zheng, Y. Gan, H. Huang, Y. Xia, C. Liang and W. Zhang, *Nano Lett.*, 2014, **14**, 5288-5294.
130. H. Wei, E. F. Rodriguez, A. S. Best, A. F. Hollenkamp, D. Chen and R. A. Caruso, *Adv. Energy Mater.*, 2017, **7**, 1601616.
131. S. Mei, C. J. Jafta, I. Lauermann, Q. Ran, M. Kärgell, M. Ballauff and Y. Lu, *Adv. Funct. Mater.*, 2017, **27**, 1701176.
132. R. Clarke and S. Harnsberger, *Am. Lab.*, 1988, **20**, 8.
133. J. Smith, F. Walsh and R. Clarke, *J. Appl. Electrochem.*, 1998, **28**, 1021-1033.
134. Z. Li, J. Zhang, B. Guan, D. Wang, L.-M. Liu and X. W. D. Lou, *Nat. Commun.*, 2016, **7**, 13065.
135. Y. Chen, S. Choi, D. Su, X. Gao and G. Wang, *Nano Energy*, 2018, **47**, 331-339.
136. J. He, L. Luo, Y. Chen and A. Manthiram, *Adv. Mater.*, 2017, **29**, 1702707.
137. J. Coey, A. Berkowitz, L. Balcells, F. Putris and A. Barry, *Phys. Rev. Lett.*, 1998, **80**, 3815.
138. X. Ji, S. Evers, R. Black and L. F. Nazar, *Nat. Commun.*, 2011, **2**, 325.
139. S. Rehman, S. Guo and Y. Hou, *Adv. Mater.*, 2016, **28**, 3167-3172.
140. S. Choi, D. Su, M. Shin, S. Park and G. Wang, *Chem. Asian. J.*, 2018, **13**, 568-576.
141. P. Wei, M. Fan, H. Chen, D. Chen, C. Li, K. Shu and C. Lv, *Int. J. Hydrog. Energy*, 2016, **41**, 1819-1827.
142. K. H. Kim, Y.-S. Jun, J. A. Gerbec, K. A. See, G. D. Stucky and H.-T. Jung, *Carbon*, 2014, **69**, 543-551.
143. H. Wu, Q. Tang, H. Fan, Z. Liu, A. Hu, S. Zhang, W. Deng and X. Chen, *Electrochimi. Acta*, 2017, **255**, 179-186.
144. C. Chen, H. Xu, B. Zhang, Q. Jiang, Y. Zhang, L. Li and Z. Lin, *Chem. Commun.*, 2020, **56**, 786-789.
145. J. Xu, W. Zhang, Y. Chen, H. Fan, D. Su and G. Wang, *J. Mater. Chem. A*, 2018, **6**, 2797-2807.
146. H. Cheng, S. Wang, D. Tao and M. Wang, *Funct. Mater. Lett.*, 2014, **7**, 1450020.
147. W. Wang, Y. Zhao, Y. Zhang, J. Wang, G. Cui, M. Li, Z. Bakenov and X. Wang, *ACS Appl. Mater. Interfaces*, 2020.
148. X. Tao, J. Wang, C. Liu, H. Wang, H. Yao, G. Zheng, Z. W. Seh, Q. Cai, W. Li and G. Zhou, *Nat. Commun.*, 2016, **7**, 11203.
149. M. Xiang, H. Wu, H. Liu, J. Huang, Y. Zheng, L. Yang, P. Jing, Y. Zhang, S. Dou and H. Liu, *Adv. Funct. Mater.*, 2017, **27**, 1702573.
150. R. Ponraj, A. G. Kannan, J. H. Ahn and D.-W. Kim, *ACS Appl. Mater. Interfaces*, 2016, **8**, 4000-4006.
151. T. Dhawa, S. Chattopadhyay, G. De and S. Mahanty, *ACS Omega*, 2017, **2**, 6481-6491.
152. C. Zhao, C. Shen, F. Xin, Z. Sun and W. Han, *Mater. Lett.*, 2014, **137**, 52-55.

153. X. Han, Y. Xu, X. Chen, Y.-C. Chen, N. Weadock, J. Wan, H. Zhu, Y. Liu, H. Li and G. Rubloff, *Nano Energy*, 2013, **2**, 1197-1206.
154. Y. Choi, B. Jung, D. Lee, J. Jeong, K. Kim, H. Ahn, K. Cho and H. Gu, *Phys. Scripta*, 2007, **2007**, 62.
155. H. Kim, J. T. Lee, D. C. Lee, A. Magasinski, W. i. Cho and G. Yushin, *Adv. Energy Mater.*, 2013, **3**, 1308-1315.
156. X. Liang, C. Y. Kwok, F. Lodi-Marzano, Q. Pang, M. Cuisinier, H. Huang, C. J. Hart, D. Houtarde, K. Kaup and H. Sommer, *Adv. Energy Mater.*, 2016, **6**, 1501636.
157. R. Carter, L. Oakes, N. Muralidharan, A. P. Cohn, A. Douglas and C. L. Pint, *ACS Appl. Mater. Interfaces*, 2017, **9**, 7185-7192.
158. L. Kong, Y. Handa and I. Taniguchi, *Mater. Res. Bull.*, 2016, **73**, 164-170.
159. Y. Zhang, L. Wang, A. Zhang, Y. Song, X. Li, H. Feng, X. Wu and P. Du, *Solid State Ionics*, 2010, **181**, 835-838.
160. C. Wang, Y. Yi, H. Li, P. Wu, M. Li, W. Jiang, Z. Chen, H. Li, W. Zhu and S. Dai, *Nano Energy*, 2020, **67**, 104253.
161. Y. Song, W. Zhao, N. Wei, L. Zhang, F. Ding, Z. Liu and J. Sun, *Nano Energy*, 2018, **53**, 432-439.
162. L. Zhou, L. Yao, S. Li, J. Zai, S. Li, Q. He, K. He, X. Li, D. Wang and X. Qian, *J. Mater. Chem. A*, 2019, **7**, 3618-3623.
163. X. Gu, C.-j. Tong, B. Wen, L.-m. Liu, C. Lai and S. Zhang, *Electrochimi. Acta*, 2016, **196**, 369-376.
164. M. Yu, A. Wang, F. Tian, H. Song, Y. Wang, C. Li, J.-D. Hong and G. Shi, *Nanoscale*, 2015, **7**, 5292-5298.
165. J. Zhang, P. Gu, J. Xu, H. Xue and H. Pang, *Nanoscale*, 2016, **8**, 18578-18595.
166. S. Choi, D. H. Seo, M. R. Kaiser, C. Zhang, Z. J. Han, A. Bendavid, X. Guo, S. Yick, A. T. Murdock and D. Su, *J. Mater. Chem. A*, 2019, **7**, 4596-4603.
167. X. Wu, Y. Du, P. Wang, L. Fan, J. Cheng, M. Wang, Y. Qiu, B. Guan, H. Wu and N. Zhang, *J. Mater. Chem. A*, 2017, **5**, 25187-25192.
168. Q. Hao, G. Cui, Y. Zhang, J. Li and Z. Zhang, *Chem. Eng. J.*, 2020, **381**, 122672.
169. W. Yang, J. Xiao, Y. Ma, S. Cui, P. Zhang, P. Zhai, L. Meng, X. Wang, Y. Wei and Z. Du, *Adv. Energy Mater.*, 2019, **9**, 1803137.
170. M. Wang, L. Fan, D. Tian, X. Wu, Y. Qiu, C. Zhao, B. Guan, Y. Wang, N. Zhang and K. Sun, *ACS Energy Lett.*, 2018, **3**, 1627-1633.
171. B. Cao, D. Li, B. Hou, Y. Mo, L. Yin and Y. Chen, *ACS Appl. Mater. Interfaces*, 2016, **8**, 27795-27802.
172. M. Qi, X. Liang, F. Wang, M. Han, J. Yin and M. Chen, *J. Alloys Compd.*, 2019, 799, 345-350.
173. P. Guo, K. Sun, X. Shang, D. Liu, Y. Wang, Q. Liu, Y. Fu and D. He, *Small*, 2019, **15**, 1902363.
174. Q. Sun, B. Xi, J. Y. Li, H. Mao, X. Ma, J. Liang, J. Feng and S. Xiong, *Adv. Energy Mater.*, 2018, **8**, 1800595.
175. Q. Fan, W. Liu, Z. Weng, Y. Sun and H. Wang, *J. Am. Chem. Soc.*, 2015, **137**, 12946-12953.
176. L. Kong, X. Chen, B. Q. Li, H. J. Peng, J. Q. Huang, J. Xie and Q. Zhang, *Adv. Mater.*, 2018, **30**, 1705219.
177. Z. Hao, R. Zeng, L. Yuan, Q. Bing, J. Liu, J. Xiang and Y. Huang, *Nano Energy*, 2017, **40**, 360-368.
178. R. Demir-Cakan, M. Morcrette, F. Nouar, C. Davoisne, T. Devic, D. Gonbeau, R. Dominko, C.

Serre, G. Férey and J.-M. Tarascon, *J. Am. Chem. Soc.*, 2011, **133**, 16154-16160.
179. J. Zheng, J. Tian, D. Wu, M. Gu, W. Xu, C. Wang, F. Gao, M. H. Engelhard, J.-G. Zhang and J. Liu, *Nano Lett.*, 2014, **14**, 2345-2352.
180. J. Zhou, R. Li, X. Fan, Y. Chen, R. Han, W. Li, J. Zheng, B. Wang and X. Li, *Energy Environ. Sci.*, 2014, **7**, 2715-2724.
181. H. Jiang, X. C. Liu, Y. Wu, Y. Shu, X. Gong, F. S. Ke and H. Deng, *Angew. Chem. Int. Ed.*, 2018, **57**, 3916-3921.
182. Y. Mao, G. Li, Y. Guo, Z. Li, C. Liang, X. Peng and Z. Lin, *Nat. Commun.*, 2017, **8**, 14628.
183. D. Su, M. Cortie, H. Fan and G. Wang, *Adv. Mater.*, 2017, **29**, 1700587.
184. M. Gong, Y. Li, H. Wang, Y. Liang, J. Z. Wu, J. Zhou, J. Wang, T. Regier, F. Wei and H. Dai, *J. Am. Chem. Soc.*, 2013, **135**, 8452-8455.
185. J. Jiang, J. Zhu, W. Ai, X. Wang, Y. Wang, C. Zou, W. Huang and T. Yu, *Nat. Commun.*, 2015, **6**, 8622.
186. X.-Q. Niu, X.-L. Wang, D. Xie, D.-H. Wang, Y.-D. Zhang, Y. Li, T. Yu and J.-P. Tu, *ACS Appl. Mater. Interfaces*, 2015, **7**, 16715-16722.
187. X.-q. Niu, X.-l. Wang, D.-h. Wang, Y. Li, Y.-j. Zhang, T. Yang, T. Yu and J.-p. Tu, *J. Mater. Chem. A*, 2015, **3**, 17106-17112.
188. J. Zhang, H. Hu, Z. Li and X. W. Lou, *Angew. Chem. Int. Ed.*, 2016, **55**, 3982-3986.
189. J. Zhang, Z. Li, Y. Chen, S. Gao and X. W. Lou, *Angew. Chem. Int. Ed.*, 2018, **57**, 10944-10948.
190. M. Chhowalla, H. S. Shin, G. Eda, L.-J. Li, K. P. Loh and H. Zhang, *Nat. Chem.*, 2013, **5**, 263.
191. C. Tan, X. Cao, X.-J. Wu, Q. He, J. Yang, X. Zhang, J. Chen, W. Zhao, S. Han and G.-H. Nam, *Chem. Rev.*, 2017, **117**, 6225-6331.
192. C. Tan and H. Zhang, *Chem. Soc. Rev.*, 2015, **44**, 2713-2731.
193. H. Tian, X. Yu, H. Shao, L. Dong, Y. Chen, X. Fang, C. Wang, W. Han and G. Wang, *Adv. Energy Mater.*, 2019, 1901560.
194. G. R. Bhimanapati, Z. Lin, V. Meunier, Y. Jung, J. Cha, S. Das, D. Xiao, Y. Son, M. S. Strano and V. R. Cooper, *ACS Nano*, 2015, **9**, 11509-11539.
195. L. Peng, Y. Zhu, D. Chen, R. S. Ruoff and G. Yu, *Adv. Energy Mater.*, 2016, **6**, 1600025.
196. Z. W. Seh, J. H. Yu, W. Li, P.-C. Hsu, H. Wang, Y. Sun, H. Yao, Q. Zhang and Y. Cui, *Nat. Commun.*, 2014, **5**, 5017.
197. S.-H. Chung, L. Luo and A. Manthiram, *ACS Energy Lett.*, 2018, **3**, 568-573.
198. S. Ogawa and T. Teranishi, *Phys. Lett. A*, 1972, **42**, 147-148.
199. Z. Yuan, H.-J. Peng, T.-Z. Hou, J.-Q. Huang, C.-M. Chen, D.-W. Wang, X.-B. Cheng, F. Wei and Q. Zhang, *Nano Lett.*, 2016, **16**, 519-527.
200. T. Chen, Z. Zhang, B. Cheng, R. Chen, Y. Hu, L. Ma, G. Zhu, J. Liu and Z. Jin, *J. Am. Chem. Soc.*, 2017, **139**, 12710-12715.
201. C. Dai, J. M. Lim, M. Wang, L. Hu, Y. Chen, Z. Chen, H. Chen, S. J. Bao, B. Shen and Y. Li, *Adv. Funct. Mater.*, 2018, **28**, 1704443.
202. R. Bouchard, P. Russo and A. Wold, *Inorg. Chem.*, 1965, **4**, 685-688.
203. H. Zhang, M. Zou, W. Zhao, Y. Wang, Y. Chen, Y. Wu, L. Dai and A. Cao, *ACS Nano*, 2019, 13, 3982-3991.
204. J. Pu, Z. Shen, J. Zheng, W. Wu, C. Zhu, Q. Zhou, H. Zhang and F. Pan, *Nano Energy*, 2017, **37**, 7-14.
205. T. Chen, L. Ma, B. Cheng, R. Chen, Y. Hu, G. Zhu, Y. Wang, J. Liang, Z. Tie and J. Liu, *Nano*

Energy, 2017, **38**, 239-248.
206. X. Zhang, Z. Lai, C. Tan and H. Zhang, *Angew. Chem. Int. Ed.*, 2016, **55**, 8816-8838.
207. G. Ye, Y. Gong, J. Lin, B. Li, Y. He, S. T. Pantelides, W. Zhou, R. Vajtai and P. M. Ajayan, *Nano Lett.*, 2016, **16**, 1097-1103.
208. X. Huang, Z. Zeng and H. Zhang, *Chem. Soc. Rev.*, 2013, **42**, 1934-1946.
209. W. Tang, Z. Chen, B. Tian, H.-W. Lee, X. Zhao, X. Fan, Y. Fan, K. Leng, C. Peng and M.-H. Kim, *J. Am. Chem. Soc.*, 2017, **139**, 10133-10141.
210. H. Lin, L. Yang, X. Jiang, G. Li, T. Zhang, Q. Yao, G. W. Zheng and J. Y. Lee, *Energy Environ. Sci.*, 2017, **10**, 1476-1486.
211. J. Xu, W. Zhang, H. Fan, F. Cheng, D. Su and G. Wang, *Nano Energy*, 2018, **51**, 73-82.
212. G. Zhou, H. Tian, Y. Jin, X. Tao, B. Liu, R. Zhang, Z. W. Seh, D. Zhuo, Y. Liu and J. Sun, *Proc. Natl. Acad. Sci. U.S.A.*, 2017, **114**, 840-845.
213. W. Xue, Z. Shi, L. Suo, C. Wang, Z. Wang, H. Wang, K. P. So, A. Maurano, D. Yu and Y. Chen, *Nat. Energy*, 2019, 4, 374-382.
214. H. Ye, L. Ma, Y. Zhou, L. Wang, N. Han, F. Zhao, J. Deng, T. Wu, Y. Li and J. Lu, *Proc. Natl. Acad. Sci. U.S.A.*, 2017, **114**, 13091-13096.
215. X. Yang, X. Gao, Q. Sun, S. P. Jand, Y. Yu, Y. Zhao, X. Li, K. Adair, L. Y. Kuo and J. Rohrer, *Adv. Mater.*, 2019, 1901220.
216. L. Ma, W. Zhang, L. Wang, Y. Hu, G. Zhu, Y. Wang, R. Chen, T. Chen, Z. Tie and J. Liu, *ACS Nano*, 2018, **12**, 4868-4876.
217. Z. Yu, N. Zhang, X. Zhang, Y. Li, G. Xie, W. Ge, L. Zhang and T. Zhang, *J. Electroanalyti. Chem.*, 2019, 113524.
218. C. Gao, C. Fang, H. Zhao, J. Yang, Z. Gu, W. Sun, W. Zhang, S. Li, L.-C. Xu and X. Li, *J. Power Sources*, 2019, **421**, 132-138.
219. C. Ye, L. Zhang, C. Guo, D. Li, A. Vasileff, H. Wang and S. Z. Qiao, *Adv. Funct. Mater.*, 2017, **27**, 1702524.
220. B. Che, D. Wang and X. Xu, *Int. J. Electrochem. Sci*, 2019, **14**, 9520-9526.
221. Y. Lu, X. Li, J. Liang, L. Hu, Y. Zhu and Y. Qian, *Nanoscale*, 2016, **8**, 17616-17622.
222. Y. Tian, H. Huang, G. Liu, R. Bi and L. Zhang, *Chem. Commun.*, 2019, **55**, 3243-3246.
223. X. Gao, X. Yang, M. Li, Q. Sun, J. Liang, J. Luo, J. Wang, W. Li, J. Liang and Y. Liu, *Adv. Funct. Mater.*, 2019, **29**, 1806724.
224. M. Wang, L. Fan, X. Wu, Y. Qiu, Y. Wang, N. Zhang and K. Sun, *Chem. Eur. J.*, 2019, **25**, 5416-5421.
225. S. Jiang, M. Chen, X. Wang, P. Zeng, Y. Li, H. Liu, X. Li, C. Huang, H. Shu and Z. Luo, *Electrochimi. Acta*, 2019, **313**, 151-160.
226. K. Sun, D. Su, Q. Zhang, D. C. Bock, A. C. Marschilok, K. J. Takeuchi, E. S. Takeuchi and H. Gan, *J. Electrochem. Soc.*, 2015, **162**, A2834-A2839.
227. K. Xi, D. He, C. Harris, Y. Wang, C. Lai, H. Li, P. R. Coxon, S. Ding, C. Wang and R. V. Kumar, *Adv. Sci*, 2019, **6**, 1800815.
228. S. S. Zhang and D. T. Tran, *J. Mater. Chem. A*, 2016, **4**, 4371-4374.
229. T. Lei, W. Chen, J. Huang, C. Yan, H. Sun, C. Wang, W. Zhang, Y. Li and J. Xiong, *Adv. Energy Mater.*, 2017, **7**, 1601843.
230. Z. Xiao, Z. Yang, L. Zhang, H. Pan and R. Wang, *ACS Nano*, 2017, **11**, 8488-8498.
231. D. Cai, L. Wang, L. Li, Y. Zhang, J. Li, D. Chen, H. Tu and W. Han, *J. Mater. Chem. A*, 2019, **7**,

806-815.
232. Z. Cheng, Z. Xiao, H. Pan, S. Wang and R. Wang, *Adv. Energy Mater.*, 2018, **8**, 1702337.
233. H. Wu, Y. Huan, D. Wang, M. Li, X. Cheng, Z. Bai, P. Wu, W. Peng, R. Zhang and Z. Ji, *J. Electrochem. Soc.*, 2019, **166**, A188-A194.
234. T. Guo, Y. Song, Z. Sun, Y. Wu, Y. Xia, Y. Li, J. Sun, K. Jiang, S. Dou and J. Sun, *J. Energy Chem.*, 2020, **42**, 34-42.
235. D. Wang, S. Zhao, F. Li, L. He, Y. Zhao, H. Zhao, Y. Liu, Y. Wei and G. Chen, *ChemSusChem*, 2019.
236. Z. Zeng, W. Li, Q. Wang and X. Liu, *Adv. Sci.*, 2019, 1900711.
237. X. Tan, X. Wang, X. Wang, Y. Wang, C. Li and D. Xia, *Ionics*, 2019, 1-10.
238. X. Lu, Q. Zhang, J. Wang, S. Chen, J. Ge, Z. Liu, L. Wang, H. Ding, D. Gong and H. Yang, *Chem. Eng. J.*, 2019, **358**, 955-961.
239. S. Wang, H. Chen, J. Liao, Q. Sun, F. Zhao, J. Luo, X. Lin, X. Niu, M. Wu and R. Li, *ACS Energy Lett.*, 2019.
240. L. Zhu, C. Yang, Y. Chen, J. Wang, C. Wang and X. Zhu, *J. Alloys Compd.*, 2019, **785**, 855-861.
241. Z. Cui, C. Zu, W. Zhou, A. Manthiram and J. B. Goodenough, *Adv. Mater.*, 2016, **28**, 6926-6931.
242. W. G. Lim, C. Jo, A. Cho, J. Hwang, S. Kim, J. W. Han and J. Lee, *Adv. Mater.*, 2019, **31**, 1806547.
243. Y. Wang, R. Zhang, Y.-C. Pang, X. Chen, J. Lang, J. Xu, C. Xiao, H. Li, K. Xi and S. Ding, *Energy Storage Mater.*, 2019, **16**, 228-235.
244. X. Gao, D. Zhou, Y. Chen, W. Wu, D. Su, B. Li and G. Wang, *Commun. Chem.*, 2019, **2**, 1-10.
245. Z. Li, Q. He, X. Xu, Y. Zhao, X. Liu, C. Zhou, D. Ai, L. Xia and L. Mai, *Adv. Mater.*, 2018, **30**, 1804089.
246. D.-R. Deng, F. Xue, Y.-J. Jia, J.-C. Ye, C.-D. Bai, M.-S. Zheng and Q.-F. Dong, *ACS Nano*, 2017, **11**, 6031-6039.
247. Z. Sun, J. Zhang, L. Yin, G. Hu, R. Fang, H.-M. Cheng and F. Li, *Nat. Commun.*, 2017, **8**, 14627.
248. L. Ma, H. Yuan, W. Zhang, G. Zhu, Y. Wang, Y. Hu, P. Zhao, R. Chen, T. Chen and J. Liu, *Nano Lett.*, 2017, **17**, 7839-7846.
249. K. Xiao, J. Wang, Z. Chen, Y. Qian, Z. Liu, L. Zhang, X. Chen, J. Liu, X. Fan and Z. X. Shen, *Small*, 2019, 1901454.
250. H. J. Peng, G. Zhang, X. Chen, Z. W. Zhang, W. T. Xu, J. Q. Huang and Q. Zhang, *Angew. Chem. Int. Ed.*, 2016, **55**, 12990-12995.
251. F. Zhou, Z. Li, X. Luo, T. Wu, B. Jiang, L.-L. Lu, H.-B. Yao, M. Antonietti and S.-H. Yu, *Nano Lett.*, 2018, **18**, 1035-1043.
252. X. Tao, L. Dong, X. Wang, W. Zhang, B. J. Nelson and X. Li, *Adv. Mater.*, 2010, **22**, 2055-2059.
253. S. Song, W. Xu, R. Cao, L. Luo, M. H. Engelhard, M. E. Bowden, B. Liu, L. Estevez, C.-M. Wang and J.-G. Zhang, *Nano Energy*, 2017, **33**, 195-204.
254. W.-B. Luo, S.-L. Chou, J.-Z. Wang and H.-K. Liu, *J. Mater. Chem. A*, 2015, **3**, 18395-18399.
255. S. Song, W. Xu, J. Zheng, L. Luo, M. H. Engelhard, M. E. Bowden, B. Liu, C.-M. Wang and J.-G. Zhang, *Nano Lett.*, 2017, **17**, 1417-1424.
256. L. Luo, S. H. Chung, H. Yaghoobnejad Asl and A. Manthiram, *Adv. Mater.*, 2018, **30**, 1804149.
257. S. Shen, X. Xia, Y. Zhong, S. Deng, D. Xie, B. Liu, Y. Zhang, G. Pan, X. Wang and J. Tu, *Adv. Mater.*, 2019, 1900009.
258. M. Naguib, M. Kurtoglu, V. Presser, J. Lu, J. Niu, M. Heon, L. Hultman, Y. Gogotsi and M. W.

Barsoum, *Adv. Mater.*, 2011, **23**, 4248-4253.
259. D. Xiong, X. Li, Z. Bai and S. Lu, *Small*, 2018, **14**, 1703419.
260. J. Pang, R. G. Mendes, A. Bachmatiuk, L. Zhao, H. Q. Ta, T. Gemming, H. Liu, Z. Liu and M. H. Rummeli, *Chem. Soc. Rev.*, 2019, **48**, 72-133.
261. N. K. Chaudhari, H. Jin, B. Kim, D. San Baek, S. H. Joo and K. Lee, *J. Mater. Chem. A*, 2017, **5**, 24564-24579.
262. M. Okubo, A. Sugahara, S. Kajiyama and A. Yamada, *Acc. Chem. Res.*, 2018, **51**, 591-599.
263. X. Liang, A. Garsuch and L. F. Nazar, *Angew. Chem. Int. Ed.*, 2015, **54**, 3907-3911.
264. X. Liang, Y. Rangom, C. Y. Kwok, Q. Pang and L. F. Nazar, *Adv. Mater.*, 2017, **29**, 1603040.
265. W. Bao, L. Liu, C. Wang, S. Choi, D. Wang and G. Wang, *Adv. Energy Mater.*, 2018, **8**, 1702485.
266. Z. Xiao, Z. Yang, Z. Li, P. Li and R. Wang, *ACS Nano*, 2019, **13**, 3404-3412.
267. Y. Shi and B. Zhang, *Chem. Soc. Rev.*, 2016, **45**, 1529-1541.
268. X. Yu, Z.-Y. Yu, X.-L. Zhang, Y.-R. Zheng, Y. Duan, Q. Gao, R. Wu, B. Sun, M.-R. Gao and G. Wang, *J. Am. Chem. Soc.*, 2019, **141**, 7537-7543.
269. G. Zhang, G. Wang, Y. Liu, H. Liu, J. Qu and J. Li, *J. Am. Chem. Soc.*, 2016, **138**, 14686-14693.
270. Y. Wang, B. Kong, D. Zhao, H. Wang and C. Selomulya, *Nano Today*, 2017, **15**, 26-55.
271. Y. Mi, W. Liu, X. Li, J. Zhuang, H. Zhou and H. Wang, *Nano Res.*, 2017, **10**, 3698-3705.
272. Y. Zhong, L. Yin, P. He, W. Liu, Z. Wu and H. Wang, *J. Am. Chem. Soc.*, 2018, **140**, 1455-1459.
273. H. Yuan, X. Chen, G. Zhou, W. Zhang, J. Luo, H. Huang, Y. Gan, C. Liang, Y. Xia and J. Zhang, *ACS Energy Lett.*, 2017, **2**, 1711-1719.
274. Y. Chen, W. Zhang, D. Zhou, H. Tian, D. Su, C. Wang, D. Stockdale, F. Kang, B. Li and G. Wang, *ACS Nano*, 2019, **13**, 4731-4741.
275. X. Chen, S. Zeng, H. Muheiyati, Y. Zhai, C. Li, X. Ding, L. Wang, D. Wang, L. Xu and Y. He, *ACS Energy Lett.*, 2019, **4**, 1496-1504.
276. Z. Wang, J. Shen, J. Liu, X. Xu, Z. Liu, R. Hu, L. Yang, Y. Feng, J. Liu and Z. Shi, *Adv. Mater.*, 2019, 1902228.
277. J. Shen, X. Xu, J. Liu, Z. Liu, F. Li, R. Hu, J. Liu, X. Hou, Y. Feng and Y. Yu, *ACS Nano*, 2019, **13**, 8986-8996.
278. C. Li, X. Liu, L. Zhu, R. Huang, M. Zhao, L. Xu and Y. Qian, *Chem. Mater.*, 2018, **30**, 6969-6977.
279. B. Guan, L. Fan, X. Wu, P. Wang, Y. Qiu, M. Wang, Z. Guo, N. Zhang and K. Sun, *J. Mater. Chem. A*, 2018, **6**, 24045-24049.
280. Q. Pang, C. Y. Kwok, D. Kundu, X. Liang and L. F. Nazar, *Joule*, 2019, **3**, 136-148.
281. S. Bud'Ko, G. Lapertot, C. Petrovic, C. Cunningham, N. Anderson and P. Canfield, *Phys. Rev. Lett.*, 2001, **86**, 1877.
282. Z. Y. Wang, L. Wang, S. Liu, G. R. Li and X. P. Gao, *Adv. Funct. Mater.*, 2019, 1901051.
283. E. Hosono, S. Fujihara, I. Honma, M. Ichihara and H. Zhou, *J. Power Sources*, 2006, **158**, 779-783.
284. L. Xu, H. Zhao, B. Huang, J. Wang, J. Xia, N. Li, D. Yin, M. Luo, F. Luo and Y. Du, *Angew. Chem. Int. Ed.*, 2019, **58**, 11491-11496.
285. X.-C. Liu, S. P. Zhou, M. Liu, G.-L. Xu, X.-D. Zhou, L. Huang, S.-G. Sun, K. Amine and F.-S. Ke, *Nano Energy*, 2018, **50**, 685-690.
286. Z. Liu, L. Zhou, Q. Ge, R. Chen, M. Ni, W. Utetiwabo, X. Zhang and W. Yang, *ACS Appl. Mater. Interfaces*, 2018, **10**, 19311-19317.
287. J. Wang, L. Jia, J. Zhong, Q. Xiao, C. Wang, K. Zang, H. Liu, H. Zheng, J. Luo and J. Yang,

Energy Storage Mater., 2019, **18**, 246-252.
288. Z. Du, X. Chen, W. Hu, C. Chuang, S. Xie, A. Hu, W. Yan, X. Kong, X. Wu and H. Ji, *J. Am. Chem. Soc.*, 2019, **141**, 3977-3985.
289. G. Zhou, S. Pei, L. Li, D. W. Wang, S. Wang, K. Huang, L. C. Yin, F. Li and H. M. Cheng, *Adv. Mater.*, 2014, **26**, 625-631.
290. K. Yuan, L. Yuan, J. Xiang, J. Liu, J. Gu, X. Chen, Z. Hao, M. Li and Y. Huang, *J. Electrochem. Soc.*, 2018, **165**, A1880-A1885.
291. G. Zhou, L. Li, D. W. Wang, X. y. Shan, S. Pei, F. Li and H. M. Cheng, *Adv. Mater.*, 2015, **27**, 641-647.
292. Z. Du, C. Guo, L. Wang, A. Hu, S. Jin, T. Zhang, H. Jin, Z. Qi, S. Xin and X. Kong, *ACS Appl. Mater. Interfaces*, 2017, **9**, 43696-43703.
293. J.-Q. Huang, Q. Zhang, H.-J. Peng, X.-Y. Liu, W.-Z. Qian and F. Wei, *Energy Environ. Sci.*, 2014, **7**, 347-353.
294. M. Gu, J. Lee, Y. Kim, J. S. Kim, B. Y. Jang, K. T. Lee and B.-S. Kim, *RSC Adv.*, 2014, **4**, 46940-46946.
295. X. Yu, J. Joseph and A. Manthiram, *Mater. Horiz.*, 2016, **3**, 314-319.
296. Y. He, Y. Qiao, Z. Chang, X. Cao, M. Jia, P. He and H. Zhou, *Angew. Chem.*, 2019, **131**, 11900-11904.
297. S. Bai, X. Liu, K. Zhu, S. Wu and H. Zhou, *Nat. Energy*, 2016, **1**, 16094.
298. Y. He, Z. Chang, S. Wu, Y. Qiao, S. Bai, K. Jiang, P. He and H. Zhou, *Adv. Energy Mater.*, 2018, **8**, 1802130.
299. J. He, Y. Chen and A. Manthiram, *Energy Environ. Sci.*, 2018, **11**, 2560-2568.
300. L. Zhang, X. Chen, F. Wan, Z. Niu, Y. Wang, Q. Zhang and J. Chen, *ACS Nano*, 2018, **12**, 9578-9586.
301. X. Yu, G. Zhou and Y. Cui, *ACS Aappl. Mater. Interfaces*, 2018, **11**, 3080-3086.
302. Z. A. Ghazi, X. He, A. M. Khattak, N. A. Khan, B. Liang, A. Iqbal, J. Wang, H. Sin, L. Li and Z. Tang, *Adv. Mater.*, 2017, **29**, 1606817.
303. L. Tan, X. Li, Z. Wang, H. Guo and J. Wang, *ACS Appl. Mater. Interfaces*, 2018, **10**, 3707-3713.
304. P. Guo, D. Liu, Z. Liu, X. Shang, Q. Liu and D. He, *Electrochimi. Acta*, 2017, **256**, 28-36.
305. L.-B. Xing, K. Xi, Q. Li, Z. Su, C. Lai, X. Zhao and R. V. Kumar, *J. Power Sources*, 2016, **303**, 22-28.
306. L. Wang, Z. Yang, H. Nie, C. Gu, W. Hua, X. Xu, X. a. Chen, Y. Chen and S. Huang, *J. Mater. Chem. A*, 2016, **4**, 15343-15352.
307. Y.-S. Su and A. Manthiram, *Chem. Commun.*, 2012, **48**, 8817-8819.
308. H. M. Kim, J.-Y. Hwang, A. Manthiram and Y.-K. Sun, *ACS Appl. Mater. Interfaces*, 2016, **8**, 983-987.
309. J. H. Kim, J. Seo, J. Choi, D. Shin, M. Carter, Y. Jeon, C. Wang, L. Hu and U. Paik, *ACS Appl. Mater. Interfaces*, 2016, **8**, 20092-20099.
310. J.-Q. Huang, Z.-L. Xu, S. Abouali, M. A. Garakani and J.-K. Kim, *Carbon*, 2016, **99**, 624-632.
311. K. Zhang, F. Qin, J. Fang, Q. Li, M. Jia, Y. Lai, Z. Zhang and J. Li, *J. Solid State Electrochem.*, 2014, **18**, 1025-1029.
312. Y. Yang, W. Sun, J. Zhang, X. Yue, Z. Wang and K. Sun, *Electrochimi. Acta*, 2016, **209**, 691-699.
313. R. Singhal, S.-H. Chung, A. Manthiram and V. Kalra, *J. Mater. Chem A*, 2015, **3**, 4530-4538.
314. J. Wang, Y. Yang and F. Kang, *Electrochimi. Acta*, 2015, **168**, 271-276.

315. S. H. Chung, P. Han, R. Singhal, V. Kalra and A. Manthiram, *Adv. Energy Mater.*, 2015, **5**, 1500738.
316. J.-Q. Huang, B. Zhang, Z.-L. Xu, S. Abouali, M. A. Garakani, J. Huang and J.-K. Kim, *J. Power Sources*, 2015, **285**, 43-50.
317. M. Liu, Q. Li, X. Qin, G. Liang, W. Han, D. Zhou, Y. B. He, B. Li and F. Kang, *Small*, 2017, **13**, 1602539.
318. L. Yan, N. Luo, W. Kong, S. Luo, H. Wu, K. Jiang, Q. Li, S. Fan, W. Duan and J. Wang, *J. Power Sources*, 2018, **389**, 169-177.
319. Y. Dong, S. Zheng, J. Qin, X. Zhao, H. Shi, X. Wang, J. Chen and Z.-S. Wu, *ACS Nano*, 2018, **12**, 2381-2388.
320. J. Song, D. Su, X. Xie, X. Guo, W. Bao, G. Shao and G. Wang, *ACS Appl. Mater. Interfaces*, 2016, **8**, 29427-29433.
321. Y. Zhang, G. Xu, Q. Kang, L. Zhan, W. Tang, Y. Yu, K. Shen, H. Wang, X. Chu and J. Wang, *J. Mater. Chem. A*, 2019.
322. Z. Wang, M. Feng, H. Sun, G. Li, Q. Fu, H. Li, J. Liu, L. Sun, A. Mauger and C. M. Julien, *Nano Energy*, 2019, **59**, 390-398.
323. D. Fang, Y. Wang, X. Liu, J. Yu, C. Qian, S. Chen, X. Wang and S. Zhang, *ACS Nano*, 2019, **13**, 1563-1573.
324. M. Waqas, Y. Han, D. Chen, S. Ali, C. Zhen, C. Feng, B. Yuan, J. Han and W. He, *Energy Storage Mater.*, 2020, **27**, 333-341.
325. J. Wu, H. Zeng, X. Li, X. Xiang, Y. Liao, Z. Xue, Y. Ye and X. Xie, *Adv. Energy Mater.*, 2018, **8**, 1802430.
326. X. Wu, L. Fan, Y. Qiu, M. Wang, J. Cheng, B. Guan, Z. Guo, N. Zhang and K. Sun, *ChemSusChem*, 2018, **11**, 3345-3351.
327. X. Song, G. Chen, S. Wang, Y. Huang, Z. Jiang, L.-X. Ding and H. Wang, *ACS Appl. Mater. Interfaces*, 2018, **10**, 26274-26282.
328. W. Sun, X. Ou, X. Yue, Y. Yang, Z. Wang, D. Rooney and K. Sun, *Electrochimi. Acta*, 2016, **207**, 198-206.
329. W. Kong, L. Yan, Y. Luo, D. Wang, K. Jiang, Q. Li, S. Fan and J. Wang, *Adv. Funct. Mater.*, 2017, **27**, 1606663.
330. Y. Yang and J. Zhang, *Adv. Energy Mater.*, 2018, **8**, 1801778.
331. M. Li, C. Wang, L. Miao, J. Xiang, T. Wang, K. Yuan, J. Chen and Y. Huang, *J. Mater. Chem. A*, 2018, **6**, 5862-5869.
332. F. Li, M. R. Kaiser, J. Ma, Z. Guo, H. Liu and J. Wang, *Energy Storage Mater.*, 2018, **13**, 312-322.
333. G. Ma, Z. Wen, Q. Wang, C. Shen, P. Peng, J. Jin and X. Wu, *J. Power Sources*, 2015, **273**, 511-516.
334. G. Ma, Z. Wen, J. Jin, M. Wu, X. Wu and J. Zhang, *J. Power Sources*, 2014, **267**, 542-546.
335. P. J. H. Kim, J. Seo, K. Fu, J. Choi, Z. Liu, J. Kwon, L. Hu and U. Paik, *NPG Asia Mater.*, 2017, **9**, e375.
336. K. Liu, D. Zhuo, H. W. Lee, W. Liu, D. Lin, Y. Lu and Y. Cui, *Adv. Mater.*, 2017, **29**, 1603987.
337. Y. Zhao, M. Liu, W. Lv, Y.-B. He, C. Wang, Q. Yun, B. Li, F. Kang and Q.-H. Yang, *Nano Energy*, 2016, **30**, 1-8.
338. T. Yim, S. H. Han, N. H. Park, M. S. Park, J. H. Lee, J. Shin, J. W. Choi, Y. Jung, Y. N. Jo and J. S. Yu, *Adv. Funct. Mater.*, 2016, **26**, 7817-7823.

339. P. Guo, K. Sun, X. Shang, D. Liu, Y. Wang, Q. Liu, Y. Fu and D. He, *Small*, 2019, 1902363.
340. Y. Tian, G. Li, Y. Zhang, D. Luo, X. Wang, Y. Zhao, H. Liu, P. Ji, X. Du and J. Li, *Adv. Mater.*, 2020, **32**, 1904876.
341. D. Tian, X. Song, M. Wang, X. Wu, Y. Qiu, B. Guan, X. Xu, L. Fan, N. Zhang and K. Sun, *Adv. Energy Mater.*, 2019, **9**, 1901940.
342. J. Sun, Y. Sun, M. Pasta, G. Zhou, Y. Li, W. Liu, F. Xiong and Y. Cui, *Adv. Mater.*, 2016, **28**, 9797-9803.
343. Y. Fan, Z. Yang, W. Hua, D. Liu, T. Tao, M. M. Rahman, W. Lei, S. Huang and Y. Chen, *Adv. Energy Mater.*, 2017, **7**, 1602380.
344. Z. Li, C. Zhou, J. Hua, X. Hong, C. Sun, H. W. Li, X. Xu and L. Mai, *Adv. Mater.*, 2020, 1907444.
345. Z. Xiao, Z. Yang, L. Wang, H. Nie, M. e. Zhong, Q. Lai, X. Xu, L. Zhang and S. Huang, *Adv. Mater.*, 2015, **27**, 2891-2898.
346. G. Liang, J. Wu, X. Qin, M. Liu, Q. Li, Y.-B. He, J.-K. Kim, B. Li and F. Kang, *ACS Appl. Mater. Interfaces*, 2016, **8**, 23105-23113.
347. B. Guan, Y. Zhang, L. Fan, X. Wu, M. Wang, Y. Qiu, N. Zhang and K. Sun, *ACS Nano*, 2019, **13**, 6742-6750.
348. S. Li, G. Ren, M. N. F. Hoque, Z. Dong, J. Warzywoda and Z. Fan, *Appl. Sur. Sci.*, 2017, **396**, 637-643.
349. J. Song, C. Zhang, X. Guo, J. Zhang, L. Luo, H. Liu, F. Wang and G. Wang, *J. Mater. Chem. A*, 2018, **6**, 16610-16616.
350. Z. Cheng, H. Pan, J. Chen, X. Meng and R. Wang, *Adv. Energy Mater.*, 2019, 1901609.
351. K. Zhang, Z. Chen, R. Ning, S. Xi, W. Tang, Y. Du, C. Liu, Z. Ren, X. Chi and M. Bai, *ACS Appl. Mater. Interfaces*, 2019, **11**, 25147-25154.
352. L. Zhang, D. Liu, Z. Muhammad, F. Wan, W. Xie, Y. Wang, L. Song, Z. Niu and J. Chen, *Adv. Mater.*, 2019, 1903955.
353. J. Xie, B. Q. Li, H. J. Peng, Y. W. Song, M. Zhao, X. Chen, Q. Zhang and J. Q. Huang, *Adv. Mater.*, 2019, 1903813.
354. H. Yuan, J. Q. Huang, H. J. Peng, M. M. Titirici, R. Xiang, R. Chen, Q. Liu and Q. Zhang, *Adv. Energy Mater.*, 2018, **8**, 1802107.
355. Q. Guo and Z. Zheng, *Adv. Funct. Mater.*, 2019, 1907931.
356. H. J. Peng, J. Q. Huang, X. B. Cheng and Q. Zhang, *Adv. Energy Mater.*, 2017, **7**, 1700260.
357. D. Lv, J. Zheng, Q. Li, X. Xie, S. Ferrara, Z. Nie, L. B. Mehdi, N. D. Browning, J. G. Zhang and G. L. Graff, *Adv. Energy Mater.*, 2015, **5**, 1402290.
358. Q. Pang, X. Liang, C. Y. Kwok, J. Kulisch and L. F. Nazar, *Adv. Energy Mater.*, 2017, **7**, 1601630.
359. C. Y. Kwok, Q. Pang, A. F. Worku, X. Liang, M. Gauthier and L. F. Nazar, *ACS Appl. Mater. Interfaces*, 2019, **11**, 22481-22491.
360. Z. W. Seh, Q. Zhang, W. Li, G. Zheng, H. Yao and Y. Cui, *Chem. Sci.*, 2013, **4**, 3673-3677.
361. P. Bhattacharya, M. I. Nandasiri, D. Lv, A. M. Schwarz, J. T. Darsell, W. A. Henderson, D. A. Tomalia, J. Liu, J.-G. Zhang and J. Xiao, *Nano Energy*, 2016, **19**, 176-186.
362. H. Wang, V. Sencadas, G. Gao, H. Gao, A. Du, H. Liu and Z. Guo, *Nano Energy*, 2016, **26**, 722-728.
363. W. Chen, T. Qian, J. Xiong, N. Xu, X. Liu, J. Liu, J. Zhou, X. Shen, T. Yang and Y. Chen, *Adv. Mater.*, 2017, **29**, 1605160.
364. G. Zhou, K. Liu, Y. Fan, M. Yuan, B. Liu, W. Liu, F. Shi, Y. Liu, W. Chen and J. Lopez, *ACS Cent.*

Sci., 2018, **4**, 260-267.
365. G. Ai, Y. Dai, Y. Ye, W. Mao, Z. Wang, H. Zhao, Y. Chen, J. Zhu, Y. Fu and V. Battaglia, *Nano Energy*, 2015, **16**, 28-37.
366. C. Milroy and A. Manthiram, *Adv. Mater.*, 2016, **28**, 9744-9751.
367. L. Wang, Y. Ye, N. Chen, Y. Huang, L. Li, F. Wu and R. Chen, *Adv. Funct. Mater.*, 2018, **28**, 1800919.
368. S. S. Zhang, *J. Power Sources*, 2013, **231**, 153-162.
369. S. S. Zhang, *Electrochimi. Acta*, 2013, **97**, 226-230.
370. J.-W. Choi, J.-K. Kim, G. Cheruvally, J.-H. Ahn, H.-J. Ahn and K.-W. Kim, *Electrochimi. Acta*, 2007, **52**, 2075-2082.
371. P. P. R. Harks, C. B. Robledo, T. W. Verhallen, P. H. Notten and F. M. Mulder, *Adv. Energy Mater.*, 2017, **7**, 1601635.
372. M. Barghamadi, A. S. Best, A. I. Bhatt, A. F. Hollenkamp, M. Musameh, R. J. Rees and T. Rüther, *Energy Environ. Sci.*, 2014, **7**, 3902-3920.
373. M. Barghamadi, M. Musameh, T. Rüther, A. I. Bhatt, A. F. Hollenkamp and A. S. Best, *Lithium–Sulfur Batteries*, 2019, 71-119.
374. A. Gupta, A. Bhargav and A. Manthiram, *Adv. Energy Mater.*, 2019, **9**, 1803096.
375. Q. Cheng, W. Xu, S. Qin, S. Das, T. Jin, A. Li, A. C. Li, B. Qie, P. Yao and H. Zhai, *Angew. Chem. Int. Ed.*, 2019, **58**, 5557-5561.
376. C.-C. Su, M. He, R. Amine, T. Rojas, L. Cheng, A. T. Ngo and K. Amine, *Energy Environ. Sci*, 2019, **12**, 1249-1254.
377. H. Zhang, U. Oteo, X. Judez, G. G. Eshetu, M. Martinez-Ibañez, J. Carrasco, C. Li and M. Armand, *Joule*, 2019, **3**,1689-1702 .
378. G. L. Xu, H. Sun, C. Luo, L. Estevez, M. Zhuang, H. Gao, R. Amine, H. Wang, X. Zhang and C. J. Sun, *Adv. Energy Mater.*, 2019, **9**, 1802235.
379. Q. Zhang, H. Wan, G. Liu, Z. Ding, J. P. Mwizerwa and X. Yao, *Nano Energy*, 2019, **57**, 771-782.
380. Y.-Z. Sun, J.-Q. Huang, C.-Z. Zhao and Q. Zhang, *Sci. Chin. Chem.*, 2017, **60**, 1508-1526.
381. A. Manthiram, X. Yu and S. Wang, *Nat. Rev. Mater.*, 2017, **2**, 16103.
382. M. Dirican, C. Yan, P. Zhu and X. Zhang, *Mater. Sci. Eng.: R: Rep.*, 2019, **136**, 27-46.
383. S. Zhang, K. Ueno, K. Dokko and M. Watanabe, *Adv. Energy Mater.*, 2015, **5**, 1500117.
384. W. Chen, T. Lei, C. Wu, M. Deng, C. Gong, K. Hu, Y. Ma, L. Dai, W. Lv and W. He, *Adv. Energy Mater.*, 2018, **8**, 1702348.
385. K. Sun, N. Li, D. Su and H. Gan, *J. Electrochem. Society*, 2019, **166**, A50-A58.
386. J. Zheng, D. Lv, M. Gu, C. Wang, J.-G. Zhang, J. Liu and J. Xiao, *J. Electrochem. Soc.*, 2013, **160**, A2288-A2292.
387. Y. V. Mikhaylik, *U.S. Patent* 7354980.
388. D. Aurbach, E. Pollak, R. Elazari, G. Salitra, C. S. Kelley and J. Affinito, *J. Electrochem. Soc.*, 2009, **156**, A694-A702.
389. W. Yang, W. Yang, A. Song, L. Gao, G. Sun and G. Shao, *J. Power Sources*, 2017, **348**, 175-182.
390. C. Hu, H. Chen, Y. Shen, D. Lu, Y. Zhao, A.-H. Lu, X. Wu, W. Lu and L. Chen, *Nat. Commun.*, 2017, **8**, 479.
391. Q. Pang, A. Shyamsunder, B. Narayanan, C. Y. Kwok, L. A. Curtiss and L. F. Nazar, *Nat. Energy*, 2018, **3**, 783-791.
392. K. Xu, *Chem. Rev.*, 2004, **104**, 4303-4418.

393. K. Xu, *Chem. Rev.*, 2014, **114**, 11503-11618.
394. D. Aurbach, Y. Talyosef, B. Markovsky, E. Markevich, E. Zinigrad, L. Asraf, J. S. Gnanaraj and H.-J. Kim, *Electrochimi. Acta*, 2004, **50**, 247-254.
395. X. Li, M. Banis, A. Lushington, X. Yang, Q. Sun, Y. Zhao, C. Liu, Q. Li, B. Wang and W. Xiao, *Nat. Commun.*, 2018, **9**, 4509.
396. C. Barchasz, J.-C. Leprêtre, S. Patoux and F. Alloin, *Electrochimi. Acta*, 2013, **89**, 737-743.
397. J. Gao, M. A. Lowe, Y. Kiya and H. c. D. Abruña, *J. Phys. Chem. C*, 2011, **115**, 25132-25137.
398. T. Yim, M.-S. Park, J.-S. Yu, K. J. Kim, K. Y. Im, J.-H. Kim, G. Jeong, Y. N. Jo, S.-G. Woo and K. S. Kang, *Electrochimi. Acta*, 2013, **107**, 454-460.
399. L. Yin, J. Wang, F. Lin, J. Yang and Y. Nuli, *Energy Environ. Sci.*, 2012, **5**, 6966-6972.
400. L. Wang, X. He, J. Li, M. Chen, J. Gao and C. Jiang, *Electrochimi. Acta*, 2012, **72**, 114-119.
401. A. Konarov, D. Gosselink, T. N. L. Doan, Y. Zhang, Y. Zhao and P. Chen, *J. Power Sources*, 2014, **259**, 183-187.
402. K. Jeddi, K. Sarikhani, N. T. Qazvini and P. Chen, *J. Power Sources*, 2014, **245**, 656-662.
403. S. Wei, L. Ma, K. E. Hendrickson, Z. Tu and L. A. Archer, *J. Am. Chem. Soc.*, 2015, **137**, 12143-12152.
404. W. Wang, Z. Cao, G. A. Elia, Y. Wu, W. Wahyudi, E. Abou-Hamad, A.-H. Emwas, L. Cavallo, L.-J. Li and J. Ming, *ACS Energy Lett.*, 2018, **3**, 2899-2907.
405. S. Xin, Y. X. Yin, L. J. Wan and Y. G. Guo, *Part. Part. Syst. Charact.*, 2013, **30**, 321-325.
406. S. Zheng, Y. Chen, Y. Xu, F. Yi, Y. Zhu, Y. Liu, J. Yang and C. Wang, *ACS Nano*, 2013, **7**, 10995-11003.
407. S. Zheng, P. Han, Z. Han, H. Zhang, Z. Tang and J. Yang, *Sci. Rep.*, 2014, **4**, 4842.
408. Z. Zhang, Z. Li, F. Hao, X. Wang, Q. Li, Y. Qi, R. Fan and L. Yin, *Adv. Funct. Mater.*, 2014, **24**, 2500-2509.
409. Q. Zhu, Q. Zhao, Y. An, B. Anasori, H. Wang and B. Xu, *Nano Energy*, 2017, **33**, 402-409.
410. X. Li, A. Lushington, Q. Sun, W. Xiao, J. Liu, B. Wang, Y. Ye, K. Nie, Y. Hu and Q. Xiao, *Nano Lett.*, 2016, **16**, 3545-3549.
411. S. Xiong, K. Xie, Y. Diao and X. Hong, *J. Power Sources*, 2014, **246**, 840-845.
412. Z. Lin and C. Liang, *J. Mater. Chem. A*, 2015, **3**, 936-958.
413. E. Umeshbabu, B. Zheng and Y. Yang, *Electrochem. Energy Rev.*, 2019, 1-32.
414. R. Xu, J. Yue, S. Liu, J. Tu, F. Han, P. Liu and C. Wang, *ACS Energy Lett.*, 2019, **4**, 1073-1079.
415. Q. Zhou, J. Ma, S. Dong, X. Li and G. Cui, *Adv. Mater.*, 2019, 1902029.
416. J. Wan, J. Xie, X. Kong, Z. Liu, K. Liu, F. Shi, A. Pei, H. Chen, W. Chen and J. Chen, *Nat. Nanotech.*, 2019, **14**, 705-711.
417. J. Zhou, T. Qian, J. Liu, M. Wang, L. Zhang and C. Yan, *Nano Lett.*, 2019, **19**, 3066-3073.
418. S. Song, Y. Wu, W. Tang, F. Deng, J. Yao, Z. Liu, R. Hu, Alamusi, Z. Wen and L. Lu, *ACS Sust. Chem. Eng.*, 2019, **7**, 7163-7170.
419. X. Li, D. Wang, H. Wang, H. Yan, Z. Gong and Y. Yang, *ACS Appl. Mater. Interfaces*, 2019, **11**, 22745-22753.
420. Q. Zhao, X. Liu, S. Stalin, K. Khan and L. A. Archer, *Nat. Energy*, 2019, **4**, 365.
421. X. Li, Y. Zheng, Q. Pan and C. Y. Li, *ACS Appl. Mater. Interfaces*, 2019, **11**, 34904-34912.
422. Z. Fan, B. Ding, T. Zhang, Q. Lin, V. Malgras, J. Wang, H. Dou, X. Zhang and Y. Yamauchi, *Small*, 2019, 1903952.
423. X. Li, D. Wang, H. Wang, H. Yan, Z. Gong and Y. Yang, *ACS Appl. Mater. Interfaces,* 2019, **11**,

22745-22753.
424. O. Garcia-Calvo, N. Lago, S. Devaraj and M. Armand, *Electrochimi。 Acta*, 2016, **220**, 587-594.
425. H. Zhang, C. Liu, L. Zheng, F. Xu, W. Feng, H. Li, X. Huang, M. Armand, J. Nie and Z. Zhou, *Electrochimi。 Acta*, 2014, **133**, 529-538.
426. F. Lee, M.-C. Tsai, M.-H. Lin, Y. L. Ni'mah, S. Hy, C.-Y. Kuo, J.-H. Cheng, J. Rick, W.-N. Su and B.-J. Hwang, *J. Mater. Chem. A*, 2017, **5**, 6708-6715.
427. X. Tao, Y. Liu, W. Liu, G. Zhou, J. Zhao, D. Lin, C. Zu, O. Sheng, W. Zhang and H.-W. Lee, *Nano Lett.*, 2017, **17**, 2967-2972.
428. S. Jeong, Y. Lim, Y. Choi, G. Cho, K. Kim, H. Ahn and K. Cho, *J. Power Sources*, 2007, **174**, 745-750.
429. J.-H. Shin, Y.-T. Lim, K.-W. Kim, H.-J. Ahn and J.-H. Ahn, *J. Power Sources*, 2002, **107**, 103-109.
430. A. Hayashi, T. Ohtomo, F. Mizuno, K. Tadanaga and M. Tatsumisago, *Electrochem. Commun.*, 2003, **5**, 701-705.
431. A. Hayashi, R. Ohtsubo, T. Ohtomo, F. Mizuno and M. Tatsumisago, *J. Power Sources*, 2008, **183**, 422-426.
432. B. R. Shin and Y. S. Jung, *J. Electrochem. Soc.*, 2014, **161**, A154-A159.
433. M. Nagao, A. Hayashi and M. Tatsumisago, *Electrochimi. Acta*, 2011, **56**, 6055-6059.
434. M. Nagao, A. Hayashi, M. Tatsumisago, T. Ichinose, T. Ozaki, Y. Togawa and S. Mori, *J. Power Sources*, 2015, **274**, 471-476.
435. N. Machida, K. Kobayashi, Y. Nishikawa and T. Shigematsu, *Solid State Ionics*, 2004, **175**, 247-250.
436. Z. Lin, Z. Liu, N. J. Dudney and C. Liang, *ACS Nano*, 2013, **7**, 2829-2833.
437. H. Nagata and Y. Chikusa, *Chem. Lett.*, 2014, **43**, 1335-1336.
438. S. Kinoshita, K. Okuda, N. Machida, M. Naito and T. Sigematsu, *Solid State Ionics*, 2014, **256**, 97-102.
439. S. Kinoshita, K. Okuda, N. Machida and T. Shigematsu, *J. Power Sources*, 2014, **269**, 727-734.
440. H. Nagata and Y. Chikusa, *J. Power Sources*, 2016, **329**, 268-272.
441. R.-c. Xu, X.-h. Xia, X.-l. Wang, Y. Xia and J.-p. Tu, *J. Mater. Chem. A*, 2017, **5**, 2829-2834.
442. R.-c. Xu, X.-h. Xia, S.-h. Li, S.-z. Zhang, X.-l. Wang and J.-p. Tu, *J. Mater. Chem. A*, 2017, **5**, 6310-6317.
443. E. Umeshbabu, B. Zheng, J. Zhu, H. Wang, Y. Li and Y. Yang, *ACS Appl. Mater. Interfaces*, 2019.
444. Q. Wang, J. Jin, X. Wu, G. Ma, J. Yang and Z. Wen, *Phys. Chem. Chem. Phys.*, 2014, **16**, 21225-21229.
445. Y. Hao, S. Wang, F. Xu, Y. Liu, N. Feng, P. He and H. Zhou, *ACS Appl. Mater. Interfaces*, 2017, **9**, 33735-33739.
446. X. Yu, Z. Bi, F. Zhao and A. Manthiram, *ACS Appl. Mater. Interfaces*, 2015, **7**, 16625-16631.
447. X. Yu, Z. Bi, F. Zhao and A. Manthiram, *Adv. Energy Mater.*, 2016, **6**, 1601392.
448. T. Kobayashi, Y. Imade, D. Shishihara, K. Homma, M. Nagao, R. Watanabe, T. Yokoi, A. Yamada, R. Kanno and T. Tatsumi, *J. Power Sources*, 2008, **182**, 621-625.
449. M. Nagao, Y. Imade, H. Narisawa, T. Kobayashi, R. Watanabe, T. Yokoi, T. Tatsumi and R. Kanno, *J. Power Sources*, 2013, **222**, 237-242.
450. A. Unemoto, S. Yasaku, G. Nogami, M. Tazawa, M. Taniguchi, M. Matsuo, T. Ikeshoji and S.-i. Orimo, *Appl. Phys. Lett.*, 2014, **105**, 083901.
451. P. López-Aranguren, N. Berti, A. H. Dao, J. Zhang, F. Cuevas, M. Latroche and C. Jordy, *J. Power*

Sources, 2017, **357**, 56-60.
452. S. Das, P. Ngene, P. Norby, T. Vegge, P. E. De Jongh and D. Blanchard, *J. Electrochem. Soc.*, 2016, **163**, A2029-A2034.
453. K. K. Fu, Y. Gong, G. T. Hitz, D. W. McOwen, Y. Li, S. Xu, Y. Wen, L. Zhang, C. Wang and G. Pastel, *Energy Environ. Sci.*, 2017, **10**, 1568-1575.
454. D. Zhou, D. Shanmukaraj, A. Tkacheva, M. Armand and G. Wang, *Chem*, 2019, **5**, 2326.
455. D. Zhou, Y. Chen, B. Li, H. Fan, F. Cheng, D. Shanmukaraj, T. Rojo, M. Armand and G. Wang, *Angew. Chem. Int.l Ed.*, 2018, **57**, 10168-10172.
456. J. Hassoun, Y.-K. Sun and B. Scrosati, *J. Power Sources*, 2011, **196**, 343-348.
457. K. Jeddi, Y. Zhao, Y. Zhang, A. Konarov and P. Chen, *J. Electrochem. Soc.*, 2013, **160**, A1052-A1060.
458. J. Wang, J. Yang, J. Xie, N. Xu and Y. Li, *Electrochem. Commun.* 2002, **4**, 499-502.
459. B. H. Jeon, J. H. Yeon, K. M. Kim and I. J. Chung, *J. Power Sources*, 2002, **109**, 89-97.
460. J. Wang, L. Liu, Z. Ling, J. Yang, C. Wan and C. Jiang, *Electrochimi. Acta*, 2003, **48**, 1861-1867.
461. S. S. Zhang and D. T. Tran, *J. Mater. Chem.A*, 2014, **2**, 7383-7388.
462. S. S. Zhang, *J. Electrochem. Soc.*, 2013, **160**, A1421-A1424.
463. H.-S. Ryu, H.-J. Ahn, K.-W. Kim, J.-H. Ahn and J.-Y. Lee, *J. Power Sources*, 2006, **153**, 360-364.
464. Q. Zhao, *Joule*, 2019, **3**, 1569-1571.
465. A. M. Stephan, *Eur. Polymer J.*, 2006, **42**, 21-42.
466. S. S. Zhang and D. T. Tran, *Electrochimi. Acta*, 2013, **114**, 296-302.
467. X. Wang, X. Hao, Y. Xia, Y. Liang, X. Xia and J. Tu, *J. Membrane Sci.*, 2019, **582**, 37-47.
468. Y. Xia, Y. Liang, D. Xie, X. Wang, S. Zhang, X. Xia, C. Gu and J. Tu, *Chem. Eng. J.*, 2019, **358**, 1047-1053.
469. Y. Liang, Y. Xia, S. Zhang, X. Wang, X. Xia, C. Gu, J. Wu and J. Tu, *Electrochimi. Acta*, 2019, **296**, 1064-1069.
470. D.-D. Han, Z.-Y. Wang, G.-L. Pan and X.-P. Gao, *ACS Appl. Mater. Interfaces*, 2019, 11, 18427-18435.
471. J. Zhou, H. Ji, J. Liu, T. Qian and C. Yan, *Energy Storage Mater.*, 2019, **22**, 256-264.
472. Y. Yuan, D. Zheng, Z. Fang, H. Lu, X. Gou, H. Liu and M. Liu, *Ionics*, 2019, **25**, 17-24.
473. D. Yang, L. He, Y. Liu, W. Yan, S. Liang, Y. Zhu, L. Fu, Y. Chen and Y. Wu, *J. Mater. Chem. A*, 2019, **7**, 13679-13686.
474. X. Wang, X. Hao, D. Cai, S. Zhang, X. Xia and J. Tu, *Chem. Eng. J.*, 2019, 122714.
475. J.-H. Park, S.-Y. Yeo, J.-K. Park and Y.-M. Lee, *J. Kore. Electrochem.l Soc.* 2010, **13**, 110-115.
476. J. Shin, S. Jung, K. Kim, H. Ahn and J. Ahn, *J. Mater. Sci.: Mater. Electron.*, 2002, **13**, 727-733.
477. H. Ryu, H. Ahn, K. Kim, J. Ahn, J.-Y. Lee and E. Cairns, *J. Power Sources*, 2005, **140**, 365-369.
478. J.-W. Choi, J.-H. Kim, G. Cheruvally, J.-H. Ahn, K.-W. Kim, H.-J. Ahn and J.-U. Kim, *J. Ind. Eng. Chem.*, 2006, **12**, 939-949.
479. J. Jin, Z. Wen, X. Liang, Y. Cui and X. Wu, *Solid State Ionics*, 2012, **225**, 604-607.
480. X. Hao, H. Wenren, X. Wang, X. Xia and J. Tu, *J. Colloid Interface Sci.*, 2020, **558**, 145-154.
481. K. Jeddi, M. Ghaznavi and P. Chen, *J. Mater. Chem. A*, 2013, **1**, 2769-2772.
482. Y. Zhang, Y. Zhao and Z. Bakenov, *Nanoscale Res. Lett.*, 2014, **9**, 137.
483. M. Li, B. Yang, Z. Zhang, L. Wang and Y. Zhang, *J. Appl. Electrochem.*, 2013, **43**, 515-521.
484. Y. Zhao, Y. Zhang, Z. Bakenov and P. Chen, *Solid State Ionics*, 2013, **234**, 40-45.
485. Y. Zhang, Y. Zhao, Z. Bakenov, D. Gosselink and P. Chen, *J. Solid State Electrochem.*, 2014, **18**,

1111-1116.
486. M. Rao, X. Geng, X. Li, S. Hu and W. Li, *J. Power sources*, 2012, **212**, 179-185.
487. S. Gao, K. Wang, R. Wang, M. Jiang, J. Han, T. Gu, S. Cheng and K. Jiang, *J. Mater. Chem. A*, 2017, **5**, 17889-17895.
488. J. H. Shin and E. J. Cairns, *J. Power Sources*, 2008, **177**, 537-545.
489. M. Baloch, A. Vizintin, R. K. Chellappan, J. Moskon, D. Shanmukaraj, R. Dedryvère, T. Rojo and R. Dominko, *J. Electrochem. Society*, 2016, **163**, A2390-A2398.
490. J.-K. Kim, *Mater. Lett.*, 2017, **187**, 40-43.
491. M. Liu, D. Zhou, Y.-B. He, Y. Fu, X. Qin, C. Miao, H. Du, B. Li, Q.-H. Yang and Z. Lin, *Nano Energy*, 2016, **22**, 278-289.
492. M. Liu, D. Zhou, H. Jiang, Y. Ren, F. Kang and T. Zhao, *Nano Energy*, 2016, **28**, 97-105.
493. C. Yan, X.-Q. Zhang, J.-Q. Huang, Q. Liu and Q. Zhang, *Trends in Chemistry*, 2019.
494. T. Tao, S. Lu, Y. Fan, W. Lei, S. Huang and Y. Chen, *Adv. Mater.*, 2017, **29**, 1700542.
495. Y. Zhao, Y. Ye, F. Wu, Y. Li, L. Li and R. Chen, *Adv.d Mater.*, 2019, **31**, 1806532.
496. S. Xiong, X. Kai, X. Hong and Y. Diao, *Ionics*, 2012, **18**, 249-254.
497. Z. Lin, Z. Liu, W. Fu, N. J. Dudney and C. Liang, *Adv. Funct. Mater.* 2013, **23**, 1064-1069.
498. F. Wu, J. T. Lee, N. Nitta, H. Kim, O. Borodin and G. Yushin, *Adv. Mater.*, 2015, **27**, 101-108.
499. M. Liu, Y. Ren, H. Jiang, C. Luo, F. Kang and T. Zhao, *Nano Energy*, 2017, **40**, 240-247.
500. Y. Guo, H. Li and T. Zhai, *Adv. Mater.*, 2017, **29**, 1700007.
501. G. Ma, Z. Wen, Q. Wang, C. Shen, J. Jin and X. Wu, *J. Mater. Chem. A*, 2014, **2**, 19355-19359.
502. J. Liu, T. Qian, M. Wang, J. Zhou, N. Xu and C. Yan, *Nano Lett.*, 2018, **18**, 4598-4605.
503. H.-K. Jing, L.-L. Kong, S. Liu, G.-R. Li and X.-P. Gao, *J. Mater. Chem. A*, 2015, **3**, 12213-12219.
504. E. Cha, M. D. Patel, J. Park, J. Hwang, V. Prasad, K. Cho and W. Choi, *Nature Nanotech.*, 2018, **13**, 337.
505. G. Ma, Z. Wen, M. Wu, C. Shen, Q. Wang, J. Jin and X. Wu, *Chem. Commun.*, 2014, **50**, 14209-14212.
506. L. Li, S. Li and Y. Lu, *Chem. Commun.*, 2018, **54**, 6648-6661.
507. D. Lin, Y. Liu, Z. Liang, H.-W. Lee, J. Sun, H. Wang, K. Yan, J. Xie and Y. Cui, *Nat. Nanotech.*, 2016, **11**, 626.
508. D. Lin, Y. Liu, W. Chen, G. Zhou, K. Liu, B. Dunn and Y. Cui, *Nano Lett.*, 2017, **17**, 3731-3737.
509. J. Zhao, G. Zhou, K. Yan, J. Xie, Y. Li, L. Liao, Y. Jin, K. Liu, P.-C. Hsu and J. Wang, *Nat. Nanotech.*, 2017, **12**, 993.
510. S. Xu, D. W. McOwen, L. Zhang, G. T. Hitz, C. Wang, Z. Ma, C. Chen, W. Luo, J. Dai and Y. Kuang, *Energy Storage Mater.*, 2018, **15**, 458-464.
511. S. Liu, J. Li, X. Yan, Q. Su, Y. Lu, J. Qiu, Z. Wang, X. Lin, J. Huang and R. Liu, *Adv. Mater.*, 2018, **30**, 1706895.
512. S. Lin, Y. Yan, Z. Cai, L. Liu and X. Hu, *Small*, 2018, **14**, 1800616.
513. C. Jin, O. Sheng, W. Zhang, J. Luo, H. Yuan, T. Yang, H. Huang, Y. Gan, Y. Xia and C. Liang, *Energy Storage Mater.*, 2018, **15**, 218-225.
514. H. Li, Z. Cheng, A. Natan, A. M. Hafez, D. Cao, Y. Yang and H. Zhu, *Small*, 2019, **15**, 1804609.
515. F. Pei, A. Fu, W. Ye, J. Peng, X. Fang, M.-S. Wang and N. Zheng, *ACS Nano*, 2019, **13**, 8337-8346.
516. J. Chang, J. Shang, Y. Sun, L. K. Ono, D. Wang, Z. Ma, Q. Huang, D. Chen, G. Liu and Y. Cui, *Nat. Commun.*, 2018, **9**, 4480.

517. P. G. Bruce, S. A. Freunberger, L. J. Hardwick and J.-M. Tarascon, *Nat. Mater.*, 2012, **11**, 19.
518. Z. Li, J. Zhang, B. Guan, D. Wang, L.-M. Liu and X. W. D. Lou, *Nat. Commun.*, 2016, **7**.
519. X. Ji, K. T. Lee and L. F. Nazar, *Nat. Mater.*, 2009, **8**, 500.
520. C. Hu, H. Chen, Y. Shen, D. Lu, Y. Zhao, A.-H. Lu, X. Wu, W. Lu and L. Chen, *Nat. Commun.*, 2017, **8**, 1-9.
521. F. Pei, L. Lin, D. Ou, Z. Zheng, S. Mo, X. Fang and N. Zheng, *Nat. Commun.*, 2017, **8**, 1-10.
522. T. Zhou, W. Lv, J. Li, G. Zhou, Y. Zhao, S. Fan, B. Liu, B. Li, F. Kang and Q.-H. Yang, *Energy Environ. Sci.*, 2017, **10**, 1694-1703.
523. W. Kong, L. Yan, Y. Luo, D. Wang, K. Jiang, Q. Li, S. Fan and J. Wang, *Adv. Funct. Mater.*, 2017, **27**, 1606663.
524. L. Wang, Z. Dong, D. Wang, F. Zhang and J. Jin, *Nano Lett.*, 2013, **13**, 6244-6250.
525. L. Suo, Y.-S. Hu, H. Li, M. Armand and L. Chen, *Nat. Commun.*, 2013, **4**, 1481.
526. G. G. Eshetu, X. Judez, C. Li, A. Bondarchuk, L. M. Rodriguez-Martinez, H. Zhang and M. Armand, *Angew. Chem. Int. Ed.*, 2017, **56**, 15368-15372.
527. N. Jayaprakash, J. Shen, S. S. Moganty, A. Corona and L. A. Archer, *Angew. Chem.*, 2011, **123**, 6026-6030.
528. C. Zhang, H. B. Wu, C. Yuan, Z. Guo and X. W. D. Lou, *Angew. Chem.*, 2012, **124**, 9730-9733.
529. M. Li, R. Carter, A. Douglas, L. Oakes and C. L. Pint, *ACS Nano*, 2017, **11**, 4877-4884.
530. R. Chen, T. Zhao, J. Lu, F. Wu, L. Li, J. Chen, G. Tan, Y. Ye and K. Amine, *Nano Lett.*, 2013, **13**, 4642-4649.
531. G. Hu, C. Xu, Z. Sun, S. Wang, H. M. Cheng, F. Li and W. Ren, *Adv. Mater.*, 2016, **28**, 1603-1609.
532. Q. Pang, X. Liang, C. Y. Kwok and L. F. Nazar, *Nat. Energy*, 2016, **1**, 16132.
533. D. Su, M. Cortie, H. Fan and G. Wang, *Adv. Mater.*, 2017, **29**, 1700587.
534. D. Su, M. Cortie and G. Wang, *Adv. Energy Mater.*, 2017, **7**, 1602014.
535. M. Yang, X. Hu, Z. Fang, L. Sun, Z. Yuan, S. Wang, W. Hong, X. Chen and D. Yu, *Adv. Funct. Mater.*, 2017, **27**, 1701971.
536. W. Bao, D. Su, W. Zhang, X. Guo and G. Wang, *Adv. Funct. Mater.* 2016, **26**, 8746-8756.
537. Z. W. Seh, W. Li, J. J. Cha, G. Zheng, Y. Yang, M. T. McDowell, P.-C. Hsu and Y. Cui, *Nat. Commun.*, 2013, **4**, 1331.
538. L. Ma, R. Chen, G. Zhu, Y. Hu, Y. Wang, T. Chen, J. Liu and Z. Jin, *ACS Nano*, 2017, 11, 7274-7283.
539. M. Xiang, H. Wu, H. Liu, J. Huang, Y. Zheng, L. Yang, P. Jing, Y. Zhang, S. Dou and H. Liu, *Adv. Funct. Mater.*, 2017, **27**, 1702573.
540. W. Xue, Q.-B. Yan, G. Xu, L. Suo, Y. Chen, C. Wang, C.-A. Wang and J. Li, *Nano Energy*, 2017, **38**, 12-18.
541. T. Chen, L. Ma, B. Cheng, R. Chen, Y. Hu, G. Zhu, Y. Wang, J. Liang, Z. Tie and J. Liu, *Nano Energy*, 2017, **38**, 239-248.
542. J. Pu, Z. Shen, J. Zheng, W. Wu, C. Zhu, Q. Zhou, H. Zhang and F. Pan, *Nano Energy*, 2017, **37**, 7-14.
543. Z. Xiao, Z. Yang, L. Zhang, H. Pan and R. Wang, *ACS Nano*, 2017, **11**, 8488-8498.
544. T. Chen, Z. Zhang, B. Cheng, R. Chen, Y. Hu, L. Ma, G. Zhu, J. Liu and Z. Jin, *J. Am. Chem. Soc.*, 2017, **139**, 12710-12715.
545. W. Tang, Z. Chen, B. Tian, H.-W. Lee, X. Zhao, X. Fan, Y. Fan, K. Leng, C. Peng and M.-H. Kim, *J. Am. Chem. Soc*, 2017, **139**, 10133-10141.

546. D.-R. Deng, F. Xue, Y.-J. Jia, J.-C. Ye, C.-D. Bai, M.-S. Zheng and Q.-F. Dong, *ACS Nano*, 2017, **11**, 6031-6039.
547. X. Li, K. Ding, B. Gao, Q. Li, Y. Li, J. Fu, X. Zhang, P. K. Chu and K. Huo, *Nano Energy*, 2017, **40**, 655-662.
548. R. Fang, S. Zhao, Z. Sun, D.-W. Wang, R. Amal, S. Wang, H.-M. Cheng and F. Li, *Energy Storage Mater.*, 2018, **10**, 56-61.
549. X. Tao, J. Wang, Z. Ying, Q. Cai, G. Zheng, Y. Gan, H. Huang, Y. Xia, C. Liang and W. Zhang, *Nano Lett.*, 2014, **14**, 5288-5294.
550. J. He, L. Luo, Y. Chen and A. Manthiram, *Adv. Mater.*, 2017, **29**, 1702707.
551. Q. Pang, J. Tang, H. Huang, X. Liang, C. Hart, K. C. Tam and L. F. Nazar, *Adv. Mater.*, 2015, **27**, 6021-6028.
552. M. Li, J. Lu, Z. Chen and K. Amine, *Adv. Mater.*, 2018, 1800561.
553. D. Su, M. Cortie and G. Wang, *Adv. Energy Mater.*, 2017, **7**, 1602014.
554. H. Jiang, X. C. Liu, Y. Wu, Y. Shu, X. Gong, F. S. Ke and H. Deng, *Angew. Chem.*, 2018, **130**, 3980-3985.
555. X. Liang, A. Garsuch and L. F. Nazar, *Angew. Chem.*, 2015, **127**, 3979-3983.
556. Y. Zhang, Z. Mu, C. Yang, Z. Xu, S. Zhang, X. Zhang, Y. Li, J. Lai, Z. Sun and Y. Yang, *Adv. Funct. Mater.*, 2018, 1707578.
557. L. Hu, C. Dai, H. Liu, Y. Li, B. Shen, Y. Chen, S. J. Bao and M. Xu, *Adv. Energy Mater.*, 2018, 1800709.
558. J. Xu, W. Zhang, H. Fan, F. Cheng, D. Su and G. Wang, *Nano Energy*, 2018, **51**, 73-82.
559. J. He, Y. Chen and A. Manthiram, *iScience*, 2018, **4**, 36-43.
560. H. Xu and A. Manthiram, *Nano Energy*, 2017, **33**, 124-129.
561. S. Yao, J. Cui, J. Q. Huang, Z. Lu, Y. Deng, W. G. Chong, J. Wu, M. Ihsan Ul Haq, F. Ciucci and J. K. Kim, *Adv. Energy Mater.*, 2018, 1800710.
562. Z. Li, J. Zhang, B. Y. Guan and X. W. Lou, *Angew. Chem.*, 2017, **129**, 16219-16223.
563. Z. Li, Q. He, X. Xu, Y. Zhao, X. Liu, C. Zhou, D. Ai, L. Xia and L. Mai, *Adv. Mater.*, 2018, 1804089.
564. L. Luo, S. H. Chung, H. Yaghoobnejad Asl and A. Manthiram, *Adv. Mater.*, 2018, 1804149.
565. M. Segall, P. J. Lindan, M. a. Probert, C. J. Pickard, P. J. Hasnip, S. Clark and M. Payne, *J. Phys.: Condensed Matter*, 2002, **14**, 2717.
566. J. P. Perdew, K. Burke and M. Ernzerhof, *Phys. Rev. Lett.*, 1996, **77**, 3865.
567. D. Vanderbilt, *Phys. Rev. B*, 1990, **41**, 7892.
568. J. Choi, T.-G. Jeong, B. W. Cho, Y. Jung, S. H. Oh and Y.-T. Kim, *J. Phys. Chem. C*, 2018, **122**, 7664-7669.
569. W. Hume-Rothery, R. E. Smallman and C. W. Haworth, *The Institute of Metals, 1 Carlton House Terrace, London SW 1 Y 5 DB, UK, 1988.*, 1988.
570. R. Smallman and K. Westmacott, *Philos. Mag.*, 1957, **2**, 669-683.
571. A. D. Sendek, E. D. Cubuk, E. R. Antoniuk, G. Cheon, Y. Cui and E. J. Reed, *Chem. Mater.*, 2018, **31**, 342-352.
572. X. Chen, T. Hou, K. A. Persson and Q. Zhang, *Mater. Today*, 2019, **22**, 142-158.